LUND UNIVERSITY

# Electrostatically Driven Structure Formation in Clay Dispersions

Jansson, Maria

2020

*Document Version:*
Publisher's PDF, also known as Version of record

Link to publication

*Citation for published version (APA):*
Jansson, M. (2020). *Electrostatically Driven Structure Formation in Clay Dispersions.* MediaTryck Lund.

*Total number of authors:*
1

**General rights**
Unless other specific re-use rights are stated the following general rights apply:
Copyright and moral rights for the publications made accessible in the public portal are retained by the authors and/or other copyright owners and it is a condition of accessing publications that users recognise and abide by the legal requirements associated with these rights.
• Users may download and print one copy of any publication from the public portal for the purpose of private study or research.
• You may not further distribute the material or use it for any profit-making activity or commercial gain
• You may freely distribute the URL identifying the publication in the public portal

Read more about Creative commons licenses: https://creativecommons.org/licenses/

**Take down policy**
If you believe that this document breaches copyright please contact us providing details, and we will remove access to the work immediately and investigate your claim.

LUND UNIVERSITY

PO Box 117
221 00 Lund
+46 46-222 00 00

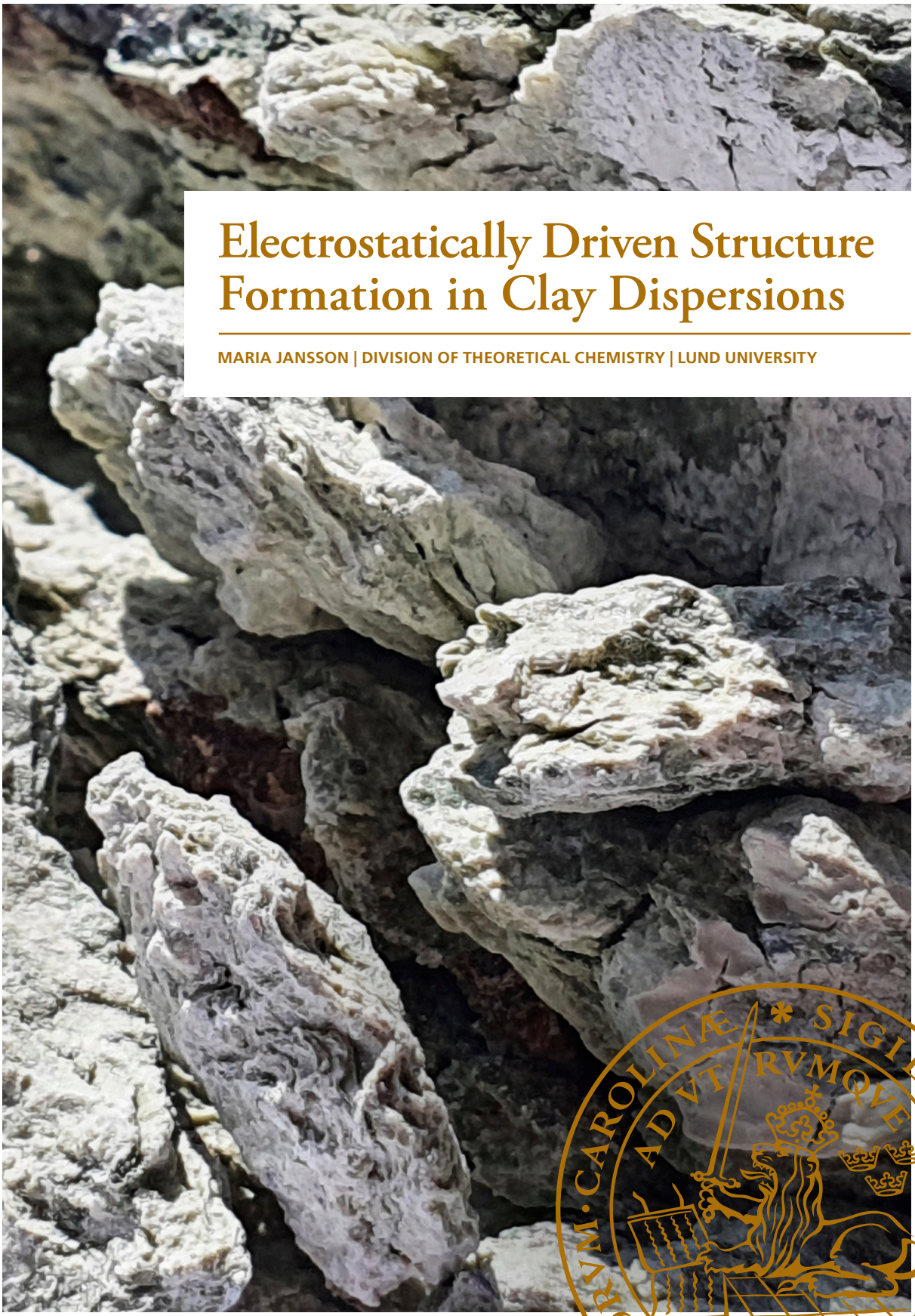

# Electrostatically Driven Structure Formation in Clay Dispersions

MARIA JANSSON | DIVISION OF THEORETICAL CHEMISTRY | LUND UNIVERSITY

# Electrostatically Driven Structure Formation in Clay Dispersions

Maria Jansson

Division of Theoretical Chemistry
Lund University, Sweden


LUND
UNIVERSITY

Doctoral Thesis

Faculty opponent:
Professor Per Hansson, Uppsala University, Sweden

To be presented, with the permission of the Faculty of Science, Lund University, for public criticism in lecture hall C, Center for Chemistry and Chemical Engineering, Lund, Friday October 16 2020, 9.00.

Organization
**LUND UNIVERSITY**
Division of Theoretical Chemistry
P. O. Box 124
SE–221 00 LUND
Sweden

Document name
**DOCTORAL DISSERTATION**

Date of disputation
2020-10-16

Sponsoring organization
eSSENCE, the Swedish national strategic e-science research program.

Author(s)
Maria Jansson

Title and subtitle
Electrostatically Driven Structure Formation in Clay Dispersions

Abstract
Clay minerals consist of clay platelets, which are anisotropic in both size and charge, and these can form a lamellar structure depending on the size, making it a seemingly perfect model system for an electrical double layer. The situation is however, from a structural point, slightly less ideal. Clay is a challenging system since it has a polydisperse distribution of anisotropic clay platelets and it is normally not a homogeneous lamellar material, it is rather described as a disordered structure of stacks of platelets, also denoted tactoids. The stability in saline solution depends strongly on the surface charge density of the platelets, and on the counterion valency. By altering the physiochemical properties, tactoid formation can be promoted, where a transition from a repulsive to an attractive system is obtained. In addition, the overcharging effect may result in tactoidal dissolution, where the tactoids dissolve into smaller sized tactoids.

The aim of this thesis has been to get a better understanding of the electrostatically driven structure formation in clay dispersions and to gain a deeper molecular knowledge of the interactions between the clay platelets, as well as the interactions of the clay platelets in the presence of other macromolecules. The research has focused on extensive studies of the tactoid formation and the tactoidal behaviour of the natural clay mineral montmorillonite and the synthetic clay mineral Laponite® by varying the valency of the counterions, the temperature, and the solvent properties, as well as with addition of multivalent salt and positively charged peptides and polyelectrolytes. It was found that it is possible to capture the behaviour of tactoid formation, tactoidal growth, and tactoidal dissolution for clay systems where the interactions are dominated by electrostatics by utilising coarse-grained molecular dynamics simulations based on the continuum model in combination with a number of different experimental techniques.

Key words
Clay, Montmorillonite, Laponite®, Nanoplatelets, Tactoid, Anisotropy, Overcharging, Intercalation, Coarse-grained modeling, MD simulations, MC simulations, SAXS, Swelling pressure, ζ-potential

Classification system and/or index terms (if any)

Supplementary bibliographical information

Language
English

ISSN and key title

ISBN
978-91-7422-754-3 (print)
978-91-7422-755-0 (pdf)

Recipient's notes

Number of pages
180

Price

Security classification

I, the undersigned, being the copyright owner of the abstract of the above-mentioned dissertation, hereby grant to all reference sources the permission to publish and disseminate the abstract of the above-mentioned dissertation.

Signature Maria Jansson Date 2020-09-03

DOKUMENTDATABLAD enl SIS 61 41 21

# Electrostatically Driven Structure Formation in Clay Dispersions

Maria Jansson

Division of Theoretical Chemistry
Lund University, Sweden


LUND
UNIVERSITY

ELECTROSTATICALLY DRIVEN STRUCTURE FORMATION IN CLAY DISPERSIONS

**Front cover:**
Bentonite clay from Cortijo de Archidona Clay Mine, Cabo de Gata, Almería, Spain.
Photo by Maria Jansson

Parts of this thesis have been published before in:
Jansson, Maria *Evaluation of the Tactoid Formation in Clay Systems* (2019).

© 2020 Maria Jansson

Theoretical Chemistry
Department of Chemistry
Faculty of Science
Lund University

ISBN: 978-91-7422-754-3 (print)
ISBN: 978-91-7422-755-0 (pdf)

Printed in Sweden by Media-Tryck, Lund University, Lund 2020


Media-Tryck is an environmentally certified and ISO 14001:2015 certified provider of printed material. Read more about our environmental work at www.mediatryck.lu.se

MADE IN SWEDEN

# Abstract

Clay minerals consist of clay platelets, which are anisotropic in both size and charge, and these can form a lamellar structure depending on the size, making it a seemingly perfect model system for an electrical double layer. The situation is however, from a structural point, slightly less ideal. Clay is a challenging system since it has a polydisperse distribution of anisotropic clay platelets and it is normally not a homogeneous lamellar material, it is rather described as a disordered structure of stacks of platelets, also denoted tactoids. The stability in saline solution depends strongly on the surface charge density of the platelets, and on the counterion valency. By altering the physiochemical properties, tactoid formation can be promoted, where a transition from a repulsive to an attractive system is obtained. In addition, the overcharging effect may result in tactoidal dissolution, where the tactoids dissolve into smaller sized tactoids.

The aim of this thesis has been to get a better understanding of the electrostatically driven structure formation in clay dispersions and to gain a deeper molecular knowledge of the interactions between the clay platelets, as well as the interactions of the clay platelets in the presence of other macromolecules. The research has focused on extensive studies of the tactoid formation and the tactoidal behaviour of the natural clay mineral montmorillonite and the synthetic clay mineral Laponite® by varying the valency of the counterions, the temperature, and the solvent properties, as well as with addition of multivalent salt and positively charged peptides and polyelectrolytes. It was found that it is possible to capture the behaviour of tactoid formation, tactoidal growth, and tactoidal dissolution for clay systems where the interactions are dominated by electrostatics by utilising coarse-grained molecular dynamics simulations based on the continuum model in combination with a number of different experimental techniques.

# Contents

# List of publications

This thesis is based on the following publications, referred to by their Roman numerals:

I **Temperature Response of Charged Colloidal Particles by Mixing Counterions Utilizing $Ca^{2+}$/$Na^{+}$ Montmorillonite as Model System**

A. Thuresson, **M. Jansson**, T. S. Plivelic and M. Skepö
Journal of Physical Chemistry C, 2017, 121, pp. 7951–7958

II **The Effect of the Relative Permittivity on the Tactoid Formation in Nanoplatelet Systems. A Combined Computer Simulation, SAXS, and Osmotic Pressure Study**

**M. Jansson**, A. Thuresson, T. S. Plivelic, J. Forsman and M. Skepö
Journal of Colloid and Interface Science, 2018, 513, pp. 575–584

III **Nanoplatelet Interactions in the Presence of Multivalent Ions: The Effect of Overcharging and Stability**

**M. Jansson**, D. Belić, J. Forsman and M. Skepö
Journal of Colloid and Interface Science, 2020, 579, pp. 573–581

IV **Intercalation of cationic peptides within Laponite layered clay minerals in aqueous suspensions: The effect of stoichiometry and charge distance matching**

**M. Jansson**, S. Lenton, T. S. Plivelic and M. Skepö
Journal for Colloid and Interface Science, 2019, 557, pp. 767–776

v **Polyelectrolyte-Nanoplatelet Complexation: Is it Possible to Predict the State Diagram?**

**M. Jansson** and M. Skepö
International Journal of Molecular Science, 2019, 20 pp. 6217

All papers are reproduced with permission of their respective publishers.

# Populärvetenskaplig sammanfattning

Lera är ett naturligt förekommande material och består utav små finkorniga lermineraler, vilka utgörs till stor del av laddade nanopartiklar, även kallade lerflak. Dessa har en platt form med en tjocklek på en miljarddels meter (1 nanometer) och diametern kan variera alltifrån fem till tusen gånger större än tjockleken. Detta kan jämföras med ett A4-ark, där längden på kortsidan är tusen gånger större än tjockleken. Lera härstammar ifrån olika typer av bergarter vilket ger upphov till lerans struktur, egenskaper samt komposition. Det är därför det finns en stor variation av leror där ingen är den andra lik. Utöver naturligt förekommande leror finns det även lerliknande mineraler som är tillverkade på syntetisk (konstgjord) väg. Fördelen med syntetisk tillverkning är att lerans egenskaper kan kontrolleras och modifieras samt att andelen orenheter är mycket lägre jämfört med naturliga leror.

Lera som material används inom en mängd olika användningsområden, bland annat vid kärnavfallsförvaring, papperstillverkning och borrning efter gas eller olja. För slutförvaringen av det farliga radioaktiva avfallet från de svenska kärnkraftverken planerar Sverige att placera avfallet i kopparkapslar som skall bäddas in i bentonitlera 500 meter under marken i urberget. Bentonitleran består till huvudsak av lermineralen montmorillonit, och tanken är att den skall skydda kopparkapseln både fysiskt och kemiskt under väldigt lång tid tills dess att det anses ofarligt för människan. Då det över tid finns variationer i grundvattnets innehåll och dess temperatur, är det viktigt att utvärdera lerans egenskaper och hur den påverkas av de yttre faktorerna, allt för att få en förståelse kring hur och varför den beter sig som den gör. Vid papperstillverkning använder man lera som fyllnadsämne för att öka papprets vithet och minska papprets genomskinlighet. Bentonitlera tillsätts även i vissa fall till borrvätskan vid borrning efter gas eller olja, detta eftersom lera är en tixotrop vätska i vatten, vilket är en egenskap som gör att vätskan har en låg viskositet vid rörelse och en hög viskositet vid stillastående. Ett klassiskt exempel på en tixotrop vätska är kvicksand. Genom att använda lera i borrvätskan fungerar den som smörjmedel samt att den förhindrar stenar att falla ner

till botten av borrhålet när man slutar pumpa upp det material man vill avlägsna ifrån borrhålet eftersom leran då stelnar. Då även andra typer av material ibland tillsätts i borrvätskan är det viktigt att förstå hur och varför dessa material interagerar med leran.

Utöver dessa användningsområden har lera också föreslagits att användas som läkemedelsbärare. Lera har egenskapen att den kan kapsla in vissa typer av läkemedelssubstanser, till exempelvis katjoniska (positivt laddade) antimikrobiella peptider, vilka används i antibiotika och läkemedel mot cancer. Detta bidrar till att frisättningen av läkemedlet i kroppen kan kontrolleras, vilket i sin tur leder till en förstärkt och/eller förlängd effekt av läkemedlet samt en minskad toxicitet (giftighet). Peptider kan ses som laddade kedjor, och beroende på sammansättning kommer de att bete sig olika vid närvaro av lera. Det är därför viktigt att studera hur och varför peptiden interagerar med leran för att få en djupare förståelse över hur man kan utnyttja lera som läkemedelsbärare till framtida läkemedel.

De leror som har undersökts i denna avhandling är den naturliga lermineralen montmorillonit samt den syntetiska lermineralen Laponite®. I dessa leror är lerflaken uppbyggda utav tre lager och den totala laddningen på lerflaket är negativ då det förekommer antingen tomrum eller utbyten av olika atomer i lagren. För att balansera den negativa laddningen sitter det positivt laddade motjoner på lerflaken, vilket gör att hela systemet blir elektroneutralt. Lerorna sväller när de blandas i vatten eftersom motjonerna frisätts ifrån lerflaken. Detta skapar ett ökat osmotiskt tryck och ger upphov till att de negativa laddningar på lerflaken exponeras vilket får dem att repellera (stöta bort) varandra. Svällningen beror på lerflakets struktur, komposition och laddning, men även på motjonernas valens (laddning) samt andra yttre faktorer såsom tillsats av salt, temperatur och vilken surhetsgrad vattnet har. Genom att förändra vissa av dessa faktorer kan man få lerflaken att aggregera till större partiklar, där lerflaken oftast staplas på varandra som en bunt pappersark, där denna struktur kallas för taktoid.

Syftet med denna avhandling har varit att få en djupare förståelse över lerornas egenskaper och beteende genom att kombinera datorsimuleringar med experiment. De experimentella teknikerna har gett information bland annat över hur lerflaken interagerar och organiserar sig i förhållande till varandra samt hur mycket de sväller genom att mäta det osmotiska trycket leran ger upphov till. Datorsimuleringar har använts för att försöka förutspå lerans beteende och förstå de mekanismer som ger upphov till lerans egenskaper.

För den naturliga lermineralen montmorillonit undersöktes svällningens beroende på temperaturen, vilken typ av motjon med avseende på dess valens samt lösningsmedlet. Vid en temperaturökning förändrades svällningen hos leran, det osmotiska trycket ökade för den lera som hade natriumjoner som motjoner, där natrium motsvarar en positiv laddning på ett. Genom att helt byta ut natriumjonerna mot kalciumjoner, där kalcium

motsvarar en positiv laddning på två, minskade det osmotiska trycket när temperaturen ökade. De experimentella resultaten kunde även fångas med datorsimuleringar där det visade sig att mekanismen kunde förstås genom förhållandet mellan krafterna i systemet och valensen på motjonerna. Detta undersöktes genom att successivt byta ut natriumjonerna mot kalciumjoner, men samtidigt behålla den totala laddningen av motjonerna i systemet, vilket gav upphov till en övergång ifrån ett repulsivt till ett attraktivt system när andelen kalciumjoner ökade. Det repulsiva systemet innehöll enstaka lerflak medan i det attraktiva systemet hade taktoider bildats. På liknande sätt visade det även sig att det är möjligt att justera krafterna i systemet genom att byta ut lösningsmedlet från vatten till exempelvis etanol. Genom att öka koncentration av etanol för leran med natriumjoner, minskade svällningen och det osmotiska trycket, vilket motsvarar samma övergång som för motjons utbytet. För leran med kalciumjoner, observerades ett icke-monotont beteende för svällningen, där det osmotiska trycket först ökade vid låg koncentration av etanol för att sedan minska vid högre etanolkoncentration. Detta kan förklaras utifrån att avståndet mellan lerflaken ökar när de mindre vattenmolekylerna byts ut till de större etanolmolekylerna, vilket i sin tur bidrar till ett ökat osmotiskt tryck.

Då svällningen och stabiliteten av lerlösningar även beror på tillsats av salt, salthalt samt typ av salt, studeras dessa effekter för den syntetiska lermineralen Laponite® med natriumjoner som motjoner. Stabiliteten syftar till hur lerflaken är organiserade i förhållande till varandra i lösningen där ett stabilt system består utav enstaka lerflak väl utspridda i lösningen medan i ett ostabilt system har lerflaken aggregerat och bildat taktoider. Vid tillsats av ett salt där den positiva saltjonen har en valens på tre, ett så kallat trivalent salt, kunde det ses att stabiliteten minskade med ökad salthalt. Även här återfanns en övergång från ett repulsivt till ett attraktivt system där de enstaka lerflaken bildade taktoider. Den största taktoiden, observerades i systemet där det trivalenta saltet helt neutraliserade de negativa laddningarna på lerflaken. Sedan med ett överskott av salt kunde det ses att taktoiderna löstes upp till mindre taktoider vilket antyder på att saltet gav upphov till att lerflaken blev överladdade, vilket hänvisar till överladdningseffekten. Dessa beteenden kunde fångas både med datorsimuleringar och experiment där resultaten överensstämde bra med varandra.

Vidare undersöktes möjligheten av att använda lera som läkemedelsbärare där en katjonisk peptid blandades med lermineralen Laponite®. När peptidkoncentrationen ökade i systemet kunde det ses att taktoider bildades, vilka sedan växte i storlek och till sist löstes upp till mindre taktoider. Detta påvisade samma beteende som sågs vid tillsats av det trivalenta saltet, där övergången ifrån repulsiva till attraktiva krafter samt överladdningseffekten kunde ses i systemet. De experimentella resultaten överensstämde bra med datorsimuleringarna vilka visade att Laponite® är en god kandidat som läkemedelsbärare för katjoniska peptider. Med hjälp utav datorsimuleringar kan egenskaperna

både hos leran och peptiden enkelt förändras och modifieras för att optimera hur peptiden interagerar med leran. Därmed är datorsimuleringar ett användbart verktyg för att hjälpa till i designen av nya effektiva läkemedelssystem.

Till sist gjordes en teoretisk studie över vilka typer av strukturer som kan bildas i ett system med negativt laddade lerflak och en positivt laddad kedja. Det visade sig att komplexen som bildades berodde både på lerflakens och kedjans egenskaper, där flera olika strukturer för komplexen erhölls. Detta styrker det faktum att datorsimuleringar är ett kraftfullt verktyg för att förstå hur och varför lera interagerar med andra typer av partiklar samt gör det möjligt att förutspå strukturen på komplexen och lerans beteende.

# List of abbreviations

| | |
|---|---|
| **$Arg_{10}$** | deca-Arginine |
| **CEC** | Cation exchange capacity |
| **cryo-TEM** | Cryogenic transmission electron microscopy |
| **DLS** | Dynamic light scattering |
| **FWHM** | Full width at half-maximum |
| **HS** | Hard-sphere |
| **LJ** | Lennard-Jones |
| **MC** | Monte Carlo |
| **MD** | Molecular dynamics |
| **O** | Octahedral sheet |
| **PB** | Poisson-Boltzmann |
| **PMF** | Potential of mean force |
| **PZC** | Point of zero charge |
| **RDF** | Radial distribution function |
| **SAXS** | Small angle X-ray scattering |
| **SC** | Strong coupling |
| **T** | Tetrahedral sheet |
| **TEM** | Transmission electron microscopy |

| | |
|---|---|
| **TLJ** | Truncated and shifted Lennard-Jones |
| **WHAM** | Weighted histogram analysis method |
| $\zeta$**-potential** | Zeta-potential |

# 1. Introduction

## 1.1 Clay and clay minerals

Clay science is a broad interdisciplinary field dating back to the mid-1930s (Bergaya et al. (2006)). Prior to the development of modern analytical techniques, it was difficult to characterise small-sized particles composed of crystal imperfections in various degrees, which quite naturally led to problems with the nomenclature of the terms clay and clay mineral. However, the development and improvements of different analytical techniques in the 1950s made it possible to accumulate information about the identification of clay. Since then, clay scientists have made attempts to unify the nomenclature and classification of clay on an international level (Bailey (1980)). One of the definitions of clay is: *a naturally occurring material composed of primarily fine-grained minerals, which is generally plastic at appropriate water contents, and will harden when dried or fired*. In the classification, the fine-grained minerals are defined to have an upper size limit of about 2-4 μm. Furthermore, clay minerals can be defined as: *phyllosilicate minerals and minerals which impart plasticity to clay and hardens upon drying or firing* (Guggenheim & Martin (1995)).

Clay minerals are formed in soils, sediments and by diagenetic alteration of volcanic ash, and depending on which type of rock it is originated from, there is a wide variation of clay minerals with different compositions, structures, and properties. These clay minerals belong to the family of phyllosilicates, or layer silicates, and the majority are aluminosilicates. The structural layers consist of two-dimensional continuous tetrahedral (T) sheets, which are linked in the unit structure to octahedral (O) sheets, or to groups of coordinated cations, or individual cations. The T sheets are composed of oxygen coordinated silicon and/or aluminium atoms ([Si,Al]-O), and the O sheet consists of oxygen coordinated aluminium, magnesium, and/or iron atoms ([Al,Mg,Fe]-O) (Bailey (1980); Deer et al. (2013)). The structure of the octahedral component is either defined as di- or trioctahedral, depending on whether each oxygen or hydroxide ion is surrounded by two or three cations. Moreover, the T and O sheets can be connected

in T-O pairs or in T-O-T groups, thus, clay minerals are divided into the two main types of 1:1 (TO) and 2:1 (TOT) layer clay minerals, which are schematically illustrated in Fig. 1.1.

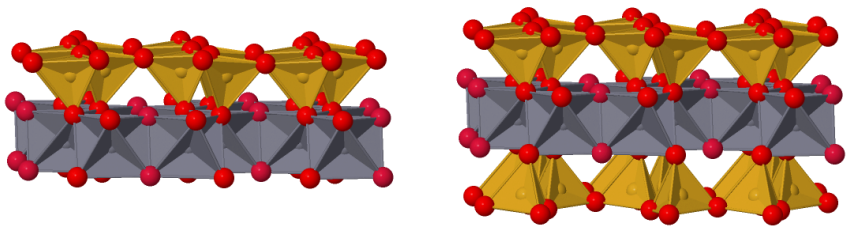

(a) (b)

**Figure 1.1:** Schematically illustrated structures of (a) a 1:1 (TO) clay mineral and (b) a 2:1 (TOT) clay mineral. The tetrahedral silica sheet is represented in beige, the octahedral alumina or magnesia sheet is represented in grey, and the connecting oxygen atoms are represented by the red spheres.

The primary groups of clay minerals are: (i) kaolinite, (ii) illite, (iii) smectite, and (iv) vermiculite. Kaolinites are dioctahedral and belongs to the 1:1 clay minerals, where the thickness of the silica T sheet and the alumina O sheet is about 0.7 nm (Fig. 1.1a). The ideal chemical formula of kaolinite is $Al_2[Si_2O_5](OH)_4$, which is a non-swelling clay mineral due to the strong attraction between the adjacent layers, arising from the hydrogen bonding between the hydroxyl (OH) groups of the O sheet and the oxygen atoms (O) of the T sheet (Grim (1953); Bergaya et al. (2006); Deer et al. (2013)).

The groups of illite, smectite, and vermiculite all belong to the 2:1 clay minerals. The structural layer consists of one central O sheet sandwiched between two T sheets with a thickness of about 1 nm, and is denoted as a clay *platelet* (Fig. 1.1b). The octahedral component for the clay minerals within the groups differs; for illites it is mostly dioctahedral, for vermiculites it is mostly trioctahedral, and for smectites it can be either di- or trioctahedral depending on the particular smectite. The main smectites are: montmorillonite, beidellite, nontronite, saponite, hectorite, and suconite, where the three former have a dioctahedral structure and the three latter are trioctahedral.

The characteristic feature of a 2:1 clay mineral is the permanent negative surface charge density, which originates from either: (i) isomorphic substitution of silica ($Si^{4+}$) ions by aluminum ($Al^{3+}$) ions in the tetrahedral sheet, (ii) isomorphic substitution of aluminum ($Al^{3+}$) ions or magnesium ($Mg^{2+}$) ions by cations with a lower valency in the octahedral sheet, or (iii) site vacancies in the crystal lattice. To conserve electroneutrality, the net-charge deficiency is balanced by charge compensating exchangeable cations adsorbed in the inter-layer between the platelets (Grim (1953); Deer et al. (2013)). The property of the ionic exchange capability is described by the cation exchange capacity (CEC),

and thus, the CEC value is a measure of the negatively charged sites on the clay platelet. Moreover, the sign and density of the clay platelet edge charges depend on the pH of the dispersion, which arises from 'broken bonds' of Si-O-Si, Al-O-Al, and/or Mg-O-Mg converting into hydroxyl groups of Si-OH, Al-OH, and/or Mg-OH. Hence, the edge of the platelet may either possess a positive, a negative, or a neutral charge (Bergaya et al. (2006); Tawari et al. (2001); Martin et al. (2002)).

In addition to the natural clay minerals, there are also synthetic hectorite-type clay minerals, such as Laponite®. These were invented in the 1960s by B. S. Neumann from Laporte Industries Ltd (Neumann (1971)) with the aim to manufacture clay-like minerals with a higher purity and better rheological properties than that of natural clay minerals. A further objective of the invention was that the synthesis could be carried out with readily available chemicals on a large commercial scale.

The anisotropic features of the clay platelet structure and charge distribution contribute significantly to the physiochemical properties of the clay suspension. When a 2:1 swelling clay mineral is dispersed in an aqueous solution, the clay platelets become ionised and a release of counterions will occur, creating an electrical double layer. The double-layer repulsion causes the clay to swell, where the swelling depends strongly on the surface charge density and the type of counterion, as well as on the addition of charged compounds such as salts. The different configurations of the clay platelets in solution have been proposed to be: (i) *House-of-Cards*, where the adjacent platelets are interacting face-to-edge, also called a $T$-configuration (Fig. 1.2a), (ii) *Stacked Platelets*, in which the platelets aggregate in a face-to-face configuration with an equidistant separation, denoted as tactoid (Fig. 1.2b), and (iii) *Overlapping Coins*, where the configuration consists of a band-like structure (Fig. 1.2c) (Delhorme et al. (2012)).

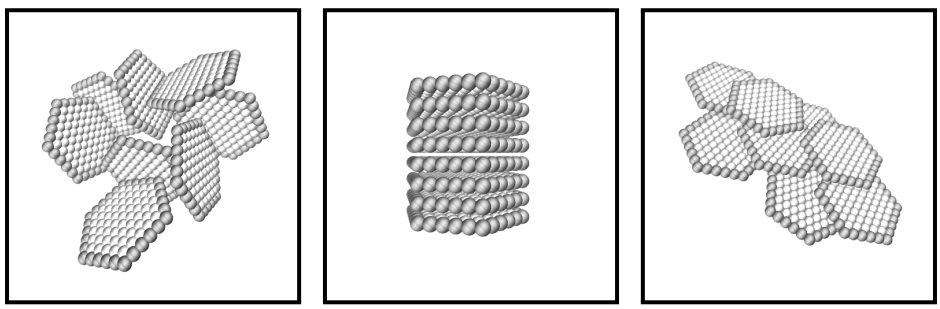


**Figure 1.2:** Illustrative representations for the configurations of the clay platelets: (a) house-of-cards, (b) stacked platelets, i.e. tactoid, and (c) overlapping coins. The platelets are represented as connected negatively (light grey) and positively (dark grey) charged spheres.

### 1.1.1 Montmorillonite

The smectite montmorillonite consists of polydisperse clay platelets in the lateral dimensions, where the diameter is typically found in the range $\sim$ 5-1000 nm (Michot et al. (2004)). The ideal chemical formula (Karnland et al. (2006); Deer et al. (2013)) is defined as:

$$M_{x+y}(Si_{8-x}Al_x)(Al_{4-y}Mg_y(Fe))O_{20}(OH)_4 \cdot nH_2O\,. \tag{1.1}$$

Here, M represents the monovalent positively charged counterions located in the interlayer between the platelets, $x$ is the amount of substituted silica ($Si^{4+}$) ions by aluminum ($Al^{3+}$) ions in the T sheet, and $y$ is the amount of substituted aluminum ($Al^{3+}$) ions by magnesium ($Mg^{2+}$) ions in the O sheet. Depending on the substitution parameters $x$ and $y$, the surface charge density for montmorillonite varies in the range of 0.4 to 1.2 unit charges per $O_{20}(OH)_4$-unit, i.e. $0.4 < ( x + y ) < 1.2$. By definition the charge of the T sheet is lower than the O sheet, i.e. $x < y$ (Karnland et al. (2006); Hedström et al. (2011)). The negative surface charge is neutralised by $( x + y )$ monovalent counterions such as sodium ($Na^+$), potassium ($K^+$), and/or lithium ($Li^+$) ions. However, the high CEC value of montmorillonite makes it possible to exchange the valency of the counterions by replacing the monovalent ions with multivalent ions, for example to calcium ($Ca^{2+}$), magnesium ($Mg^{2+}$), and/or lanthanum ($La^{3+}$) ions. The structural and swelling properties of montmorillonite are strongly affected by the valency and the type of counterion. For the monovalent ions of sodium and lithium, the clay platelets can dissociate and swell extensively, whereas for multivalent counterions, tactoids are formed with an equidistant separation of about 2 nm (Bergaya et al. (2006); Segad et al. (2015)).

In paper I and II, the Wyoming bentonite clay MX-80 was used, which is produced by the American Colloid Company and has a high content of the montmorillonite clay mineral. MX-80 contains about 80% of montmorillonite, and the counterions are usually a mixture of both mono- and divalent cations, where sodium is the dominating counterion. The bentonite clay is often described through its dominating counterion, since it, to a large extent determines the swelling property in water. Thus, MX-80 is referred as sodium bentonite or sodium saturated montmorillonite from MX-80 with the chemical formula (Karnland et al. (2006)):

$$Na_{0.65}(Si_{7.89}Al_{0.11})(Al_{3.10}Mg_{0.49}Fe_{0.38}Ti_{0.01})O_{20}(OH)_4\,. \tag{1.2}$$

Bentonite clay is planned to be used as a barrier material in repositories for final storage of highly radioactive spent nuclear fuel, where MX-80 is a suggested candidate. The clay

will act as an sealing buffer and should fulfil the following properties: (i) high swelling capacity in order to seal itself around the canister and fill any cracks in the bedrock, (ii) low hydraulic conductivity to minimise any mass transport to and from the canister in order to protect it from corrosion and, in case a canister breaks, prevent any radioactive substances to leak into the bedrock, (iii) appropriate plasticity and stiffness to retain the canister in its position and reduce the force from any movements of the bedrock, (iv) long-term stability, since the time period for the radioactive material to become harmless to humans can be up to one million years, and (v) high thermal conductivity to ensure rapid transfer of the heat generated by the decay of the radioactive material (Karnland et al. (2006); SKB (2011)).

### 1.1.2 Laponite®

The products of the synthetic trioctahedral smectite Laponite® from BYK Additives (BYK (2016)) are divided into groups of gel forming and sol forming grades, where the former is a high viscosity and the latter is a low viscosity colloidal dispersion. The synthesis process is based on abundant inorganic mineral sources by combining salts of sodium, magnesium, and lithium along with sodium silicate. The chemical composition is analogue to naturally occurring smectite clay minerals, such as hectorite, and the empirical formula of the Laponite® clay mineral is:

$$\mathrm{Na}_{0.7}(\mathrm{Si}_8)(\mathrm{Mg}_{5.5}\mathrm{Li}_{0.3})\mathrm{O}_{20}(\mathrm{OH})_4\,. \tag{1.3}$$

The benefit of Laponite® is that it is free of crystalline silica and it has a high purity with a low content of transition metals or other impurities. Thus, it is widely used as a rheology-modifier in many technological applications, for example in household and personal care products, paper and polymer films, paints, and surface coatings. Moreover, the size distribution of the Laponite® platelets is monodisperse and the average size is much smaller than for natural clay minerals, where the thickness is $\sim$ 1 nm and the diameter is $\sim$ 25 nm (BYK (2016)).

The Laponite® clay mineral used in Paper III and IV was the gel forming grade product of Laponite®-XLG XR. The platelets surface charge density is evaluated from the CEC, which is $\sim$ 0.5 mEq/g for Laponite®-XLG XR according to the technical information (BYK (2016)). The edge charges of the platelet (described in section 1.1) is pH-dependent due to the exposed magnesium hydroxyl groups (Mg-OH), where the point of zero charge (PZC) is at pH $\approx$ 11. Approximately 10% of the total charge of the platelet is represented by the edge charges (Tawari et al. (2001); Martin et al. (2002); BYK (2016)). The net negative charge of the platelet is confirmed from measured values of the zeta-potential ($\zeta$-potential) reported in the literature, i.e. $\sim$ -21 to -29 mV (Jansson

et al. (2019)), $\sim$ -52 mV (Labanda & Llorens (2005); Labanda et al. (2007)), $\sim$ -40 to -45 mV (Huang & Berg (2006)), $\sim$ -58 mV (Zhang et al. (2008)), and $\sim$ -45 mV (Manilo et al. (2014)). The difference between the values derives from the type of Laponite® used in the studies.

In aqueous suspensions below the pH correlated with the PZC (pH < 11), Laponite® acts as a weak base due to dissociation of hydroxide ions ($OH^-$) from the edges, which causes an increase in the pH of the solution (Tawari et al. (2001); Jatav & Joshi (2014)). Moreover, the chemical stability of Laponite® in aqueous suspensions depends on the pH of the solution, the Laponite® concentration, and the concentration of added salt. It has been found that dissolution of Laponite® occurs at pH below 9 due to leaching of magnesium ions ($Mg^{2+}$) and hydrogen ion ($H^+$) attacks (Thompson & Butterworth (1992); Mohanty & Joshi (2016)). The rate of chemical degradation is lower at high pH ($pH > 9$) and high Laponite® and/or salt concentrations (Thompson & Butterworth (1992); Jatav & Joshi (2014)), hence, the dissolution can be stabilised. Further, the degradation can be delayed by working under nitrogen atmosphere in order to reduce the dissolution of carbon dioxide ($CO_2$) from the ambient air and the formation of carbonic acid (Mourchid & Levitz (1998)).

Furthermore, Laponite® has a rich phase and rheological behaviour and its phase (state) diagram has been extensively studied in the literature, e.g. see the comprehensive review articles by Ruzicka & Zaccarelli (2011) and Suman & Joshi (2018), and the references therein. The dependent factors contributing to the different phases are the Laponite® concentration and the concentration of ionic compounds, such as added salts, as well as on the time of gelling, i.e. aging. The diverse phase diagram contains flocculants, isotropic liquids, isotropic gels, and nematic gels, where the tactoidal size distribution and the exfoliation process depends on the Laponite® concentration (Rosta & von Gunten (1990)). For an aqueous salt-free dispersion with increasing Laponite® concentration ($C_{\mathrm{L}}$), the phase diagram can be described as follows: (i) for $C_{\mathrm{L}} \leq 1$ wt%, the dispersion undergoes a sol/gel transition, i.e. a phase separation between a sol (clay-poor) and gel (clay-rich) phase (Mourchid et al. (1995); Tanaka et al. (2004); Mongondry et al. (2005); Ruzicka et al. (2011)). (ii) For $1 < C_{\mathrm{L}} \lesssim 3$ wt%, the dispersion is in an arrested attractive or repulsive gel state, hence, this region is usually divided into two different types: for $C_{\mathrm{L}} < 2$ wt%, an attractive gel, consisting of more individual platelets, is present, while for $C_{\mathrm{L}} \geq 2$ wt%, a glassy state is found where small tactoids are present in the gel and the process of structural aging has been observed (Mongondry et al. (2005); Ruzicka et al. (2008); Yu et al. (2015); Jatav & Joshi (2018)), the latter type has been interpreted in terms of a Wigner glass (Ruzicka et al. (2010)), or a repulsive glass (Jabbari-Farouji et al. (2008)). (iii) For $C_{\mathrm{L}} \gtrsim 3$ wt%, the formation of a nematic ordered phase has been observed (Mourchid et al. (1998); Shahin et al. (2011)). In addition, for a dispersion with a salt concentration of sodium chloride (NaCl) higher than

20 mM, phase separation occurs in the form of flocculation or sedimentation of larger aggregates (Mourchid et al. (1998); Mongondry et al. (2005)). A schematic illustration of the Laponite® phase (state) diagram is shown in Fig. 1.3, where the waiting time for the dispersions is considered to be long enough for no further macroscopic changes to occur in the samples (Ruzicka & Zaccarelli (2011)).

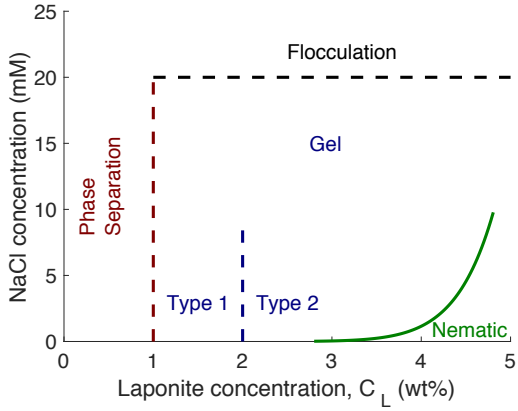


**Figure 1.3:** A schematic illustration of the Laponite® phase (state) diagram for an aqueous dispersion with increasing Laponite® concentration ($x$-axis) and increasing NaCl salt concentration ($y$-axis).

## 1.2 Polymer-clay nanocomposites

A polymer is a large molecule composed of linked repeating subunits, called monomers, and depending on the sequence of the monomers, the polymers are referred to as homopolymers, heteropolymers, or block copolymers. Moreover, polymers can either be found in nature or be prepared by a chemical reaction, hence, polymers may be divided into two categories: biopolymers or synthetic polymers (Evans & Wennerström (1999)). Examples of biopolymers are cellulose, DNA, and starch, whereas synthetic polymers include, for instance, polyvinyl chloride (PVC), polystyrene, and silicone. In addition, if the functional group in the monomeric unit carries a charge, it is referred as an ionic polymer or a polyelectrolyte. Depending on how the charges are localised within the polymer these are classified as univalent or multivalent polymers. The former has a homogenous distribution in terms of the sign of the functional group charge, such as cationic polyelectrolytes or anionic polyelectrolytes, whereas the latter possess both cationic and anionic functional groups within the polymer chain and are thus amphoteric (Shaikh et al. (2017)).

A composite material can be defined as a combination of at least two materials, or constituents, that are physically well-defined and dispersed in a controlled manner in order

to achieve optimum properties, in which the properties are pre-eminent from those of the individual constituents (Chen et al. (2008)). For a nanocomposite, at least one of the constituent phases need to have one dimension in the nanoscale range ($<$ 100 nm) (Raquez et al. (2013)). Materials that can be found in the category of nanocomposites are: nanoparticles dispersed in a continuous matrix, dispersion of carbon nanotubes in a matrix, and smectite minerals that are intercalated and/or exfoliated within a continuous phase. The latter refers to a polymer-clay nanocomposite, in which the research interest skyrocketed in the early 1990s thanks to the pioneering work of Toyota automotive corporation (Okada et al. (1988)). In addition, the enhanced properties of the polymer in polymer-clay nanocomposites makes it suitable to use in packing and construction materials, flame retardants, protective films, electrical appliances, and for biodegradable applications. However, sometimes the polymer and the clay does not form a nanocomposite, and thus, modification of either the polymer or the clay is necessary. For clay it is usually done by exchanging the inter-layer cations with organic cations, hence, creating an organophilic clay which can host non-polar organic polymers (Chen et al. (2008); Raquez et al. (2013)).

The structures of a polymer-clay nanocomposite are usually divided into three different types with respect to the inter-layer distance between the platelets: (i) *conventional*, also called phase separated, in which there are weak polymer-clay interactions, and thus, the inter-layer spacing between the platelets remains unchanged, and is referred to as a microcomposite (Fig. 1.4a), (ii) *intercalated*, where the polymer chains are partially or completely located between the clay platelets, resulting in an increased inter-layer spacing (Fig. 1.4b), and (iii) *exfoliated*, also called delaminated structure, where the clay platelets are homogeneously dispersed as individual sheets in the polymer phase (Fig. 1.4c) (Chen et al. (2008); Raquez et al. (2013)).

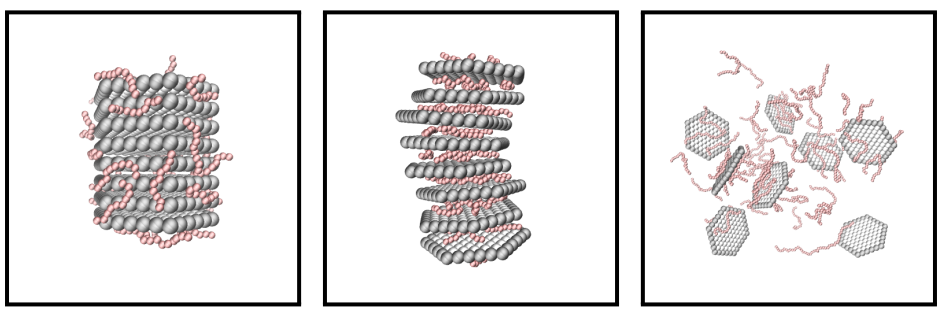


**Figure 1.4:** Illustrative representations for the different types of structures of a clay-polymer nanocomposite: (a) conventional, (b) intercalated, and (c) exfoliated. The platelets are represented as connected negatively (light grey) and positively (dark grey) charged spheres, and the polymer chain is represented as connected positively charged beads (red).

Furthermore, there has been an enhanced interest in exploiting the possibility of using Laponite® clay as a drug delivery vehicle, since it has been shown that it possesses the ability to sequester cationic peptides (Häffner et al. (2019)). The addition of cationic peptides to a dispersion of Laponite® results in the formation of tactoids creating an intercalated peptide-clay nanocomposite. The structure is stabilised by charge-charge interactions between the peptide and the clay, where the process is entropically driven due to the release of counterions associated with the clay when the peptide adsorbs onto the clay surface. The intercalation process is proposed to result in higher efficiency, controlled release, and increased target efficacy for cationic therapeutic compounds (Wang et al. (2013); Zazo et al. (2016); Tomás et al. (2018)).

## 1.3 Peptides

For a peptide, the polymer chain is built up from amino acids linked together by peptide bonds, where each amino acid is a monomer with the general structure of [R-CH($NH_2$)COOH], with R denoting the side chain of the amino acid. The peptide bond is formed when the carboxyl group ([-COOH]) of one amino acid reacts with the amino group ([-$NH_2$]) of another amino acid, thus, forming a covalent bond between the amino acid residues with the release of a water molecule (Fig. 1.5) (McNaught & Wilkinson (1997)).

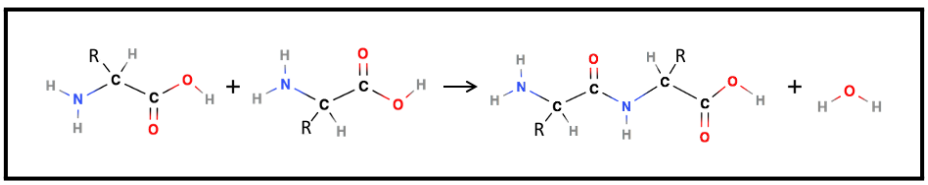

**Figure 1.5:** The formation of a peptide bond between two amino acids, with the side chains of the amino acids represented as R, and the remaining atoms comprises the backbone of the peptide.

The function of peptides is important in biological and medical systems, where they may have antimicrobial, bacterial, fungal and/or gastrointestinal properties, as well as many others. The classification of peptides depends either on their function or the number of amino acid residues within the chain. The latter may be categorised in three main groups: (i) a peptide with one to ten amino acids is referred to the corresponding name of mono- to decapeptide, (ii) a peptide with two to twenty amino acids is called an oligopeptide, and (iii) a peptide composed of a chain of many amino acids is denoted polypeptide. In addition, proteins are a type of polypeptides, however, a peptide and a protein differ, for instance all proteins consist of peptides, but not all peptides form proteins. Also, proteins usually consist of more than 50 amino acids or multiple

polypeptides, and often display more complex structure than a peptide. Regardless, it is common for the terms peptide and protein to be interchanged (Berg et al. (2012)).

Additionally, cationic antimicrobial peptides (CAMPs) is the most well-known class of antibiotics and anticancer drugs that are cationic in nature, and due to the increase in bacterial resistance against conventional antibiotics, a great interest in developing novel therapeutic compounds has arisen in recent years (Latendorf et al. (2019); Ciumac et al. (2019)).

### 1.3.1 deca-Arginine

deca-Arginine ($Arg_{10}$) is a peptide with a relative short sequence of ten amino acids, all of which are arginine (Arg, R). It has a highly cationic nature originating from the guanidinium cation ($Gdm^+$) group in the arginine side chain. The $Gdm^+$ group is a planar, symmetric ion composed of three amino groups each bonded to the central carbon with the chemical formula of $[C(NH_2)_3{}^+]$. It is highly stable in water due to strong hydrogen bond and charge-dipole interactions with the water molecules, and thus, solvates efficiently, where the aqueous $Gdm^+$ moieties form like-charge ion-pairs. The characteristics of the $Gdm^+$ group allow arginine-rich polypeptides to interact with membranes, self-associate, or penetrate across cellular membranes, hence making them promising candidates for intracellular drug delivery (Robison et al. (2016); Tesei et al. (2017); Vazdar et al. (2018)).

Moreover, the equilibrium acid dissociation constant, i.e. $pK_a$ value, of $Gdm^+$ in water has been reported in literature to be 13.6 (Vazdar et al. (2018)), and $13.8 \pm 0.1$ (Fitch et al. (2015)). This high intrinsic value results in the fact that the arginine side chain is predominantly positively charged, even at high pH values. Hence at physiological pH, $Arg_{10}$ has a net positive charge of ten, which are delocalised over the three nitrogen's in the side chains. In addition, the peptide exists in its zwitterionic form, with the amino group of the N-terminal protonated, and the carboxyl group of the C-terminal deprotonated. An atomistic representation of the peptide $Arg_{10}$ is shown in Fig. 1.6.

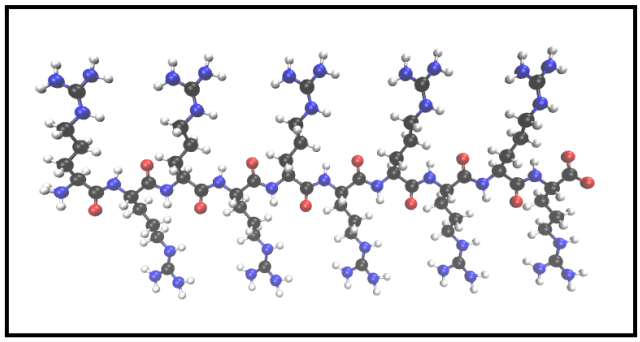

**Figure 1.6:** Atomistic illustration of the peptide deca-Arginine ($Arg_{10}$) represented in its zwitterion form where the stereochemistry of each arginine as that of the L-isomer. The colour codes are: carbon (black), nitrogen (blue), oxygen (red), and hydrogen (white).

In Paper IV, $Arg_{10}$ was used as a model peptide in order to investigate the intercalation process of a highly cationic peptide within Laponite® layered clay minerals, where the tactoidal behaviour was studied as an effect of the $Arg_{10}$ concentration.

# 2. Fundamental theory

## 2.1 Statistical mechanics and thermodynamics

Statistical mechanics aims to provide a molecular interpretation of equilibrium properties of macroscopic systems. The approach is to derive the system's thermodynamic properties from statistical averages of the system's microscopic properties. For instance, thermodynamic properties include: energy, volume, particle number, pressure, temperature, and density. The three former are extensive properties, and the three latter are intensive properties. In this section, some of the key concepts of statistical mechanics and thermodynamics will be explained. For a more detailed and in-depth description, the following references are recommended: Callen (1985); Hill (1986).

## 2.2 Statistical thermodynamics

The part of statistical mechanics where the thermodynamic behaviour of large systems is explained by extending the classical thermodynamics is known as equilibrium statistical mechanics or statistical thermodynamics.

In a classical system, all the possible states are represented in the *phase space*. For a system with $N$ particles, the phase space is a $6N$-dimensional space where each state is represented by a vector describing the position ($x$, $y$, $z$) and the momenta ($p_x$, $p_y$, $p_z$), of all $N$ particles. After a long time, when all of the phase space has been explored, and no macroscopic flow of energy or matter is present, the system has reached *thermodynamic equilibrium*. This refers to the first postulate of statistical mechanics: *the (long) time average of a mechanical variable $M$ in the thermodynamic system of interest is equal to the ensemble average of $M$* (the concept of an ensemble is explained in Section 2.3). Hence, $M$ is expected to have a constant value at equilibrium if measured over a long time, where $M$ refers to variables such as energy or pressure.

## 2.3 Thermodynamic ensembles

A central concept in statistical mechanics is the *thermodynamic ensemble*. This is an imaginary collection of a very large number of systems, representing the set of all possible states of a system in equilibrium. According to the *ergodic hypothesis*, the average value measured over a long time is equal to the *ensemble average*. Within an ensemble, the systems differ on a microscopic level while being equal on a thermodynamic level, and thus the ensemble is classified according to the representative macroscopic system.

The *microcanonical* ensemble represents the set of all possible states of an *isolated* system, which is a completely disconnected system where there is no transport of energy or matter in or out of the system. This means that the number of particles, the volume ($V$), and the total energy ($U$) are constant within the system. For the microcanonical ensemble, the second postulate of statistical mechanics is valid, which states that: *for an ensemble representative of an isolated thermodynamic system, the systems of the ensemble are distributed uniformly with equal probability over the possible quantum states consistent with the specified values N, V, U*. This is also known as the principle of equal a *priori* probabilities, that is, all microscopic states consistent with the microcanonical constraints are equally probable. The entropy ($S$) of the microcanonical ensemble is given by:

$$S = k_{\mathrm{B}} \ln \Omega_{N,V,U} \,, \tag{2.1}$$

where $k_{\mathrm{B}} \approx 1.381 \cdot 10^{-23}$ J/K is the Boltzmann constant and $\Omega_{N,V,U}$ is the *microcanonical partition function*, corresponding to the possible states for constant number of particles, volume, and total energy. The maximum entropy is found at equilibrium, where the system's thermodynamic properties, such as the temperature and the pressure, can be obtained if the entropy function is known. An isolated system is usually not very useful by itself from an experimental point of view since it is rarely studied. However, there are other more useful ensembles, like the *canonical* ensemble, the *grand canonical* ensemble, and the *isobaric* ensemble. The canonical ensemble represents a closed and isothermal system, where the number of particles, the volume, and the temperature ($T$) are constant. The *canonical partition function* is defined as:

$$Q_{N,V,T} = \sum_i \Omega_{N,V,U_i} \mathrm{e}^{-\beta U_i} \,, \tag{2.2}$$

where the sum is over all energy levels and $\beta = 1/(k_{\mathrm{B}}T)$. For the grand canonical ensemble, the system is open and isothermal, where the chemical potential ($\mu$), the

volume, and the temperature are constant. The *grand canonical partition function* is defined according to:

$$\Xi_{\mu,V,T} = \sum_i Q_{N_i,V,T} \mathrm{e}^{-\beta\mu N_i} \,, \tag{2.3}$$

where the sum is over all number of particles. In the isobaric ensemble the number of particles, the pressure ($P$), and the temperature are constant. The *isobaric partition function* is given by:

$$\Delta_{N,P,T} = \sum_i Q_{N,V_i,T} \mathrm{e}^{-\beta P V_i} \,, \tag{2.4}$$

where the sum is over all volumes. The applicability of the above-mentioned ensembles makes it possible to compare the results obtained from computer simulations with experimental observations. For instance, from the canonical partition function (Eq. (2.2)), the average pressure within the canonical ensemble can be calculated and compared with the experimentally measured swelling pressure from a closed test cell. By considering the probability $\rho_i$ of a state with energy $U_i$:

$$\rho_i = \frac{\mathrm{e}^{-\beta U_i}}{Q_{N,V,T}} \,, \tag{2.5}$$

the average pressure within the canonical ensemble ($\langle P \rangle$) can then be found by:

$$\langle P \rangle = \sum_i P_i \rho_i \,. \tag{2.6}$$

The sum is over all states and $P_i = -\frac{\delta U_i}{\delta V}$ is the pressure of the $i$:th configuration. Furthermore, the *Helmholtz free energy* has a similar connection within the canonical ensemble as the entropy (Eq. (2.1)) within the microcanonical ensemble, and is expressed as:

$$A = -k_\mathrm{B} T \ln Q_{N,V,T} \,. \tag{2.7}$$

At equilibrium, the Helmholtz free energy is minimised, and if known for the system, the average pressure can be calculated as:

$$\langle P \rangle = -\left(\frac{\delta A}{\delta V}\right)_{T,N} . \tag{2.8}$$

Note that the equations of Eq. (2.8) and Eq. (2.6) are equivalent, following the thermodynamic definition of Helmholtz free energy:

$$A = \langle U \rangle - TS \,, \tag{2.9}$$

where $\langle U \rangle$ is the average energy of the system.

## 2.4 Classical statistical mechanics

For the calculation of the partition function in the classical approach, the set of states at the quantum level are replaced by the classical continuum approach. For instance, the classical version of the canonical partition function (Eq. (2.2)) is given by:

$$Q_{class} = \frac{1}{N! \Lambda^{3N}} \int_V \mathrm{e}^{-\beta U(\Gamma)} \mathrm{d}\Gamma \,, \tag{2.10}$$

where $\Gamma$ is a $3N$-dimensional vector describing the *x*, *y*, and *z* coordinates of particle $N$ in the system, $U(\Gamma)$ is the system's potential energy as a function of the particles positions, and the integral is over the entire volume available to each particle. The kinetic part of the system is integrated beforehand and included in the *de Broglie wavelength*:

$$\Lambda = \frac{h}{(2\pi m k_\mathrm{B} T)^{1/2}} \,, \tag{2.11}$$

where $h \approx 6.626 \cdot 10^{-34}$ Js is Planck's constant and $m$ is the mass of the particle. The pressure in Eq. (2.6) can now be written as:

$$\langle P \rangle = \frac{\int_V P(\Gamma) \mathrm{e}^{-\beta U(\Gamma)} \mathrm{d}\Gamma}{Z_N} \,, \tag{2.12}$$

where $Z_N = \int_V \mathrm{e}^{-\beta U(\Gamma)} \mathrm{d}\Gamma$ is the *configurational integral* and $P(\Gamma)$ is the pressure as a function of the particle positions.

# 3. Molecular interactions

## 3.1 Intermolecular interactions

The molecular interactions within a system can be divided into intra- and intermolecular interactions. The former describes the interactions within a molecule, such as the chemical bonds, whereas the latter describes the interactions between molecules or colloidal particles. The intricate balance between attractive and repulsive forces is used in order to understand why colloidal dispersions are formed under some circumstances, and why flocculation occurs in other cases. Thus, the intermolecular interactions provide information about the structural and thermodynamical properties of a colloidal system. For large systems, it is not possible to include all particles when trying to capture the different behaviours, and therefore, approximations and simplifications are made. For instance, in a 'realistic' colloidal system, the colloidal particles are dispersed in a solvent composed of a large number of water molecules, where the number of particles is usually reduced by treating the solvent implicitly as a continuum throughout space.

## 3.2 Coulomb interactions

The electrostatic interaction in vacuum between two isolated charged particles $i$ and $j$, at a fixed distance $r_{ij}$ is described by Coulomb's law:

$$u(r_{ij}) = \frac{q_i q_j}{4\pi\epsilon_0 r_{ij}} \,, \tag{3.1}$$

where $q_i$ is the charge of particle $i$ and $\epsilon_0 \approx 8.854 \cdot 10^{-12}$ C$^2$/(Jm) is the permittivity of vacuum. If the two particles are immersed in a polar solvent, for example water, the pair interaction is then given by:

$$\beta w(r_{ij}) = \beta \frac{q_i q_j}{4\pi\epsilon_0\epsilon_r(T) r_{ij}} = \frac{l_B z_i z_j}{r_{ij}} \,, \tag{3.2}$$

where $l_B = \beta e^2/(4\pi\epsilon_0\epsilon_r(T))$ is the *Bjerrum length*, $e$ is the elementary charge, $z_i = q_i/e$ is the valency of particle $i$, and $\epsilon_r(T)$ is the relative permittivity of the solvent. Note that the latter is temperature-dependent (Israelachvili (2011)). In Eq. (3.2), the interactions with the solvent molecules are averaged, i.e. the solvent is treated implicitly, and thus the pair interaction is a free energy. The Bjerrum length is the separation between two charged particles at which the electrostatic interaction is equivalent to the thermal energy $k_B T$ and, for an aqueous solution, the Bjerrum length increases with temperature due to the temperature-dependent relative permittivity.

## 3.3 Poisson-Boltzmann equation

The Poisson-Boltzmann (PB) equation describes, among other things, how colloidal dispersions are formed from charged colloids and how the intermolecular electrostatic interactions changes by additional salt. It is given by a combination of the Poisson's equation and the Boltzmann distribution according to:

$$\epsilon_r\epsilon_0 \nabla\Phi(\mathbf{r}) = -\sum_i q_i c_i \mathrm{e}^{-\beta q_i \Phi(\mathbf{r})} \,, \tag{3.3}$$

where $\nabla$ is the Laplace operator, $\Phi(\mathbf{r})$ is the *mean electrostatic potential* at position $\mathbf{r}$, and $c_i$ is the concentration of the ionic species $i$ with charge $q_i$. In the PB equation a mean-field approximation is implemented, where the true ion distribution is replaced by its mean distribution, and the mean electrostatic potential is defined as the average value of the potential distribution at each position in space over a long time. At low electrostatic potential, the linearised PB equation is valid, and for a spherical geometry, the solution of the interaction potential between two charged particles is:

$$\beta w(r_{ij}) = l_B z_i z_j \frac{\mathrm{e}^{-\kappa r_{ij}}}{r_{ij}} \,. \tag{3.4}$$

Here, $1/\kappa$ is the *Debye screening length*, where $\kappa^2 = 4\pi l_B \sum_i z_i^2 c_i$ (Evans & Wennerström (1999)). For an increase in salt concentration or the valency of the salt, the Debye screening length decreases, and the long-ranged electrostatic interactions between charged particles is effectively screened, hence, the electrostatic interactions become more short-ranged. This phenomenon is illustrated in Fig. 3.1.

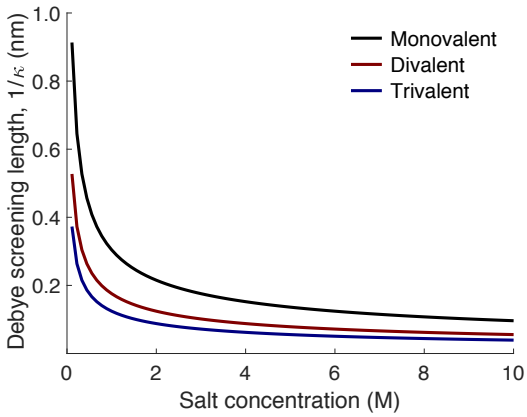


**Figure 3.1:** The Debye screening length ($1/\kappa$) as a function of salt concentration for a monovalent (red dashed line), a divalent (blue dashed line), and a trivalent (green dashed line) salt.

Furthermore, for a system with two like-charged surfaces in the salt-free case, where only counterions are present, an exact solution of the PB equation can be obtained. In this case, the osmotic pressure ($\Pi$) is equal to the pressure, and given by the so-called *mid-plane approach* (Evans & Wennerström (1999)):

$$\Pi_{PB} = P_{PB} = k_{\mathrm{B}} T c(0)\,, \tag{3.5}$$

where $c(0) = 2k_{\mathrm{B}}Ts^2\epsilon_r\epsilon_0/(zeh)^2$ is the counterion concentration at the mid-plane, $s$ represents a dimensionless parameter, where $s\tan(s) = |\sigma|zeh/(2k_{\mathrm{B}}T\epsilon_r\epsilon_0)$, $h$ is the separation between the charged surfaces, and $\sigma$ is the surface charge density which is smeared out on each surface. According to the PB equation, the pressure between two like-charged surfaces will always be positive, resulting in a repulsive force. On the other hand, it is possible to obtain a negative osmotic pressure, and thus, an attractive force at short separations between two highly like-charged particles mediated by multivalent ions if the ion-ion correlation forces are taken into account (Jönsson & Wennerström (2001)). However, these are not included in the PB equation.

## 3.4 Coupling theory

The coupling theory is useful for understanding the interactions within a system of two like-charged surfaces with respect to either weak or strong coupling (SC). In the limit of weak coupling, the PB equation is asymptotically exact. In this case, there is a large distance between the surfaces, which have a low surface charge density, and

the counterions have a low valency. For the opposite limit, the SC theory is asymptotically exact. Here, the surfaces are separated at short distances with a high surface charge density, and the counterions have a high valency. The limits can be found by considering the coupling parameter:

$$\Xi = 2\pi z^3 l_B^2 \sigma_s \,, \tag{3.6}$$

where $\sigma_s$ is the surface charge number density. The PB equation is valid for small values of $\Xi$ and the SC theory is valid for $\Xi \to \infty$, called the SC limit. Moreover, the SC theory is valid if the lateral distance $\alpha$ between the ions is greater than the separation $h$ between the surfaces, i.e. $h < \alpha$. In this case, the ions almost move independently along the vertical direction due to the strong ion-ion correlation forces (Fig. 3.2a) (Netz (2001)). The PB equation is valid in systems where each ion interacts with a diffuse cloud of other ions (Fig. 3.2b).

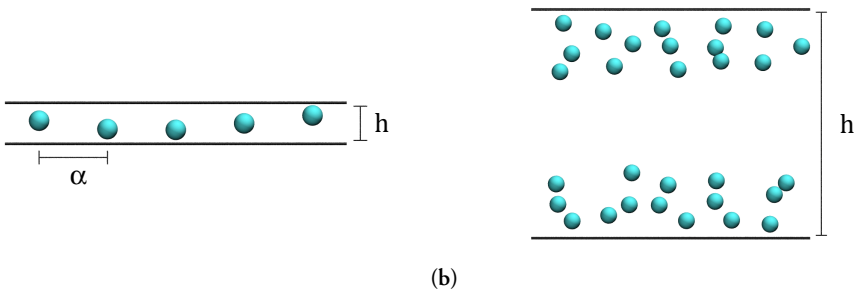


**Figure 3.2:** Schematic illustration of two like-charged surfaces (represented as horizontal black lines) mediated by counterions (represented as cyan spheres). (a) The lateral distance $\alpha$ between the ions is greater than the separation $h$ between the charged surfaces. (b) The charged surfaces attract two separate layers of counterions, where the lateral distance between the ions is small (Jansson et al. (2018)).

## 3.5 Short-ranged interactions

In addition to the long-ranged electrostatic interactions, particles also exhibit short-ranged interactions, which implies that two interacting particles repel each other at close separations. This originates from the Pauli exclusion principle which states that two or more identical electrons cannot occupy the same quantum state. The *hard-sphere* (HS) potential and the *truncated and shifted Lennard-Jones* (TLJ) potential are two simple potentials that describe this interaction (Fig. 3.3). The hard-sphere potential between two particles $i$ and $j$ is defined as:

$$u(r_{ij}) = \begin{cases} +\infty & \text{if } r_{ij} < \sigma_{ij} \\ 0 & \text{otherwise} \end{cases} , \tag{3.7}$$

where $\sigma_{ij} = (\sigma_i + \sigma_j)/2$, and $\sigma_i$ is the diameter of particle *i*. The truncated and shifted Lennard-Jones potential is strictly repulsive and defined as:

$$u(r_{ij}) = \begin{cases} \epsilon \left( (\frac{\sigma_{ij}}{r_{ij}})^{12} - 2(\frac{\sigma_{ij}}{r_{ij}})^{6} + 1 \right) & \text{if } r_{ij} < \sigma_{ij} \\ 0 & \text{otherwise} \end{cases} , \tag{3.8}$$

where $\epsilon$ determines the strength of the interaction. There is also an attraction between the particles which is described by the van der Waals forces. These are a collection of interactions proportional to $r^{-6}$ and originates from: (i) the Keesom force for the rotational average between two dipoles, (ii) the Debye force for the rotational average between a dipole and a corresponding induced dipole, and (iii) the London dispersion force considering the instantaneous induced dipole. By combining the Pauli exclusion principle with the van der Waals forces, the *Lennard-Jones* (LJ) potential is obtained and defined as:

$$u(r_{ij}) = 4\epsilon \left( (\frac{\sigma_{ij}}{r_{ij}})^{12} - (\frac{\sigma_{ij}}{r_{ij}})^{6} \right) . \tag{3.9}$$

The minimum value of the potential is found at $r_{ij} = 2^{1/6}\sigma_{ij}$ (Fig. 3.3). The theory that describes the electrostatic interactions with the linearised PB equation and the short-ranged interactions with the van der Waals forces is known as the DLVO-theory (Derjaguin & Landau (1941); Verwey & Overbeek (1948)).

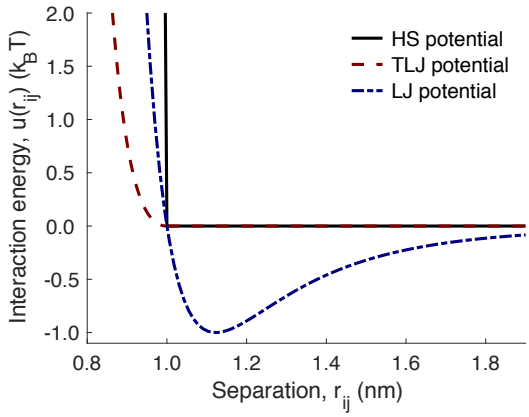


**Figure 3.3:** An comparison between the short-ranged interaction potentials, with $\epsilon = 1\ k_B T$ and $\sigma = 1$ nm, for the hard-sphere (HS) potential (red solid line), the truncated and shifted Lennard-Jones (TLJ) potential (blue dashed line), and the Lennard-Jones (LJ) potential (green dashed line).

# 4. Simulation techniques

## 4.1 Simulation methods

In classical statistical mechanics, the most commonly used simulation methods are Monte Carlo (MC) and Molecular Dynamics (MD) simulations. The advantage by using simulations over analytical solutions obtained from theory is that the latter contains a large number of approximations and are limited to small and simple systems. The disadvantage, however, is that if the model is too complex and includes many parameters, it may be difficult to gain physical insight into the system. The difference between MC and MD simulations can be explained by the ergodic hypothesis: *(i) the average value of a certain property after a long time is equal to (ii) the ensemble average*. The latter, *(ii)*, is described by MC simulations, where the concept of time is absent and instead a large number of configurations are considered within the ensemble, where the average value of a property is obtained by the ensemble average. The former, *(i)*, is considered in MD simulations, where the dynamics of the system is captured due to the particle's movement according to Newton's law of motion. Hence, the average value of a property is obtained after a long time. To verify whether a system is in equilibrium or not, knowledge of the system is required. The criteria that should be fulfilled for equilibrium is generally that the average energy of the system is converged and independent simulations with different initial configurations generate the same averages for the observables.

## 4.2 Monte Carlo simulations

In MC simulations, the system is described from the ensemble average. The straightforward MC technique is the random sampling, or brute force MC, where the coordinates of the particles are selected at random for a large set of configurations. The disadvantage with this approach is that it is very inefficient for dense systems, since the majority

of the generated configurations will not contribute significantly to the average. For a randomly generated configuration in dense systems, there is a high probability that the coordinates of the particles will overlap. This will increase the energy of the configuration due to short-ranged repulsive interactions, and thus, the total energy of a dense system will be above $k_{\mathrm{B}}T$, i.e. $\mathrm{e}^{-\beta U(\Gamma)} \gg 1$. A more efficient and robust approach is to implement *importance sampling*, in which the majority of the configurations are sampled in the region of space where it will contribute significantly to the average. One of the most recognized importance sampling techniques is the Metropolis method (Metropolis et al. (1953); Allen & Tildesley (1989)).

### 4.2.1 Metropolis method

The Metropolis method is a sampling method in MC simulations for dense and more complex systems. Each generated configuration is proportional to the Boltzmann weight, and described by the probability density $\rho = \mathrm{e}^{-\beta U(\Gamma)}/Z_N$, where $\Gamma$ is the coordinates of the configuration. For a system to reach equilibrium, the criterion of *detailed balance* is introduced:

$$\rho_{\mathrm{o}}\pi_{\mathrm{o}\to\mathrm{n}} = \rho_{\mathrm{n}}\pi_{\mathrm{n}\to\mathrm{o}}\,, \tag{4.1}$$

where $\pi_{\mathrm{o}\to\mathrm{n}}$ and $\pi_{\mathrm{n}\to\mathrm{o}}$ are the transition probability densities from the old to the new configuration, and vice versa. In the Metropolis scheme, the detailed balanced is fulfilled by the following condition:

$$\pi_{\mathrm{o}\to\mathrm{n}} = \begin{cases} \gamma_{\mathrm{o}\to\mathrm{n}} & \text{if } \rho_{\mathrm{n}} \geq \rho_{\mathrm{o}} \\ \gamma_{\mathrm{o}\to\mathrm{n}} \cdot \alpha & \text{if } \rho_{\mathrm{n}} < \rho_{\mathrm{o}} \end{cases}, \tag{4.2}$$

where $\gamma_{\mathrm{o}\to\mathrm{n}} = \gamma_{\mathrm{n}\to\mathrm{o}}$ describes a symmetric random *trial move* and $\alpha$ is the acceptance ratio from an old to a new configuration. The trial moves in MC simulations have no physical meaning, and there is a vast number of trial moves optimised for different types of systems. For instance, the *single particle displacement* is a trial move where a single particle is selected at random and then translated or rotated randomly. For the translation of a single particle, the random trial move describes the uniform probability for the movement of the particle in any direction within a maximum allowed distance. The symmetry arises from the fact that the probability of finding a certain new position is equal to finding the old position when the particle is at the new position. By rewriting Eq. (4.1) the acceptance ratio is described as:

$$\alpha = \frac{\pi_{\mathrm{o}\to\mathrm{n}}}{\pi_{\mathrm{n}\to\mathrm{o}}} = \frac{\rho_{\mathrm{n}}}{\rho_{\mathrm{o}}} = \frac{\mathrm{e}^{-\beta U(\Gamma_{\mathrm{n}})}}{Z_N} \frac{Z_N}{\mathrm{e}^{-\beta U(\Gamma_{\mathrm{o}})}} = \mathrm{e}^{-\beta(U(\Gamma_{\mathrm{n}})-U(\Gamma_{\mathrm{o}}))} \,. \tag{4.3}$$

The advantage with the Metropolis method is that unphysical moves are possible. However, the disadvantage is that a new configuration can only be generated if the previous configuration is known. Therefore, an initial configuration is required that includes the particle positions, where the geometry and boundary conditions of the system are defined. The following steps can be used to summarise the method:

1. A random trial move is selected.
2. A random particle or a set of particles as required by the trial move is selected, and the move is performed in order to generate a new configuration.
3. The acceptance ratio is calculated, and the new configuration is accepted if $\alpha \leq 1$ (when $\rho_{\mathrm{n}} \geq \rho_{\mathrm{o}}$) or $\alpha > R$ (when $\rho_{\mathrm{n}} < \rho_{\mathrm{o}}$), where $R$ is a random number between zero and one, otherwise the new configuration is rejected.
4. The observables of interest are sampled when the system has reached equilibrium.
5. The scheme is repeated from step 1.

## 4.3 Molecular dynamics simulations

In MD simulations, the particles in the system move according to Newton's laws of motion. The advantages with MD are that it captures the dynamics of the system, where parallelisation is straightforward, and the algorithms are universal for most types of systems. The disadvantage, however, is that it may take a long time for the system to cross energy barriers much larger than $k_{\mathrm{B}}T$. Furthermore, the interaction potentials and the forces are required to be continuous functions in most MD packages (e.g. GROMACS (Pronk et al. (2013); Abraham et al. (2014))).

The movement of the particles is derived from the forces acting on each particle, where the force is obtained from the potential energy gradient at each particle position. According to Newton's second law of motion in classical mechanics, the force **F** acting on a particle is equal to the product of the particles mass $m$ and acceleration **a**, i.e. $\mathbf{F} = m \cdot \mathbf{a}$, assumed that the mass is constant. For a system with many particles, the force acting on particle $i$ at time $t$ is:

$$\mathbf{F}_i(t) = \sum_{j \neq i} \nabla u_{ij}(|\mathbf{r}_i(t) - \mathbf{r}_j(t)|) = -\sum_{j \neq i} \nabla u_{ij}(r_{ij}(t)) \,, \tag{4.4}$$

where the sum is over all particles except particle $i$ itself, $\mathbf{r}_i(t)$ is the position of particle $i$ at time $t$, and $u_{ij}(r_{ij})$ is the pair potential between particles $i$ and $j$. For numerical integration of the equation of motion, the Velocity Verlet algorithm can be used, where the particles initial position and velocity at time $t$ are defined. The Velocity Verlet algorithm can be described in the following steps:

1. The particle's position at time $t + \delta t$ is calculated according to:

$$\mathbf{r}(t + \delta t) = \mathbf{r}(t) + \mathbf{v}(t)\delta t + \frac{\mathbf{a}(t)}{2}\delta t^2 \,, \tag{4.5}$$

   where $\delta t$ is the timestep, $\mathbf{a}(t) = \mathbf{F}(t)/m$ is the acceleration obtained from Eq. (4.4), $\mathbf{v}(t)$ is the velocity, and $\mathbf{r}(t)$ is the position of the particle.

2. The acceleration $\mathbf{a}(t + \delta t)$ is calculated for the particle position $\mathbf{r}(t + \delta t)$.

3. The velocity of the particle at time $t + \delta t$ is calculated as:

$$\mathbf{v}(t + \delta t) = \mathbf{v}(t) + \frac{\mathbf{a}(t) + \mathbf{a}(t + \delta t)}{2}\delta t \,. \tag{4.6}$$

4. The algorithm is repeated from step 1 in order to find the positions of the particles at time $t + 2\delta t$.

In MD integrators, the number of particles, the volume, and the energy of a system are conserved if the timestep $\delta t$ is small enough, thus, representing the microcanonical ensemble. For simulations of a system within the canonical or isobaric ensemble, thermostats (Berendsen et al. (1984); Nosé (1984); Hoover (1985); Bussi et al. (2007)) and barostats (Parrinello & Rahman (1981); Nosé & Klein (1983); Berendsen et al. (1984)) are implemented. For a more detailed description of the methods, the reader is referred to the above-mentioned references.

### 4.3.1 Enhanced umbrella sampling

The MD simulation technique is a powerful computational tool for the investigation of thermodynamic and kinetic properties in a wide range of systems. However, for complex systems, the energy landscape is usually not smooth and may consist of several metastable states separated by high-energy barriers, which can cause the system to get trapped in an energy well. Moreover, the time scale reached in MD simulations is not always sufficient when compared to that observed in experimental measurements. Therefore, enhanced sampling methods have been developed to facilitate the crossing

of energy barriers and extend the sampling timescales. In these methods, the efficiency is improved in the sampling over the phase or configuration space by adding a bias potential to the Hamiltonian, which reduces the energy barriers and can be added in a variety of ways to achieve efficient conformation sampling (Yang et al. (2019)). Widely used enhanced sampling methods include: umbrella sampling, metadynamics, simulated annealing, replica-exchange molecular dynamics, and many more (Kästner (2011); Bernardi et al. (2015)).

The umbrella sampling introduced by Torrie & Valleau (1977) is one of the first established and historically most important enhanced sampling methods. In this method, the sampling is accelerated by reducing the energy landscape through an artificial umbrella potential that mirrors, and thus annihilate, the real energy barriers. The umbrella potential, however, cannot account for all the degrees of freedom in the system, hence, only a few are included. Predefined degrees of freedom, often called collective variables or reaction coordinates, are used to effectively steer the simulation. To achieve an accurate and unbiased calculation of the state probabilities, the sampling of the system is considered complete when all values of the collective variables have been explored more than once.

Umbrella sampling provides an accurate estimation of the potential of mean force (PMF), where the convergence of the system is usually very fast. The simulations consist of a pulling simulation, where the particles of interest are harmonically restrained at increasing centre-of-mass distance from each other by the umbrella potential. The restraint allows the configurational space to be sampled in a defined region along a reaction coordinate, creating equally spaced windows connecting two endpoints of the collective variable. For each window, an independent simulation is performed, creating a histogram of configurations. It is important that there is a slight overlap between neighbouring windows such that a continuous and proper construction of the PMF curve can be derived.

The procedure of the umbrella sampling used with the MD package GROMACS (Abraham et al. (2018)) in Paper III is described as followed:

1. The starting configurations are generated with the *pull code*, where the particles are pulled apart along a reaction coordinate with a certain spring constant and pull rate.
2. The frames corresponding to the selected centre-of-mass separation between the particles are extracted from the trajectory obtained from step 1.
3. Independent umbrella sampling simulations are performed for each frame in order to restrain it within an umbrella sampling window corresponding to the selected centre-of-mass distance.

4. The PMF is integrated from all windows utilising the weighted histogram analysis method (WHAM) (Kumar et al. (1992); Hub et al. (2010)).

For a more in-depth and detailed description over the input parameters in the pull code and the WHAM analysis method, the reader is referred to the above-mentioned references.

## 4.4 Boundary conditions

In order for a simulation to represent a 'realistic' system, the simulation box need to contain a vast number of particles. This kind of systems would be far too complex to simulate and also too expensive with respect to the computational resources available. To circumvent this issue, implementations of boundary conditions are necessary in order to limit the size of the system. For instance, *periodic boundary conditions* are a set of boundary conditions where a large system is approximated by a small model system, corresponding to a unit cell. The periodicity ensures that the size effects in the system are reduced at the boundaries and the conditions mimics the presence of an infinite bulk surrounding the unit cell. For a cubic simulation box, the periodic boundary conditions imply replicates of the cubic unit cell in all directions, yielding a periodic infinite lattice throughout space (Fig. 4.1). The replicates are identical images of the unit cell, hence, if a particle moves outside the unit cell, one of its images will enter the unit cell from the opposite face.

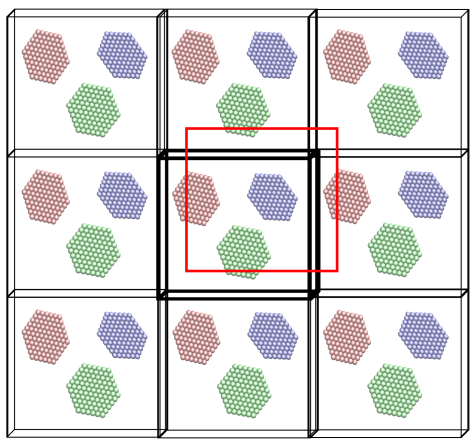

**Figure 4.1:** A schematic illustration of a system with periodic boundary conditions where all particles are located in the central cubic unit cell which is replicated in all directions. Applying the minimum image convention corresponds to a cubic cut-off represented as the red box.

## 4.5 Minimum image convention

For a system with periodic boundary conditions, the cubic unit cell is placed in an imaginary infinite lattice of images. This gives rise to a system composed of an infinite number of particles and by considering all the interactions within the system it would result in an infinite sum. To restrict this outcome, an approximation is performed by applying the *minimum image convention*. This approach states that each particle only interacts with the closest image of the other particles, and thus, corresponds to a cubic cut-off (Fig. 4.1).

# 5. Simulation models

## 5.1 Coarse-grained modeling

In a coarse-grained model, the description of a system is simplified by reducing the number of degrees of freedom, thereby reducing the complexity of the system. The advantage of this approach is that it is possible to study large-scale systems at a reduced computational cost, in contrast to atomistic models. On the other hand, it is usually not possible to obtain a quantitative agreement with experiments. Instead, a qualitative correspondence can be captured where the overall trends can be understood. To represent a colloidal particle as a coarse-grained model, a set of atoms is replaced by a coarse-grained site, where the resolution of the model depends on the number of atoms within the set. Bonded interactions, like harmonic stretching potentials and/or harmonic angle potentials, are used to connect the sites with each other and maintain their shape. Furthermore, the interactions between the coarse-grained sites consist of non-bonded effective pair-potentials, where the parameters have been chosen from either a more detailed model and/or experimental data.

The coarse-grained models used in this thesis are at the level of the *primitive model* (McQuarrie (1976)), in which all of the charged species are treated as charged hard- or soft-spheres. In addition, the solvent is treated implicitly through the relative permittivity and regarded as temperature-dependent.

## 5.2 Clay platelets

The clay platelets have been described with two different coarse-grained models, where the platelets are either represented as two parallel infinite surfaces or as a finite hexagonal monolayer of connected charged sites in bulk conditions. The former model was used in Paper I and II, in order to study how the pressure between the surfaces depends on the counterion valency, the fraction of monovalent/divalent counterions, as well as

the solvent. For the latter model, used in Paper I–V, structural and thermodynamical bulk properties of the clay platelets were investigated as an effect of the counterion valency, the fraction of monovalent/divalent counterions, the solvent, as well as with the addition of multivalent salt, peptides and polyelectrolytes.

### 5.2.1 Parallel infinite surface model

In the parallel infinite surface model, two clay platelets are represented as two negatively charged planar surfaces with a uniform surface charge density $\sigma$ neutralised with mobile counterions, each with a diameter of 0.4 nm. The surfaces are separated with a certain distance $h$, and the *mid-plane* is defined as half the distance between the surfaces ($h/2$) (Fig. 5.1). The simulation box is finite with the length $L$ in the directions parallel to the surfaces, hence, the volume is equal to $V = hL^2$. The system takes into account both ion-surface interactions and ion-ion pairwise interactions, where the latter is described by a combination of Eq. (3.2) and Eq. (3.7). For the long-ranged interactions outside the box, an external potential is applied. Moreover, periodic boundary conditions are implemented for the ions, such that if an ion moves outside the box ($x > L/2$) in the direction parallel to the surfaces, the ion will reappear at $x = x - L$. The ion-ion separation is calculated by the minimum image convention, which gives that if $r_x > L/2$ then $r_x = |r_x - L|$.

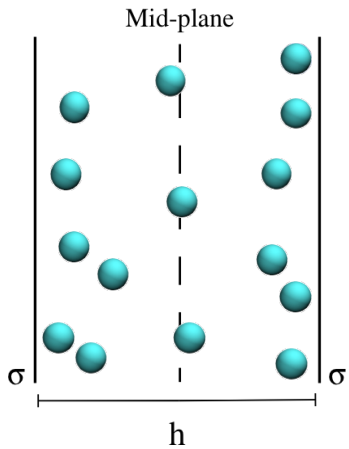


**Figure 5.1:** A schematic illustration of the parallel infinite surface model. Two parallel clay platelets are modeled as two negatively charged planar surfaces with surface charge density $\sigma$ (represented as the two vertical black lines) separated with a distance $h$ and neutralised by mobile counterions (represented as cyan spheres). The mid-plane is represented as the dashed black line.

### 5.2.2 Finite monolayer model

For the finite monolayer model, the clay platelet is represented as a finite monolayer of connected coarse-grained spheres in a hexagonal pattern. The spheres are denoted as sites with a diameter of 1 nm and correspond to a set of atoms in the clay platelet unit cell. The negative surface charge density of the platelet is equally distributed among the sites, defined as the total electrical charge of $Q_p$ unit charges, where each site holds $Q_s = Q_p/N_s$ unit charges located in the centre of the site. From the assumption that the sites are arranged in an infinite hexagonal plane, the surface charge density can be determined from $\sigma = Q_s \cdot \frac{2}{\sqrt{3}}$.

Besides the negative surface charge density, a positive linear edge charge density was implemented in the model in Paper IV and V in order to mimic the anisotropic charge distribution of the clay platelet. The linear edge charge density was determined from the circumference of the platelet by taking into account the number of sites along the edge and its corresponding charge. The total amount of positive edge charges was in the order of $\sim$ 10% of the total platelet charge. Hence, the low number of positive charged sites along the edge results in a net negative charge of the platelet. Moreover, the platelet is neutralised with mobile counterions corresponding to either mono- and/or divalent cations, each with a diameter of 0.4 nm. Illustrative representations of the finite monolayer model are shown in Fig. 5.2, where in Fig. 5.2a the platelet has a uniform negative surface charge density, whereas in Fig. 5.2b both a negative surface charge density and a positive linear edge charge density have been implemented.

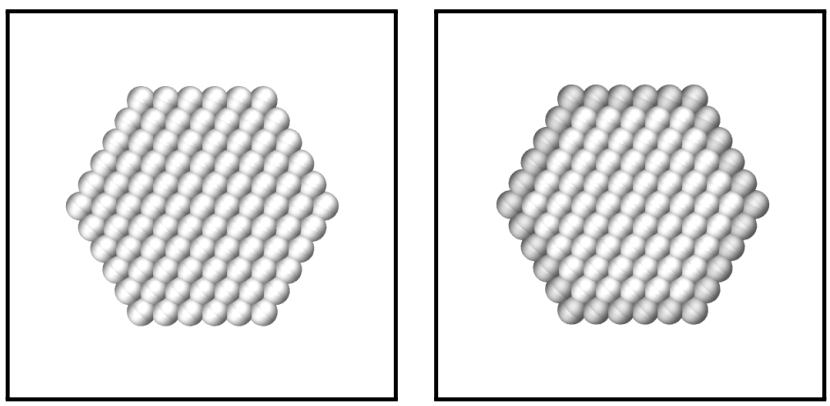

(a) (b)

**Figure 5.2:** Illustrative representations of the finite monolayer model where the clay platelet is represented as a finite hexagonal monolayer of connected charged spheres. In (a) the platelet has a uniform negative surface charge density and in (b) both a negative surface charge density and a positive linear edge charge density have been implemented. The negatively and positively charged sites are represented as light and dark grey spheres, respectively.

In the model, all the interactions between the particles are assumed to be pairwise additive, where the electrostatic pair potential is defined in Eq. (3.2). The particles also interact via the strictly repulsive, truncated, and shifted Lennard-Jones potential in Eq. (3.8). Moreover, in order to render rigid bonds between the adjacent sites within the platelet, they are connected by a harmonic bond stretching potential:

$$u_b(r_{ij}) = \frac{1}{2} k^b (r_{ij} - b)^2 \,, \tag{5.1}$$

where $k^{\mathrm{b}}$ = 4000 $k_{\mathrm{B}}T$/nm² is the force constant, $r_{ij}$ is the separation between site $i$ and $j$, and $b$ = 1 nm is the equilibrium bond length. The flexibility of the platelet is constrained by a harmonic bending potential between triplets of bonded sites:

$$u_a(\theta_{ijk}) = \frac{1}{2} k^\theta (\theta_{ijk} - \theta^\circ)^2 \,, \tag{5.2}$$

where $k^\theta$ = 4000 $k_{\mathrm{B}}T$/rad² is the angular force constant, $\theta_{ijk}$ is the bond angle between the sites $i$, $j$ and $k$, and $\theta^\circ$ = $\pi$ rad is the equilibrium bond angle.

The concentration of the platelets in the system was determined from the volume fraction $\phi$ which takes into account the number of platelets ($N_{\mathrm{p}}$), the number of sites ($N_{\mathrm{s}}$), the radius of the sites ($r$), and the volume of the simulation box ($V$) according to:

$$\phi = \frac{4\pi r^3 N_{\mathrm{p}} N_{\mathrm{s}}}{3V} \,. \tag{5.3}$$

Furthermore, the fraction of divalent counterion charge $\eta_{\mathrm{Di}}$ was altered in Paper I by gradually replacing the number of monovalent cations ($N_{\mathrm{Mon}}$) with an equivalent number charge of divalent cations ($N_{\mathrm{Di}}$) defined as:

$$\eta_{\mathrm{Di}} = \frac{2N_{\mathrm{Di}}}{2N_{\mathrm{Di}} + N_{\mathrm{Mon}}} \,. \tag{5.4}$$

## 5.3 Peptides and polyelectrolytes

The peptides and the polyelectrolytes are modelled as positively charged chains consisting of connected coarse-grained spheres (beads), each with a diameter of 0.4 nm and an elementary charge of one, located in the centre of the sphere. In the chain, one sphere represents one amino acid in the peptide or one monomer in the polyelectrolyte. The

interactions between the chains are assumed pairwise additive and the electrostatic pair potential is defined in Eq. (3.2). The beads within the chain also interact via the strictly repulsive, truncated and shifted Lennard-Jones potential in Eq. (3.8). Furthermore, all the adjacent beads within the chain are connected by the harmonic bond stretching potential in Eq. (5.1) with $k^{\mathrm{b}}$ = 4000 $k_{\mathrm{B}}T$/nm$^2$ and $b$ = 0.5 nm. The flexibility of the chain is constrained between triplets of beads by the harmonic bending potential in Eq. (5.2). The angular force constant $k^{\theta}$ is set to 0, 40, or 400 $k_{\mathrm{B}}T$/rad$^2$ in order to either mimic a flexible, a semiflexible, or a stiff chain. Illustrative representations over the chain model are shown in Fig. 5.3, where Fig. 5.3a represents the peptide and Fig. 5.3b represents the polyelectrolyte.

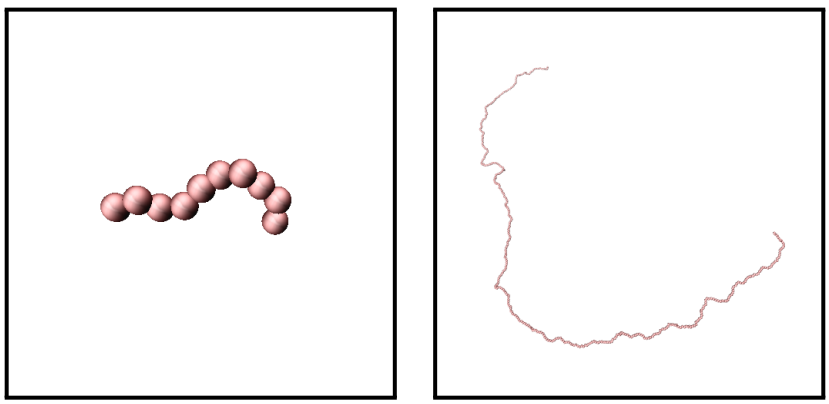

(a) (b)

**Figure 5.3:** Illustrative representations of the chain model for (a) a small peptide chain and (b) a long polyelectrolyte chain. The chain is represented by connected coarse-grained beads (red spheres), each with a positive elementary charge of one and a diameter of 0.4 nm.

In Paper IV and V, the dimensionless stoichiometric charge-ratio $\beta$ between the number of positive charges of the chains and the net negative charges of the platelets was defined in order to describe the chain-platelet systems with respect to under- and overcharging. The charge-ratio was defined somewhat different in the two papers, however, the species that was not altered with respect to the number and the charge was placed in the denominator, and thus, the denominator was kept constant throughout each study.

For Paper IV, the addition of peptide chains to systems with a constant number of clay platelets was studied, hence, the charge-ratio was defined as:

$$\beta = \left| \frac{N_{\mathrm{c}} \cdot Z_{\mathrm{c}}}{N_{\mathrm{p}} \cdot Z_{\mathrm{p}}} \right| . \tag{5.5}$$

In Paper v, the polyelectrolyte-nanoplatelet complexation was studied by addition of clay platelets to a system with one polyelectrolyte chain, and thus, the number of polyelectrolytes was constant, and the charge-ratio was defined as:

$$\beta = \left| \frac{N_{\mathrm{p}} \cdot Z_{\mathrm{p}}}{N_{\mathrm{b}} \cdot Z_{\mathrm{b}}} \right| . \tag{5.6}$$

In Eq. (5.5) and Eq. (5.6), $N$ and $Z$ are the number and the charge of the species, respectively, where the subscript is either referring to the chain (*c*), the bead (*b*), or the platelet (*p*).

## 5.4 Counterions and salt

The counterions and salt ions in the simulation models are added explicitly and modelled as freely moving charges centred in truncated and shifted Lennard-Jones spheres. All of the particles within the systems interact pairwise by combining Eq. (3.2) with Eq. (3.7) or Eq. (3.8). For the systems where the platelets also possess an edge charge, both cationic and anionic counterions are added in order to neutralise the negative surface charge density and the positive linear edge charge density with their respective ions. In addition, for the systems with both platelets and peptides or polyelectrolytes, the corresponding counterions for each species are implemented in the model.

In Paper iii, the interactions of Laponite® clay in the presence of multivalent ions were studied. Here, the stoichiometric charge-ratio is defined as the absolute value of the total charge of all mono- or multivalent positive salt ions, divided by the total net negative charge of the platelets:

$$\beta = \left| \frac{N_{\mathrm{ion}} \cdot Z^{+}_{\mathrm{ion}}}{N_{\mathrm{p}} \cdot Z_{\mathrm{p}}} \right| , \tag{5.7}$$

where $N_{\mathrm{ion}}$ and $Z^{+}_{\mathrm{ion}}$ are the number and the charge of the positive salt ions, respectively.

# 6. Simulation analyses

## 6.1 Osmotic pressure

For the parallel infinite surface model used for the MC simulations, the systems were in equilibrium with salt-free water, and thus, the pressure between the surfaces was equal to the osmotic pressure. This was calculated according to the mid-plane approach by extending Eq. (3.5) to:

$$\Pi = \Pi^{\mathrm{id}} + \Pi^{\mathrm{corr}} + \Pi^{\mathrm{coll}} . \tag{6.1}$$

Here, $\Pi^{\mathrm{id}} = k_{\mathrm{B}}T \sum_{i=1}^{2} c_i(\mathrm{mp})$ is the ideal contribution where $c_i(\mathrm{mp})$ is the counterion concentration at the mid-plane with valency $i$. In addition, an attractive term arising from ion-ion correlations on either side of the mid-plane ($\Pi^{\mathrm{corr}}$) and a collision term originating from the finite size of the ions due to the hard-core radius ($\Pi^{\mathrm{coll}}$) was added (Guldbrand et al. (1984)).

## 6.2 Radial distribution function

The radial distribution function (RDF), also called the pair correlation function ($g(r)$), describes the average density distribution surrounding a reference particle. By dividing the space in the radial direction from the reference particle into spherical shells of equal width, the RDF calculates the probability of finding another particle in a shell of width $dr$ at the distance $r$ from the reference particle (Fig. 6.1a). The distance ranges from zero up to half the simulation box length, and the width of the spherical shells are set by the bin width. By calculating the distance between all particle pairs, the algorithm produces a histogram of the total number distribution, which is normalised with respect to the volume of each spherical shell, as well as the average density of the particles in the selected set (Hill (1986); Abraham et al. (2014)).

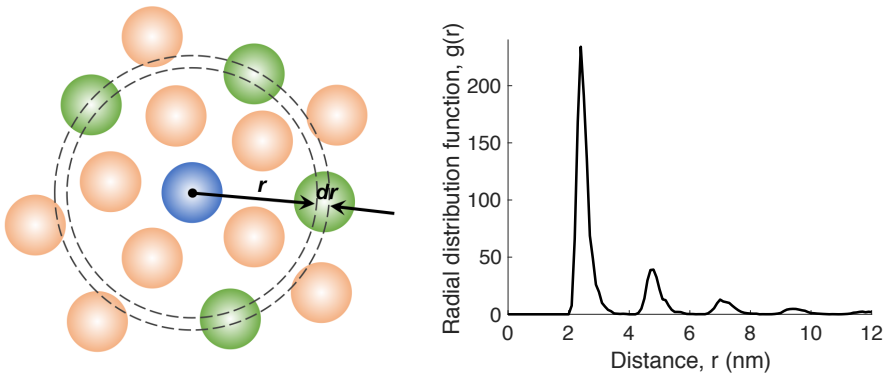


**Figure 6.1:** (a) Schematic illustration of the algorithm used for the calculation of the radial distribution function with the reference particle (blue sphere), a spherical shell of bin width *dr* at a distance *r* from the particle, and the selected particles within the spherical shell (green spheres). Also, the particles that are not within the shell are shown (beige spheres). (b) Illustrative representation of the radial distribution function ($g(r)$) as a function of the distance *r*.

For the finite monolayer model used for the MD simulations, the RDF (Fig. 6.1b) for the platelets gives information of the tactoids structural properties. The inter-layer distance is determined from the position of the peak maximum, the number of visible peaks gives an indication of the average number of platelets per tactoids, and the height of the peak is related to the probability of finding the corresponding configuration.

## 6.3 Structure factor

Structural analysis for the platelets was performed in the MD simulations with the finite monolayer model. By taking into account the total number of platelets in the system and the total volume of the simulation box, the total structure factor between the platelets can be calculated according to:

$$S(q) = \left\langle \frac{1}{N} \sum_{i=1}^{N} \sum_{j=1}^{N} \frac{\sin(qr_{ij})}{qr_{ij}} \right\rangle . \tag{6.2}$$

The simulation box length $L$ determines the scale of the scattering vector $q$, according to $q = 2\pi/L$. Hence, a large box size results in lower $q$-values, while high $q$-values can be sampled with a smaller box size. For the assumption of an isotropic scattering pattern, and by considering the RDF between all the platelet sites in the system, Eq. (6.2) can be rewritten as:

$$S(q) = 1 + 4\pi \frac{N}{V} \int_0^\infty (g(r) - 1) r^2 \frac{\sin(qr)}{qr} \mathrm{d}r \,. \tag{6.3}$$

In the simulations, a finite size of the cubic simulation box is used, and if $g(r)$ does not approach one at large separation, artefacts arising from the finite box length can be reduced by applying the following window function:

$$S_w(q) = 1 + 4\pi \frac{N}{V} \int_0^\infty (g(r) - 1) r^2 \frac{\sin(qr)}{qr} \frac{\sin(\pi r / R_c)}{\pi r / R_c} \mathrm{d}r \,. \tag{6.4}$$

Here, the maximum distance in $g(r)$ is denoted $R_c$ (Gutiérrez & Johansson (2002)).

The calculated total structure factor obtained from computer simulations is a good complement to experimentally measured scattered intensities from small angle X-ray scattering (SAXS) (described in Section 7.3). With these techniques and analyses, it is possible to determine if the clay dispersion is dominated by repulsive or attractive interactions. For the structural configuration of tactoids, where the platelets aggregate face-to-face, Bragg peaks are observed in the structure factor (Fig. 6.2b), arising from the periodicity of the system due to the equidistant separation between the platelets. However, for a clay dispersion that is dominated by repulsive interactions, and thus, consists of only single clay platelets, no Bragg peaks are found in the structure factor (Fig. 6.2a).

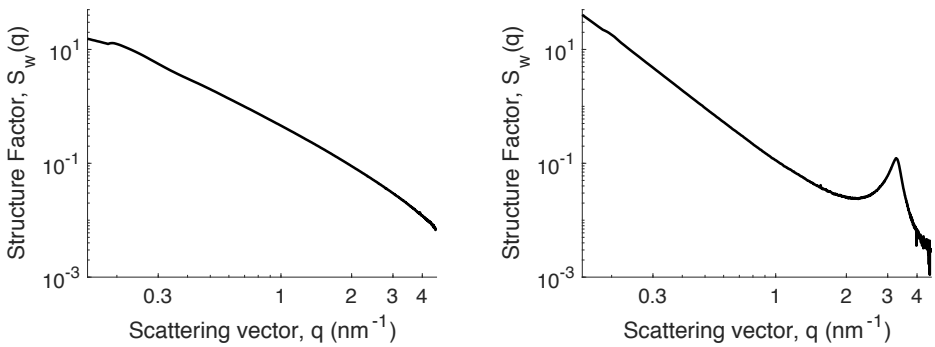


**Figure 6.2:** Illustrative representations of the total structure factor ($S_w(q)$) as a function of the $q$-vector, where (a) represents a repulsive system with only single platelets present and for (b) a Bragg peak is obtained due to the structural configuration of tactoids, representing an attractive system.

### 6.3.1 Kratky plot

In order to evaluate the shape and the compactness of formed complexes, such as polymer-clay nanocomposites, the structure factor may be presented as a Kratky plot. A Kratky plot is obtained by multiplying the total structure factor ($S_w(q)$) with the $q$-vector squared, i.e. $S_w(q) \cdot q^2$. For a more compact shape, the Kratky plot has a bell-shaped curve feature in the low $q$-region, which is usually associated with a Bragg peak in the high $q$-region (Fig. 6.3a), while for a more extended shape, the curve in the Kratky plot reaches a plateau value at higher $q$-values due to the absence of a Bragg peak (Fig. 6.3b).

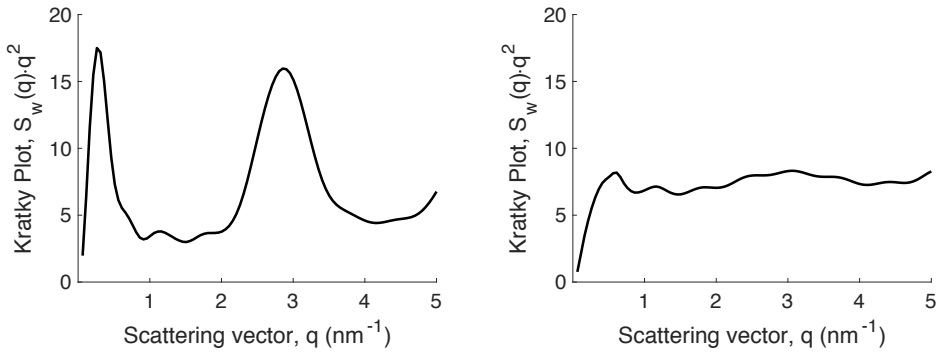


**Figure 6.3:** Illustrative representations of Kratky plots in order to evaluate the shape and compactness of formed complexes, where (a) represents the feature of a more compact shape and for (b) a more extended shape is expected.

## 6.4 Radius of gyration

The structural analyses of the polyelectrolyte chain in Paper v were performed by calculating the radius of gyration ($R_g$) of the chain. $R_g$ is an average measure of the compactness of the chains structure, and thus, is a measure of the size of the chain. It is defined as the root-mean-square distance between the mass elements in the chain and the centre-of-mass of the chain (Stepto et al. (2015)), according to:

$$R_g = \sqrt{\frac{\sum_{i=1}^{n} m_i(\mathbf{r}_i - \mathbf{r}_{com})^2}{\sum_{i=1}^{n} m_i}}\,. \tag{6.5}$$

The sum is over the total number of mass elements $n$, where $m_i$ is the mass of element $i$, and $\mathbf{r}_i$ and $\mathbf{r}_{com}$ is the position of element $i$ and the position of the chains centre-of-

mass, respectively. Furthermore, in Paper v, the conformation of the polyelectrolyte chain was analysed by the normalised $R_g$, defined as $R_g/R_g^\circ$. $R_g$ is the radius of gyration of the chain in the presence of platelets and $R_g^\circ$ is the radius of gyration for the undisturbed chain, that is, a single chain in bulk without platelets.

# 7. Experimental methods

## 7.1 Sample preparation

### 7.1.1 Bentonite clay – purification and cationic exchange

The Wyoming bentonite MX-80 used in Paper I and II consists mainly of the swelling clay mineral montmorillonite with sodium ($Na^+$) ions as the natural dominating counterion. Prior to use it is important to purify the raw bentonite clay to ensure that the majority of the accessory minerals, such as feldspars, quartz, gypsum, calcite, and pyrite, are removed.

The purification process involves dispersion of the raw clay in deionised water for at least one day in order to allow the larger particles ( > 2 μm) to sediment, after which the supernatant is recovered. Afterwards, an ionic exchange process is performed to either ensure that no additional counterions, other than sodium, are present in the clay or to exchange the counterions to calcium. For the ionic exchange process, the clay is washed three times with a salt solution of 1 M sodium chloride (NaCl) or 0.5 M calcium chloride ($CaCl_2$). Between each wash, the clay is centrifuged and redispersed in a fresh salt solution. Thereafter, the excess salt is removed by dialysing the clay suspension against deionised water in a large reservoir until the electrical conductivity is stabilised below 10 μS/cm. The water is frequently replaced, and the last replacements are usually with Milli-Q water. Finally, the clay is dried in an oven at around 90°C until completely dry and then milled into a fine powder.

### 7.1.2 Clay dispersions

The procedure for the sample preparation of clay dispersions can affect the obtained results, therefore it is important to consider the order in which the various components are added. For example, it is better to disperse the clay in Milli-Q water before adding

any other components, such as salts, peptides, or polyelectrolytes, to ensure that the clay platelets are completely dispersed. Then, after equilibrium, the dispersion can be filtered to prevent that any aggregates, which may originate from the dry state of the clay, remains in the dispersion. For the addition of another component, it is recommended to prepare a stock solution of the component of interest before adding it to the clay dispersion. Hence, it is preferable to mix the stock solutions of the clay and the other component, instead of mixing them in the dry state, which may result in non-equilibrium states. Furthermore, the pH of the dispersion can be an important factor, especially when studying clay in the presence of peptides and/or polyelectrolytes, where the charge of the peptide and the polyelectrolyte is highly pH dependent. A clay dispersion in an aqueous solution is alkaline, where it is possible to lower the pH of the dispersion with either a strong buffer or a strong acid, however, the pH will increase over time as the clay acts as a weak base. Moreover, the clay may not be stable in acidic solutions, and therefore, it is important to perform the measurement shortly after the preparation of the sample, as well as to measure the pH of the sample after the measurement.

### 7.1.3 deca-Arginine – purification

The deca-Arginine ($Arg_{10}$) peptide used in Paper IV was purchased as a lyophilised powder. In order to remove impurities and buffer components remnant from the synthesis, the peptide was purified through a dialysis process. First, the peptide powder was dissolved in Milli-Q water to a concentration of 20 mg/mL, after which the peptide solution was transferred into dialysis membranes with the size of 500-1000 Da. The pore size of the dialysis membranes should be much smaller than the molecular weight of the peptide in order to prevent any leakage of the peptide during the dialysis process. The peptide solution was dialysed against Milli-Q water, with a volume 500 times greater than the solution, whilst stirring in room temperature, and the dialysis step was repeated three times against fresh Milli-Q water. Finally, the peptide solution was freeze-dried and collected as a lyophilised powder. For the preparation of the stock solutions of $Arg_{10}$, the peptide powder was dissolved in Milli-Q water and the concentration was determined from the absorbance at 214 nm, using a NanoDrop 2000 Spectrophotometer with the extinction coefficient of $10800 \pm 100\ M^{-1}\ cm^{-1}$ (Tesei et al. (2017)).

## 7.2 Swelling pressure in a test cell

The swelling pressure, or the net osmotic pressure, of clay dispersions for different counterion valency, different solvent compositions, as well as addition of salt, can be

directly measured using a test cell (Karnland et al. (2006); Birgersson et al. (2010)). The experimental setup and a schematically depicted test cell are shown in Fig. 7.1. The clay, with a mass of approximately one gram, is placed inside a cylindrical cell with a radius of 1 cm and enclosed by two semi-permeable membranes at the top and bottom of the cell. The function of the semi-permeable membranes is to allow solvent molecules and ions to freely diffuse between the two compartments while the clay is retained. Then, the clay is confined in a predefined volume by a piston, which is attached to a force transducer, and the clay is set to equilibrate with water or the solvent composition of interest by slowly circulating the bulk solution through the test cell via the connected tubes. From the recorded force $F$ and the area of the cell $A = 0.01^2\pi$ m$^2$, the swelling pressure of the system is calculated as $P = F/A$ N/m$^2$. By measuring the force over time, it is possible to find a stable value of the swelling pressure for the clay sample with a certain solvent composition, where the clay is assumed to be in equilibrium with the bulk. Furthermore, the swelling properties of clays depend on the counterion valency, solvent composition, and addition of salt, where the system can either be dominated by repulsive or attractive interactions. Hence, from these measurements, it is possible to determine the dominating interactions within the system.

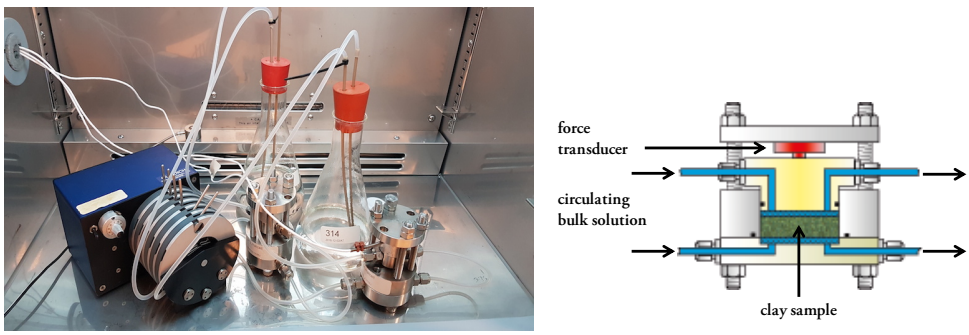


(a) (b)

**Figure 7.1:** Swelling pressure measured in a test cell, where (a) is the experimental setup and (b) a schematic illustration of the test cell (Karnland et al. (2006)).

After the measurement, the dry density $D_\mathrm{d}$ and the volume fraction $\phi$ of the clay sample can be determined. For aqueous clay dispersions, this is achieved by determining the clay water content $w = m_\mathrm{w}/m_s$, where $m_\mathrm{w}$ and $m_\mathrm{s}$ are the mass of the water and the solid (clay), respectively. The water content is obtained by disassembling the test cell and measuring the total mass $m_\mathrm{tot} = m_\mathrm{w} + m_\mathrm{s}$ of the clay and the water in the sample. The clay sample is then dried in an oven at around 100°C for 24 h to recover the mass of the clay. Thereafter, the dry density of the clay can be determined according to:

$$D_{\mathrm{d}} = \frac{m_{\mathrm{s}}}{V_{\mathrm{tot}}} = \frac{D_{\mathrm{w}}}{w + \frac{D_{\mathrm{w}}}{D_{\mathrm{s}}}}\,, \tag{7.1}$$

where $D_{\mathrm{s}}$ = 2750 kg/m³ is the density of the clay (montmorillonite) and $D_{\mathrm{w}}$ = 1000 kg/m³ is the density of water. Moreover, from the dry density, the volume fraction is obtained from $\phi = D_{\mathrm{d}}/D_{\mathrm{s}}$ (Karnland et al. (2006)). The same procedure is performed for clay dispersions in different solvent compositions, however, $D_{\mathrm{w}}$ is replaced with the corresponding density of the solvent composition.

An advantage of this experimental technique is that the bulk solvent can be replaced *in situ*, therefore, it is possible to study the clay-solvent interactions by, for instance, alternating the solvent composition with respect to the relative permittivity. Hence, the clay system is set to equilibrate with different solvent compositions throughout the measurement by successively increasing one component in the bulk solvent, resulting in a continuous transition. During the exchange to the new solvent composition, it is important to pump the new solvent carefully through the test cell to ensure that a complete exchange has taken place in the clay system. Moreover, the reversibility of the clay system can also be studied by replacing the solvent back to the original bulk solvent.

## 7.3 Small angle X-ray scattering

SAXS is a technique appropriate to study the microstructure of systems of the colloidal scale. For clay systems, the information extracted from SAXS is usually the platelet size, the inter-layer distance between the platelets, the size of the aggregates from the average number of clay platelets per tactoid, and the fractal dimensions. The principle of the technique is that a coherent monochromatic beam of X-rays with wavelength $\lambda$ is sent through a sample with an incident wavevector $\mathbf{k}_i$, where the outgoing scattered beam has the wavevector $\mathbf{k}_s$. The scattering intensity $I(q)$ is recorded as a 2D interference pattern on a detector and is represented as a function of the magnitude of the scattering vector $q$, where $q = |\mathbf{q}| = |\mathbf{k}_s - \mathbf{k}_i| = 4\pi \sin(\theta)/\lambda$, and $2\theta$ is the scattering angle (Glatter & Kratky (1982)). A schematic illustration of the technique with its main components is found in Fig. 7.2.

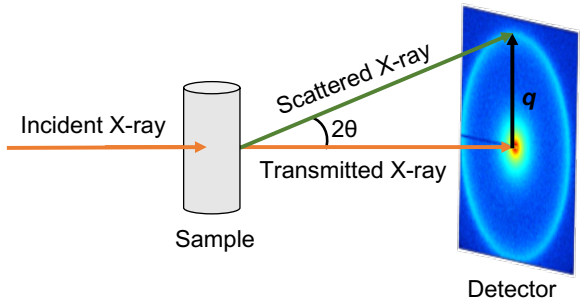


**Figure 7.2:** A schematic illustration of the SAXS technique and the main components. An incident X-ray beam is sent through a sample, the scattering angle between the transmitted and the scattered beam is denoted $2\theta$, and the corresponding $q$-vector is displayed on the 2D detector.

The scattering intensity for systems with spherical particles can be divided into two separate functions, the form factor $P(q)$ and the structure factor $S(q)$ according to $I(q) \propto P(q)S(q)$. The form factor contains information about the average particle size and shape, and the structure factor describes the distances between the particles, as well as the intermolecular interactions in the system. For dilute systems, the form factor can be extracted since $S(q) \approx 1$, and once the form factor of the system is known, the structure factor for more dense systems can be determined provided that the form factor is concentration independent (Schnablegger & Singh (2017)). For anisotropic particles, such as clay platelets, the decomposition of the scattering intensity is an approximation and a more accurate description of the system can be performed by comparing the experimental scattering intensity with the calculated total structure factor (Gutiérrez & Johansson (2002)) from computer simulations (described in Section 6.3).

For the structural configuration of tactoids, where the clay platelets aggregate in a face-to-face configuration, the periodicity of the system arising from the equidistant separation between the platelets, results in Bragg peaks in the SAXS spectra. This is in analogue to the feature shown for the total structure factor in Fig. 6.2b. From the Bragg peak, the inter-layer distance between the platelets in the tactoid can be determined according to Bragg's law: $d = 2\pi/q_{max}$, where $q_{max}$ is the position of $q$ at the maximum intensity of the Bragg peak (Schnablegger & Singh (2017)). Moreover, the full width at half-maximum (FWHM) of the Bragg peak is related to the size of the aggregates, which is determined from the average number of platelets per tactoid ($\langle N \rangle$) according to the Scherrer equation (Patterson (1939)):

$$\langle N \rangle d = \frac{K\lambda}{\Delta\theta \cos(\theta)}, \tag{7.2}$$

where $K \approx 0.9$ is the Scherrer constant, $\Delta\theta = \theta_2 - \theta_1$ is the FWHM of the Bragg peak

between the angles $\theta_1$ and $\theta_2$, and $2\theta$ is the scattering angle, also called Bragg angle. For small angles, the FWHM of the Bragg is $\Delta\theta \approx \sin(\theta_2)$ - $\sin(\theta_1)$ and the Scherrer equation can be approximated as:

$$\langle N \rangle \approx \frac{q_{max}}{2\pi(\sin(\theta_2) - \sin(\theta_1))/\lambda} = \frac{q_{max}}{(\Delta q)/2} = \frac{q_{max}}{w} \,. \tag{7.3}$$

Here, the Scherrer constant is set to one and $\Delta q = 2w$ is the FWHM in units of $nm^{-1}$. The method used to estimate the FWHM of the Bragg peak was to fit a Lorentzian function to the structure factor, where it is assumed that the scattering intensity can be divided into $P(q)$ and $S(q)$. Furthermore, the form factor is approximated to be $P(q) \propto q^{-2}$, and the data was fitted between $q_{max} = \pm$ 0.5 $nm^{-1}$ (Segad (2013); Thuresson et al. (2016b)), according to:

$$q^2 I(q) \propto \frac{w}{(q - q_{max})^2 + w^2} + b \,, \tag{7.4}$$

where $b$ is a fitting parameter for the background contribution. This method can describe the size of the aggregate for clay platelets with a large aspect ratio and with relatively narrow Bragg peaks. Hence, this method has proven to be accurate for montmorillonite clay and for Laponite® clay with addition of cationic peptides. For the SAXS measurements of clay dispersions, the samples were measured in 1 mm sealed glass capillaries, and an average of ten frames were collected for each sample to obtain accurate statistics and to check for any radiation damage. The homogeneity and concentration effects of the dispersions were also evaluated by performing measurements at approximately three different positions of the sample.

### 7.3.1 Kratky plot

The Bragg peak obtained in the SAXS spectra can be emphasised by presenting the data as a Kratky plot. Here, the scattering intensity is multiplied with the $q$-vector squared, i.e. $I(q) \cdot q^2$. This is analogue to the Kratky plot of the total structure factor described in Section 6.3.1, where the Bragg peak is shown in the high $q$-region in Fig. 6.3a.

## 7.4 Dynamic light scattering

The size distribution of colloidal particles can be determined from the technique of dynamic light scattering (DLS), also known as photon correlation spectroscopy (PCS).

DLS is based on the principle of extracting information about diffusion and size properties of colloidal particles by illuminating the particles with a laser light and analysing the intensity fluctuations of the scattered light caused by the movement of the particles. The DLS instrument Malvern Zetasizer Nano ZS (Malvern Instruments) (Zetasizer Nano Series (2012)) is equipped with a 4.0 mW He-Ne gas laser with a wavelength of 632.8 nm and a detector unit comprised with an Avanlanche Photo Diode with a backscatter detector angle of 173°. The advantage with backscatter detection is that samples with higher concentrations can be measured, since the path length of the incident beam through the sample becomes shorter, as well as that it reduces the effect of multiple scattering, where the scattered light from one particle is itself scattered by other particles.

All particles suspended in a liquid medium undergo Brownian motion, which is the continuous random movement of particles caused by collisions with the solvent molecules, which themselves move randomly due to their thermal energy. A fundamental feature of Brownian motion is that smaller particles move faster while larger particles move slower. In addition, all particles are capable of scattering light, and the scattered light from a moving particle experiences a Doppler shift, which is a small frequency shift of the scattered light compared to the unscattered light. The magnitude of the Doppler shift increases with the velocity of the particles, and thus, smaller particles exhibit a large Doppler shift, while larger particles exhibit a small Doppler shift (Ford (1985); Schmitz (1990); Pusey (2002); Uskoković (2012)).

In the DLS technique, a liquid sample is illuminated by coherent light, where the phase of the detected scattered light from all of the particles either interferes constructively or destructively. The photon counter detects the intensity of the scattered light and measures the fluctuations that result from the Doppler shift. The fluctuations in the intensity signal are measured over a period of time by comparing the signal at one point in time $t$ with the signal at a timestep $\delta t$ later, i.e. $(t + \delta t)$, from which the correlation between the signals is determined. The data is processed into a correlation function against time (Fig. 7.3), where the correlation ranges from one to zero, corresponding to perfect or no correlation, respectively. The correlation function decays exponentially with time, since the signals will experience less correlation with time due to the movements of the particles, where the rate of decay is faster for smaller than for larger particles (Zetasizer Nano Series (2012)).

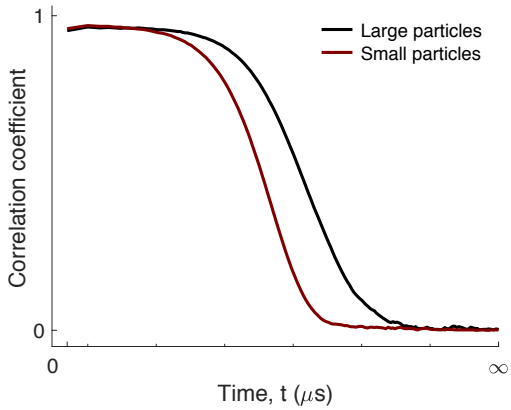


**Figure 7.3:** A representation of the correlation function against time ($t$), illustrating the behaviour in the exponential decay for large and small particles.

The decay of the correlation function is characterised by the *translational diffusion coefficient* ($D_{\mathrm{T}}$) of the particle. Hence, $D_{\mathrm{T}}$ is determined by measuring the Doppler shift of the light scattered by the moving particles, and is related to the size of the scattered particle by the Stokes-Einstein equation:

$$D_{\mathrm{T}} = \frac{k_{\mathrm{B}}T}{3\pi\eta d}\,. \tag{7.5}$$

Here $\eta$ is the viscosity of the medium and $d$ is the equivalent spherical diameter, or hydrodynamic diameter, of the scattered particle, where it is assumed that the particles move independently of each other (Ford (1985); Schmitz (1990); Pusey (2002); Artemyeva et al. (2020)). It should be mentioned that $d$ is not the effective diameter of a hydrated particle in solution, it is rather the diameter of a hard-sphere that diffuses at the same rate as the particle, which includes both hydration and shape effects. For non-spherical particles, such as clay platelets, the particle will be detected as a spherical particle with the diameter averaged over three axes, since the particles also undergo rotational diffusion around their axes. Therefore, more extended particles will have a larger $d$ compared to more compact particles with the same molecular weight. For clay dispersions, DLS is a rapid and robust method to determine the size distributions of clay platelets, however, it is important to work with dilute dispersions due to the sensitivity of the measurements, since the scattering intensity of a particle is proportional to the sixth power of the particles diameter. Furthermore, the particle interactions in dilute dispersions becomes negligible, and thus, Eq. (7.5) is valid for the calculation of the clay platelets diameter. The DLS measurements were performed for freshly made samples to avoid any time aging effect or sedimentation, and each sample was meas-

ured for a minimum of three times to obtain good statistics. The correlation functions were analysed and compared with respect to the exponential decay of the curve, the initial correlation value, and the similarity between them. In the correlation function, there should not be any irregularity or peaks at a large time, which could result from dust or large aggregates in the sample. The initial correlation should be in the range of 0.6–1.0, where a lower initial correlation usually means that the sample is too dilute. In addition, the size distributions, obtained as intensity distributions, were evaluated to ensure that there were no additional or double peaks in the distribution, as that would indicate the presence of impurities or large aggregates.

## 7.5 Zeta-potential

The $\zeta$-potential is the electrokinetic potential in charged colloidal dispersions arising from the electrical double layer created by the counterions, which consists of two parts: an inner and an outer region. The inner region is referred as the *Stern layer*, where the ions are strongly bound to the particle, whereas in the outer region the ions are less firmly attached, and thus, it is referred as the diffuse layer. Moreover, the *slipping plane* is the boundary defining the electrical double layer, where the ions within the boundary follow the particle movements, while the ions outside the boundary do not. Hence, the potential at the slipping plane is the $\zeta$-potential, which is determined from the electrophoretic mobility of the particle. Furthermore, $\zeta$-potential is used as a quantity to evaluate the magnitude of the repulsive electrostatic interactions between charged colloidal particles, hence, it gives an indication of the stability of the system. Generally, the limit of a stable dispersion is at $\pm$ 30 mV and above, whereas the threshold for aggregation is at $\pm$ 15 mV, and in the range of 15–30 mV, the system may either be aggregated or dispersed. The technique is based on a combination of electrophoresis and laser doppler velocimetry in order to determine the velocity of a particle in a medium with an applied field. From the electrophoretic mobility ($U_{\mathrm{E}}$) of the particle, the $\zeta$-potential is obtained by applying the Henry equation (Zetasizer Nano Series (2012)):

$$U_{\mathrm{E}} = \frac{2\epsilon\zeta f(\kappa a)}{3\eta}\,. \tag{7.6}$$

Here, $\epsilon$ is the dielectric constant, $\zeta$ is the $\zeta$-potential, and $f(\kappa a)$ is Henry's function, which depends on the thickness of the electrostatic double layer $1/\kappa$ and the particle radius $a$. Two values are considered as approximations for the determination of $f(\kappa a)$, either 1.0 or 1.5. In the limit of a thick double layer, where $\kappa a \ll 1.0$, $f(\kappa a) \rightarrow 1.0$, which corresponds to the *Hückel mobility* and is mainly used for samples in non-aqueous media. For compact (thin) double layers, where $\kappa a \gg 1.0$, $f(\kappa a) \rightarrow 1.5$

and is referred to the *classical Smoluchowski limit*, which was used for the $\zeta$-potential measurements of Laponite® clay dispersions in Paper III and IV. The samples were freshly made and a minimum of three measurements were performed for each sample. An advantage of combining the techniques of DLS and $\zeta$-potential measurements is that the same sample can be used, providing both structural and stability properties for the same system, hence, reducing any source of error in the sample preparation.

## 7.6 Transmission electron microscopy

Transmission electron microscopy (TEM) and cryogenic TEM (cryo-TEM) are microscopy techniques where an electron beam is transmitted through a specimen (a thin liquid film) in order to provide information over the size, the shape, and the microstructure of colloidal particles. A description of the technique and examples of studied systems used with cryo-TEM can be found in the following reference: Almgren et al. (2000).

The techniques of TEM and cryo-TEM were used in Paper III to study the tactoid formation of Laponite® platelets with addition of the trivalent salt lanthanum chloride ($LaCl_3$). For the TEM measurements, the sample suspension was pipetted onto a TEM grid (continuous formvar-carbon film on 200 mesh copper), gently blotted using a filter paper and allowed to air dry. Afterwards, the grid was mounted on a standard JEOL single tilt holder and imaged at room temperature on a JEOL JEM-2200FS TEM. For the cryo-TEM measurements, the grids (lacey formvar-carbon film on 200 mesh copper) were first glow discharged. Thereafter, the sample suspension was pipetted onto the grid in a Leica EM GP automatic plunge freezer operating at 21°C and relative humidity of >90%, backside blotted for 2.5 s and plunged into liquid ethane. The vitrified samples were stored in liquid nitrogen until used. For imaging, the samples were transferred onto a cryogenic sample holder and imaged on a JEOL JEM-2200FS TEM, where the temperature was maintained below -175°C. In both TEM and cryo-TEM, the microscope was operating at an accelerating voltage of 200 kV, utilising the omega energy filter for contrast enhancement. The imaging was performed in low-dose mode, keeping the total electron dose per image below 50 e/Å$^2$. The acquired images were processed in ImageJ Software (Schneider et al. (2012)). A representative cryo-TEM image for the Laponite® dispersion at the stochiometric charge-ratio (defined in Eq. (5.7)) of four is shown in Figure 7.4.

For anisotropic colloidal particles, such as clay platelets, the contrast depends strongly on their orientation with respect to the electron beam. The diffraction contrast is strong when the basal plane of the platelets is oriented parallel to the electron beam, where the platelets appear as dark lines (or "filaments") in the TEM and cryo-TEM image.

In addition, Fresnel fringes may appear on both sides of the platelets, which are more or less pronounced depending on the defocus of the objective lens, and these can artificially increase the value of the platelet thickness (Herrera et al. (2004)). For the platelets where the basal plane is relatively perpendicular to the electron beam, the diffraction contrast is much weaker, hence, these platelets are hard to detect due to the small platelet thickness of $\sim$ 1 nm. Furthermore, it is possible to perform quantitative analysis from cryo-TEM if sufficient statistics on the sample are obtained. These analyses include the thickness of the platelets, the mean-cross sectional length, and the average inter-layer distance, or *d*-spacing. For the sample in Figure 7.4 , the thickness was estimated to 1.2 $\pm$ 0.1 nm, the mean-cross sectional length as 15 $\pm$ 6 nm, and two preferential *d*-spacings were found: one more prominent at 2.2 $\pm$ 0.2 nm and another weaker at 1.3 $\pm$ 0.1 nm.

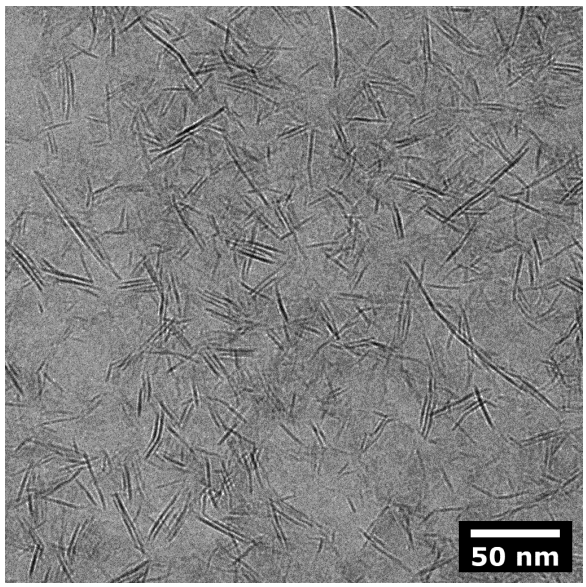


**Figure 7.4:** A representative cryo-TEM image for the Laponite® clay dispersion with addition of the trivalent salt lanthanum chloride ($LaCl_3$) at the stoichiometric charge-ratio between the positive salt ions and the clay platelets equal to four. The dark lines are the Laponite® platelets seen with the basal plane oriented parallel to the electron beam.

# 8. The research

## 8.1 The effect of Bjerrum length

The physiochemical properties of colloidal dispersions, such as clay dispersions, are primarily determined by the mechanism of ionic exchange in the double layer and the release of counterions, along with the charge distribution, the concentration, the volume, as well as the size and the shape of the colloidal particle. Moreover, the electrostatic interactions within the system are enhanced with temperature in an aqueous solution, arising from the decrease in the relative permittivity with temperature. This correlates to the Bjerrum length, according to:

$$l_{\mathrm{B}} \propto \frac{1}{\epsilon_r(T)T}\,, \tag{8.1}$$

where the product of the relative permittivity and the temperature decreases with an increase in temperature for aqueous solutions. Hence, the Bjerrum length increases, and the attractive ion-ion correlation forces become enhanced. The effect of the Bjerrum length can therefore be studied by either varying the temperature or the solvent composition, which correlates to a change in the relative permittivity. The former was investigated in Paper I for the natural clay montmorillonite, where it was observed from the MD simulations in the NPT ensemble that the system with monovalent counterions, corresponding to $Na^+$-montmorillonite, was dominated by entropic repulsive interactions, where the platelets preferred to be far apart. This was determined from the large volume per platelet, which increased with temperature, indicating that the swelling pressure increases with temperature. The swelling behaviour of $Na^+$-montmorillonite was validated with SAXS, where no Bragg peaks were obtained regardless of temperature, which is corroborated by the swelling pressure measured using the test cell (Thuresson et al. (2016a)), and in agreement with the DLVO theory.

For the clay system with predominantly divalent counterions, corresponding to $Ca^{2+}$-

montmorillonite, a reduced osmotic pressure and an increase in the average number of platelets per tactoid with temperature were obtained from MD simulations in the NVT ensemble. This arises from the enhanced ion-ion correlation forces due to the increased Bjerrum length. The same behaviour was found for the swelling pressure of $Ca^{2+}$-montmorillonite, which decreased with an increased temperature (Thuresson et al. (2016a)). This observation is in disagreement with the DLVO theory, which predicts that the osmotic pressure increases with temperature, for monovalent as well as divalent counterions. From the SAXS measurements (Fig. 8.1a) it was found that the FWHM decreased with an increased temperature, indicating that the tactoids grow in size. For the temperatures of 55°C and 90°C, a small difference in the average number of platelets was found, whereas a larger deviation was obtained for 25°C. This may be associated with a change in the microstructure of the system. The position of the Bragg peak shifted towards higher $q$-values with temperature, indicating that the average inter-layer distance between the platelets decreased, from ∼1.93 to 1.89 nm, corresponding to three water layers, for 25°C to 90°C. At 5°C, the SAXS data was composed by a superposition of two Bragg peaks, with an average distance of ∼1.9–2.1 nm, corresponding to a combination of three to four water layers, in agreement with the previous work by Svensson & Hansen (2013). A qualitative agreement between the simulations and the experimental data were observed for the effect of temperature, where the following trends were captured: (i) the inter-layer distance between the platelets decreased and (ii) the average number of platelets per tactoid increased. The latter is illustrated in Figs. 8.1b–8.1d, where representative configurations from the MD simulations are shown for the temperatures of 5°C, 25°C, and 95°C.

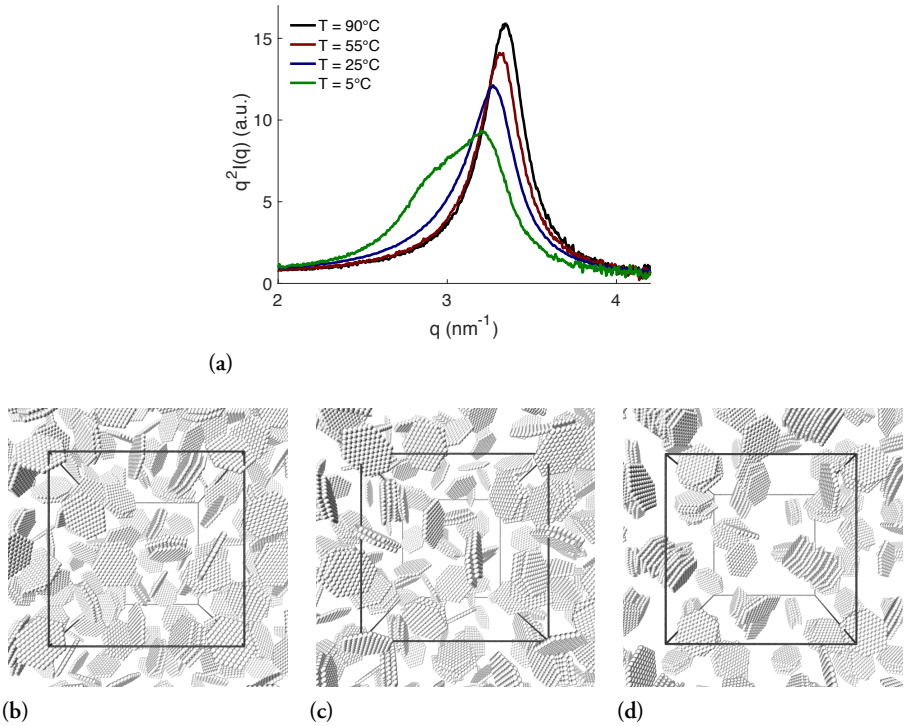


**Figure 8.1:** (a) SAXS intensities represented as Kratky plots over a narrow $q$-range for the temperature measurements of $Ca^{2+}$-montmorillonite. The intensities are normalised at $q \approx 1\,nm^{-1}$. (b) – (d) Representative configurations obtained from the MD simulations for $Ca^{2+}$-montmorillonite at the temperatures of (b) 5°C, (c) 25°C, and (d) 95°C. The counterions are omitted for clarity, the platelets are shown in grey, and the cubic simulation box is shown in black (periodic images are shown outside the simulation box).

Furthermore, the effect of the surface charge density on the crossover between a negative and a positive osmotic pressure response with temperature was studied for two parallel surfaces with MC simulations. It was found that the DLVO theory is qualitatively valid with divalent counterions if the net surface charge density is below 0.2 e/nm², where a positive osmotic pressure response with temperature was obtained. This confirms that the electrostatic interactions within the system alone can give a positive, negative, or constant osmotic pressure response with temperature depending on the surface charge density as well as on the counterion charge ratio.

The electrostatic interactions within a system of charged colloidal particles can also be tuned via the solvent properties, where a reduced relative permittivity results in an increased Bjerrum length (Eq. 8.1), whereby ion-ion correlation forces become enhanced. For clay dispersions, the clay-solvent interactions have been extensively studied for the natural montmorillonite clay in water (Norrish (1954)) and organic solvents (Brindley & Ray (1964); Dowdy & Mortland (1967); Metz et al. (2015)), as well as in water/organic

mixtures (Brindley et al. (1969)). The swelling of dry $Na^+$-montmorillonite with ethanol has been studied with atomistic computer simulations by Metz et al. (2015). They found that the initial swelling was associated with a large energy barrier when the first ethanol molecule is moved into the inter-layer region, which is in contrast to the swelling behaviour observed in water. However, the possibility of the formation of a monolayer and a transition to a bilayer of ethanol was still captured, where it was found that the behaviour of the sodium ions was different in ethanol compared to water. In ethanol, the sodium ions tend to aggregate at the clay surface rather than being dispersed in the solvent.

The effect of Bjerrum length for the alternation of the solvent properties was studied in Paper II for the natural clay mineral montmorillonite in water/ethanol mixtures. By reducing the relative permittivity of the bulk solvent, a transition from a repulsive to an attractive system was observed for $Na^+$-montmorillonite. This behaviour was captured with SAXS (Fig. 8.2a), where Bragg peaks were observed for the fractions of $\geq$ 60 wt% ethanol, indicating the formation of tactoids. For a further increase in ethanol, up to 95 wt%, the position of the Bragg peak shifted towards higher $q$-values and the FWHM decreased, corresponding to a reduced average inter-layer distance between the platelets within the tactoids of $\sim$ 2.18 to 1.70 nm and an increased average number of platelets per tactoid of $\sim$11 to 25. The experimental results were in qualitative agreement with the obtained results from the MD and MC simulations, where the solvent was treated implicitly and represented by the temperature-dependent relative permittivity of the bulk solvent. The crossover is illustrated in Figs. 8.2b – 8.2c, where representative configurations from the MD simulations are shown for 0 and 100 wt% ethanol. At 0 wt% ethanol (water), only single platelets were found in the system and as the concentration of ethanol was increased, the platelets started to aggregate until all platelets had aggregated and formed tactoids at 100 wt% ethanol.

In addition, the intracrystalline swelling, which was directly measured using the test cell, was significantly reduced when increasing the fraction of ethanol, which confirms the transition from a repulsive to an attractive system. The reversibility was captured by changing the solvent back to water, where the swelling pressure returned to its initial value. During this exchange, a large peak emerged in the swelling pressure data, and our hypothesis is that during this transition, the intercalated ethanol molecules were successively replaced by water molecules.

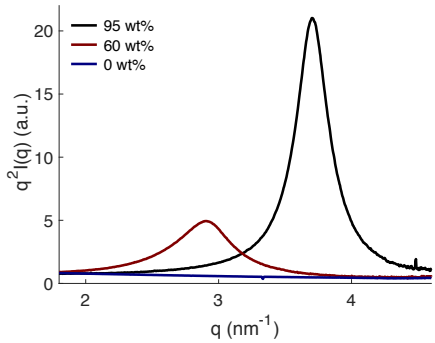


(a)

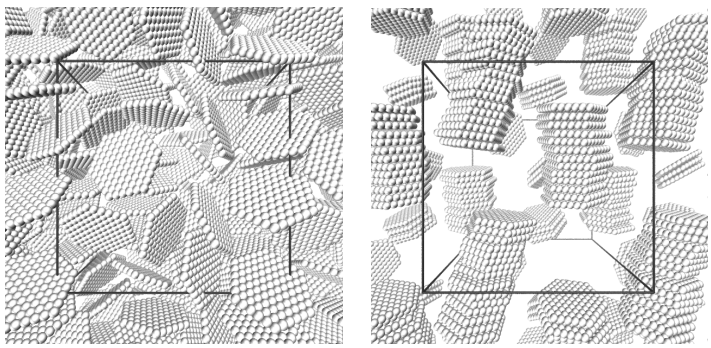

(b) (c)

**Figure 8.2:** (a) SAXS intensities represented as Kratky plots over a narrow $q$-range for the measurements of $Na^+$-montmorillonite in water/ethanol mixtures. The intensities are normalised at $q \approx 1$ nm$^{-1}$. (b) and (c) Representative configurations for $Na^+$-montmorillonite in water/ethanol mixtures obtained from the MD simulations with (b) 0 and (c) 100 wt% ethanol. The counterions are omitted for clarity, the platelets are shown in grey, and the cubic simulation box is shown in black (periodic images are shown outside the simulation box).

In order to further evaluate if the structural properties of $Na^+$-montmorillonite in a water/ethanol mixture can behave qualitatively similar as $Ca^{2+}$-montmorillonite in water, the systems of $Na^+$-montmorillonite at 95 wt% ethanol and $Ca^{2+}$-montmorillonite at 0 wt% ethanol were compared. From the SAXS data, the Bragg peak for $Na^+$-montmorillonite was located at a higher $q$-value and had a narrower FWHM. Hence, a smaller inter-layer distance between the platelets in the tactoids and a greater average number of platelets per tactoid were obtained for $Na^+$-montmorillonite at 95 wt% ethanol compared to $Ca^{2+}$-montmorillonite at 0 wt% ethanol. This can be qualitatively explained from the coupling parameter, which is $\sim$28 for monovalent ions in ethanol and $\sim$25 for divalent ions in water. Thus, there are stronger attractive interactions due to the stronger coupling for monovalent ions in ethanol compared to divalent ions in water.

For $Ca^{2+}$-montmorillonite, a non-monotonic behaviour of the intracrystalline swelling as a function of ethanol concentration was captured experimentally, where both the swelling pressure and the position of the Bragg peaks in the SAXS data displayed a strong dependence on the ethanol concentration (Fig. 8.3). The swelling pressure increased until the ethanol fraction of 20 wt% was reached in the sample and the Bragg peak shifted towards lower $q$-values comparing the samples of 0 and 20 wt% ethanol. This indicates that there are stronger short-ranged repulsive forces at lower concentrations of ethanol and that the inter-layer distance between the platelets in the tactoids increases. At 60 wt% ethanol, a superposition of two Bragg peaks was found in the scattering data and the swelling pressure was approximately in the same regime as for the sample in water. This indicates that there is a competition between two different inter-layer distances, either for the intercalated ethanol and water or for two ethanol concentrations. With a further increase in the fraction of ethanol up to 95 wt%, the Bragg peak shifted to higher $q$-values, corresponding to an inter-layer distance between the platelets of $\sim$1.70 nm, and the swelling pressure reduced significantly, due to the enhanced ion-ion correlation forces. Moreover, from the swelling pressure measurements, the reversibility of the system was confirmed when changing the solvent back to water.

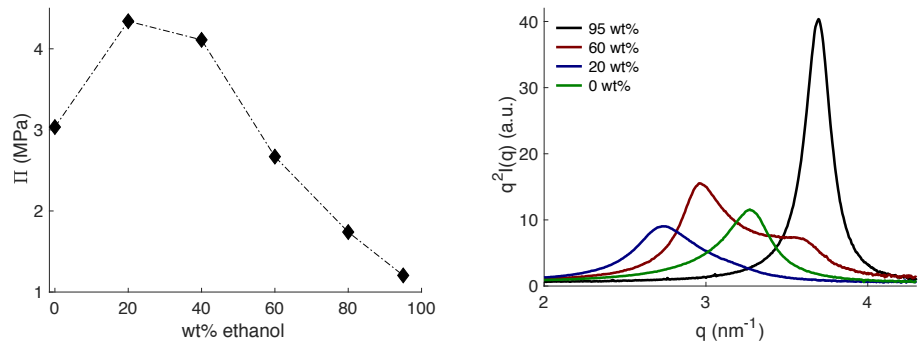


**Figure 8.3:** (a) The swelling pressure as a function of the fraction of ethanol for $Ca^{2+}$-montmorillonite, where the dash-dotted line is a guide for the eye. (b) SAXS intensities represented as Kratky plots over a narrow $q$-range for the measurements of $Ca^{+}$-montmorillonite in water/ethanol mixtures. The intensities are normalised at $q \approx 1$ nm$^{-1}$.

The non-monotonic behaviour of the intracrystalline swelling in water/ethanol mixtures for $Ca^{2+}$-montmorillonite is in agreement with the results obtained from X-ray diffractometry (Brindley et al. (1969)). It was observed that the basal spacing increased at low concentrations of ethanol, and beyond the maximum expansion, the basal spacing diminished abruptly. The initial increase in the basal spacing was explained to arise from the replacement of water molecules with the larger ethanol molecules, hence, an

excluded volume effect. It was also concluded that the initial increase is not compatible with the reduced relative permittivity due to the fact that this would enhance the attractive electrostatic forces. However, both effects can be present in the system and the interactions can be explained through the intricate balance of: (i) the partitioning of the solvent molecules, (ii) the electrostatic repulsive forces, and (iii) the enhanced ion-ion correlation forces.

Theoretically, a monotonic trend for the osmotic pressure as a function of ethanol concentration was captured for $Ca^{2+}$-montmorillonite, which was not consistent with the experimental observations. Hence, the non-monotonic behaviour of the intracrystalline swelling could not be captured with the continuum model, which is probably due to the lack of partitioning of the solvent molecules and the limitation that the electrostatic interactions solely enters the Hamiltonian via the Bjerrum length. In principle, the continuum model should be valid with respect to the electrostatic interactions, however, the effect of the alternation of the relative permittivity with water/ethanol mixtures could be overruled by other effects, for example: (i) the difference in size between the solvent molecules, (ii) the density changes associated with the solvent interactions, and/or (iii) the geometry of the solvent molecules. In order to capture the behaviours observed experimentally, a theoretical model considering the interactions between the solvent molecules and the clay platelets is needed. A good candidate is a model where the solvent is treated explicitly.

## 8.2 The effect of counterion valency and salt

The swelling and stability of like-charged colloidal dispersions, such as clay dispersions, are strongly dependent on the counterion valency and the surface charge density. In Paper I, the effect of the counterion valency was studied by varying the ratio of monovalent/divalent counterions for the clay montmorillonite. By increasing the amount of divalent counterions in the system, a crossover was obtained, corresponding to a transition from repulsive to attractive interactions within the system. From the MD simulations in the NPT ensemble, the crossover was observed for the volume response with temperature, which changed sign from positive to negative with an increase in divalent counterion charge. In the vicinity of the crossover, a minimum was found, where the decrease in volume arises from the effects of: (i) the single platelets form tactoids, (ii) the tactoids grow in size, and (iii) the inter-layer distance between the platelets within a tactoid is reduced. The crossover was at $\sim$80% and $\sim$90% calcium for the pressures of 1.0 and 0.2 bar, respectively. The theoretical results were validated with SAXS, where clay dispersions of $Ca^{2+}/Na^{+}$-montmorillonite mixtures were measured. From the scattering intensities (Fig. 8.4), no Bragg peaks were visible for the samples with $\leq$ 60% calcium, indicating that the systems were dominated by repulsive interactions,

whereas for $\geq$ 80% calcium, Bragg peaks were clearly observed, confirming that tactoids were formed in the samples. The tactoidal growth was confirmed from the FWHM, which decreased with an increase in fraction of divalent counterions. These results are in agreement with the experimental (Hedström et al. (2011)) and theoretical (Segad et al. (2010)) studies for mixtures of $Ca^{2+}$/$Na^{+}$-montmorillonite dispersions, where it was found that clay dispersions with ∼20% or more sodium behaves qualitatively like $Na^{+}$-montmorillonite.

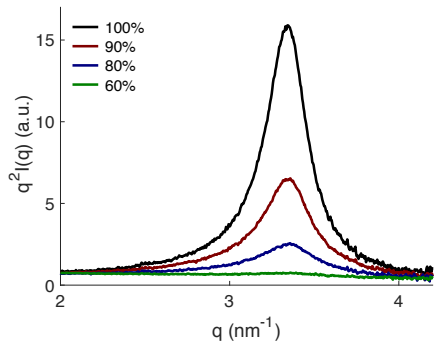


**Figure 8.4:** SAXS intensities represented as Kratky plots over a narrow $q$-range for the measurements of $Ca^{2+}$/$Na^{+}$-montmorillonite mixtures with different fractions of calcium counterions. The intensities are normalised at $q \approx 1$ nm$^{-1}$.

Furthermore, the destabilisation of like-charged colloidal dispersions is more evident with addition of multivalent salt and high salt concentrations due to the existence of attractive ion-ion correlation forces (Oncsik et al. (2014); Terao & Nakayama (2001); Delville (2002)). Upon addition of multivalent salt to clay dispersions with monovalent counterions, there will be an ionic exchange in the double layer and a release of monovalent counterions, where it has been observed that the stability depends both on the valency of the salt cation and the stoichiometric charge-ratio $\beta$ between the salt ions and the clay. This was investigated in Paper III for Laponite® dispersions in the presence of mono- and multivalent salt. With the addition of mono- and divalent salt, the PMF extracted from the MD simulations utilising enhanced umbrella sampling (Fig. 8.5a), was positive regardless of $\beta$, indicating that the systems were dominated by repulsive interactions. However, the PMF was lower for the divalent salt compared to the monovalent salt, which suggests that the attractive interactions become enhanced when the valency of the salt ion was increased. For the addition of trivalent salt, a crossover in the PMF was observed (Fig. 8.5a), indicating that the long-ranged repulsion was screened and that there was a transition from repulsive to attractive interactions within the system. At short distances, global minima were obtained in the PMF, suggesting the formation of small aggregates or tactoids due to the enhanced ion-ion correlation forces. By decreasing the surface charge density of the platelets, a

non-monotonic trend in the PMF was found, where the interactions within the system were repulsive, attractive, and then repulsive again. This implied that tactoidal dissolution occurred in the system due to the overcharging effect, which was confirmed from the measured $\zeta$-potential (Fig. 8.5b), where a transition from a negative to a positive value was obtained at a large excess of salt.

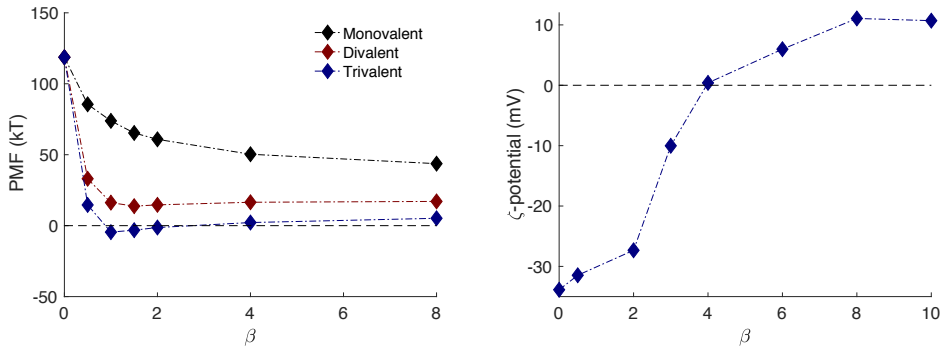


(a) (b)

**Figure 8.5:** (a) The potential of mean force (PMF) at the separation of 1.5 $\pm$ 0.2 nm between two parallel platelets and (b) the $\zeta$-potential for the Laponite® dispersions with the addition of trivalent salt as a function of the stoichiometric charge-ratio $\beta$. The dash-dotted lines are a guide for the eye.

Experimentally, the structural properties were analysed from the size distribution obtained from DLS (Fig. 8.6a), where the mean radius increased up to $\beta$ = 4, after which it decreased until a plateau was reached. The maximum value of the mean radius corresponded to the point where the $\zeta$-potential was equal to zero, hence, the overall charge of the complex was zero and the maximum size of the tactoids was found when the trivalent salt fully neutralised the net negative charge of the clay platelets. Further structural analyses were performed with cryo-TEM, where it was observed that for the Laponite® sample without addition of salt, the platelets were well separated and no aggregates were found, confirming that the system was dominated by repulsive interactions and consisted mainly of single platelets. Upon addition of trivalent salt, the distance between the platelets decreased, and more platelets were found in close vicinity to each other. The number of platelets parallel to the beam increased up to $\beta$ = 4, and thereafter, at $\beta$ = 8, less platelets parallel to the beam were observed. A representative cryo-TEM image for the system with $\beta$ = 4 is shown in Fig. 8.6b. These results indicated that tactoid formation was promoted by the addition of trivalent salt due to that the long-ranged repulsion between the platelets was screened. Then, tactoidal growth was observed, which arose from the enhanced attractive ion-ion correlation forces, and finally, the overcharging effect caused tactoidal dissolution to occur in the system.

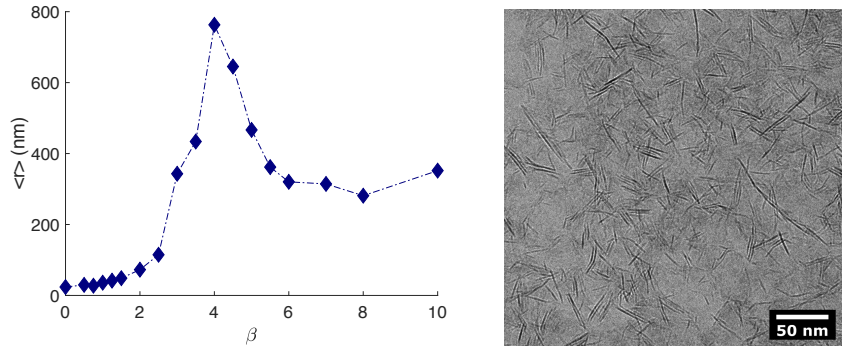


(a) (b)

**Figure 8.6:** (a) The mean size of the particles for the Laponite® clay dispersion with the addition of trivalent salt, represented as the mean radius (<*r*>), as a function of the stoichiometric charge-ratio $\beta$. The dash-dotted line is a guide for the eye. (b) A representative cryo-TEM image for the Laponite® clay dispersion with the addition of trivalent salt at $\beta$ = 4. The dark lines are the Laponite® platelets seen with the basal plane oriented parallel to the electron beam.

In addition, quantitative analyses were performed from the cryo-TEM imaging, where the prominent average inter-layer distance was 2.2 $\pm$ 0.2 nm, corresponding to four water layers, in agreement with the average separation of Laponite® platelets in the presence of lanthanum chloride measured with SAXS (Thuresson et al. (2017)). Theoretically, the structural properties obtained from the MD bulk simulations displayed the same trend as the experimental observations, where Bragg peaks were observed in the high $q$-region for $\beta$ = 4 and 8 in the calculated structure factors represented as Kratky plots. The former had the highest intensity, indicating that the most well-ordered structure was obtained at $\beta$ = 4, which was confirmed from the low $q$-region, where the high intensity peak of $\beta$ = 4 corresponded to that the formed complex possessed the most compact configuration.

The captured trends of the overcharging effect and the stability of the Laponite® dispersions with addition of trivalent salt are in correlation with studies for other colloidal systems. For instance, the observed mean force between two like-charged spherical particles with addition of trivalent salt display that the stability of a colloidal dispersion passes through three stages with an increase in salt: (i) a stable dispersion, (ii) a two-phase region, and (iii) redissolution (Angelescu & Linse (2003)). In stage (i), the colloidal particles are well separated by an effective repulsive potential, in stage (ii) the double-layer repulsion between the colloidal particles is strongly reduced and the interaction between the colloidal particles is dominated by attractive ion-ion correlation forces, and in stage (iii) the attractive forces are reduced and the double-layer repulsion between the colloidal particles is enhanced. The same trend was also found when exchanging the counterion valency from monovalent to divalent and finally to trivalent

(Angelescu & Linse (2003); Linse & Lobaskin (2000)). The discrepancy between the attractive forces found for the montmorillonite dispersion dominated by calcium counterions and the lack of attractive forces found for the Laponite® dispersion with addition of divalent salt, arises from the size of the platelets as well as on the surface charge density. The interaction is to a first approximation proportional to the area of the platelets, and the surface charge density is related to the strength of the attractive ion-ion correlation forces, which is lower for Laponite® compared to montmorillonite. Hence, the attraction between Laponite® platelets in the presence of multivalent cations should theoretically be less significant compared to montmorillonite platelets.

## 8.3 Structure formation induced by peptides or polyelectrolytes

The behaviours of the overcharging effect and the stability have also been found for latex particles with addition of the branched spherical polyelectrolyte dendrimer (Lin et al. (2004); Trulsson et al. (2009); Popa et al. (2009)), indicating that systems consisting of like-charged spherical particles are qualitatively similar to systems containing like-charged platelets with respect to the electrostatic interactions. This was further evaluated in Paper IV for Laponite® dispersions in the presence of the cationic peptide $Arg_{10}$, where the peptide was selected due to its relatively short sequence of ten amino acids and highly cationic nature. Upon addition of $Arg_{10}$, Bragg peaks were observed in the Kratky plots (Fig. 8.7a) for all $Arg_{10}$ concentrations investigated, indicating tactoid formation within the systems. The tactoidal structure is stabilised by charge-charge interactions between the peptide and the platelet, and the process is entropically driven due to the release of counterions associated with the clay when the peptide adsorbs onto the platelet. The maxima of the Bragg peaks were consistent between the samples, corresponding to an average $d$-spacing of $\sim$ 1.8 nm. Moreover, a monotonic increase of the intensity and a decrease in the FWHM were observed up to $\beta$ = 2.5, suggesting that the tactoids grow in size. Thereafter, a lower intensity was obtained, which can be explained by a tactoidal dissolution due to overcharging of the platelets caused by the presence of the peptide, which thereby induces repulsive interactions. The overcharging effect was confirmed from the measured $\zeta$-potential (Fig. 8.7b), which changed sign from negative to positive with an increase in $\beta$.

Moreover, the overcharging effect was studied at two different ionic strengths, where it was found that the effect was more pronounced at low ionic strength, which emphasises the importance of the electrostatic interactions in the system. These results validate that the Laponite® clay and the peptide $Arg_{10}$ form an intercalated peptide-clay nanocomposite, which is in correlation with previous studies for the intercalation of antimicrobial peptides within layered clay minerals (Thompson & Butterworth (1992); Häffner et al. (2019)).

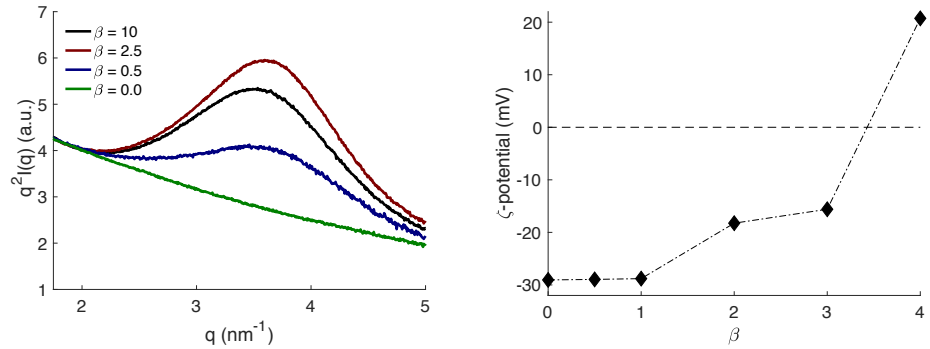


(a) (b)

**Figure 8.7:** (a) SAXS intensities represented as Kratky plots over a narrow $q$-range for the Laponite® dispersions with addition of the cationic peptide $Arg_{10}$ with varying stoichiometric charge-ratio $\beta$. The intensities are normalised at $q \approx 2$ nm$^{-1}$. (b) The $\zeta$-potential for the Laponite® dispersions with the addition of the cationic peptide $Arg_{10}$ as a function of $\beta$. The dash-dotted line is a guide for the eye.

The intercalation of the peptide within the clay platelets was further studied with MD simulations in order to identify at which $\beta$ the tactoid formation was initiated, maximised, as well as when tactoidal dissolution due to overcharging occurred. It was found that at low number of peptides ($\beta < 1$), several smaller tactoids were observed in the systems, and by increasing the number of peptides, the size of the tactoids increased until all platelets had aggregated into one tactoid ($\beta = 1$), thereafter at an excess of peptides ($\beta > 1$), tactoidal dissolution occurred, where the tactoid dissolved into smaller tactoids again. This was observed in the radial distribution functions and the calculated structure factors and confirmed from the calculated average number of platelets per tactoid. The overall behaviour was in qualitative agreement with the experimental observations and the process is illustrated in Fig. 8.8, where representative configurations from the MD simulations are shown for an increase in $\beta$. In addition, the extent of overcharging, and to which degree a platelet can be overcharged by a peptide, was investigated by single platelet MD simulations. From the distribution of $Arg_{10}$ as a function of distance from the platelet surface, the gradient corresponding to the tendency for the $Arg_{10}$ to interact with the platelet was extracted. It was observed that the gradient increased with $\beta$, indicating that more chains were in close contact with the platelet, and that the platelets became overcharged by the peptides, in qualitative agreement with the measured $\zeta$-potentials.

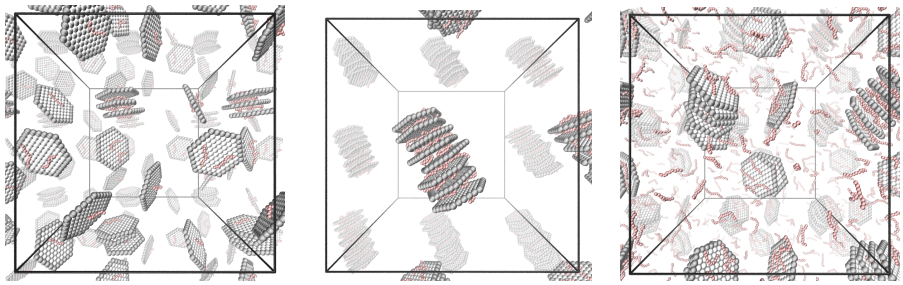


**Figure 8.8:** Representative configurations for Laponite® dispersions with addition of the cationic peptide $Arg_{10}$ at the stoichiometric charge-ratio $\beta$ of (a) 0.5, (b) 1, and (c) 2. The counterions are omitted for clarity, the platelets are shown in grey, the peptides are shown in red, and the cubic simulation box is shown in black (periodic images are shown outside the simulation box).

Furthermore, the general applicability of the model and the impact of the electrostatic interactions were evaluated by altering the peptide properties. Hence, the possibility to make predictions of the behaviour of the peptide intercalation based on the characteristics of the peptide was investigated. This is important to study since peptides that exert a biological function do not typically contain a homogeneous sequence of charged residues. The peptide was altered by: (i) the sequence length, (ii) the net charge of the chain, (iii) the number of beads as well as the charge of each bead, whilst keeping the total charge of the chain constant, and (iv) the charge distance matching between the chain and the platelet. The following results were obtained for the respective alternation of the peptide:

(i) By increasing the length of the peptide chain, the tactoids increased in size until a peptide sequence of ten, after which the tactoid size decreased slightly.

(ii) With an increase in the net charge, tactoid formation was promoted, which was followed by tactoidal growth.

(iii) An optimum with respect to the peptide properties for the intercalation process was observed, suggesting that this alternation has a greater influence than the total charge of the chain.

(iv) An optimal bond length of the peptide with respect to the tactoid formation was found, where three beads of the peptide matched two charges of the platelet.

These results conclude that when considering intercalation of charged peptides by synthetic clays, physical properties of both the peptide of interest, and the clay, need to be considered. However, the ability of Laponite® to sequester cationic peptides suggest

that Laponite® may prove to be a useful candidate as a drug delivery vehicle, since many of the novel therapeutical compounds, including antibiotics and anticancer drugs, are cationic in nature. The intercalation of cationic therapeutic peptides, within clays, can protect them from proteolysis, as well as provide a mechanism where the release of the peptides both can be controlled and target oriented, and therefore increase the bioavailability and the efficiency of the peptide, as well as other therapeutic drug compounds (Wang et al. (2013); Zazo et al. (2016); Tomás et al. (2018)). Hence, the method presented here could be a useful tool for testing and refining the properties of both the clay and the peptide in order to optimise intercalation, and consequently aid in the design and testing of efficient drug delivery systems.

Considering polymer-clay nanocomposites, the complexation between nanoplatelets and oppositely charged polymers, such as cationic peptides and/or polyelectrolytes, is strongly dependent on their properties, where one specific feature is that a suspension of charged colloids can either be stabilised or destabilised with the addition of an oppositely charged polyelectrolyte (Pefferkorn (1995); Hierrezuelo et al. (2010); Szilagyi et al. (2012)). This was investigated in Paper v, where the complexation between negatively charged nanoplatelets and an oppositely charged polyelectrolyte was studied utilising MD simulations. It was observed that for the systems where the polyelectrolyte was either under- or overcharged by the opposite charges of the nanoplatelets, the complex possessed a more extended configuration, whereas when the polyelectrolyte was net neutral, or only slightly overcharged, the complex obtained a compact configuration. The interaction between the polyelectrolyte and the nanoplatelet is governed by electrostatic interactions and the driving force of complexation is due to the gain in entropy upon counterion release. Furthermore, the inherent polyelectrolyte properties were altered with respect to: (i) the chain length, (ii) the total charge of the chain, and (iii) the flexibility of the chain. The obtained results for the complexation are summarised as follows:

(i) For the alternation of the chain length, the complexes attained a compact configuration, and by increasing the length of the chain, small distinct clusters of nanoplatelets was formed along the chain.

(ii) By reducing the total charge of the chain, the complex possessed a more elongated configuration, where the chain became more contracted.

(iii) With a decrease in the flexibility of the chain, the complex obtained a more extended configuration, with the nanoplatelets less tightly bound to the chain.

A selection of the different structures of the formed complexes obtained in this study is illustrated in the representative configurations in Fig. 8.9, where the structures can be

described as a stack of nanoplatelets, a band-like formation, an overlapping formation, and a cluster formation. These results are in correlation with previous studies of the complexation between a polyelectrolyte and oppositely charged spherical macroions (Jonsson & Linse (2001a,b)), where it was found that the complex capacity decreased with a reduction in the chain length or in the linear charge density of the chain. The former resulted in a more compact complex and the latter in a looser structure. It was also observed that the ability of overcharging the complex increased with a reduced flexibility of the chain, where the macroions in the complex became more linearly arranged.

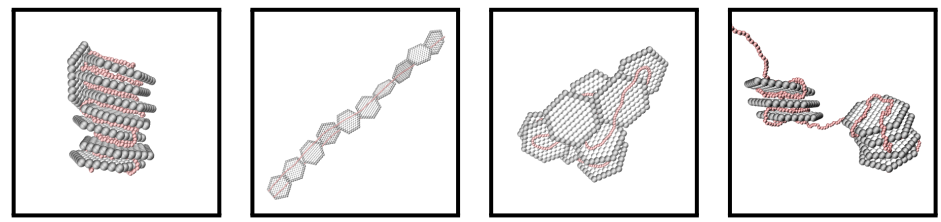


**Figure 8.9:** Representative configurations for a selection of the different structures obtained from the nanoplatelet-polyelectrolyte complexation, described as (a) a stack of nanoplatelets, (b) a band-like formation, (c) an overlapping formation, and (d) a cluster formation. The counterions are omitted for clarity, the nanoplatelets are shown in grey, and the polyelectrolyte is shown in red.

The information gained in this study concludes that the complexation between polyelectrolytes and nanoplatelets could result in a rich and versatile state diagram, which depends on both the properties of the polyelectrolyte and the nanoplatelet. The state diagram is indeed difficult to predict, however, by utilising MD simulations it is possible to achieve knowledge of the composition and the configuration of the formed complex and how it is affected by the characteristics of the chain.

# 9. Conclusions and future perspectives

The aim of this thesis has been to get a better understanding of the electrostatically driven structure formation in clay dispersions, and to gain a deeper molecular knowledge of the interactions between the clay platelets, as well as the interactions of the clay platelets in the presence of other macromolecules, by altering the physiochemical properties. To this end, we have extensively studied the tactoid formation and the tactoidal behaviour by varying the valency of the counterions, the temperature, and the solvent properties, as well as with addition of multivalent salt and positively charged peptides and polyelectrolytes.

The anisotropic clay platelets, depending on the size, can form a lamellar structure, making it a seemingly perfect model system for an electrical double layer, where the stability in saline solution depends strongly on the surface charge density of the platelets and on the counterion valency. The situation is however, from a structural point, slightly less ideal. Clay is a challenging system since it has a polydisperse distribution of anisotropic clay platelets and it is normally not a homogeneous lamellar material, where it might better be described as a disordered structure of stacks of platelets, also denoted tactoids. These structures can be irregular and organised in a way that gives rise to complex hierarchical morphologies. By altering the physiochemical properties, tactoid formation can be promoted, and a transition from a repulsive to an attractive system can be obtained. Furthermore, the overcharging effect may result in tactoidal dissolution, where the tactoids dissolve into smaller sized tactoids.

In conclusion, we have shown that it is possible to capture the behaviours of tactoid formation, tactoidal growth, and tactoidal dissolution for clay systems where the interactions are dominated by electrostatics by utilising coarse-grained MD simulations based on the continuum model. Hence, the simulation model is a useful tool to achieve physical insight of these systems and the role of the electrostatic interactions. Furthermore, with the ability to tune the characteristic of the clay platelets, as well as the added

species of peptides or polyelectrolytes, it is possible to make predictions on the behaviour of the peptide intercalation and the complexation between a polyelectrolyte and clay platelets. The results from the simulations were compared with experimental findings, where qualitative agreements have been obtained, confirming the accuracy and applicability of the simulation model. A number of different experimental techniques were employed in an attempt to characterise the swelling and the structural properties of the clay minerals montmorillonite and Laponite®. These techniques include: (i) SAXS, (ii) measurements of the swelling pressure in a test cell, (iii) $\zeta$-potential measurements, (iv) DLS, (v) TEM, and (vi) cryo-TEM.

Although we have made progress towards the understanding of the electrostatically driven structure formation in clay dispersions, there is still a considerable amount to investigate in future studies. For instance, it is known that the tactoid formation depends on the size of the clay platelets, and thus, this is an interesting aspect to study. Theoretically, this can be achieved by implementing a polydisperse distribution of the platelet diameter in the simulations in order to investigate the structural properties and complexation between small and large platelets. Experimentally, it is possible to mix size-fractionated montmorillonite dispersions to evaluate if the tactoid formation differs compared to non-fractionated dispersions. Additionally, a dispersion containing a mixture of the clay minerals montmorillonite and Laponite® can be prepared to study if the structural properties for the mixture differs between pure dispersions of montmorillonite and Laponite®. Furthermore, a fruitful extension of this work is to expand the simulations towards atomistic simulations in order to increase the resolution and the detail of the simulation model, which is an ongoing PhD-project in our group. With atomistic simulations it is possible to study realistic cationic peptides for the intercalation process within layered clay minerals which is of great interest from a clinical perspective, since clay has been suggested as a candidate for drug delivery. Another interesting feature that may be possible to implement in atomistic simulations is titration of the edge groups, from which the effect of the rim charges on the structural properties can be studied as a function of pH. Moreover, to my knowledge, no atomistic simulations have been used for bulk simulations with freely rotating platelets, and it would be very interesting to evaluate whether it is possible to capture tactoid formation and tactoidal dissolution in these systems.

# References


Abraham, M. J., van der Spoel, D., Lindahl, E., Hess, B., & the GROMACS development team. 2014, GROMACS User Manual version 5.0.4, www.gromacs.org

—. 2018, GROMACS User Manual version 2018.2, www.gromacs.org

Allen, M. P., & Tildesley, D. J. 1989, Computer Simulation of Liquids (New York: Oxford University Press)

Almgren, M., Edwards, K., & Karlsson, G. 2000, Colloids and Surfaces A: Physicochemical and Engineering Aspects, 174, 3

Angelescu, D. G., & Linse, P. 2003, The Journal of Physical Chemistry C, 19, 9661

Artemyeva, Z., Kirillova, N., Danchenko, N., Kogut, B., & Taller, E. 2020, Journal of Dispersion Science and Technology, 53, 446

Bailey, S. W. 1980, Clay Minerals, 15, 85

Berendsen, H. J. C., Postma, J. P. M., van Gunsteren, W. F., DiNola, A., & Haak, J. R. 1984, The Journal of Chemical Physics, 81, 3684

Berg, J. M., Tymoczko, J. L., & Stryer, L. 2012, Biochemistry, 7th edn. (New York, USA: W. H. Freeman and Company)

Bergaya, F., Theng, B. K. G., & Lagaly, G. 2006, Developments in Clay Science, Vol. 1, Handbook of Clay Science (Elsevier)

Bernardi, R. C., Melo, M. C., & Schulten, K. 2015, Biochimica et Biophysica Acta (BBA) - General Subjects, 1850, 872

Birgersson, M., Karnland, O., & Nilsson, U. 2010, SKB Technical Report, TR-10-40

Brindley, G. W., & Ray, S. 1964, American Mineralogist, 49, 106

Brindley, G. W., Wiewiora, K., & Wiewiora, A. 1969, American Mineralogist, 54, 1635

Bussi, G., Donadio, D., & Parrinello, M. 2007, The Journal of Chemical Physics, 126, 014101

BYK. 2016, Technical Information B-RI 21, LAPONITE® Performance Additives

Callen, H. B. 1985, Thermodynamics and an Introduction to Thermostatistics, 2nd edn. (New York: Wiley)

Chen, B., Evans, J. R. G., Greenwell, H. C., et al. 2008, Chemical Society Reviews, 37, 568

Ciumac, D., Gong, H., Hu, X., & Lu, J. R. 2019, Journal of Colloid and Interface Science, 537, 0021

Deer, W. A., Howie, R. A., & Zussman, J. 2013, An Introduction to the Rock-Forming Minerals, 3rd edn. (London: The Mineralogical Society)

Delhorme, M., Jönsson, B., & Labbez, C. 2012, Soft Matter, 8, 9691

Delville, A. 2002, The Journal of Physical Chemistry B, 106, 7860

Derjaguin, B. V., & Landau, L. 1941, Acta Physico Chemica URSS, 14, 633

Dowdy, R. H., & Mortland, M. M. 1967, Clays and Clay Minerals, 15, 259

Evans, D. F., & Wennerström, H. 1999, The Colloidal Domain: Where Physics, Chemistry, Biology, and Technology Meet, 2nd edn. (USA: Wiley-WHC)

Fitch, C. A., Platzer, G., Okon, M., Garcia-Moreno E., B., & McIntosh, L. P. 2015, Protein Science, 24, 752

Ford, N. C. 1985, in Dynamic Light Scattering, ed. P. R. (Boston, MA: Springer), 7–58

Glatter, O., & Kratky, O. 1982, Small Angle X-ray Scattering (London: Academic Press)

Grim, R. E. 1953, Clay Mineralogy (New York: McGraw-Hill Book Company Inc.)

Guggenheim, S., & Martin, R. T. 1995, Clays and Clay Minerals, 43, 255

Guldbrand, L., Jönsson, B., Wennerström, H., & Linse, P. 1984, The Journal of Chemical Physics, 80, 2221

Gutiérrez, G., & Johansson, B. 2002, Physical Review B

Häffner, S. M., Nyström, L., Browning, K. L., et al. 2019, Applied Materials and Interfaces, 11, 15389

Hedström, M., Birgersson, M., Nilsson, U., & Karnland, O. 2011, Physics and Chemistry of the Earth, Parts A/B/C, 36, 1564

Herrera, N. N., Letoffe, J.-M., Putaux, J.-L., David, L., & Bourgeat-Lami, E. 2004, Langmuir, 20, 1564

Hierrezuelo, J., Sadeghpour, A., Szilagyi, I., Vaccaro, A., & Borkovec, M. 2010, Langmuir, 26, 15109

Hill, T. L. 1986, An Introduction to Statistical Thermodynamics (New York: Dover Publications Inc.)

Hoover, W. G. 1985, Physical Review A, 31, 1695

Huang, A. Y., & Berg, J. C. 2006, Journal of Colloid and Interface Science, 296, 159

Hub, J. S., de Groot, B. L., & van der Spoel, D. 2010, Journal of Chemical Theory and Computation, 6, 3713

Israelachvili, J. N. 2011, Intermolecular and Surface Forces, 3rd edn. (USA: Academic Press)

Jabbari-Farouji, S., Tanaka, H., Wegdam, G. H., & Bonn, D. 2008, Physical Review E, 78, 061405

Jansson, M., Lenton, S., Plivelic, T. S., & Skepö, M. 2019, Journal of Colloid and Interface Science, 557, 767

Jansson, M., Thuresson, A., Plivelic, T. S., Forsman, J., & Skepö, M. 2018, Journal of Colloid and Interface Science, 513, 575

Jatav, S., & Joshi, Y. M. 2014, Applied Clay Science, 97–98, 72

—. 2018, Langmuir, 33, 2370

Jönsson, B., & Wennerström, H. 2001, Electrostatic Effects in Soft Matter and Biophysics (Netherlands: Springer), 171–204

Jonsson, M., & Linse, P. 2001a, The Journal of Chemical Physics, 115, 3406

—. 2001b, The Journal of Chemical Physics, 115, 10975

Karnland, O., Olsson, S., & Nilsson, U. 2006, SKB Technical Report, TR-06-30

Kästner, J. 2011, WIREs Computational Molecular Science, 1, 932

Kumar, S., Rosenberg, J. M., Bouzida, D., Swendsen, R. H., & Kollman, P. A. 1992, Journal of Computational Chemistry, 13, 1011

Labanda, J., & Llorens, J. 2005, Journal of Colloid and Interface Science, 289, 86

Labanda, J., Sabaté, J., & Llorens, J. 2007, Colloids and Surfaces A: Physicochem. Eng. Aspects, 301, 8

Latendorf, T., Gerstel, U., Wu, Z., et al. 2019, Scientific Reports, 9, 3331

Lin, W., Galletto, P., , & Borkovec, M. 2004, Langmuir, 20, 7465

Linse, P., & Lobaskin, V. 2000, The Journal of Physical Chemistry C, 112, 3917

Manilo, M., Lebovka, N., & Barany, S. 2014, Colloids and Surfaces A: Physicochem. Eng. Aspects, 462, 211

Martin, C., Pignon, F., Piau, J.-M., et al. 2002, Physical Review E, 66, 021401

McNaught, A. D., & Wilkinson, A. 1997, IUPAC. Compendium of Chemical Terminology (the "Gold Book"), 2nd edn. (Oxford: Blackwell Scientific Publications), Online version (2019–) created by S. J. Chalk. ISBN 0–9678550–9–8, doi:10.1351/goldbook

McQuarrie, D. A. 1976, Statistical Mechanics (New York: Harper & Row)

Metropolis, N., Rosenbluth, A. W., Rosenbluth, M. N., Teller, A. H., & Teller, E. 1953, The Journal of Chemical Physics, 21, 1087

Metz, S., Anderson, R. L., Geatches, D. L., et al. 2015, The Journal of Physical Chemistry C, 119, 12625

Michot, L. J., Bihannic, I., Porsch, K., et al. 2004, Langmuir, 20, 10829

Mohanty, R. P., & Joshi, Y. M. 2016, Applied Clay Science, 119, 243

Mongondry, P., Tassin, J. F., & Nicolai, T. 2005, Journal of Colloid and Interface Science, 283, 397

Mourchid, A., Delville, A., Lambard, J., Lécolier, E., & Levitz, P. 1995, Langmuir, 11, 1942

Mourchid, A., Lécolier, E., van Damme, H., & Levitz, P. 1998, Langmuir, 14, 4718

Mourchid, A., & Levitz, P. 1998, Physical Review E, 57, R4887

Netz, R. R. 2001, The European Physical Journal E, 5, 557

Neumann, B. S. 1971, Synthetic Hectorite-Type Clay Minerals, U.S. Patent 3,586,478

Norrish, K. 1954, Discussions of the Faraday Society, 18, 120

Nosé, S. 1984, Molecular Physics, 52, 255

Nosé, S., & Klein, M. L. 1983, Molecular Physics, 50, 1055

Okada, A., Fukushima, Y., Kawasumi, M., et al. 1988, Composite material and process for manufacturing same, U.S. Patent 4,739,007

Oncsik, T., Trefalt, G., Csendes, Z., Szilagyi, I., & Borkovec, M. 2014, Langmuir, 30, 733

Parrinello, M., & Rahman, A. 1981, Journal of Applied Physics, 52, 7182

Patterson, A. L. 1939, Physical Review, 56

Pefferkorn, E. 1995, Advances in Colloid and Interface Science, 56, 33

Popa, I., Trulsson, M., Papastavrou, G., Borkovec, M., & Jönsson, B. 2009, Langmuir, 25, 12435

Pronk, S., Páll, S., Schulz, R., et al. 2013, Bioinformatics, 29, 845

Pusey, P. N. 2002, in Neutron, X-rays and Light. Scattering Methods Applied to Soft Condensed Matter, ed. L. P. & Z. Th. (Amsterdam: Elsevier), 203–220

Raquez, J.-M., Habibi, Y., Murariu, M., & Dubois, P. 2013, Progress in Polymer Science, 38, 1504

Robison, A. D., Sun, S., Poyton, M. F., et al. 2016, The Journal of Physical Chemistry B, 120, 9287

Rosta, L., & von Gunten, H. R. 1990, Journal of Colloid and Interface Science, 134, 397

Ruzicka, B., & Zaccarelli, E. 2011, Soft Matter, 7, 1268

Ruzicka, B., Zulian, L., Angelini, R., et al. 2008, Physical Review E, 77, 020402

—. 2010, Physical Review E, 104, 085701

Ruzicka, B., Zaccarelli, E., Zulian, L., et al. 2011, Nature Materials, 10, 56

Schmitz, K. S. 1990, An Introduction to Dynamic Light Scattering by Macromolecules (San Diego: Academic Press Inc.)

Schnablegger, H., & Singh, Y. 2017, The SAXS Guide, 4th edn. (Austria: Anton Paar GmbH)

Schneider, C. A., Rasband, W. S., & Eliceiri, K. W. 2012, Nature Methods, 9, 671

Segad, M. 2013, Journal of Applied Crystallography, 46, 1316

Segad, M., Cabane, B., & Jönsson, B. 2015, Nanoscale, 7, 16290

Segad, M., Jönsson, B., Åkesson, T., & Cabane, B. 2010, Langmuir, 26, 5782

Shahin, A., Joshi, Y. M., & Ramakrishna, S. A. 2011, Langmuir, 27, 14045

Shaikh, S. M., Nasser, M. S., Hussein, I., et al. 2017, Separation and Purification Technology, 187, 137

SKB. 2011, SKB Technical Report, TR-11-01

Stepto, R., Chang, T., Kratochvíl, P., et al. 2015, Pure and Applied Chemistry, 87, 71

Suman, K., & Joshi, Y. M. 2018, Langmuir, 34, 13079

Svensson, P. D., & Hansen, S. 2013, Clays and Clay Minerals, 61, 328

Szilagyi, I., Sadeghpour, A., & Borkovec, M. 2012, Langmuir, 28, 6211

Tanaka, H., Meunier, J., & Bonn, D. 2004, Physical Review E, 69, 031404

Tawari, S. L., Koch, D. L., & Cohen, C. 2001, Journal of Colloid and Interface Science, 240, 54

Terao, T., & Nakayama, T. 2001, Physical Review E, 63, 041401

Tesei, G., Vazdar, M., Jensen, M. R., et al. 2017, Proceedings of the National Academy of Sciences (PNAS), 114, 11428

Thompson, D. W., & Butterworth, J. T. 1992, Journal of Colloid and Interface Science, 151, 236

Thuresson, A., Karnland, O., & Jönsson, B. 2016a, EPL (Europhysics Letters), 114, 38002

Thuresson, A., Segad, M., Plivelic, T. S., & Skepö, M. 2017, The Journal of Physical Chemistry C, 121, 7387

Thuresson, A., Segad, M., Turesson, M., & Skepö, M. 2016b, Journal of Colloid and Interface Science, 466, 330

Tomás, H., Alves, C. S., & Rodrigues, J. 2018, Nanomedicine: Nanotechnology, Biology and Medicine, 14, 2407

Torrie, G., & Valleau, J. 1977, Journal of Computational Physics, 23, 187

Trulsson, M., Forsman, J., Åkesson, T., & Jönsson, B. 2009, Langmuir, 25, 6106

Uskoković, V. 2012, Journal of Dispersion Science and Technology, 33, 1762

Vazdar, M., Heyda, J., Mason, P. E., et al. 2018, Accounts of Chemical Research, 51, 1455

Verwey, E. J. W., & Overbeek, J. T. G. 1948, Theory of the Stability of Lyophobic Colloids (Amsterdam: Elsevier Publishing Company Inc.)

Wang, S., Wu, Y., Guo, R., et al. 2013, Langmuir, 29, 5030

Yang, Y. I., Shao, Q., Zhang, J., Yang, L., & Gao, Y. Q. 2019, The Journal of Chemical Physics, 151, 070902

Yu, J., Andersson, O., & Johari, G. P. 2015, Colloid and Polymer Science, 293, 901

Zazo, H., Colino, C. I., & Lanao, J. M. 2016, Journal of Controlled Release, 224, 86

Zetasizer Nano Series. 2012, Malvern Instruments Ltd., User Manual MAN0317, 1.1

Zhang, S., Lan, Q., Liu, Q., Xu, J., & Sun, D. 2008, Colloids and Surfaces A: Physicochem. Eng. Aspects, 317, 406

# Acknowledgements

During my time as a PhD student at Theoretical Chemistry, I have had the opportunity to collaborate with many people who have supported me at different times during my PhD studies. Here, I want to mention the people I believe have contributed and helped me the most.

**Marie Skepö**, thank you for giving me the opportunity to become a PhD student and for being my supervisor with your endless support and guidance.

**Axel Thuresson**, thanks for introducing me to the world of clay and for sharing all your knowledge with me, I really appreciate it.

**Jan Forsman**, thank you for all valuable discussions and feedback during my projects.

**Tomás Plivelic**, thank you for all the experimental expertise and all the valuable discussions about data analysis and implementations, and of course for all pleasant trips.

**Clay Technology**, thanks for allowing me to work in your laboratory.

**Dom Belić**, thank you for all your expertise with the microscopy techniques and graphical design.

**Mona Koder Hamid**, thanks for allowing me to be your co-supervisor during your master project, I really enjoyed it.

The former/current members in **Skepö research group**, thank you all for making the days so pleasant and for all the nice trips we have made as well as for all good discussions it has provided. A special thanks to **Stephanie**, **Ellen**, **Amanda**, and **Sam**.

To all former/current colleagues at **teokem**, thank you all for creating such a pleasant work environment and for all great moments, like all the good laughs at fika.

# Scientific publications

## Author contributions

### Paper I: Temperature Response of Charged Colloidal Particles by Mixing Counterions Utilizing $Ca^{2+}/Na^{+}$ Montmorillonite as Model System

Prepared the samples and conducted the SAXS experiments together with the co-authors. Performed the MD simulations, the MC simulations, and the corresponding analyses together with the first author. Involved in the planning and the writing of the manuscript.

### Paper II: The Effect of the Relative Permittivity on the Tactoid Formation in Nanoplatelet Systems. A Combined Computer Simulation, SAXS, and Osmotic Pressure Study

Conducted the sample preparation and the measurements for the SAXS and the swelling pressure experiments together with the co-authors. Responsible for the MD simulations and the MC simulations as well as the writing of the article.

### Paper III: Nanoplatelet Interactions in the Presence of Multivalent Ions: The Effect of Overcharging and Stability

Responsible for the DLS and the $\zeta$-potential measurements and participated in the TEM and the cryo-TEM experiments. Conducted the MD simulations and the corresponding analyses. Responsible for writing the article.

**Paper IV: Intercalation of cationic peptides within Laponite layered clay minerals in aqueous suspensions: The effect of stoichiometry and charge distance matching**

Responsible for the $\zeta$-potential measurements. Prepared the samples for the SAXS experiments, performed the measurements, and analysed the results together with the co-authors. Performed the MD simulations and the corresponding analyses. Responsible for writing the article.

**Paper V: Polyelectrolyte-Nanoplatelet Complexation: Is it Possible to Predict the State Diagram?**

Performed the MD simulations and the corresponding analyses. Responsible for writing the article.

# Paper I

Reprinted from *J. Phys. Chem. C.*, 2017, **121**, 7951–7958
A. Thuresson, M. Jansson, T. S. Plivelic and M. Skepö
©2017 with permission from American Chemical Society.

THE JOURNAL OF PHYSICAL CHEMISTRY C

Article

pubs.acs.org/JPCC

# Temperature Response of Charged Colloidal Particles by Mixing Counterions Utilizing $Ca^{2+}/Na^{+}$ Montmorillonite as Model System

Axel Thuresson,*[,†] Maria Jansson,[†] Tomás S. Plivelic,[‡] and Marie Skepö*[,†]

[†]Theoretical Chemistry and [‡]MAX IV Laboratory, Lund University, SE-221 00 Lund, Sweden

**ABSTRACT:** The osmotic pressure and the aggregation of charged colloids as a function of temperature have been investigated using Monte Carlo and molecular dynamics simulations for different ratios of monovalent and divalent counterions. In the simulations the water is treated as a temperature-dependent dielectric continuum, and only the electrostatic interactions are considered. It was found that the temperature response can be controlled, i.e., the osmotic pressure can increase, decrease, or be kept constant, as a function of temperature depending on the monovalent/divalent counterion ratio. The increase in osmotic pressure with temperature, which occurs at low enough surface charge density and/or low fraction of divalent ions, can be understood from the DLVO theory. The origin of the opposite behavior can be explained by the enhanced attractive electrostatic ion−ion correlation interactions with temperature. The constraint is that the absolute value of the surface charge density of the colloids must be above a certain threshold, i.e., high enough such that the attractive ion−ion correlations can dominate the interaction regarding the divalent ions. The current conclusions are supported by the microstructural characterization of $Ca^{2+}/Na^{+}$-montmorillonite clay using small-angle X-ray scattering. A qualitative agreement is observed between the simulations and the experimental data.

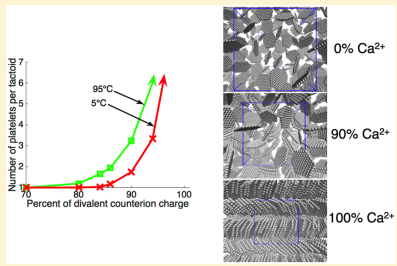


## INTRODUCTION

When a charged colloid is dissolved in aqueous or polar solvents, the macromolecule becomes ionized, and there will be a release of counterions. Since macromolecules usually are highly charged, there will be counterions that confer enormous entropies of mixing. The counterions will form an electrical double layer, where the first layer is the surface charge of the macromolecule, and the second layer is composed of oppositely charged ions screening the first layer. Upon addition of multivalent ions to a system comprising monovalent counterions, there will be an ionic exchange in the double layer, and monovalent counterions will be released. With monovalent counterions in the system solely, the electrostatic interaction between the particles is repulsive, whereas when multivalent counterions are introduced, the interaction can be attractive due to the electrostatic ion−ion correlation effects. The latter is only valid under the constraint that the surface charge density is above a certain threshold.[1−8]

The above given mechanisms along with the charge distribution, the volume, the size, and the shape of the macromolecule, as well as the hydrophobic interactions, are the parameters that primarily determines the physicochemical properties of macromolecular solutions.

The model system of this study is montmorillonite, although we would like to emphasize that the obtained results are generally valid. Swelling 2:1 clay minerals consist of platelets with a thickness of about 1 nm and lateral dimensions varying from 25 nm in synthetic Laponite clays up to 1000 nm in natural montmorillonite. When water is added, the clay platelets become ionized, and the rising osmotic pressure in the solution causes the clay to swell.[9−11] Depending on the size, the platelets can form a lamellar structure, making it a seemingly perfect model system for an electrical double layer, where the swelling and the stability in saline solution depend strongly on the counterion valency and the surface charge density.[12−14] The situation is however, from a structural point, slightly less ideal. Clay is normally not a homogeneous lamellar material; it might better be described as a disordered structure of stacks of platelets, also denoted tactoids.[15−17]

Experimentally[18] and theoretically,[19] it has been found that for mixtures of $Ca^{2+}/Na^{+}$-montmorillonite (with ∼20% sodium or more) the clay is behaving qualitatively as $Na^{+}$-montmorillonite. Recently, it has also been shown that the swelling pressure of the clay mineral in aqueous solution, as a function of temperature, can be understood from electrostatic ion−ion correlation interactions.[20] In an aqueous clay dispersion dominated by monovalent counterions, the swelling pressure increases with temperature due to entropic reasons, whereas in a clay with predominantly divalent counterions, the opposite behavior was found. The explanation is that the ion−ion correlations increase with temperature since the product $\epsilon_r T$ decreases, i.e., the dielectric permittivity multiplied with temperature. The latter is an effect of the fact that $\epsilon_r$ drops when $T$ increases. The aim of this study is to investigate the

**Received:** January 27, 2017
**Revised:** March 15, 2017
**Published:** March 16, 2017

ACS Publications © 2017 American Chemical Society



DOI: 10.1021/acs.jpcc.7b00882
J. Phys. Chem. C 2017, 121, 7951−7958

possibility to control the osmotic pressure response with temperature of charged colloidal particles by varying the ratio of monovalent/divalent counterions in the system.

For this purpose a coarse-grained model has been used, and the simulations assume that the solvent can be represented as an uniform temperature-dependent dielectric permittivity. The limitations of the model are that: (i) it does not explain the extralamellar swelling[19] that is found for homoionic $Ca^{2+}$-montmorillonite nor, (ii) the reverse swelling pressure trend with temperature for $Na^{+}$-montmorillonite, i.e., when the average distance between the platelets is smaller than 1 nm. The former is to the authors knowledge not well understood, and the latter is due to the fact that the water is represented by the dielectric permittivity of bulk water.[20,21] The theoretical predictions are verified by small-angle X-ray scattering (SAXS) data, and a good qualitative correspondence is achieved.

## MATERIALS AND METHODS

**Experimental Details.** *Material and Sample Preparation.* In this study, Wyoming Bentonite (MX-80), which consists mainly of the swelling clay mineral sodium montmorillonite, has been used. Sodium saturated montmorillonite from MX-80 has the chemical formula:[22]

$$(Al_{3.1}Mg_{0.49}Fe_{0.38}Ti_{0.01})(Si_{7.89}Al_{0.11})O_{20}(OH)_4,\ 0.65Na^{+} \quad (1)$$

The thickness and the average lateral size of the montmorillonite platelets are approximately 1 and 250 nm, respectively.[23] The purification and ion exchange procedures for MX-80 are described elsewhere.[24] Analytical grade sodium chloride (purity, 99.5%) and calcium chloride (purity, 99.5%) were purchased from MERCK. The purified $Na^{+}$- and $Ca^{2+}$-montmorillonite were dried at 105 °C overnight and milled into a fine powder. The clay powder from respective clay were mixed in different proportions to obtain different fractions of calcium (divalent) counterion charge that is neutralizing the clay:

$$\eta_{Di} = \frac{m_{Ca-clay}}{m_{Ca-clay} + m_{Na-clay}} \approx \frac{2N_{Di}}{2N_{Di} + N_{Mon}} \quad (2)$$

where $m_{Ca-clay}$ is the mass of $Ca^{2+}$-montmorillonite and $m_{Na-clay}$ is the mass of the $Na^{+}$-montmorillonite, whereas $N_{Mon}$ and $N_{Di}$ are the number of monovalent and divalent counterions, respectively. An excess of Millipore water was added to the mixed clay powder such that the counterions could diffuse and equilibrate within the sample for 24 h. All the $Ca^{2+}/Na^{+}$-montmorillonite mixtures were dried at 105 °C overnight and milled into a fine powder. Finally, Millipore water was added to each mixture in order to obtain a water mass ratio equal to six, and the samples were set to equilibrate for one month. $w = 6$ corresponds to a clay volume fraction $\phi_c \approx D_w/(D_c w + D_w) = 6\%$, where $D_c = 2750$ kg/m$^3$ is the density of the clay[18] and $D_w = 1000$ kg/m$^3$ is the density of water.

*SAXS.* SAXS experiments were performed at beamline ID02 at the European Synchotron Radiation Facility (ESRF) in Grenoble, France.[25] The $q$-range in the measurements was $0.2 < q < 4.5$ nm$^{-1}$, where $q = 4\pi \sin(\theta)/\lambda$, $2\theta$ is the scattering angle, and $\lambda = 0.1$ nm is the monochromatic beam wavelength. The detector was a 2D CCD Raynomix MX 170 HS with binning 4 × 4. For data reduction, the software SAXSutilities[26] was used. The montmorillonite samples were measured in 1 mm sealed glass capillaries, and the background scattering (water) was subtracted. SAXS measurements were collected at different temperatures: 5, 25, 55, and 90 °C. The thermalization time of each temperature was 12 min.

In order to estimate the size of the aggregates, i.e., the average number of clay platelets per aggregate, a model scattering peak has been fitted to the experimental data. The scattering function was approximated with a Lorentzian line shape:

$$q^2 I(q) \propto \frac{w}{(q - q_{max})^2 + w^2} + b \quad (3)$$

where $I(q)$ is the scattering intensity, $b$ is a fitting parameter for the background contribution, and $w$ is a measure of the width. The full width at half-maximum (fwhm) of the peak is equal to $2w$, and the average tactoid size can be expressed as $\langle N \rangle \approx q_{max}/w$.[24,27,28] The data was fitted between $q_{max} \pm 0.5$ nm$^{-1}$, in order to make the peak fitting procedure as reasonable as possible.

**Model and Simulations.** *Bulk Simulations.* The interaction potentials and the platelet description are given elsewhere.[29] The electrostatic potential between particle $i$ and $j$ is defined as:

$$\beta u_{ij}^{EL}(r_{ij}, T) = \frac{l_B z_i z_j}{r_{ij}} \quad (4)$$

where $\beta = 1/(k_B T)$, $k_B$ is the Boltzmann constant, $l_B = e^2/(4\pi\epsilon_0\epsilon_r(T)k_B T)$ is the Bjerrum length, $e$ is the elementary unit charge, $\epsilon_0$ is the permittivity of vacuum, $z_i$ is the valency of particle $i$, and $r_{ij}$ is distance between the particles. The solvent, i.e. the water molecules, is treated as a temperature-dependent, $T$, uniform dielectric permittivity, $\epsilon_r(T)$, with experimentally measured values of the dielectric permittivity of water.[30] The electrostatic interactions are enhanced as a function of temperature; i.e., the Bjerrum length increases as shown in Table 1. A truncated and shifted Lennard-Jones (TLJ) potential

**Table 1. Bjerrum Length as a Function of Temperature**[a]

| $T$ (°C) | $T$ (K) | $\epsilon_r(T)$ | $l_B$ (nm) |
|---|---|---|---|
| 5 | 278.15 | 85.76 | 0.700 |
| 25 | 298.15 | 78.30 | 0.716 |
| 95 | 368.15 | 57.01 | 0.796 |

[a]The Bjerrum length, $l_B$, at three different temperatures, $T$, and given dielectric permittivity, $\epsilon_r(T)$.[30]

has been used to represent the excluded volume of all particles in the system and is defined as:

$$u_{ij}^{TLJ}(r_{ij}) = \begin{cases} \epsilon\left[\left(\frac{\sigma_{ij}}{r_{ij}}\right)^{12} - 2\left(\frac{\sigma_{ij}}{r_{ij}}\right)^{6} + 1\right] & \text{if } r_{ij} \geq \sigma_{ij} \\ 0 & \text{otherwise} \end{cases} \quad (5)$$

where $\sigma_{ij} = (\sigma_i + \sigma_j)/2$, $\sigma_{ion} = 4$ Å, and $\sigma_{site} = 10$ Å. This potential has been chosen to be temperature independent and the strength of the short-ranged potential was set to $\epsilon = k_B \cdot 298$ J. Hence, the distribution of uncharged particles behaves independently of the temperature, with the aim to study the electrostatic effects solely.

The bulk molecular dynamics (MD) simulations were performed with the software package GROMACS (version 5.0.4).[31] Fifty negatively charged platelets with their corre-



DOI: 10.1021/acs.jpcc.7b00882
J. Phys. Chem. C 2017, 121, 7951−7958

sponding counterions were placed into a cubic simulation box with three-dimensional periodic boundary conditions. The platelets consist of 91 connected charged sites, and the one-sided surface charge density $\sigma = -2.6$ e/nm$^2$.[29] The absolute value of the surface charge density is chosen much higher than that of montmorillonite due to the small size of the simulated platelets. If the simulated platelets would be larger, the surface charge density can be reduced to have similar probability of aggregation as the smaller ones with divalent counterions.[29] On average, montmorillonite has a one-sided surface charge density of $-1.5$ e/nm$^2$.[32]

Newton's equations of motion of the freely moving species (platelets + ions) were integrated using the leapfrog algorithm. The time step was chosen to be 10 fs and gave the same results as using 1 fs time step (data not shown). The pressure was set by isotropic Berendsen pressure coupling for the NPT simulations, and the temperature was set by velocity-rescaling temperature coupling. All simulations assume equilibrium with salt-free water, and hence, the pressure is equal to the osmotic pressure. To account for the long-ranged electrostatic interactions, fast particle-mesh Ewald summation (PME) was used with a 6 nm real-space Coulomb cutoff (the largest and smallest box length used in the simulations are 70 and 20 nm, respectively) and a Fourier spacing equal to 0.6 nm. Different starting configurations for the equilibration simulation were performed both from a dilute and a compressed system to confirm that the mean volume and mean energy converged to the same value. For an in-depth description of the input parameters, see the online user manual.[31]

The volume fraction is a function of temperature, $T$, and osmotic pressure, $\Pi$, and is defined as:

$$\phi(T, \Pi) = \frac{4\pi r^3 N_{\text{sites}}}{3V_s(T, \Pi)} \tag{6}$$

where $r = 0.5$ nm is the radius of a platelet site, $N_{\text{sites}}$ is the number of connected charged sites per platelet, and $V_s(T,\Pi)$ is the volume per platelet.

*Two Parallel Surfaces.* Two infinite parallel surfaces with a specific surface charge density and its corresponding counterions were simulated using Monte Carlo (MC) simulations described elsewhere.[19] The surface charge is smeared out, and the ions are treated as charged hard spheres. The electrostatic interactions between two ions are defined similarly as in the bulk simulations. The counterions in the bulk simulations are free to explore the volume between the surfaces, whereas in the MC simulations it is assumed that the counterion ratio is constant. An alternative to this simplification is to use a variant of the grand canonical ensemble.[33] For a given separation between the surfaces, $h$, and temperature, the osmotic pressure, $\Pi = \Pi(T,h)$, can be calculated using a midplane approach[1] written as:

$$\Pi = \Pi^{\text{id}} + \Pi^{\text{corr}} + \Pi^{\text{coll}} \tag{7}$$

where $\Pi^{\text{id}} = k_B T \sum_{i=1}^{2} c_i(\text{mp})$ is the ideal contribution, $c_i(\text{mp})$ is the concentration of counterions at the midplane with valency $i$, $\Pi^{\text{corr}}$ is an attractive term due to the ion−ion correlations on either side of the midplane, and $\Pi^{\text{coll}}$ is the collision term due to the finite-sized ions. The osmotic pressure response with temperature is calculated between 25 and 95 °C:

$$\Delta\Pi = \Pi(T = 95\ ^\circ\text{C}, h_{\text{fix}}) - \Pi(T = 25\ ^\circ\text{C}, h_{\text{fix}}) \tag{8}$$

where $h_{\text{fix}}$ is defined to be the separation where the osmotic pressure is 4 bar for 25 °C.

## RESULTS AND DISCUSSION

**NVT Bulk Simulations.** Three radial distribution functions (rdfs) are shown with respect to the center-of-mass between the platelets from NVT bulk simulations in Figure 1a. The

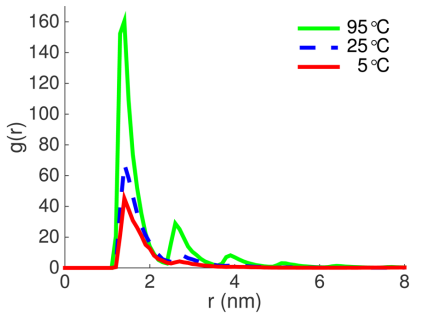


(a) Radial distribution functions for three different temperatures.

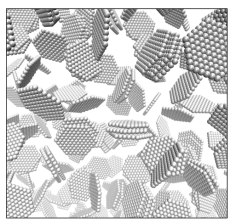

(b) T=5°C, $\epsilon_r$=85.7

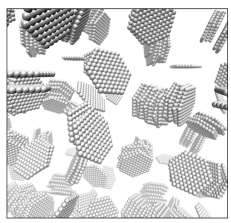

(c) T=95°C, $\epsilon_r$=57.0

**Figure 1.** (a) Radial distribution functions between the platelets from NVT simulations at three different temperatures with $\eta_{\text{Di}} = 0.96$. (b, c) Representative configurations from the simulations for two temperatures. The counterions are omitted due to clarity, and the platelets are shown in gray.

volume of the platelets divided by the total volume is 4% ($\phi$ = 0.04), and $\eta_{\text{Di}} = 0.96$; i.e., 96% of the charge of the platelets are neutralized by divalent cations. The first peak at ∼1.3 nm corresponds to two platelets aggregated face-to-face. The height of the peak is related to the probability of finding that configuration. If three platelets have aggregated, a second peak arises at ∼1.3·2 = 2.6 nm. If four platelets have aggregated, a third peak arises at ∼1.3·3 = 3.9 nm and so on. Thus, the number of visible peaks in the rdfs gives an indication of the average number of platelets per tactoid, $\langle N \rangle$, and it can been seen that $\langle N \rangle$ increases with temperature. As the temperature is increasing from 5 to 95 °C, the attractive ion−ion correlations are enhanced[20] due to the ∼14% increase in Bjerrum length (see Table 1), which consequently leads to larger aggregates and a reduced osmotic pressure ($\langle N \rangle \sim 1.5$, $\Pi \sim 0.25$ bar at 5 °C, and $\langle N \rangle \sim 3.0$, $\Pi \sim 0.20$ bar at 95 °C). Typical configurations from the simulations are shown in Figure 1b,c, where it is displayed that larger aggregates are found at higher temperatures. Thus, for the particular surface charge density, volume fraction, and fraction of divalent counterions, we find:



DOI: 10.1021/acs.jpcc.7b00882
J. Phys. Chem. C 2017, 121, 7951−7958

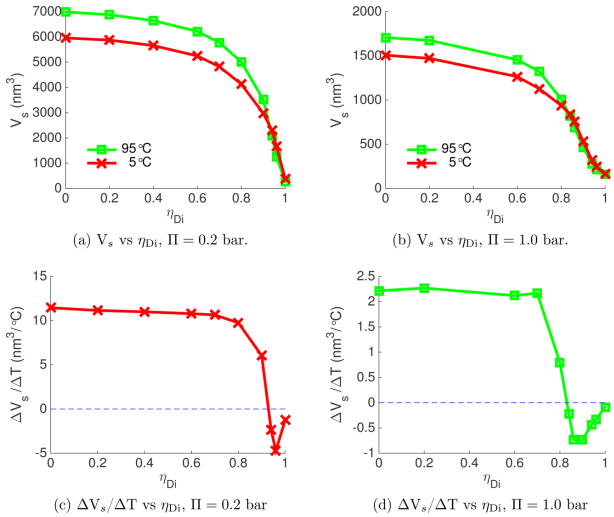


(a) $V_s$ vs $\eta_{Di}$, $\Pi = 0.2$ bar. (b) $V_s$ vs $\eta_{Di}$, $\Pi = 1.0$ bar.

(c) $\Delta V_s/\Delta T$ vs $\eta_{Di}$, $\Pi = 0.2$ bar (d) $\Delta V_s/\Delta T$ vs $\eta_{Di}$, $\Pi = 1.0$ bar

**Figure 2.** (a, b) Volume per platelet as a function of the fraction of charges that is neutralized by divalent counterions. (c, d) Difference in volume per platelet between 5 and 95 °C divided by the temperature difference as a function of $\eta_{Di}$. For 1 bar the crossover is found at $\eta_{Di} \sim 0.8$. That is, the volume per platelet is increased below $\eta_{Di} \sim 0.8$ and reduced above $\eta_{Di} \sim 0.8$ when the temperature is increased. For $\Pi = 0.2$ bar the crossover is found at $\eta_{Di} \sim 0.9$. Because of counterion dilution at lower pressures, the crossover occurs at higher divalent content.

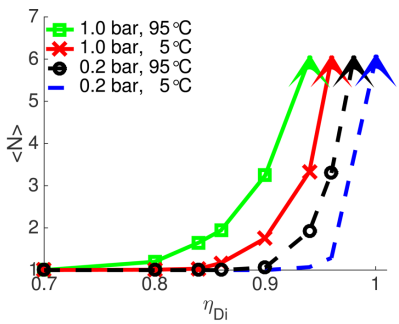


(a) $\langle N \rangle$ vs $\eta_{Di}$

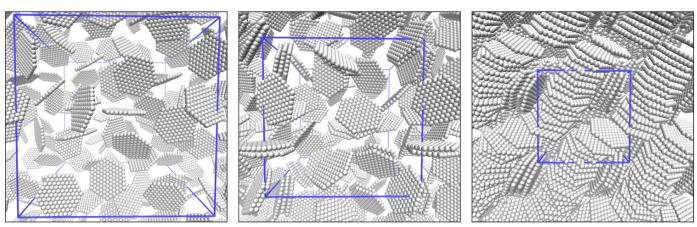

(b) $\eta_{Di} = 0$ (c) $\eta_{Di} = 0.84$ (d) $\eta_{Di} = 1.0$

**Figure 3.** (a) The average number of platelets per tactoid, $\langle N \rangle$, as a function of $\eta_{Di}$ for 0.2 and 1.0 bar, respectively. The aggregation is initiated at lower fractions of divalent counterions when the temperature and/or pressure are increased. (b–d) Three configurations from the simulations for $T = 95$ °C, $\Pi = 1$ bar at different $\eta_{Di}$. The counterions are omitted due to clarity, the platelets are shown in gray, and the cubic simulation box is shown in blue (periodic images are shown outside the simulation box).



DOI: 10.1021/acs.jpcc.7b00882
J. Phys. Chem. C 2017, 121, 7951−7958

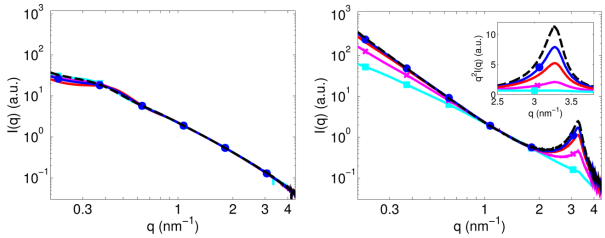


(a) $\eta_{Di}$ =0, 0.05, 0.1, 0.2, and 0.4 at T=25°C (b) $\eta_{Di}$ =0.6, 0.8, 0.9, 0.95, and 1.0 at T=25°C

**Figure 4.** X-ray scattering intensities as a function of the scattering vector at $T$ = 25 °C of the $Ca^{2+}/Na^{+}$-montmorillonite fractions with $\phi$ = 0.06 for (a) $\eta_{Di}$ = 0 (cyan square), 0.05 (magenta cross), 0.1 (red line), 0.2 (blue circle), and 0.4 (black dashed) and, (b) $\eta_{Di}$ = 0.6 (cyan square), 0.8 (magenta cross), 0.9 (red line), 0.95 (blue circle), and 1.0 (black dashed). The inset in (b) shows the Kratky plots over a narrow $q$-range. The scattering intensities are normalized at $q \approx 1$ nm$^{-1}$.

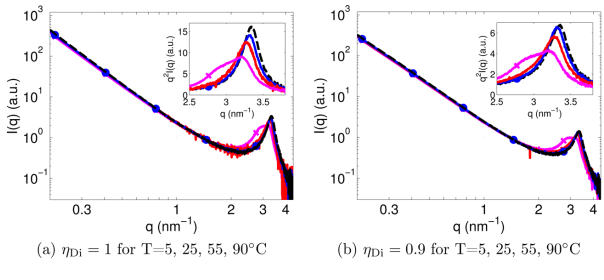


(a) $\eta_{Di}$ = 1 for T=5, 25, 55, 90°C (b) $\eta_{Di}$ = 0.9 for T=5, 25, 55, 90°C

(c) $\eta_{Di}$ = 0.8 for T=5, 25, 55, 90°C (d) $\eta_{Di}$ = 0.6 for T=5, 25, 55, 90°C

**Figure 5.** X-ray scattering intensities as a function of the scattering vector for the temperature measurements of the $Ca^{2+}/Na^{+}$-montmorillonite fractions with $\phi$ = 0.06 for (a) $\eta_{Di}$ = 1, (b) $\eta_{Di}$ = 0.9, (c) $\eta_{Di}$ = 0.8, and (d) $\eta_{Di}$ = 0.6. The temperatures were 5 °C (magneta cross), 25 °C (red line), 55 °C (blue circle), and 90 °C (black dashed). The inset shows the Kratky plot over a narrow $q$-range.The scattering intensities are normalized at $q \approx 1$ nm$^{-1}$.

$$\Delta\Pi/\Delta T = \frac{\Pi(T = 95°C) - \Pi(T = 5°C)}{95°C - 5°C} \approx -60 \text{ Pa/°C}$$

which is in disagreement with the DLVO theory[34,35] that predicts $\Delta\Pi/\Delta T > 0$ for both monovalent and divalent counterions. With monovalent counterions and/or low enough surface charge density of the colloids, the DLVO theory predicts the correct trend as will be shown below.

**NPT Bulk Simulations.** In Figure 2a,b the volume per platelet as a function of fraction of divalent counterions can be seen for two different temperatures at two different pressures, 0.2 and 1.0 bar. At a low fraction of divalent counterions, the entropic repulsion dominates the system and the particles prefer to be far apart, which is clearly indicated by the large volume per platelet. At a high enough fraction of divalent counterions ($\eta_{Di} \sim 0.8$ for $\Pi$ = 1.0 bar and $\eta_{Di} \sim 0.9$ for $\Pi$ = 0.2 bar), the volume per platelet is decreasing rapidly, and the colloids tend to aggregate. In Figure 2c,d, the difference in volume per platelet divided by the temperature difference is shown as a function of the fraction divalent counterion charge. A crossover can be found where $\Delta V_s/\Delta T$ changes sign from positive to negative ($\eta_{Di} \sim 0.8$ for 1.0 bar and $\eta_{Di} \sim 0.9$ for 0.2 bar), and hence the conclusion is that $\Delta V_s/\Delta T$ can be chosen to be positive, negative, or kept constant by mixing counterions of different valency. Note that the volume response with temperature, $\Delta V_s/\Delta T$, in the NPT simulations is analogous to the osmotic pressure response, $\Delta\Pi/\Delta T$, in the NVT simulations. A minimum is found in the vicinity of the



DOI: 10.1021/acs.jpcc.7b00882
J. Phys. Chem. C 2017, 121, 7951−7958

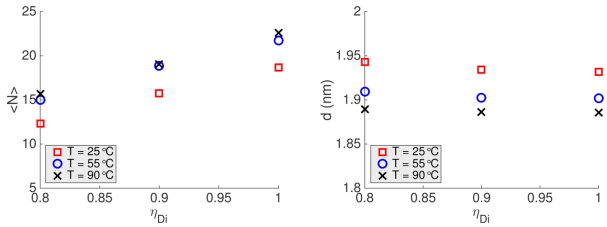


(a) ⟨N⟩ vs $\eta_{Di}$ for T=25, 55, 90°C (b) d vs $\eta_{Di}$ for T=25, 55, 90°C

**Figure 6.** (a) Average number of platelets per tactoid, ⟨N⟩, and (b) the average distance between the platelets as a function of the fraction divalent charges neutralizing the colloids, $\eta_{Di}$, obtained from the temperature measurements performed with SAXS for the $Ca^{2+}/Na^{+}$-montmorillonite fractions with $\phi$ = 0.06.

crossover where there are three effects that decreases the volume as the fraction of divalent counterions increases: (i) the single platelets form tactoids, (ii) the tactoids grow in size, and (iii) the separation between the platelets in a tactoid decreases. With 100% divalent counterions, all tactoids have aggregated at Π = 1 bar (see Figure 3d), and the change is due to to effect (iii) solely. The microstructure of the colloids is analyzed in Figure 3, where the average tactoid size is shown as a function of fraction of divalent counterions. As $\eta_{Di}$ increases, the distance between single platelets decreases slightly (Figure 3b), and at the crossover the platelets start to aggregate into doublets and triplets (Figure 3c). The tactoids continue to grow in size, and finally, for a high enough fraction of divalent counterions and pressure ($\eta_{Di}$ > 0.95 for Π = 1 bar), all tactoids have aggregated (Figure 3d). It should be emphasized that for ⟨N⟩ > 6 (indicated by the arrows) the average tactoid size cannot be calculated due to the limited size of the system, i.e., 50 platelets. The tactoid size for aggregated platelets has previously been investigated for parallel platelets with MC simulations,[32] and aggregates of spherical particles have been investigated with MC/MD simulations.[36]

**SAXS.** Scattering experiments were performed for the corresponding $Ca^{2+}/Na^{+}$-montmorillonite mixtures used in the bulk MD simulations. The scattering intensities for all mixtures at $T$ = 25 °C and $\phi_c$ = 0.06 are shown in Figure 4. Bragg peaks are clearly observed for $\eta_{Di}$ = 1, 0.95, 0.9, and 0.8 (Figure 4b), indicating that there are tactoids in these samples. Moreover, the fwhm of the Bragg peak is decreasing, which indicates that the tactoids are growing in size (see Figure 6a) as $\eta_{Di}$ approaches one. For $\eta_{Di} \leq 0.6$ (Figure 4a), all the scattering intensity curves are qualitatively equal, and no Bragg peaks are visible, indicating that the systems are dominated by repulsive interactions. Hence, the SAXS measurements are in qualitative agreement with the simulations in Figure 3 and also agree well with the study by Hedström et al.,[18] i.e., $Ca^{2+}/Na^{+}$-montmorillonite with ∼20% sodium or more, behaves qualitatively as a $Na^{+}$-montmorillonite, whereas montmorillonite with 90% or more calcium in the interlayer behaves similar to homoionic $Ca^{2+}$-montmorillonite.

The scattering intensities and the Kratky plots for $\eta_{Di}$ = 1, 0.9, 0.8, and 0.6 with $\phi_c$ = 0.06 at four different temperatures, 5, 25, 55, and 90 °C, are shown in Figure 5. The positions of the Bragg peaks for $\eta_{Di}$ = 1, 0.9, and 0.8 shift toward higher $q$-values as the temperature increases, as shown in Figure 5a−c. For $\eta_{Di}$ = 0.6 no Bragg peak is visible, indicating that there are no tactoids in the system for any of the temperatures investigated (see Figure 5d). By comparing the value of ⟨N⟩ for the three different temperatures ($T$ = 25 °C, $T$ = 55 °C, and $T$ = 90 °C), it is found that there is only a small difference between 55 and 90 °C. A larger deviation is found for 25 °C, which can be associated with changes in the microstructure of the system. The shift toward higher $q$-values in the Bragg peak with temperature indicates that the average distance between the platelets decreases with an increase in temperature, from ∼1.93 to 1.89 nm, i.e., three water layers, for $T$ = 25−90 °C (see Figure 6b). At 5 °C, the SAXS data seems to be composed by a superposition of two Bragg peaks, with an average distance of ∼1.9−2.1 nm, corresponding to a combination of three and four water layers. These results are in agreement with the previous work done by Svensson and Hansen.[37,38]

The two trends where: (i) the spacing between the platelets in the tactoids is reducing, and (ii) the increase in number of platelets per tactoid with temperature for $\eta_{Di} \geq 0.8$, are found both in the simulations as well as in the experiments. Obviously, the model cannot find discrete distances between the platelets, such as three or four water layers, since the water molecules are represented as a uniform dielectric permittivity. Hence, a quantitative agreement at 5 °C is not possible.

**Crossover for Two Parallel Surfaces.** The platelets in the bulk simulations above have a fixed surface charge density, and the crossover from positive to negative change in pressure with temperature was found to be at approximately 90% and 80% divalent counterions, for 0.2 and 1 bar, respectively (Figure 2a,b). In Figure 7 the crossover between two parallel surfaces for Π($T$ = 25 °C) = 4 bar (eq 8) has been simulated (MC

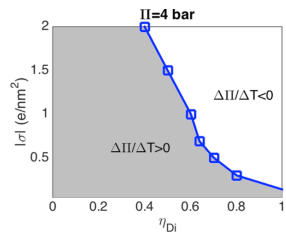


**Figure 7.** Crossover from increasing to decreasing osmotic pressure response with temperature is shown as a function of the surface charge density and the percentage of divalent counterions neutralizing the colloids. The osmotic pressure is 4 bar, and the temperature is 25 °C. The areas left/right of the line correspond to an increased/decreased osmotic pressure with increasing temperature.



DOI: 10.1021/acs.jpcc.7b00882
J. Phys. Chem. C 2017, 121, 7951−7958

simulations) for different absolute values of the surface charge density ranging from 0.05 to 2 e/nm$^2$. The pressure was chosen high enough to avoid any two-phase coexistence with opposite sign of $\Delta\Pi/\Delta T$. Furthermore, the crossover of the two parallel surfaces differs from the bulk simulations due to the exclusion of the rotational entropy, and the difference in electrostatic interaction between a small colloid and an infinite surface. The dark gray area on the left-hand side of the crossover-line corresponds to an increasing osmotic pressure with temperature, and the area on the right-hand side of the crossover-line corresponds to a decreasing osmotic pressure with temperature, as indicated in Figure 7. If $|\sigma| < 0.2$ e/nm$^2$, the DLVO theory is valid, even with 100% divalent counterions. As the surface charge density increases, a crossover appears, and it shifts toward a lower percentage of divalent counterions with an increased surface charge density. The latter is due to the fact that the attractive ion−ion correlations increase with increasing surface charge density.[6,32]

Finally, we would like to emphasize that the midplane approach is useful for understanding the importance of the different contributions to the pressure defined in eqs 7 and 8 as well as for understanding the limitations of the DLVO theory where the correlation term is neglected. In Table 2, it is shown that the difference in the ideal contribution, $\Delta\Pi^{id}$, is found to increase with the fraction of divalent counterions mainly due to the reduced separation. Although, by taking into account the difference in the correlation contribution, $\Delta\Pi^{corr}$, it is found that $\Delta\Pi/\Delta T < 0$ for $\eta_{Di} > 0.7$. Hence, the osmotic pressure response can be negative if the correlation difference is the leading term. The contribution $\Delta\Pi^{coll}$ is negligible and not shown.

**Table 2. Osmotic Pressure Response from the MC Simulations**[a]

| $\eta_{Di}$ | $h_{fix}$ (nm) | $\Delta\Pi^{id}$ | $\Delta\Pi^{corr}$ | $\Delta\Pi$ |
|---|---|---|---|---|
| 0.6 | 2.6 | 0.69 | −0.43 | 0.26 |
| 0.7 | 2.1 | 1.00 | −0.96 | 0.04 |
| 0.8 | 1.5 | 2.30 | −3.50 | −1.20 |

[a]The osmotic pressure response, $\Delta\Pi = \Delta\Pi^{id} + \Delta\Pi^{corr} + \Delta\Pi^{coll}$, between 25 and 95 °C, and the main components, $\Delta\Pi^{id}$ and $\Delta\Pi^{corr}$, are shown for $|\sigma| = 0.5$ e/nm$^2$ where the osmotic pressure is 4 bar at 25 °C.

## CONCLUSIONS

We have shown that the electrostatic interactions alone can give a positive, negative, or constant osmotic pressure response with temperature, depending on the monovalent/divalent counterion ratio, if $|\sigma| > 0.2$ e/nm$^2$. The fraction of divalent counterions, where a crossover from positive to negative pressure response with temperature is found, depends on the surface charge density, the pressure (or volume fraction), and other components such as the rotational entropy and the size of the colloid. Mixtures of $Ca^{2+}$-montmorillonite and $Na^{+}$-montmorillonite in water were measured with SAXS at four different temperatures. It was found that Bragg peaks appear for a sodium content of ∼20% or less, which indicates that tactoids exist in those compositions. As the sodium content was reduced, the number of platelets per tactoid increased. By increasing the temperature, the separation between the platelets in the tactoids decreased and the number of platelets per tactoid seems to increase slightly. For a sodium content of ∼40% or more, no tactoids were found, which indicates that the interaction between the platelets are dominated by repulsive interactions. Our theoretical predictions are in good agreement with the SAXS experiments, giving a further indication that our model can explain the underlying physics. The theory presented here is general and predicts that the temperature response for all types of charged colloids can be controlled by mixing counterions of different valency if the interactions in the system are dominated by electrostatics. Even though the applied model is very simple, and only face charges are taken into consideration, we still believe that this study shed light on the fundamental physics of these systems, the formation of tactoids, and role of electrostatic interactions.

## AUTHOR INFORMATION


### Corresponding Authors

*E-mail: axel.thuresson@teokem.lu.se (A.T.).
*E-mail: marie.skepo@teokem.lu.se (M.S.).

### ORCID

Axel Thuresson: 0000-0001-8459-1394


### Notes

The authors declare no competing financial interest.

## ACKNOWLEDGMENTS

Computational resources were provided by the Swedish National Infrastructure for Computing (SNIC) through Lunarc, the Center for Scientific and Technical Computing at Lund University. We acknowledge Dr. T. Narayanan and Dr. J. Möller for providing assistance during measurements at ESRF. The work was performed within the framework of the Swedish national strategic e-science research program eSSENCE. The Lars Hierta Memorial Foundation is greatly acknowledged for financial support.

## REFERENCES


(1) Guldbrand, L.; Jönsson, B.; Wennerström, H.; Linse, P. Electric double layer forces. A Monte Carlo study. *J. Chem. Phys.* **1984**, *80*, 2221−2228.
(2) Guldbrand, L.; Nilsson, L.; Nordenskiöld, L. A Monte Carlo simulation study of electrostatic forces between hexagonally packed DNA double helices. *J. Chem. Phys.* **1986**, *85*, 6686−6698.
(3) Attard, P.; Kjellander, R.; Mitchell, D. J.; Jönsson, B. Electrostatic fluctuation interactions between neutral surfaces with adsorbed, mobile ions or dipoles. *J. Chem. Phys.* **1988**, *89*, 1664−1680.
(4) Kjellander, R.; Marčelja, S. Inhomogeneous Coulomb fluids with image interactions between planar surfaces. I. *J. Chem. Phys.* **1985**, *82*, 2122−2135.
(5) Kjellander, R.; Marčelja, S.; Pashley, R. M.; Quirk, J. P. Double-layer ion correlation forces restrict Calcium clay swelling. *J. Phys. Chem.* **1988**, *92*, 6489−6492.
(6) Pellenq, R. J.-M.; Caillol, J. M.; Delville, A. Electrostatic attraction between two charged surfaces: A (N,V,T) Monte Carlo simulation. *J. Phys. Chem. B* **1997**, *101*, 8584−8594.
(7) Netz, R. Electrostatistics of counter-ions at and between planar charged walls: From Poisson-Boltzmann to the strong-coupling theory. *Eur. Phys. J. E: Soft Matter Biol. Phys.* **2001**, *5*, 557−574.
(8) Jönsson, B.; Nonat, A.; Labbez, C.; Cabane, B.; Wennerström, H. Controlling the cohesion of cement paste. *Langmuir* **2005**, *21*, 9211−9221.
(9) Mongondry, P.; Tassin, J. F. T.; Nicolai, T. Revised state diagram of Laponite dispersions. *J. Colloid Interface Sci.* **2005**, *283*, 397−405.
(10) Mourchid, A.; Lécolier, E.; Van Damme, H.; Levitz, P. On viscoelastic, birefringent, and swelling properties of Laponite clay suspensions: Revisited phase diagram. *Langmuir* **1998**, *14*, 4718−4723.




DOI: 10.1021/acs.jpcc.7b00882
J. Phys. Chem. C 2017, 121, 7951−7958

(11) Pignon, F.; Magnin, A.; Piau, J.-M.; Cabane, B.; Lindner, P.; Diat, O. Yield stress thixotropic clay suspension: Investigations of structure by light, neutron, and X-ray scattering. *Phys. Rev. E: Stat. Phys., Plasmas, Fluids, Relat. Interdiscip. Top.* **1997**, *56*, 3281.
(12) Blackmore, A. V.; Warkentin, B. P. Swelling of calcium montmorillonite. *Nature* **1960**, *186*, 823−824.
(13) Jönsson, B.; Wennerström, H. *Electrostatic Effects in Soft Matter and Biophysics*; Springer: Netherlands, 2001; pp 171−204.
(14) Karnland, O.; Olsson, S.; Nilsson, U.; Sellin, P. Experimentally determined swelling pressures and geochemical interactions of compacted Wyoming bentonite with highly alkaline solutions. *Phys. Chem. Earth, Parts A/B/C* **2007**, *32*, 275−286.
(15) Banin, A. Tactoid formation in montmorillionite: effect on ion exchange kinetics. *Science* **1967**, *155*, 71−72.
(16) Meunier, A. *Clays*; Springer Science & Business Media: 2005.
(17) Shalkevich, A.; Stradner, A.; Bhat, S. K.; Muller, F.; Schurtenberger, P. Cluster, glass, and gel formation and viscoelastic phase separation in aqueous clay suspensions. *Langmuir* **2007**, *23*, 3570−3580.
(18) Hedström, M.; Birgersson, M.; Nilsson, U.; Karnland, O. Role of cation mixing in the sol formation of Ca/Na-montmorillonite. *Phys. Chem. Earth, PT A/B/C* **2011**, *36*, 1564−1571.
(19) Segad, M.; Jönsson, B.; Åkesson, T.; Cabane, B. Ca/Na montmorillonite: Structure, forces and swelling properties. *Langmuir* **2010**, *26*, 5782−5790.
(20) Thuresson, A.; Karnland, O.; Jönsson, B. Anomalous temperature behavior in clay swelling due to ion-ion correlations. *EPL* **2016**, *114*, 38002.
(21) Birgersson, M.; Karnland, O.; Nilsson, U. Freezing of bentonite. Experimental studies and theoretical considerations. SKB Technical Report, 2010; TR-10-40, 1-1.
(22) Karnland, O.; Olsson, S.; Nilsson, U. Mineralogy and sealing properties of various bentonites and smectite-rich clay materials. SKB Technical Report, 2006; TR-06-30, 1-1.
(23) Michot, L. J.; Bihannic, I.; Porsch, K.; Maddi, S.; Baravian, C.; Mougel, J.; Levitz, P. Phase diagrams of Wyoming Na-montmorillonite clay. Influence of particle anisotropy. *Langmuir* **2004**, *20*, 10829−10837.
(24) Segad, M.; Jönsson, B.; Cabane, B. Tactoid formation in montmorillonite. *J. Phys. Chem. C* **2012**, *116*, 25425−25433.
(25) van Vaerenbergh, P.; Léonardon, J.; Sztucki, M.; Boesecke, P.; Gorini, J.; Claustre, L.; Sever, F.; Morse, J.; Narayanan, T. An upgrade beamline for combined wide, and ultra and ultra -angle X-ray scattering at the ESRF. *AIP Conf. Proc.* **2015**, *1741*, 030034.
(26) Sztucki, M. (2011) SAXSutilities download page: http://www.sztucki.de/SAXSutilities, (accessed Mar 2017).
(27) Segad, M.; Hanski, S.; Olsson, U.; Ruokolainen, J.; Åkesson, T.; Jönsson, B. Microstructural and swelling properties of Ca and Na montmorillonite: (In situ) Observations with Cryo-TEM and SAXS. *J. Phys. Chem. C* **2012**, *116*, 7596−7601.
(28) Segad, M. Microstructure determination of IQ-WB clays: a direct procedure by small-angle X-ray scattering. *J. Appl. Crystallogr.* **2013**, *46*, 1316−1322.
(29) Thuresson, A.; Ullner, M.; Turesson, M. Interaction and aggregation of charged platelets in electrolyte solutions: A coarse-graining approach. *J. Phys. Chem. B* **2014**, *118*, 7405−7413.
(30) Malmberg, C. G.; Maryott, A. A. Dielectric constant of water from 0° to 100° C. *J. Res. Nat. Bureau Stand* **1956**, *56*, 1−8.
(31) Abraham, M.; van der Spoel, D.; Lindahl, E.; Hess, B. the GROMACS development team, GROMACS User Manual version 5.0.1, 2014.
(32) Thuresson, A.; Ullner, M.; Åkesson, T.; Labbez, C.; Jönsson, B. Monte Carlo simulations of parallel charged platelets as an approach to tactoid formation in clay. *Langmuir* **2013**, *29*, 9216−9223.
(33) Turesson, M.; Forsman, J.; Åkesson, T.; Jönsson, B. Simulation of phase equilibria in lamellar surfactant systems. *Langmuir* **2004**, *20*, 5123−5126.
(34) Derjaguin, B. V.; Landau, L. Theory of the stability of strongly charged lyophobic sols and of the adhesion of strongly charged particles in solutions of electrolytes. *Acta Phys. Chim. URSS* **1941**, *14*, 633−662.
(35) Verwey, E. J. W.; Overbeek, J. T. G. *Theory of the Stability of Lyophobic Colloids*; Elsevier Publishing Company Inc.: Amsterdam, 1948.
(36) Linse, P.; Lobaskin, V. Electrostatic attraction and phase separation in solutions of like-charged colloidal particles. *J. Chem. Phys.* **2000**, *112*, 3917−3927.
(37) Svensson, P. D.; Hansen, S. Combined salt and temperature impact on montmorillonite hydration. *Clays Clay Miner.* **2013**, *61*, 328−341.
(38) Svensson, P. D. Ph.D. Thesis, Lund University, Lund, Sweden, 2015.



DOI: 10.1021/acs.jpcc.7b00882
*J. Phys. Chem. C* 2017, 121, 7951−7958

# Paper II

Reprinted from *J. Colloid Interface Sci.*, 2018, **513**, 575–584
M. Jansson, A. Thuresson, T. S. Plivelic, J. Forsman and M. Skepö
©2018 with permission from Elsevier.

Journal of Colloid and Interface Science 513 (2018) 575–584

Contents lists available at ScienceDirect

Journal of Colloid and Interface Science

journal homepage: www.elsevier.com/locate/jcis

Regular Article

# The effect of the relative permittivity on the tactoid formation in nanoplatelet systems. A combined computer simulation, SAXS, and osmotic pressure study

Maria Jansson [a,*], Axel Thuresson [a], Tomás S. Plivelic [b], Jan Forsman [a], Marie Skepö [a,*]

[a] Theoretical Chemistry, Lund University, P.O. Box 124, SE-221 00 Lund, Sweden
[b] MAX IV Laboratory, Lund University, P.O. Box 118, SE-221 00 Lund, Sweden

## GRAPHICAL ABSTRACT

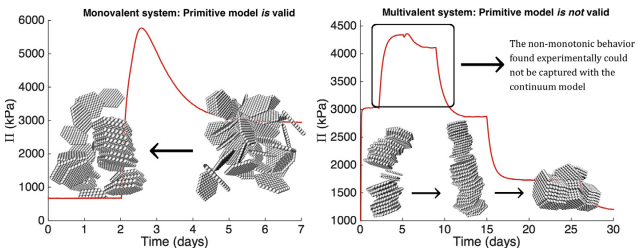


## ARTICLE INFO

*Article history:*
Received 6 October 2017
Revised 14 November 2017
Accepted 16 November 2017
Available online 20 November 2017

*Keywords:*
Nanoplatelets
Clay
Montmorillonite
Molecular dynamics simulations
Monte Carlo simulations
Electrostatic interactions
Ion-ion correlations
Relative permittivity
Ethanol
Small angle X-ray scattering

## ABSTRACT

The structural properties, and the intracrystalline swelling of $Na^+$-, and $Ca^{2+}$-montmorillonite (Na-, and Ca-mmt) have been investigated as an effect of decreasing the relative permittivity of the solvent, i.e. from water to ethanol (EtOH), utilizing the experimental techniques; small angle X-ray scattering (SAXS) and osmotic pressure measurements. The experimental data were compared with the continuum model, utilizing coarse-grained molecular dynamics bulk simulations, Monte Carlo simulations of two infinite parallel surfaces corresponding to two clay platelets, and the strong coupling theory. It was found that it is possible to tune the electrostatic interactions to obtain a transition from a repulsive to an attractive system for the Na-mmt by increasing the EtOH concentration, i.e. the Bjerrum length increases, and hence, the attractive ion-ion correlation forces are enhanced. A qualitative agreement was observed between the simulations and the experimental results. Moreover, a non-monotonic behavior of the intracrystalline swelling of Ca-mmt as a function of EtOH concentration was captured experimentally, where an increase in the osmotic pressure, and hence, an increase in the *d*-spacing was found at low concentrations, indicating that repulsive short-ranged interactions dominate in the system. Theoretically, the non-monotonic behavior could not be captured with the continuum model, probably due to the limitation that the electrostatic interactions solely enters the Hamiltonian via the Bjerrum length.

© 2017 Elsevier Inc. All rights reserved.

* Corresponding authors.
*E-mail addresses:* maria.jansson@teokem.lu.se (M. Jansson), marie.skepo@teokem.lu.se (M. Skepö).

https://doi.org/10.1016/j.jcis.2017.11.051
0021-9797/© 2017 Elsevier Inc. All rights reserved.

## 1. Introduction

Clay is a complex colloidal system and refers to naturally occurring aluminosilicate layered minerals, denoted phyllosilicates. The clay platelet has a strong negative surface charge density compensated with interlayer exchangeable cations. The physiochemical properties, and also the colloidal behavior, are determined by the charge distribution, the volume, and the shape of the colloid. When dispersed in water, the clay platelet becomes ionized and a rising osmotic pressure in the solution causes the clay to swell [1,2]. Semi-dilute dispersions can behave as gels, i.e. they have the ability to form yield stress materials [3–5], which are comprehensively used in various industrial applications, such as in paint, in drilling fluids, and in food as well as in cosmetic industry. For this reason, clay-solvent interactions have been extensively studied by evaluating the intracrystalline swelling of montmorillonite (mmt) in water [6,7], in different organic solvents [8–10], as well as water/organic mixtures [11]. Theoretically, the understanding of the swelling behavior of $Na^+$-montmorillonite (Na-mmt) in water and ethanol (EtOH) have been studied by Metz et al. [9] utilizing atomistic computer simulations. They have found that the initial solvation of dry clay with EtOH is energetically unfavourable by comparing the solvation energetics with the energy of the bulk, and that the formation of an EtOH monolayer is associated with a large energy barrier to move the first EtOH molecules into the interlayer region. Moreover, they found that the $Na^+$ ions behave differently in EtOH compared to in water, where the density profiles showed that the ions aggregate at each clay surface in the former rather than being dispersed in the solvent. Experimentally, the intracrystalline swelling of $Ca^{2+}$-montmorillonite (Ca-mmt) in water/EtOH mixtures was studied by Brindley et al. [11] using X-ray diffractometry. In their study, they found that for Ca-mmt the equilibrium basal spacing increased to about 35 mol percent of EtOH, and beyond the maximum expansion, the $d$-spacing diminished abruptly. Their explanation of the initial increase in basal spacing is due to an increased repulsion arising from the replacement of water molecules by the larger EtOH molecules, i.e. an excluded volume effect. Moreover, Brindley et al. concluded that the initial increase is not compatible with the accompanying decrease of the relative permittivity, due to the fact that it would cause an increase in the attractive electrostatic forces. However, to the authors knowledge, both effects can be present in the system, where the increase in basal spacing can be explained through an intricate balance of the partitioning of the solvent molecules, the electrostatic repulsive forces, and the enhanced ion-ion correlation forces.

The aim of this work is to study how the structural properties of the tactoids, and the intracrystalline swelling, are affected by changing the solvent i.e. by decreasing the relative permittivity for Na-, and Ca-mmt in water/EtOH mixtures. The focus is on describing under which conditions the structural properties of Na-mmt behaves as Ca-mmt, i.e. the possibility to tune the electrostatic interactions to obtain a transition from a repulsive to an attractive clay system via the solvent properties. For this purpose the experimental techniques, *Small Angle X-ray Scattering* (SAXS) and osmotic pressure measurements have been used. The experimental data are compared with theoretical models, such as: coarse-grained molecular dynamics (MD) bulk simulations, Monte Carlo (MC) simulations of two infinite parallel surfaces corresponding to two clay platelets, and with strong coupling theory.

Our main findings are that when increasing the concentration of EtOH, the attractive ion-ion correlation forces are enhanced, concluding that the structural properties of Na-mmt do indeed behave similarly as Ca-mmt. This is confirmed both experimentally and theoretically, where the transition from a repulsive to an attractive system is found. For Ca-mmt, a non-monotonic behavior of the intracrystalline swelling as a function of EtOH concentration was found experimentally, where the distance between the platelets and the osmotic pressure increased at low concentrations of EtOH, indicating that repulsive short-ranged interactions are dominating in the system. This behavior could, however, not be captured theoretically, probably due to the limitation in the continuum model, i.e. that the solvent is represented by the relative permittivity of the bulk solvent.

## 2. Experimental section

### 2.1. Chemicals and materials

The type of natural clay used throughout this study was Wyoming bentonite (MX-80), which is mainly composed of the swelling clay mineral Na-mmt. The chemical formula for the sodium saturated montmorillonite from MX-80 can be written as [12]:

$$(Al_{3.1}Mg_{0.49}Fe_{0.38}Ti_{0.01})(Si_{7.89}Al_{0.11})O_{20}(OH)_4, 0.65Na^+. \quad (1)$$

The purification and ion exchange procedures for MX-80 are described elsewhere [13]. Analytical grade sodium chloride (purity, 99.5%), and calcium chloride (purity, 99.5%) were purchased from MERCK. The purified Na-mmt and Ca-mmt were dried in an oven at 105 °C over night, and milled into a fine powder. EtOH solutions were prepared by dilution of EtOH 95 wt% (analytical grade, SOLVECO) with millipore water. The Na-, and Ca-mmt powder were added to different water/EtOH solutions, respectively, in order to obtain a clay volume fraction of 6% ($\phi_c \approx 0.06$). After the sample preparations, the samples were left to equilibrate for one month.

### 2.2. Methods and instruments

SAXS experiments were performed at beamline ID02 at the European Synchotron Radiation Facility (ESRF) in Grenoble-France [14]. For data reduction, the software SAXS-utilities [15] was used. The $q$-range reported in this study is $6.1 \cdot 10^{-2} < q < 4.5\ \mathrm{nm}^{-1}$, where $q = 4\pi\sin(\theta)/\lambda, 2\theta$ is the scattering angle, and $\lambda = 0.1$ nm is the monochromatic beam wavelength. The detector was a 2D CCD Rayonix MX 170 HS with binning $4 \times 4$. SAXS measurements were collected at different water/EtOH solutions: 0, 20, 40, 60, and 95 wt% EtOH, and at two different temperatures, room temperature, and the other significantly higher, 27, and 63 °C, respectively, where the thermalization time of each temperature was 12 min. For accurate statistics, and to control possible radiation damage effects, an average over ten frames was collected for each sample. The liquid samples were measured in 1 mm sealed glass capillaries, and the solid sample was placed between two mica sheets in a customized sample holder [14]. The background scattering was subtracted, where the corresponding water/EtOH solution was used for the liquid samples, and one empty cell with two mica sheets for the solid samples.

In order to estimate the size of the aggregates, i.e. the average number of clay platelets per tactoid, a model scattering peak has been fitted to the experimental data. The scattering function can be approximated with a Lorentzian line shape:

$$q^2 I(q) \propto \frac{w}{(q - q_{max})^2 + w^2} + b, \quad (2)$$

where $I(q)$ is the scattering intensity, $w$ is a measure of the width of the Bragg peak, $q_{max}$ is the position of maximum intensity of the Bragg peak, and $b$ is a fitting parameter for the background

**Table 1**
The Bjerrum length as a function of EtOH concentration and temperature.[a]

| wt% EtOH | $\epsilon_r$(T = 20 °C) | $l_B$ (nm) | $\epsilon_r$(T = 60 °C) | $l_B$ (nm) |
|---|---|---|---|---|
| 0 | 80.4 | 0.708 | 66.6 | 0.753 |
| 20 | 68.7 | 0.829 | 56.4 | 0.889 |
| 40 | 56.5 | 1.008 | 45.8 | 1.095 |
| 60 | 44.7 | 1.274 | 35.7 | 1.407 |
| 80 | 33.9 | 1.679 | 26.3 | 1.906 |
| 90 | 29.0 | 1.963 | 22.5 | 2.228 |
| 95 | 27.0 | 2.111 | 21.0 | 2.388 |
| 100 | 25.0 | 2.277 | 19.6 | 2.566 |

[a] The Bjerrum length, $l_B$, at eight different wt% of EtOH, and two temperatures, T, with corresponding relative permittivity, $\epsilon_r$(T) [20].

contribution. The full width at half maximum (FWHM) of the peak is equal to 2*w*, and the average tactoid size can be expressed as $\langle N\rangle \approx q_{max}/w$ [13,16,17]. The average distance, i.e. *d*-spacing, between the midplane of two adjacent clay platelets was obtained from $q_{max}$ via the relation: $d_{Bragg} = 2\pi/q_{max}$. The data was fitted between $q_{max} \pm 0.5$ nm$^{-1}$.

To achieve an indication of how the solvent properties affect the intracrystalline swelling, the osmotic pressures of the clay systems were directly measured using a test cell [12,18]. Approximately one gram of clay was placed within the test cell and confined by a piston, which is attached to a force transducer. The Na-, and Ca-mmt were set to equilibrate with a successive replacement of different solvent compositions corresponding to 0, 20, 40, 60, 80, and 95 wt% EtOH, through a semipermeable membrane, which was permeable to the solvent, but not to the clay particles. For the solvent composition of 0 wt% EtOH, used for the Na-mmt, NaCl with a salt concentration above the critical coagulation concentration (CCC) was added, i.e. 50 mM NaCl, to prevent any leakage through the membrane. The resulting osmotic pressure was calculated from the recorded force and piston contact area. With this experimental technique it is difficult to prepare the test cell to give an exact final volume, and hence, two separate measurements are rarely identical. However, it is possible to accurately determine the clay water content after the measurement, and thus the clay system was set to equilibrate with 0 wt% EtOH in the final stage. The clay water content is defined as $w = m_w/m_s$, where $m_w$ is the mass of the water, and $m_s$ is the mass of the solid. From the clay water content, the dry density of the clay defined as $D_d = m_s/V$ can be determined, utilizing $D_d = D_w/(w + D_w/D_s)$, where $V$ is the total volume of the system, $D_s$ (2750 kg/m$^3$) and $D_w$ (1000 kg/m$^3$) are the densities of the solid, and the water, respectively.

## 3. Theoretical section

### 3.1. Model and simulations

Molecular dynamics bulk simulations were used to study the structural and the thermodynamical properties of the formed tactoids of Na-mmt as a function of EtOH concentration, where the interaction potentials and the platelet description are given elsewhere [19]. The electrostatic (EL) pair-potential between particle *i* and *j* is defined as:

$$\beta u_{ij}^{\mathrm{EL}}(r,T) = \frac{l_B z_i z_j}{r_{ij}}, \tag{3}$$

where $\beta = 1/(k_B T)$, $k_B$ is the Boltzmann constant, $l_B = e^2/(4\pi\epsilon_0\epsilon_r(T)k_B T)$ is the Bjerrum length, $e$ is the elementary unit charge, $\varepsilon_0$ is the permittivity of vacuum, $z_i$ is the valency of particle *i*, and $r_{ij}$ is the center-to-center distance between the particles. The solvent is treated implicitly through the relative permittivity $\epsilon_r(T)$, and regarded as temperature ($T$) dependent. The solvent effect was studied by varying the value of $\epsilon_r(T)$ for the medium corresponding to experimentally measured values of the relative permittivity of water, EtOH, and water/EtOH mixtures, see Table 1 [20]. When increasing the EtOH concentration, the Bjerrum length increases, resulting in enhanced attractive ion-ion correlation forces due to an increased repulsion between the ions.

In addition to the electrostatic pair-potential, the particles also interact via a strictly repulsive, truncated, and shifted Lennard-Jones (LJ) potential, defined as:

$$u_{ij}^{\mathrm{LJ}}(r_{ij}) = \begin{cases} \epsilon_{\mathrm{LJ}}\left[\left(\frac{\sigma_{ij}}{r_{ij}}\right)^{12} - 2\left(\frac{\sigma_{ij}}{r_{ij}}\right)^{6} + 1\right], & \text{if } r_{ij} < \sigma_{ij} \\ 0, & \text{otherwise} \end{cases}, \tag{4}$$

where $\sigma_{ij} = (\sigma_i + \sigma_j)/2$, $\sigma_{ion} = 4$ Å, and $\sigma_{site} = 10$ Å. The strength of the short-ranged repulsion was set to $\epsilon_{LJ} = k_B \cdot 293$ J, with the motivation to obtain a temperature independent LJ potential. Thus, the distribution of uncharged particles behaves independently of the temperature, since the aim is to study the electrostatic effects exclusively.

The MD simulations were performed with the software package GROMACS (version 5.0.4.) [21]. The model consisted of 50 negatively charged finite plates, i.e. clay platelets, and their corresponding counterions in a cubic simulation box with three-dimensional periodic boundary conditions. The platelets had a hexagonal symmetry and were constructed from monolayers of 91 connected charged, truncated, and shifted LJ spheres, i.e. sites. The mean radius of the platelet was 5.5 nm, and the one-sided surface charge density was set to $\sigma = -2.6$ e/nm$^2$. Since the interaction is proportional to the area of the platelet, the absolute value of the surface charge density is chosen much higher than the estimated value of natural mmt to compensate for the small size of the simulated platelets. The reader should notice, that if the size of the simulated platelets would be larger, the surface charge density can be reduced to have similar probability of aggregation as the smaller platelets with divalent counterions [19]. Furthermore, the reason for this is that the interaction is to a first approximation proportional to the area of the platelets. On average, mmt has a one-sided surface charge density of $-1.5$ e/nm$^2$ [22].

Newton's equations of motion of freely moving species, i.e. the platelets and the counterions, were integrated using the leap-frog algorithm. The temperature was set by velocity-rescaling temperature coupling. Fast particle-mesh Ewald summation (PME) was used with a 6 nm real-space Coulomb cutoff, and a Fourier spacing equal to 0.6 nm to account for the long-ranged electrostatic contribution. For an in-depth description of the input parameters, the reader is referred to the user manual [21]. The box length used in the NVT simulations was 30 nm, corresponding to a volume fraction of 9% ($\phi \approx 0.09$). This value was chosen higher than the experimental samples due to the small size of the simulated platelets, where the average lateral size of a natural mmt platelet is approximately 250 nm [23]. The time step was set to 10 fs, with a total of $10^7$ steps.

From the bulk MD simulations structural information were obtained via the total structure factor between the platelets, defined as:

$$S(q) = \left\langle \frac{1}{N}\sum_{i=1}^{N}\sum_{j=1}^{N}\frac{\sin(qr_{ij})}{qr_{ij}}\right\rangle, \tag{5}$$

where $N$ is the total number of platelet sites in the system. Assuming an isotropic scattering, the equation of the total structure factor can be rewritten as:

$$S(q) = 1 + 4\pi\frac{N}{V}\int_0^{\infty}(g(r)-1)r^2\frac{\sin(qr)}{qr}dr, \tag{6}$$

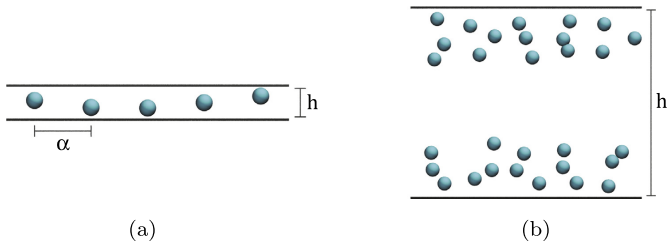


**Fig. 1.** Schematic illustration of two charged surfaces (represented as horizontal black lines) mediated by counterions (represented as cyan spheres). (a) The lateral distance, $\alpha$, between the ions is larger than the separation, $h$, between the two charged surfaces. (b) The charged surfaces attract two separate layers of counterions, and the lateral distance between the ions is small.

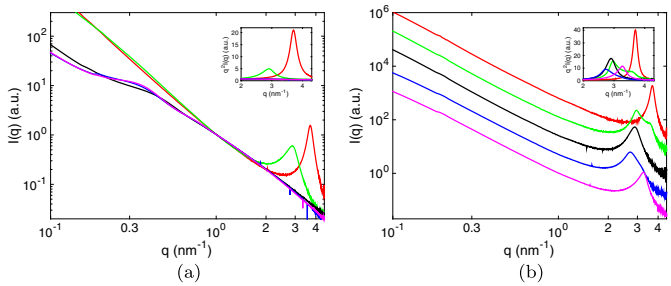


**Fig. 2.** The X-ray scattering intensities as a function of the scattering vector at T = 25 °C and $\phi_c \approx 0.06$ for (a) $Na^+$-, and (b) $Ca^{2+}$-montmorillonite at 95 (red), 60 (green), 40 (black), 20 (blue), and 0 (magenta) wt% EtOH. The insets show the Kratky plots of the corresponding systems. In (a) the scattering intensities are normalized at $q \approx 1$ nm$^{-1}$, and in (b) the scattering curves are scaled to enhance the different shape of the Bragg peaks. (For interpretation of the references to color in this figure legend, the reader is referred to the web version of this article.)

where $g(r)$ is the radial distribution function between all the platelet sites in the system. If $g(r)$ is not approaching one at large separations due to the finite length of the box, a window function can be used to reduce artefacts, according to:

$$S_w(q) = 1 + 4\pi\frac{N}{V}\int_0^\infty (g(r)-1)r^2\frac{\sin(qr)}{qr}\frac{\sin(\pi r/R_c)}{\pi r/R_c}dr, \quad (7)$$

where $R_c$ is the maximum distance in $g(r)$ [24].

Two parallel infinite surfaces mimicking the clay platelets with corresponding counterions were simulated using Monte Carlo simulations. The model is described elsewhere [25]. The surfaces have a uniform surface charge density of $\sigma = -1.3$ e/nm$^2$, separated at a distance $h$. The counterions are treated as charged hard spheres, where the electrostatic interactions are defined similarly as for the bulk simulations. The system assumes equilibrium with salt-free water, and thus, the pressure is equal to the osmotic pressure. For a given temperature and separation between the surfaces, the osmotic pressure, $\Pi = \Pi(T,h)$, can be calculated using a midplane approach defined as: $\Pi = \Pi^{id} + \Pi^{corr} + \Pi^{coll}$, where $\Pi^{id} = k_BT\Sigma_{i=1}^2 c_i(mp)$ is the ideal contribution, $c_i(mp)$ is the concentration of counterions at the midplane with valency $i$. $\Pi^{corr}$ is an attractive term due to the ion-ion correlation interactions on either side of the midplane, and $\Pi^{coll}$ is the collision term due to the finite ion size, where the diameter of an ion is $d_{hc} = 4$ Å [26].

For two equally charged surfaces the interactions in the system can be explained either with the weak or the strong coupling (SC) theory [27]. The Poisson-Boltzmann (PB) equation is asymptotically exact in the limit of weak coupling, i.e. long distances between the surfaces, low surface charge density, and low counterion valence. The SC theory is asymptotically exact in the opposite limit, i.e. short distances between the surfaces, high surface charge density, and high counterion valence. The limits can be found by considering the coupling parameter:

$$\Xi = 2\pi z^3 l_B^2 \sigma_s, \quad (8)$$

where $\sigma_s$ is the surface charge number density. The SC theory is valid for $\Xi \to \infty$ (the SC limit), and the PB equation is valid for small values of $\Xi$. A schematic illustration of two charged surfaces mediated by counterions are shown in Fig. 1. The SC theory is valid if the lateral distance between the ions, $\alpha$, is larger than the separation, $h$, between the surfaces, i.e. $h < \alpha$, see Fig. 1a, where the ions move independently of each other perpendicular to the surfaces due to the strong ion-ion correlation forces. The PB equation is valid in Fig. 1b, where each ion interacts with a diffuse cloud of other ions [27].

## 4. Results and discussion

### 4.1. SAXS

Scattering experiments were performed for different water/EtOH mixture conditions for Na-, and Ca-mmt, where the scattering intensities, and the Kratky plots ($q^2I(q)$ vs $q$), at T = 25 °C and $\phi_c \approx 0.06$, are shown in Fig. 2. Bragg peaks are clearly observed

**Table 2**
The position of the Bragg peak maximum ($q_{max}$), $d$-spacing ($d_{Bragg}$), full width at half maximum (FWHM), and average number of platelets per tactoid ($\langle N \rangle$), for $Na^+$-, and $Ca^{2+}$-montmorillonite.

| wt% EtOH | $q_{max}$ ($nm^{-1}$) | $d_{Bragg}$ (nm) | FWHM ($nm^{-1}$) | $\langle N \rangle$ |
|---|---|---|---|---|
| *Na-mmt* | | | | |
| 60 | 2.88 | 2.18 | 0.53 | 11 |
| 95 | 3.70 | 1.70 | 0.30 | 25 |
| *Ca-mmt* | | | | |
| 0 | 3.25 | 1.93 | 0.38 | 17 |
| 20 | 2.77 | 2.27 | 0.54 | 10 |
| 40 | 2.90 | 2.17 | 0.40 | 15 |
| 95 | 3.69 | 1.70 | 0.20 | 37 |

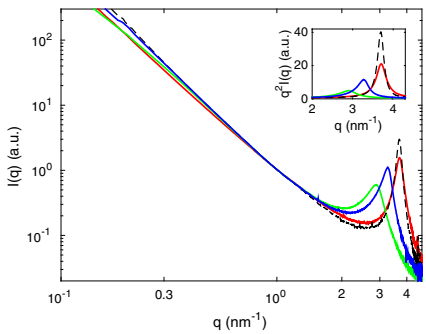


**Fig. 3.** The X-ray scattering intensities as a function of the scattering vector at T = 25 °C and $\phi_c \approx 0.06$ of $Na^+$-montmorillonite with 95 (red), and 60 (green) wt% EtOH, and $Ca^{2+}$-montmorillonite with 95 (dashed black), and 0 (blue) wt% EtOH. The inset shows the Kratky plots of the corresponding systems. The scattering intensities are normalized at $q \approx 1\ nm^{-1}$. (For interpretation of the references to color in this figure legend, the reader is referred to the web version of this article.)

for Na-mmt at water/EtOH mixtures above 60 wt% (Fig. 2a), indicating that tactoids are formed when increasing the concentration of EtOH, hence, it is possible to capture a crossover from a repulsive to an attractive system. As the concentration of EtOH increases from 60 to 95 wt% with respect to EtOH, the Bragg peak moves towards higher values of $q$, i.e. the separation between the platelets decreases from ~ 2.18 to 1.70 nm. Moreover, the full width at half maximum of the Bragg peaks decreases, indicating that the tactoids are growing in size, where the average number of platelets in the tactoids increases from $\langle N \rangle \sim 11$ to 25. For Ca-mmt (Fig. 2b) the position of the Bragg peak is strongly dependent on the EtOH concentration. When the concentration increases from 0 to 20 wt% EtOH, the separation between the platelets in the tactoids increases from ~ 1.93 to 2.27 nm. At 60 wt% EtOH the scattering pattern is a superposition of two Bragg peaks, indicating that there is a competition between two different separations, either of intercalated EtOH and water, or two EtOH concentrations. Above 60 wt% EtOH the separation between the platelets decreases, for example for 95 wt% EtOH it becomes ~ 1.70 nm. The values of the position of the Bragg peak, the $d$-spacing, the full width at half maximum, and the average number of platelets per tactoid for both Na-, and Ca-mmt, are shown in Table 2.

By comparing the scattering curves of Na-, and Ca-mmt with 95 and 0 wt% EtOH, respectively (Fig. 3), it is shown that the position of the Bragg peak of Na-mmt occurs at a higher q-value than Ca-mmt, i.e. ~ 3.70 and 3.25 $nm^{-1}$. This corresponds to a separation between the platelets in the tactoids of ~ 1.70 and 1.93 nm, respectively, indicating that there are stronger attractive interactions in the system with Na-mmt. The full width at half maximum is broader for Ca-mmt, resulting in a smaller average number of platelets in the tactoids c.f. $\langle N \rangle \sim 17$, while for Na-mmt $\langle N \rangle \sim 25$. Hence, by changing the solvent composition from water to EtOH, i.e. by decreasing the relative permittivity of the solvent, the structural properties of Na-mmt do indeed behave similarly as Ca-mmt.

**Table 3**
The coupling parameter as a function of EtOH concentration for $Na^+$-, and $Ca^{2+}$-montmorillonite.[a]

| wt% EtOH | Ξ | $d_{Bragg}$ (nm) | $\langle N \rangle$ |
|---|---|---|---|
| *Na-mmt* | | | |
| 0 | 3 | – | – |
| 95 | 28 | 1.70 | 25 |
| *Ca-mmt* | | | |
| 0 | 25 | 1.93 | 17 |
| 95 | 224 | 1.70 | 37 |

[a] The coupling parameter (Ξ), $d$-spacing ($d_{Bragg}$), and the average number of platelets in the tactoid ($\langle N \rangle$) for $Na^+$-, and $Ca^{2+}$-montmorillonite in 0, and 95 wt% EtOH, respectively.

The experimental results above can be qualitatively explained by comparing the coupling parameter, where $\Xi \sim 28$ for monovalent ions in 95 wt% EtOH, and $\Xi \sim 25$ for divalent ions in water at T = 20 °C, see Table 3. Thus, there are indeed stronger attractive interactions due to the stronger coupling with monovalent ions in EtOH compared to divalent ions in water. For divalent ions in 95 wt % EtOH, the coupling parameter is even higher, i.e. $\Xi \sim 224$. This effect is captured in the SAXS data, where the position of the Bragg peak is approximately the same for Na-, and Ca-mmt in 95 wt% EtOH, i.e. ~ 3.7 $nm^{-1}$. However, the FWHM of the peak is narrower for Ca-mmt corresponding to $\langle N \rangle \sim 37$, indicating that there are stronger attractive forces for the system with divalent counterions. Moreover, when monovalent counterions are replaced by divalent counterions, the number of ions decreases with a factor of two, which corresponds to a decreased double-layer repulsion.

The scattering intensities obtained from the temperature measurements of Na-, and Ca-mmt in 60, and 20 wt% EtOH, respectively, at T = 27, and 63 °C, with $\phi_c \approx 0.06$, are shown in Fig. 4. From the analysis of the Bragg peaks it is shown that there is only a minor deviation between the two temperatures for the two different systems, where the difference in separation between the temperatures, i.e. $\Delta d_{Bragg} = d_{Bragg}(T = 63\ °C) - d_{Bragg}(T = 27\ °C)$, were estimated to be ~ 0.01, and ~ 0.08 nm for Na-, and Ca-mmt, respectively, resulting in an average separation between the platelets in the tactoids of ~ 2.2 nm. Also, the FWHM is in the same order for all scattering curves, corresponding to an average number of platelets in the tactoids of ~ 10. From these measurements it can be concluded that there is only a minor temperature effect in the systems, in correlation to what has been noticed for Na-, and Ca-mmt in pure water [7].

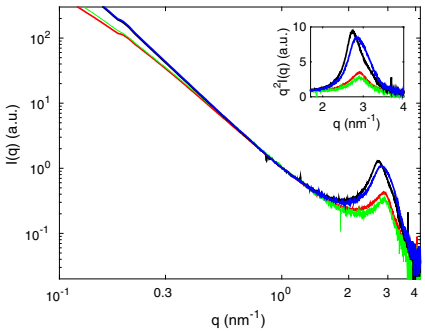


**Fig. 4.** The X-ray scattering intensities as a function of the scattering vector for the temperature measurements with $\phi_c \approx 0.06$ of $Na^+$-montmorillonite with 60 wt% EtOH at T = 27 (red), and 63 °C (green), and $Ca^{2+}$-montmorillonite with 20 wt% EtOH at T = 27 (black), and 63 °C (blue), respectively. The inset shows the Kratky plots for the corresponding systems. The scattering intensities are normalized at $q \approx 1$ nm$^{-1}$. (For interpretation of the references to color in this figure legend, the reader is referred to the web version of this article.)

### 4.2. Osmotic pressure

Fig. 5a shows the results from the osmotic pressure measurements of Ca-mmt at room temperature for two different values of the dry density: 1230, and 1180 kg/m$^3$. Each plateau corresponds to an equilibrium osmotic pressure of the clay system for the respective water/EtOH mixture in the order of 0, 20, 40, 60, 80, 95, and 0 wt% EtOH. By extracting the equilibrium osmotic pressures, it is clearly shown that there is a non-monotonic behavior of the osmotic pressure as a function of EtOH concentration, regardless of dry density (Fig. 5c), which correlates both with the SAXS data (Fig. 2b), as well as with the work done by Brindley et al. [11]. When the bulk solution is gradually changed from 0 to 95 wt% EtOH, the osmotic pressure increases at low concentrations, followed by a steady decrease at higher concentrations. The reversibility of the clay systems was confirmed by changing the solvent back to 0 wt% EtOH, where the osmotic pressure returns to its initial value. During this exchange, a large peak arises, which is enhanced in Fig. 5b. Our hypothesis is that the transition occurs via a successively replacement of intercalated EtOH molecules with water molecules, which is supported by analysing the height of the peak, where it is shown that the same magnitude is obtained at the highest recorded osmotic pressure. The same trend is also visible for the transition from 95 to 0 wt% EtOH for Na-mmt as for Ca-mmt, see Fig. 5b. The reader should notice, that the addition of 50 mM NaCl to the solution of 0 wt% EtOH with Na-mmt will not affect the measured osmotic pressure to a great extent, as shown in a previous publication [12]. The reason for this is due to the high volume fraction of the clay sample, where the counterion concentration is about one order of magnitude larger than the added salt concentration. For the same reason, with 95 wt% EtOH, the addition of 50 mM NaCl will only moderately increase the ion-ion correlation forces. However, the long-ranged repulsion is screened for more dilute samples [22]. The values of

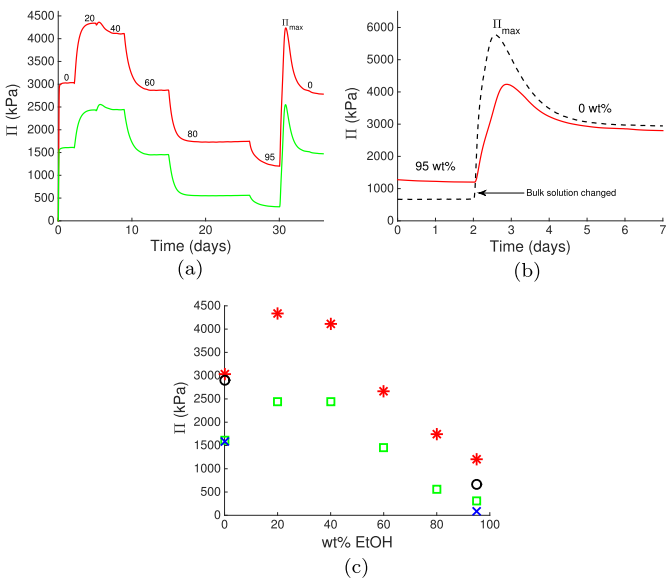


**Fig. 5.** (a) The osmotic pressure as a function of time and EtOH concentration of $Ca^{2+}$-montmorillonite at two different clay dry densities ($D_d$). (b) The transition from 95 to 0 wt% EtOH of both $Na^+$-, and $Ca^{2+}$-montmorillonite. (c) The equilibrium osmotic pressures of the respective EtOH concentrations for all systems. The color codes are: $D_d = 1230$ (red), and 1180 (green) kg/m$^3$ for $Ca^{2+}$-montmorillonite, and $D_d = 1070$ (black), and 1030 (blue) kg/m$^3$ for $Na^+$-montmorillonite. (For interpretation of the references to color in this figure legend, the reader is referred to the web version of this article.)

**Table 4**
The equilibrium osmotic pressures as a function of clay dry density for $Na^+$-, and $Ca^{2+}$-montmorillonite.[a]

| $D_d$ (kg/m$^3$) | $\Pi_0$ (kPa) | $\Pi_{95}$ (kPa) | $\Pi_{max}$ (kPa) |
|---|---|---|---|
| *Na-mmt* | | | |
| 1070 | 2910 | 670 | 5770 |
| 1030 | 1590 | 90 | 2630 |
| *Ca-mmt* | | | |
| 1180 | 1610 | 310 | 2550 |
| 1230 | 3040 | 1210 | 4240 |

[a] The osmotic pressure of 0 ($\Pi_0$), and 95 ($\Pi_{95}$) wt% EtOH, and at the position of the peak maximum ($\Pi_{max}$) for $Na^+$-, and $Ca^{2+}$-montmorillonite, as a function of clay dry density ($D_d$).

the equilibrium osmotic pressures of 0 ($\Pi_0$), and 95 ($\Pi_{95}$) wt% EtOH, as well as the osmotic pressure at the position of the peak maximum ($\Pi_{max}$) for both Na-, and Ca-mmt, are given in Table 4.

### 4.3. Simulations

Radial distribution functions (rdfs) with respect to the center-of-mass between the platelets were extracted from the NVT MD bulk simulations at T = 20 °C, and with a volume fraction of 9% ($\phi \approx 0.09$). The number of peaks in the rdfs are an indication of the average number of platelets in the tactoids, $\langle N \rangle$, where the height of the peak gives the probability of finding that configuration. The first peak is equivalent to a structure when two platelets have aggregated face-to-face at a distance of $\sim 1.3$ nm, and the second peak corresponds to the situation where three platelets have aggregated at a distance of $\sim 1.3 \cdot 2$, and so on. As shown, both the number of peaks, and the probability of aggregation, increase with a decrease in the relative permittivity. When decreasing the relative permittivity of the solvent, the attractive ion-ion correlations are enhanced due to the increase in Bjerrum length, and thus an increase in the coupling parameter. This behavior is captured in the Na-mmt system (Fig. 6a), where peaks in the rdfs are found above 90 wt% EtOH. As expected, the simulated SAXS spectras (Fig. 6b) show Bragg peaks for 95, and 100 wt% EtOH, where the positions of the peaks are corresponding to a $d$-spacing of $\sim$1.2 nm for both systems. The discrepancy of the smoothness in the scattering pattern of the simulated SAXS spectra arises from the small size of the platelets. No Bragg peaks are observed at an EtOH concentration of 90 wt%, or lower, indicating the existence of a repulsive system. The transition from a repulsive to an attractive system is illustrated in Fig. 6c-d, where representative configurations of the Na-mmt system in 0, and 100 wt% EtOH, are shown. At 0 wt% EtOH, only single platelets are found in the system, whereas for 100 wt% EtOH, all platelets have aggregated and formed tactoids. In the latter, the average number of platelets per tactoid was determined to $\langle N \rangle \sim 4$. The MD simulations are in qualitative agreement with the SAXS data (Fig. 2a), where a transition from a repulsive to an attractive system is found for Na-mmt. In the simulations, the transition occurs at a higher EtOH concentration compared to the experimental data, which could arise from the selected input parameters, such as the volume fraction of the platelets, the surface charge density, and the size of the platelets.

By comparing the rdfs of Na-mmt at 95 wt% EtOH with Ca-mmt at 0 wt% EtOH (Fig. 7a), it is shown that the height of the first peaks are of the same magnitude, indicating that the probability of finding a face-to-face configuration is of the same order. For the Ca-mmt system, the second peak is more pronounced, indicating that larger aggregates have been formed. This is confirmed by comparing the representative configurations of the systems (Fig. 7c-d),

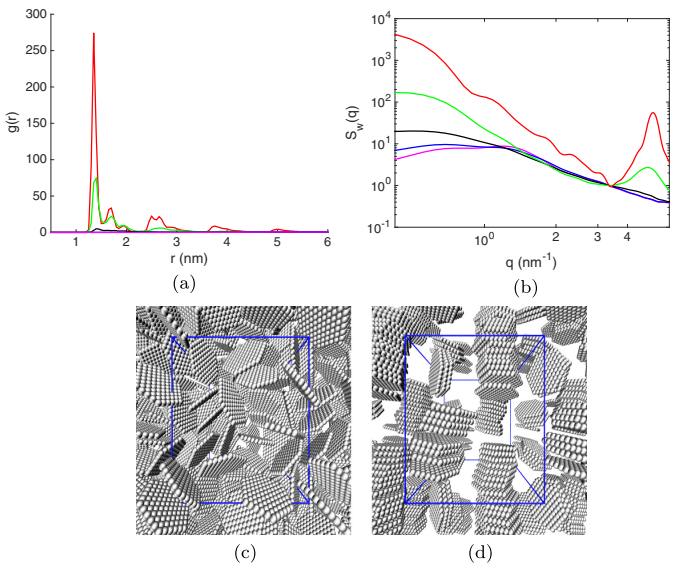


**Fig. 6.** (a) Radial distribution functions, and (b) simulated SAXS spectras from the NVT MD bulk simulations at T = 20 °C of $Na^+$-montmorillonite at 100 (red), 95 (green), 90 (black), 60 (blue), and 0 (magenta) wt% EtOH. Illustrative configurations of $Na^+$-montmorillonite at (c) 0, and (d) 100 wt% EtOH. The volume fraction of the system was 9% ($\phi \approx 0.09$). (For interpretation of the references to color in this figure legend, the reader is referred to the web version of this article.)

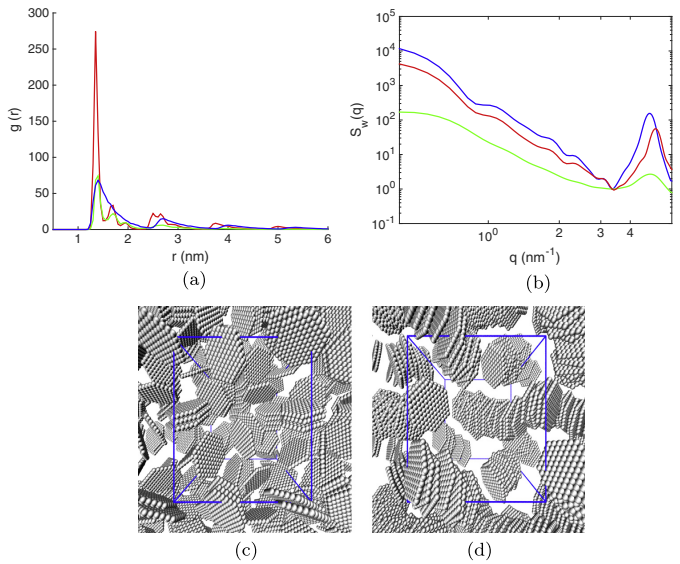


**Fig. 7.** (a) Radial distribution functions, and (b) simulated SAXS spectras from the NVT MD bulk simulations at T = 20 °C of $Na^+$-montmorillonite at 100 (red), and 95 (green) wt% EtOH, and $Ca^{2+}$-montmorillonite at 0 (blue) wt% EtOH. Illustrative configurations of (c) $Na^+$-montmorillonite at 95 wt% EtOH, and (d) $Ca^{2+}$-montmorillonite at 0 wt% EtOH. The volume fraction of the system was 9% ($\phi \approx 0.09$). (For interpretation of the references to color in this figure legend, the reader is referred to the web version of this article.)

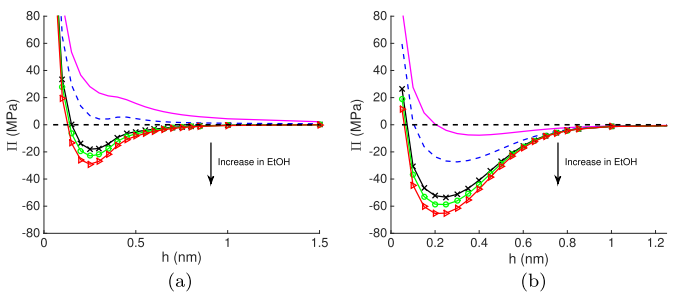


**Fig. 8.** The osmotic pressure as a function of separation between the surfaces from the MC simulations at T = 20 °C of (a) $Na^+$-, and (b) $Ca^{2+}$-montmorillonite at 100 (red), 95 (green), 90 (black), 60 (dashed blue), and 0 (magenta) wt% EtOH. The surface charge density was $\sigma = -1.3$ e/nm$^2$. (For interpretation of the references to color in this figure legend, the reader is referred to the web version of this article.)

where smaller tactoids are found for Na-mmt at 95 wt% EtOH compared to Ca-mmt at 0 wt% EtOH. Here the average number of platelets per tactoid becomes $\langle N \rangle \sim 2$, and 4 for each system, respectively. From the simulated SAXS spectras (Fig. 7b), the Bragg peak of the Ca-mmt system is shifted towards lower values of $q$ compared to the Na-mmt system, which corresponds to a $d$-spacing of $\sim 1.3$, and 1.2 nm, respectively. The MD simulations have a reasonable agreement with the SAXS data (Fig. 3), indicating slightly stronger attractive interactions in the Na-mmt system at 95 wt% EtOH, in comparison with the Ca-mmt system at 0 wt% EtOH.

The osmotic pressure as a function of separation between the surfaces from the MC simulations at T = 20 °C are shown in Fig. 8. For the Na-mmt system (Fig. 8a) both the osmotic pressure, and the equilibrium separation between the surfaces determined from $\Pi(h) = 0$ decrease with an increase in EtOH concentration. The transition from a repulsive to an attractive system occurs between 60, and 90 wt% EtOH, where a global minimum is found for the systems at 90 wt% EtOH and above. These results correlate with the SAXS data and the bulk MD simulations, indicating that the model also captures the behavior for Na-mmt in water/EtOH mixtures. This is, however, not the case for the Ca-mmt system

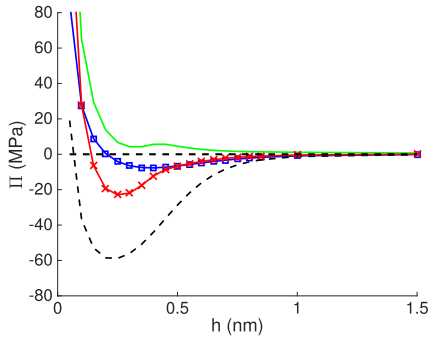


**Fig. 9.** The osmotic pressure as a function of separation between the surfaces from the MC simulations at T = 20 °C of $Na^+$-montmorillonite at 95 (red), and 60 (green) wt% EtOH, and $Ca^{2+}$-montmorillonite at 95 (dashed black), and 0 (blue) wt% EtOH. The surface charge density was $\sigma = -1.3$ e/nm$^2$. (For interpretation of the references to color in this figure legend, the reader is referred to the web version of this article.)

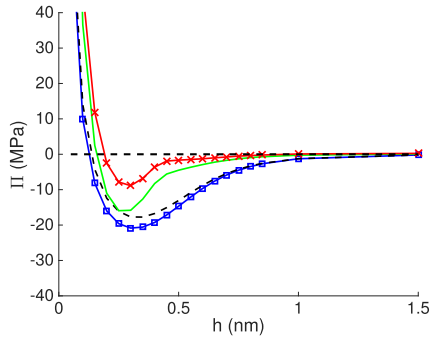


**Fig. 10.** The osmotic pressure as a function of separation between the surfaces for the MC simulations of $Na^+$-montmorillonite at 80 wt% EtOH, at T = 20 (red), and 60 °C (green), and $Ca^{2+}$-montmorillonite at 40 wt% EtOH, at T = 20 (black), and 60 °C (blue). The surface charge density was $\sigma = -1.3$ e/nm$^2$. (For interpretation of the references to color in this figure legend, the reader is referred to the web version of this article.)

(Fig. 8b), where the monotonic trend for the osmotic pressure as a function of EtOH concentration captured in the MC simulations, is not consistent with neither the SAXS nor the experimental osmotic pressure data. This non-monotonic behavior could not be captured utilizing the continuum model, probably due to the lack of partitioning of the solvent molecules. In principle, the continuum model should be valid with respect to the electrostatic interactions. However, the effect of the variation of the relative permittivity could be overruled by other effects, such as the difference in size between the solvent molecules, the density changes associated with the solvent interactions, as well as the geometry of the solvent molecules.

Comparisons between the osmotic pressure data obtained from the MC simulations for the Na-, and the Ca-mmt systems (Fig. 9), show the same trend as is found in the SAXS data. The attractive interaction forces are stronger, and the separation between the surfaces are smaller for Na-mmt at 95 wt% EtOH in comparison to Ca-mmt at 0 wt% EtOH. These results conclude that the model can accurately capture the behavior of the transition from a repulsive to an attractive system by tuning the electrostatic interactions, and confirm that the structural properties of Na-mmt do indeed behave similarly as a Ca-mmt when changing the solvent from water to EtOH.

The temperature effect has also been analyzed with the MC model. The simulated osmotic pressure of Na-, and Ca-mmt at two different temperatures are presented in Fig. 10. In order to capture the corresponding behavior as for the SAXS data (Fig. 4), a higher concentration of EtOH was chosen for both of the systems. An exact agreement is possible to find by tuning the fitting parameters. However, as for the MD bulk simulations, our goal with the model is to understand the physics behind the clay behavior, rather than obtaining correct fitting parameters. From these simulations it was found that there is only a minor temperature effect, where the attraction increases with an increase in temperature, resulting in a decrease in the separation between the surfaces. The separation differences between the two temperatures, i.e. $\Delta d_{Bragg} = d_{Bragg}(T = 60\,°C) - d_{Bragg}(T = 20\,°C)$, for Na-, and Ca-mmt were estimated to $\sim 0.03$, and $\sim 0.01$ nm respectively, and they are of the same order of magnitude as for the SAXS data.

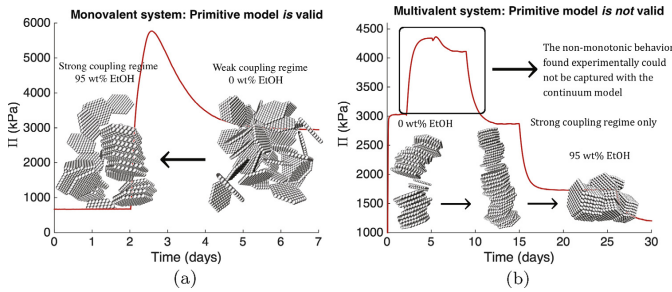


**Fig. 11.** (a) The osmotic pressure response of $Na^+$-montmorillonite, with illustrative configurations corresponding to 95 (left), and 0 (right) wt% EtOH. (b) The osmotic pressure response of $Ca^{2+}$-montmorillonite, where the black box represents the limitation regime of the continuum model, and the illustrative configurations correspond to 0 (left), 20 (middle), and 95 (right) wt% EtOH.

## 5. Conclusions

We have shown that it is possible to tune the electrostatic interactions to obtain a transition from a repulsive to an attractive system for Na-mmt via the solvent properties, i.e. by decreasing in the relative permittivity. From the SAXS data, Bragg peaks were found at 60, and 95 wt% EtOH, corresponding to a *d*-spacing of $\sim 2.18$, and 1.70 nm, respectively. The Bragg peaks are an indication of tactoid formation, and the decrease in *d*-spacing concludes that the interaction between the platelets are dominated by attractive ion-ion correlation forces, which are enhanced as the concentration of EtOH increases. From the experimentally osmotic pressure measurements reversibility of the Na-mmt system was obtained. Our hypothesis is that the transition from 95 to 0 wt% EtOH occurs via a successively replacement of intercalated EtOH molecules with water molecules (future work). The results from the theoretical models are in qualitative agreement with the experimental data, giving a further indication of that the given models can explain the underlying physics in the system containing monovalent ions. This is illustrated in Fig. 11a, where the transition between weak and strong coupling regime is visible.

Moreover, a non-monotonic behavior of the intracrystalline swelling of Ca-mmt as a function of EtOH concentration was captured experimentally. It was found that the osmotic pressure increased until 20 wt% EtOH was reached in the sample, whereas the *d*-spacing obtained from SAXS in the 20 wt% EtOH sample increased in comparison with 0 wt% EtOH. Hence, this indicates that there are stronger repulsive forces in the Ca-mmt systems at lower concentrations of EtOH. At 60 wt% EtOH the scattering pattern from the SAXS data was found to be a superposition of two Bragg peaks, and the osmotic pressure is in same regime as at 0 wt% EtOH, indicating that there is a competition between two different separations, either for the intercalated EtOH and water, or for two EtOH concentrations. At 95 wt% EtOH the *d*-spacing was decreased to $\sim 1.70$ nm, and the osmotic pressure was markedly reduced, due to the enhanced ion-ion correlation forces. The non-monotonic behavior found experimentally could not be captured utilizing the continuum model, probably due to the lack of partitioning of the solvent molecules. This is illustrated in Fig. 11b, where the limitation regime of the model is highlighted by the black box, i.e. the increase in osmotic pressure, and the representative configurations of the Ca-mmt systems at 0, 20, and 95 wt% EtOH, show that the separation between the platelets decreases with an increase in EtOH concentration. Thus, in the continuum model a monotonic behavior is found for the intracrystalline swelling of Ca-mmt as a function of EtOH concentration, where the enhanced attractive ion-ion correlation forces increase with a decrease in relative permittivity. To be able to capture this effect theoretically, a model considering the interactions between the solvent molecules and the clay platelets is needed. For example, a model where the solvent is treated explicitly is a good candidate.

## Acknowledgement

Computational resources were provided by the Swedish National Infrastructure for Computing (SNIC) through LUNARC, the Center for Scientific and Technical Computing at Lund University. We acknowledge the European Synchrotron Radiation Facility (ESRF) in Grenoble, France, for providing beamtime, Dr. T. Narayanan and Dr. J. Möller, for providing assistance during measurements at ESRF. The pressure measurement facilities were kindly provided by Clay Technology AB in Lund, Sweden. The work was performed within the framework of the Swedish national strategic e-science research program eSSENCE.

## References

[1] L. Guldbrand, B. Jönsson, H. Wennerström, P. Linse, Electrical double layer forces. A Monte Carlo study, J. Phys. Chem. 80 (1984) 2221–2228, https://doi.org/10.1063/1.446912.
[2] P. Mongondry, J.F. Tassin, T. Nicolai, Revised state diagram of Laponite dispersions, J. Colloid Interface Sci. 283 (2005) 397–405, https://doi.org/10.1016/j.jcis.2004.09.043.
[3] F. Pignon, A. Magnin, J.-M. Piau, B. Cabane, P. Lindner, O. Diat, Yield stress thixotropic clay suspension: investigations of structure by light, neutron, and X-ray scattering, Phys. Rev. E 56 (1997) 3281–3289.
[4] S. Cocard, J.F. Tassin, T. Nicolai, Dynamical mechanical properties of gelling colloidal disks, J. Rheol. 44 (2000) 585–594, https://doi.org/10.1122/1.551107.
[5] C. Martin, F. Pignon, A. Magnin, M. Meireles, V. Lelièvre, P. Lindner, B. Cabane, Osmotic compression and expansion of highly ordered clay dispersions, Langmuir 22 (2006) 4065–4075, https://doi.org/10.1021/la052605k.
[6] K. Norrish, The swelling of montmorillonite, Discuss. Faraday Soc. 18 (1954) 120–134, https://doi.org/10.1039/DF9541800120.
[7] A. Thuresson, M. Jansson, T.S. Plivelic, M. Skepö, Temperature response of charged colloidal particles by mixing counterions utilizing Ca/Na montmorillonite as model system, J. Phys. Chem. C 121 (2017) 7951–7958, https://doi.org/10.1021/acs.jpcc.7b00882.
[8] R.H. Dowdy, M.M. Mortland, Alcohol-water interactions on montmorillonite surfaces. I. Ethanol*, Clays Clay Miner. 15 (1967) 259–271, https://doi.org/10.1346/CCMN.1967.0150131.
[9] S. Metz, R.L. Anderson, D.L. Geatches, J.L. Suter, R. Lines, H.C. Greenwell, Understanding the swelling behavior of modified nanoclay filler particles in water and ethanol, J. Phys. Chem. C 119 (22) (2015) 12625–12642, https://doi.org/10.1021/jp512257z.
[10] G.W. Brindley, S. Ray, Complexes of Ca-montmorillonite with primary monohydric alcohols (clay-organic studies – VIII), Am. Mineral. 49 (1964) 106–115.
[11] G.W. Brindley, K. Wiewiora, A. Wiewiora, Intracrystalline swelling of montmorillonite in some water-organic mixtures (clay-organic studies. XVII), Am. Mineral. 54 (1969) 1635–1644.
[12] O. Karnland, S. Olsson, U. Nilsson, Mineralogy and Sealing Properties of Various Bentonite and Smectite-rich Clay Materials, SKB Technical Report TR-06-30, 2006, pp. 1–1.
[13] M. Segad, B. Jönsson, B. Cabane, Tactoid formation in montmorillonite, J. Phys. Chem. C 116 (48) (2012) 25425–25433, https://doi.org/10.1021/jp3094929.
[14] P. Van Vaerenbergh, J. Léonardon, M. Sztucki, P. Boesecke, J. Gorini, L. Claustre, F. Sever, J. Morse, T. Narayanan, An upgrade beamline for combined wide, small and ultra small-angle X-ray scattering at the ESRF, AIP Conf. Proc. 1741 (1) (2016) 030034. https://doi.org/10.1063/1.4952857.
[15] M. Sztucki, SAXS Utilities Download Page, 2011. <http://www.sztucki.de/SAXSutilities> (accessed Mar 2017).
[16] M. Segad, S. Hanski, U. Olsson, J. Ruokolainen, T. Åkesson, B. Jönsson, Microstructural and swelling properties of Ca and Na montmorillonite: (in situ) observations with cryo-TEM and SAXS, J. Phys. Chem. C 116 (13) (2012) 7596–7601, https://doi.org/10.1021/jp300531y.
[17] M. Segad, Microstructure determination of IQ-WB clays: a direct procedure by small-angle X-ray scattering, J. Appl. Cryst. 46 (2013) 1316–1322, https://doi.org/10.1107/S0021889813020931.
[18] M. Birgersson, O. Karnland, U. Nilsson, Freezing of Bentonite. Experimental Studies and Theoretical Considerations, SKB Technical Report TR-10-40, 2010, pp. 1–1.
[19] A. Thuresson, M. Ullner, M. Turesson, Interaction and aggregation of charged platelets in electrolyte solutions: a coarse-graining approach, J. Phys. Chem. B 118 (2014) 7405–7413, https://doi.org/10.1021/ja01350a001.
[20] G. Åkerlöf, Dielectric constants of some organic solvent-water mixtures at various temperatures, J. Am. Chem. Soc. 54 (11) (1932) 4125–4139, https://doi.org/10.1021/jp502015g.
[21] M. Abraham, van der Spoel, E. Lindahl, B. Hess, The GROMACS Developer Team, GROMACS User Manual, version 5.0.4, 2014.
[22] A. Thuresson, M. Ullner, T. Åkesson, C. Labbez, B. Jönsson, Monte Carlo simulations of parallel charged platelets as an approach to tactoid formation in clay, Langmuir 29 (2013) 9216–9223, https://doi.org/10.1021/la401272u.
[23] J.L. Michot, I. Bihannic, K. Porsch, S. Maddi, C. Baravian, J. Mougel, P. Levitz, Phase diagrams of Wyoming Na-montmorillonite clay. Influence of particle anisotropy, Langmuir 20 (2004) 10829–10837, https://doi.org/10.1021/la0489108.
[24] G. Gutiérrez, B. Johansson, Molecular dynamics study of structural properties of amorphous $Al_2O_3$, Phys. Rev. B 65 (2002) 104202, https://doi.org/10.1103/PhysRevB.65.104202.
[25] M. Segad, B. Jönsson, T. Åkesson, B. Cabane, Ca/Na montmorillonite: structure, forces and swelling properties, Langmuir 26 (2010) 5782–5790, https://doi.org/10.1021/la9036293.
[26] A. Thuresson, O. Karnland, B. Jönsson, Anomalous temperature behavior in clay swelling due to ion-ion correlations, EPL 114 (2016) 38002, https://doi.org/10.1209/0295-5075/114/38002.
[27] R. Netz, Electrostatistics of counter-ions at and between planar charged walls: from Poisson-Boltzmann to the strong-coupling theory, Eur. Phys. J. E 5 (2001) 557, https://doi.org/10.1007/s101890170039.

# Paper III

Reprinted from *J. Colloid Interface Sci.*, 2020, **579**, 573–581
M. Jansson, D. Belić, J. Forsman and M. Skepö
©2020 with permission from Elsevier.

Journal of Colloid and Interface Science 579 (2020) 573–581

Contents lists available at ScienceDirect

Journal of Colloid and Interface Science

journal homepage: www.elsevier.com/locate/jcis

# Nanoplatelet interactions in the presence of multivalent ions: The effect of overcharging and stability

Maria Jansson [a,*], Domagoj Belić [b], Jan Forsman [a], Marie Skepö [a,c,*]

[a] Theoretical Chemistry, Lund University, P.O. Box 124, SE-221 00 Lund, Sweden
[b] Physical Chemistry, Lund University, P.O. Box 124, SE-221 00 Lund, Sweden
[c] LINXS – Lund Institute of Advanced Neutron and X-ray Science, Scheelevägen 19, SE-223 70 Lund, Sweden

## GRAPHICAL ABSTRACT

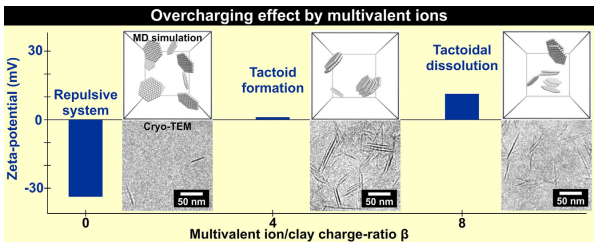


## ARTICLE INFO

*Article history:*
Received 7 May 2020
Revised 8 June 2020
Accepted 9 June 2020
Available online 19 June 2020

*Keywords:*
Overcharging
Stability
Nanoplatelet
Clay
Laponite®
Multivalent ions
Molecular dynamics simulations
Potential of mean force
Zeta-potential
Cryo-TEM

## ABSTRACT

*Hypothesis:* The stability of colloidal dispersions in the presence of multivalent ions depends strongly on the electrostatic interactions between the suspended particles. Of particular interest are colloidal particles having dimensions in the nanometric range and with an anisotropic shape due to its high surface area per unit mass, for example clay, which has the key characteristic of a negatively charged surface, surrounded by an oppositely charged rim.
*Experiments:* In this study, we investigate the interactions in nanoplatelet dispersions for the model system of Laponite® clay with addition of mono- and multivalent salt. Molecular dynamics simulations with enhanced umbrella sampling have been utilised in combination with the experimental techniques of zeta-potential measurements, dynamic light scattering, and transmission electron microscopy.
*Findings:* It was observed that tactoid formation and tactoidal dissolution due to overcharging occur upon the addition of trivalent salt. The overcharging effect was captured from calculated potential of mean force and confirmed from the zeta-potential, which changed sign from negative to positive when increasing the stoichiometric charge-ratio between the positive salt ions and the clay. Consequently, the gained information could provide useful physical insight of nanoplatelet interactions in the presence of multivalent ions.
© 2020 The Author(s). Published by Elsevier Inc. This is an open access article under the CC BY-NC-ND license (http://creativecommons.org/licenses/by-nc-nd/4.0/).

## 1. Introduction

There has been an enhanced interest in colloidal dispersions containing multivalent ions, primarily due to the importance of

* Corresponding authors at: Theoretical Chemistry, Lund University, P.O. Box 124, SE-221 00 Lund, Sweden (M. Skepö).
*E-mail addresses:* maria.jansson@teokem.lu.se (M. Jansson), marie.skepo@teokem.lu.se (M. Skepö).

https://doi.org/10.1016/j.jcis.2020.06.045
0021-9797/© 2020 The Author(s). Published by Elsevier Inc.
This is an open access article under the CC BY-NC-ND license (http://creativecommons.org/licenses/by-nc-nd/4.0/).

the electrostatic interactions for the colloidal stability, which is of importance for many technological and biological systems [1,2]. A colloidal dispersion in the presence of multivalent ions is more prone to be destabilised than in the presence of monovalent ions. Moreover, it has also been observed that the destabilisation is more evident at higher salt concentrations [3]. Another interesting phenomenon is the attractive electrostatic interaction between like-charged colloidal particles with multivalent ions [4,5]. When a charged colloidal particle is suspended in a liquid medium, the counterions adsorb on the surface, creating a layer with the opposite sign of the charge. Under certain conditions, the charge of the counterions within this layer can overcompensate the surface charge, where the overcharging effect implies that there is an excess of charges at the surface. This results in an effective reversed electrical field and is captured from the reversed sign of the electrophoretic mobility [6,7].

The properties of colloidal dispersions depend on the features of the suspended particles, in particular their shape, size, and charge. In addition, colloidal particles with dimensions in the nanometric range and with an anisotropic shape are of particular interest. These particles can spontaneously self-assemble in a liquid medium due to its high surface area per unit mass and specific surface functionality, thus, forming a wide range of microstructures [8]. In the literature, clay has been extensively studied due to the interest in exploiting its physical properties, which is one of the most prominent and widely available anisotropic nanoparticle system.

Clays are inorganic materials composed of fine-grained minerals, where the clay minerals belong to the family of phyllosilicates, or layered silicates. These can either be provided from natural sources or produced synthetically by combining the inorganic mineral sources of sodium silicate and the salts of sodium, magnesium, and lithium [9]. The most well known synthetic clay mineral is Laponite®, which is a trioctahedral smectite with a chemical composition similar to the natural clay mineral Hectorite. The Laponite® clay mineral is composed of a negatively charged surface, with a diameter of $\sim 25$ nm and a thickness of $\sim 1$ nm, and the ideal chemical formula is written as $Na_{0.7}(Si_8Mg_{5.5}Li_{0.3})O_{20}(OH)_4$ [9]. The anisotropic clay platelets can form a lamellar structure, which is normally not homogeneous, and is described as a disordered structure of stacks of platelets, also denoted tactoids [10]. The structure is seemingly a perfect model system for an electrical double layer, where the stability in saline solution depends strongly on the surface charge density of the platelets, as well as on the valency of the counterion and the salt ion [11]. The negative surface charge density is defined from the pH-dependent cationic exchange capacity (CEC), where several values have been reported for Laponite® depending on its grade, e.g. $\sim 0.5$ mEq/g [9], $\sim 0.65$ mEq/g [12], and $\sim 0.75$ mEq/g [13,14]. Moreover, the surface of the platelet is surrounded by a rim with exposed magnesium hydroxyl (MgOH) groups, where the rim can either possess a negative, a neutral, or a positive charge depending on the pH of the solution. The point of zero charge, i.e. where the rim charge is neutral, is at pH $\approx 11$, hence, the rim has a positive charge at lower pH and a negative charge at higher pH [15].

The advantages of synthetic clay minerals, and especially Laponite®, are that the clay platelets are monodisperse and have a high purity with a low content of transition metals and other impurities. In addition, Laponite® has the ability to improve the stability of a suspension by altering its rheological properties, and is thereby widely used as a rheology-modifier in many technological applications, such as in household and personal care products, in paints, and in surface coatings. The rich phase behaviour of Laponite®, and its diverse phase (state) diagram, which includes flocculants, isotropic liquids, isotropic gels, and nematic gels, have been extensively studied, e.g. see the comprehensive review articles by Ruzicka & Zacarelli (2011) [16] and Suman & Joshi (2018) [17], and the references therein. The different phases observed in the state diagram depend on the Laponite® concentration, the concentration of the ionic compounds, such as added salt, as well as on the time of gelling, i.e. aging. For an aqueous solution with a Laponite® concentration of $\leq 1$ wt%, the dispersion undergoes a sol/gel transition, i.e. a phase transition from a sol (clay-poor) phase to a gel (clay-rich) phase [18–20]. In addition, for a dispersion with a salt concentration of NaCl higher than 20 mM, phase separation occurs as flocculation and sedimentation [20,21].

In this study, we investigate the interactions between nanoplatelets and multivalent ions by using the model system of Laponite® clay with addition of mono- and multivalent salt. By utilising molecular dynamics (MD) simulations with enhanced umbrella sampling, we show the importance of the valency of the salt ion and the stoichiometric charge-ratio between the salt ions and Laponite® for the stability of the dispersion. The overcharging effect is captured from the free energy of interaction, i.e. the potential of mean force (PMF), between two parallel platelets. Moreover, the tactoid formation and the tactoidal dissolution are observed for the addition of trivalent salt by employing MD bulk simulations. The results obtained from the simulations are confirmed by the experimental techniques of zeta-potential ($\zeta$-potential) measurements, dynamic light scattering (DLS), transmission electron microscopy (TEM), and cryogenic TEM (cryo-TEM).

## 2. Experimental section

### 2.1. Materials and sample preparation

The clay used in this study was the synthetic sodium Laponite®-XLG XR (BYK Additives) with a CEC of $\sim 0.5$ mEq/g according to the technical information [9]. Analytical grade sodium chloride (NaCl, purity, 99.5%), calcium chloride ($CaCl_2$, purity, 99.5%), and lanthanum chloride ($LaCl_3$, purity, 99.0%) were purchased from MERCK. A stock solution of Laponite® was prepared by dispersing 0.2 g of clay in 10 g Milli-Q water, and after equilibration, the suspension was filtered through a 0.22 μm Millex-GV filter unit (MERCK). Thereafter, the Laponite® suspensions were mixed with stock solutions of the respective salt in varying concentrations, in order to obtain a Laponite® mass fraction of 1 wt%.

### 2.2. $\zeta$-potential measurements

For the $\zeta$-potential measurements, the samples were measured in disposable folded capillary cells at 25°C utilising a Malvern Zetasizer Nano ZS (Malvern Instruments). The method determines the velocity of a particle in a medium with an applied field by combining electrophoresis and laser doppler velocimetry techniques. From the electrophoretic mobility ($U_E$) of the particle, the $\zeta$-potential is obtained by applying the Henry equation [22]:

$$U_E = \frac{2\epsilon\zeta f(\kappa a)}{3\eta}. \quad (1)$$

Where $\epsilon$ is the dielectric constant, $\zeta$ is the $\zeta$-potential, and $\eta$ is the viscosity of the medium. Henry's function is defined as $f(\kappa a)$, where the thickness of the electrostatic double layer is $1/\kappa$ and the particle radius is $a$. $\kappa a \gg 1$ corresponds to the classical Smoluchowski limit for compact double layers, which was used for the measurements.

### 2.3. Dynamic light scattering

In order to evaluate the size distribution of the Laponite® dispersions with addition of trivalent salt, DLS measurements were

performed. The samples were measured in disposable cuvettes at 25°C, utilising a Malvern Zetasizer Nano ZS (Malvern Instruments) [22]. The instrument is equipped with a 4.0 mW He-Ne gas laser with a wavelength of 632.8 nm and a detector unit comprised with an Avanlanche Photo Diode with a backscatter detector angle of 173°. The DLS technique is based upon the principle that a liquid sample is illuminated by coherent light, where the phase of the detected scattered light from all of the particles either interfere constructive or destructive. The size of the particles is obtained from the random movements of the particles through the medium due to Brownian motion via the time correlation function. This is extracted from the intensity fluctuation, where the rate of decay for the time correlation function is related to the particle size.

### 2.4. Transmission electron microscopy

To obtain more information about how the tactoid formation and the tactoidal dissolution depend on the amount of added trivalent salt, the techniques of TEM and cryo-TEM were utilised, which were performed at the National Center for High-Resolution Electron Microscopy at Lund University. For the TEM measurements, 3 μL of freshly prepared sample suspension was pipetted onto a TEM grid (continuous formvar-carbon film on 200 mesh copper from Ted Pella, Redding, USA), gently blotted using a filter paper and let to air dry. The grid was mounted on a standard JEOL single tilt holder and imaged at room temperature on a JEOL JEM-2200FS (JEOL, Tokyo, Japan) TEM. For the cryo-TEM measurements, the grids (lacey formvar-carbon film on 200 mesh copper from Ted Pella, Redding, USA) were first glow discharged in a Quorum GloCube system (Quorum Technologies, Laughton, UK). Thereafter, 4 μL of sample suspension was pipetted onto the grid in a Leica EM GP automatic plunge freezer (Leica Microsystems, Stockholm, Sweden) operating at 21°C and relative humidity of >90%, backside blotted for 2.5 s and plunged into liquid ethane. The vitrified samples were stored in liquid nitrogen until used. For imaging, the samples were transferred onto a Fischione 2550 cryogenic sample holder and imaged on a JEOL JEM-2200FS (JEOL, Tokyo, Japan) TEM. The sample temperature was maintained below −175 °C during the cryo-TEM imaging. In both TEM and cryo-TEM, the microscope was operating at an accelerating voltage of 200 kV, utilising the omega energy filter for contrast enhancement. The zero-loss images were acquired on an F416.0 camera (TVIPS, Gauting, Germany) using SerialEM software [23]. Imaging was performed in low-dose mode, keeping the total electron dose per image below 50 e/Å$^2$ (5000 e/nm$^2$). The cryo-TEM images were acquired using the defocus values in the range $-3 \pm 1$ μ m. The acquired images were processed in ImageJ software [24].

## 3. Theoretical section

### 3.1. The coarse-grained model

In the simulation model, the clay platelet is represented as a finite hexagonal monolayer of connected coarse-grained spheres, called sites. The thickness and the diameter of the platelet are 1 and 11 nm, respectively, where the lateral dimensions are smaller in the model compared to the experiments, in order to reduce the computational cost. The unit charges were located at the centre of each site to obtain a homogeneous charge distribution. The total charge of the platelet was neutralised by monovalent counterions, and the stability of the suspensions was studied by addition of mono- and multivalent salt. The ions were added explicitly as freely moving charges with an excluded volume. The systems dimensionless stoichiometric charge-ratio ($\beta$) is defined as the absolute value of the number of positive mono- or multivalent salt ion charges, divided by the platelets total net negative charge, i.e.

$$\beta = \left| \frac{N_{\text{ion}} \cdot Z^{+}_{\text{ion}}}{N_{\text{p}} \cdot Z_{\text{p}}} \right|, \tag{2}$$

where $N_{\text{ion}}$ and $Z^{+}_{\text{ion}}$ are the number and the charge of the positive salt ions, and $N_{\text{p}}$ and $Z_{\text{p}}$ are the number and the charge of the platelet. The number of ions were varied in order to obtain $\beta = 0 - 8$, where $\beta = 0$ corresponds to a system with only monovalent counterions. The effect of the platelet charge was studied by varying the total net negative charge of the platelet, which was set to −45 e and −90 e, corresponding to a one-sided surface charge density of $\sigma \approx -0.5$ e/nm$^2$ and $\sigma \approx -1.0$ e/nm$^2$, respectively.

In the simulations, the solvent is treated as a dielectric continuum with a uniform dielectric constant of $\epsilon_r = 78.3$. The particles are interacting pairwise and the electrostatic pair potential is defined as:

$$u^{\text{EL}}_{ij}(r_{ij}) = \frac{e^2 z_i z_j}{4\pi\epsilon_0\epsilon_r r_{ij}}, \tag{3}$$

where $e$ is the elementary charge, $z_i$ is the valency of particle $i$, $\epsilon_0$ is the permittivity of vacuum, and $r_{ij}$ is the center-to-center distance between particles $i$ and $j$. In addition, particles interact through a strictly repulsive, truncated, and shifted Lennard-Jones (TLJ) potential, defined as:

$$u^{\text{TLJ}}_{ij}(r_{ij}) = \begin{cases} \epsilon_{\text{TLJ}} \left[ \left(\frac{\sigma_{ij}}{r_{ij}}\right)^{12} - 2\left(\frac{\sigma_{ij}}{r_{ij}}\right)^{6} + 1 \right], & \text{if } r_{ij} < \sigma_{ij} \\ 0, & \text{otherwise} \end{cases}. \tag{4}$$

$\epsilon_{\text{TLJ}}$ determines the strength of the short-ranged potential, which was set to 1 kT. $\sigma_{ij} = (\sigma_i + \sigma_j)/2$, where $\sigma_i$ is the diameter of species $i$, and in the model, $\sigma_{site} = 1.0$ nm and $\sigma_{ion} = 0.4$ nm. The total potential between all pairs is thus defined as:

$$u_{ij}(r_{ij}) = u^{\text{TLJ}}_{ij}(r_{ij}) + u^{\text{EL}}_{ij}(r_{ij}). \tag{5}$$

Furthermore, within the platelet, all the adjacent sites are connected by a harmonic bond-stretching potential:

$$u_b(r_{ij}) = \frac{1}{2} k^b (r_{ij} - b)^2, \tag{6}$$

where $k^b$ is the force constant and $b$ is the equilibrium bond length. The platelets flexibility was constrained by a harmonic angular potential between triplets of sites:

$$u(\theta_{ijk}) = \frac{1}{2} k^{\theta} (\theta_{ijk} - \theta^0)^2, \tag{7}$$

where $k^{\theta}$ is the force constant, $\theta^0 = \pi$, and $\theta_{ijk}$ is the bond angle between the triplet of sites $i$, $j$, and $k$.

### 3.2. Molecular dynamics simulations

MD simulations were performed with the software package GROMACS (version 2018.2) [25]. Newtons equation of motion for the freely moving species, i.e. the platelets, the counterions, and the salt ions, were integrated using a leap-frog algorithm. To account for the long-ranged electrostatic contribution, fast particle-mesh Ewald summation was utilised with a 6 nm real-space Coulomb cutoff and a Fourier spacing equal to 0.6 nm. For an in depth description of the input parameters, the reader is referred to the user manual [25].

The free energy of interaction between two platelets was extracted as PMF utilising the enhanced sampling method of umbrella sampling [26,27]. For these MD simulations, two parallel platelets were immersed in a rectangular box with the dimensions of 20 × 20 × 40 nm and three-dimensional periodic boundary conditions were implemented. The center-of-mass (COM) of the platelets was restrained to only move along the $z$-axis, located at the

center of the box, with a COM separation between the platelets of 1.2 nm. The restriction allows the platelets to rotate freely around the *z*-axis, hence the centre of gravity is on the *z*-axis. A schematic representation of the model is shown in Fig. 1.

Monovalent counterions as well as mono- or multivalent salt were added to the system, and equilibration was performed for 100 ns to ensure convergence, which was evaluated from the total energy of the system. To generate the starting configurations for the umbrella sampling, the parallel platelets were pulled apart along the *z*-axis using the *pull code* [25], with a spring constant of 1000 kJ/(mol · nm$^2$) and a pull rate of 1 nm/ns. The starting configurations were typically 0.1–0.2 nm apart for the total sampling interval of 1.2–11 nm. Each configuration was equilibrated for 1 ns, and then sampled for 10 ns. Finally, the PMF was extracted utilising the Weighted Histogram Analysis Method (WHAM) [28,29].

The bulk simulations were carried out to study the structural properties of the platelets with addition of trivalent salt. For these MD simulations, eight platelets with a surface charge density of $\sigma \approx -1.0$ e/nm$^2$ were placed in a cubic simulation box with three-dimensional periodic boundary conditions. The box length was 33 nm, corresponding to a volume fraction with respect to the platelets of 1% ($\phi_c \approx 0.01$). The simulations were sampled for at least 100 ns, and the equilibration was approximately 50 ns to ensure convergence, which was evaluated from the total energy of the system.

### 3.3. Structural analysis

The structural information obtained from the bulk simulations was analysed from the platelet-platelet structure factor, defined as:

$$S(q) = \left\langle \frac{1}{N} \sum_{i=1}^{N} \sum_{j=1}^{N} \frac{\sin(qr_{ij})}{qr_{ij}} \right\rangle, \tag{8}$$

where $N$ is the total number of platelet sites in the system. Assuming an isotropic scattering, the equation above can be rewritten as:

$$S(q) = 1 + 4\pi \frac{N}{V} \int_0^\infty (g(r) - 1) r^2 \frac{\sin(qr)}{qr} dr, \tag{9}$$

where $g(r)$ is the radial distribution function between all the platelet sites in the system and $V$ is the total volume of the simulation box. At large separations, if $g(r)$ is not approaching one due to the finite box length, a window function can be used to reduce the artefacts:

$$S_w(q) = 1 + 4\pi \frac{N}{V} \int_0^\infty (g(r) - 1) r^2 \frac{\sin(qr)}{qr} \frac{\sin(\pi r/R_c)}{\pi r/R_c} dr, \tag{10}$$

where $R_c$ is the maximum distance in $g(r)$. [30]

## 4. Results and discussion

### 4.1. Experimental characterisation of the systems

The measured ζ-potentials of the Laponite® dispersions with addition of mono- and multivalent salt are presented in Fig. 2a. For the dispersion without addition of salt, i.e. $\beta = 0$, the ζ-potential was ∼ −34 mV, confirming that the surface charge density of the clay platelet is negative. This value is, however, less negative than other ζ-potentials reported in the literature, e.g. ∼ −40 to −45 mM [31], ∼ −45 mV [14], ∼ −52 mV [32,33], and ∼ −58 mV [13]. The discrepancy is reasonable since the ζ-potential is correlated with the CEC of Laponite®, which is dependent on the Laponite® grade. In previous studies, the CEC was reported to be ∼ 0.75 mEq/g for the general purpose grade Laponite®-RD, while in this study the personal care grade Laponite®-XLG with a CEC of ∼ 0.5 mEq/g was used. With addition of salt, it is observed that the ζ-potential both depends on $\beta$ as well as on the valency of the salt ion. By increasing $\beta$ or the valency, the ζ-potential increases for the trivalent salt of $LaCl_3$ and a transition from a negative to a positive ζ-potential is found at $\beta = 4$, whereas for the mono- and divalent salt, i.e. NaCl and $CaCl_2$, the ζ-potential remained negative regardless the value of $\beta$. Hence, this indicates that the system with trivalent salt becomes overcharged.

In order to further investigate the overcharging effect observed for the Laponite® dispersions with addition of the trivalent salt $LaCl_3$, the size distribution was measured with DLS (Fig. 2b). For these measurements it was necessary to reduce the concentration of the dispersion with a factor of 100 due to the sensitivity of the instrument, since the scattered intensity is related to the number of particles. However, $\beta$ remained constant, and thus, qualitative information can still be derived. For the Laponite® dispersion without addition of salt, the obtained mean radius was ∼24 nm, which is almost twice the expected radius. Further, it was found that the mean radius increases with $\beta$ until a maximum is found at $\beta = 4$, indicating that tactoids are formed. This is in correlation with the ζ-potential, which is approximately zero at $\beta = 4$, thus the overall charge of the complex is zero and the maximum size of the tactoids is found when the trivalent salt fully neutralises the net negative charge of the clay platelets. Then, at $\beta > 4$, the mean radius decreases until a plateau is reached at $\beta \approx 6$ to approximately 300–400 nm, suggesting that the process of tactoidal dissolution occurs in the system.

The tactoid formation observed in the Laponite® dispersions was also studied with TEM. Since the Laponite® dispersion of 1 wt% are rather dense, the concentrations was reduced with a

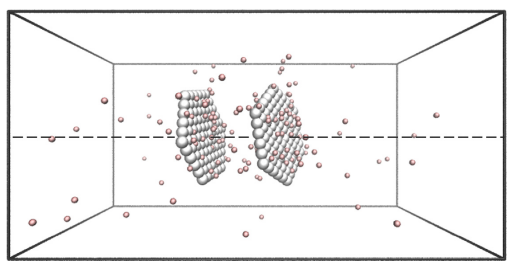

**Fig. 1.** Schematic representation of the coarse-grained model for the system with two parallel platelets (grey), each with a total charge of $Z_p = -90$ e, corresponding to a one-sided surface charge density of $\sigma \approx -1.0$ e/nm$^2$. The platelets are neutralised with monovalent counterions (red spheres), and the center-of-mass of the platelets is restrained to only move along the *z*-axis (dashed line). (For interpretation of the references to colour in this figure legend, the reader is referred to the web version of this article.)

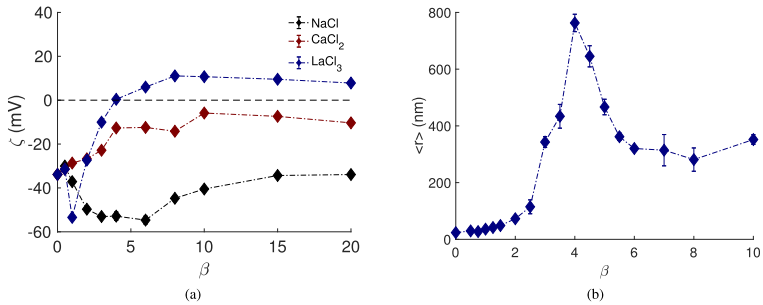


**Fig. 2.** (a) The ζ-potential for Laponite® dispersions (1 wt%) with addition of salt as a function of the stoichiometric charge-ratio ($\beta$). (b) The mean size of the particles for the Laponite® dispersions (0.01 wt%) with addition of trivalent salt, represented as the mean radius (<r>), as a function of $\beta$. Error bars are included, and for some data points they are smaller than the symbol size. The dash-dotted lines are a guide for the eye.

factor of 100. In this technique, the contrast of the platelets depends strongly on their orientation with respect to the electron beam. The diffraction contrast is strong when the basal plane of the platelets is oriented parallel to the beam, where the platelets appear as sharp dark lines (or "filaments") in the TEM image. In addition, Fresnel fringes may appear on both sides of the diffracting platelets, which are more or less pronounced depending on the defocus of the objective lens, and can artificially increase the value of the platelet thickness [34]. For the platelets where the basal plane is not parallel to the electron beam, the diffraction contrast is much weaker due to the small thickness of $\sim 1$ nm, hence, it was difficult to clearly determine the size. From the TEM measurements it was observed that the formation of tactoids was promoted by the addition of trivalent salt. To gain further insight about the structural properties, cryo-TEM was used, where the samples are vitrified to preserve the original microstructures. The TEM images are shown in Fig. S1 in the Supplementary Materials and the cryo-TEM images are shown in Fig. 3. For the sample without addition of trivalent salt ($\beta = 0$), the platelets are well separated and no aggregates are observed. This confirms that the system is dominated by repulsive interactions and consists mainly of single platelets. With addition of trivalent salt, the distance between the platelets decreases, and more platelets are found in close vicinity to each other. The number of platelets oriented parallel to the beam increases to $\beta = 4$, indicating that the tactoids grow in size. Thereafter, at $\beta = 8$, there are less platelets oriented parallel to the beam, which imply that tactoidal dissolution occurs in the system. In addition, for the slightly darker areas observed in the image, our hypothesis is that this might depend on that the sample contains aggregates of less ordered clay platelets.

In addition, quantitative analyses were performed for the Laponite® dispersion at $\beta = 2$. Only the platelets whose normal are perpendicular to the electron beam were taking into account. The thickness of the platelets was estimated to $1.2 \pm 0.1$ nm, in agreement with the reported thickness of Laponite®. The mean cross-sectional length was $15 \pm 6$ nm, obtained from the size distribution analysis (Fig. S2). This result indicates that the typical size of the platelets in our samples was slightly smaller than the expected diameter. Moreover, two preferential average inter-layer distances, or $d$-spacings, between the platelets were found (Fig. S3): the more prominent $d$-spacing is at $2.2 \pm 0.2$ nm and the other weaker $d$-spacing is at $1.3 \pm 0.1$ nm. The former corresponds to the average inter-layer distance composed of four water layers and is in agreement with the average separation between Laponite® platelets in the presence of the trivalent salt lanthanum chloride measured with small angle X-ray scattering [35], whereas the latter may suggest that there is a monolayer of water between the platelets, which has been observed for dry Laponite® films exposed to the relative humidity in the atmosphere [36]. Hence, this implies that the Laponite® platelets can adopt two different states with respect to the number of water layers between the platelets. Furthermore, the $d$-spacing distribution was calculated for the Laponite® dispersion at $\beta = 4$ and 8 (Fig. S3). The same inter-layer distances were found as for $\beta = 2$, however, the occurrence of the $d$-spacing at $1.3 \pm 0.1$ nm decreased slightly with an increase in $\beta$.

### 4.2. Characterisation by computer simulations

#### 4.2.1. Free energy between parallel platelets

The free energy of interaction, thus the PMF, between two parallel platelets including counterions and addition of mono- and multivalent salt has been calculated utilising the coarse-grained model and MD simulations with enhanced umbrella sampling (Figs. S4 and S5). In the simulations, the addition of salt gives rise to a Debye screening length $\kappa$, where $\beta$ correlates to a specific value of $\kappa$. These values differs slightly between the valency of the salt, however, they are in the same regime of $\kappa \approx 0.6 - 3.1$ nm for $\beta = 0.5 - 8$ (Table S1).

In order to evaluate how the interaction free energy depends on the valency of the salt ion, $\beta$, and the surface charge density, the PMF has been extracted at a certain separation between the platelets in Fig. 4. The separation was chosen at the location of the minima found for the trivalent salt, except for the system with $\sigma \approx -1.0$ e/nm$^2$ and monovalent salt, where the separation was chosen from the nearest possible separation between the platelets at 1.7 nm. However, the trends between the different salts can still be captured from a electrostatic point of view. It is observed that the PMF decreases with an increase in the valency of the salt ion due to the enhanced attractive electrostatic interactions within the system. For the salt-free case, i.e. with only monovalent counterions, as well as for the addition of mono- and divalent salt, the PMF is positive, confirming that the systems are dominated by repulsive interactions. It is observed that the PMF decreases with $\beta$ for the monovalent salt, while for the divalent salt, the PMF decreases up to $\beta = 1$, after which a plateau value is reached. Furthermore, the PMF between the parallel platelets with a surface charge density of $\sigma \approx -1.0$ e/nm$^2$ and addition of trivalent salt is negative for $\beta \geqslant 1$, indicating that the long-ranged repulsion is screened. Global minima are found at the short distance of $\sim 1.4$ nm, suggesting that formation of small aggregates or tactoids

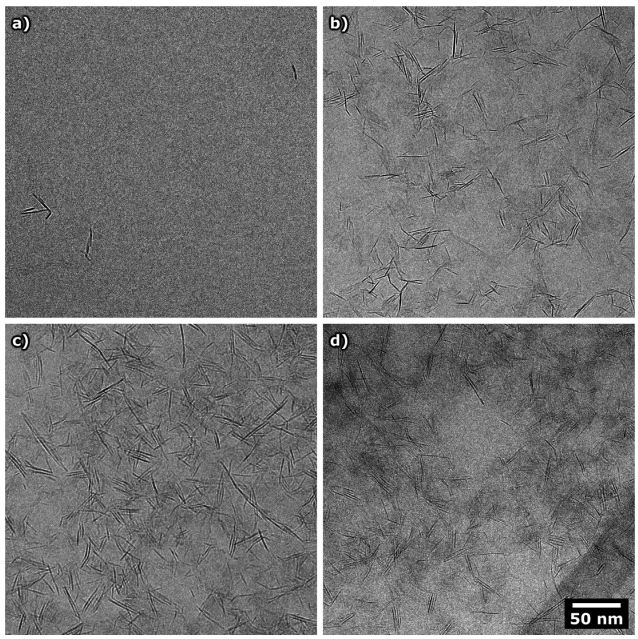


**Fig. 3.** Representative cryo-TEM images for the Laponite® dispersions (0.01 wt%) with addition of trivalent salt at the stoichiometric charge-ratio of (a) 0, (b) 2, (c) 4, and (d) 8. The scale bar applies to all images.

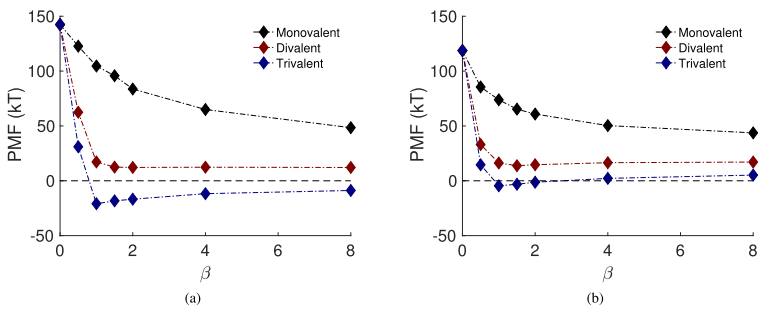


**Fig. 4.** The potential of mean force (PMF) at the separation of $1.5 \pm 0.2$ nm between two parallel platelets with (a) $\sigma \approx -1.0$ e/nm$^2$ and (b) $\sigma \approx -0.5$ e/nm$^2$ as a function of the stoichiometric charge-ratio ($\beta$). The dash-dotted lines are a guide for the eye.

occur in the system due to enhanced ion-ion correlation forces. The deepest minimum is at $\beta = 1$ with the magnitude of $-20.9$ kT, and thereafter, the free energy minima decreases in magnitude (Table S2). By decreasing the surface charge density of the platelets to $\sigma \approx -0.5$ e/nm$^2$, a non-monotonic transition in the PMF is obtained for the addition of trivalent salt. It is positive for $\beta < 1$, negative for $1 \leqslant \beta \leq 2$, and then positive again for $\beta > 2$. This trend indicates that overcharging is present in the system, where the interactions within the system are repulsive, attractive, and then repulsive again. Hence, for $1 \leqslant \beta \leq 2$, the long-ranged repulsion is screened and the global free energy minima are located at $\sim 1.5$ nm, where the deepest minimum is found at $\beta = 1$ with the magnitude of $-4.6$ kT. The magnitudes of the global minima are lower than for the platelets with $\sigma \approx -1.0$ e/nm$^2$ (Table S2).

*4.2.2. Structural properties from bulk simulations*

The structural properties of the platelets with trivalent salt were studied from the bulk MD simulations via the calculated

platelet-platelet structure factors $S_w(q)$, presented as Kratky plots in Fig. 5a. Bragg peaks are observed in the high-$q$ region for $\beta = 4$ and 8, where the former has the highest intensity. The periodicity between the platelets is correlated to the intensity, and thus, implies that the most well ordered structure is obtained at $\beta = 4$. This is confirmed from the low-$q$ region, where the high intensity peak of $\beta = 4$ indicates that the formed complex possess the most compact shape. From the Bragg peak, the average distance, i.e. the $d$-spacing, between the mid-plane of two adjacent platelets was $d_{\text{Bragg}} = 1.4$ nm for $\beta = 4$ and 8, determined from the relation: $d_{\text{Bragg}} = 2\pi/q_{\text{max}}$, where $q_{\text{max}}$ is the position of the maximum intensity of the Bragg peak. In addition, the $g(r)$ with respect to the platelets COM are presented in Fig. 5b. Here, the peak is consistent with a structure of two platelets in a face-to-face configuration at $\sim 1.5$ nm, where the probability of finding that configuration is related to the height of the peak. It is observed that the height increases to $\beta = 4$, after which it decreases, implying that the most pronounced attractive interactions are found in the system with $\beta = 4$. To further validate this, representative configurations from the simulations were extracted (Fig. 5c–f). It is observed that for $\beta = 0$, only single platelets are present, hence, the system is dominated by repulsive interactions. Then, at $\beta = 4$, the platelets have aggregated into small tactoids, and at $\beta = 8$, the tactoids are dissolved into smaller complexes. It should be mentioned that the size of the complexes changes throughout the simulations, however on average, the largest complexes are obtained at $\beta = 4$, confirming that this system possess the strongest attractive electrostatic interactions. Finally, at $\beta = 12$, there is almost only single platelets, which confirms that the overcharging effect is present in the system.

## 5. Conclusion

The stability of Laponite® dispersions with addition of mono- and multivalent salt was studied as a function of $\beta$. It was found that the formation of tactoids was promoted by the addition of trivalent salt, while for mono- and divalent salt, the systems were dominated by repulsive interactions. The tactoid formation results from the enhanced attractive ion-ion correlation forces with the increase in valency of the positive salt ions. Further, tactoidal dissolution was observed for a large excess of salt, i.e. $\beta > 4$, due to the overcharging effect, confirmed from the $\zeta$-potential measurements, which changed sign from negative to positive at $\beta = 4$. Moreover, the tactoid formation was studied with TEM and cryo-TEM, where quantitative analyses were obtained from the cryo-TEM imaging. The thickness and the mean cross-sectional length of the platelets were estimated to $1.2 \pm 0.1$ and $15 \pm 6$ nm, respectively. Two preferential average inter-layer distances, or $d$-spacings, between the platelets were found: the more prominent at $2.2 \pm 0.2$ nm and another weaker at $1.3 \pm 0.1$ nm. Furthermore, the overcharging effect was captured from MD simulations with enhanced umbrella sampling, where a transition from a positive to a negative PMF was obtained. Global minima were found, where the deepest minimum was obtained for $\beta = 1$, suggesting the formation of small aggregates or tactoids. This was confirmed from the structural analyses from the bulk simulations, where tactoid formation followed by tactoidal dissolution was observed.

The information gained from our study provides evidence of the existence of attractive ion-ion correlation forces between like-charged nanoplatelets in the presence of multivalent ions in aqueous solutions. This is in correlation with a previous study of the

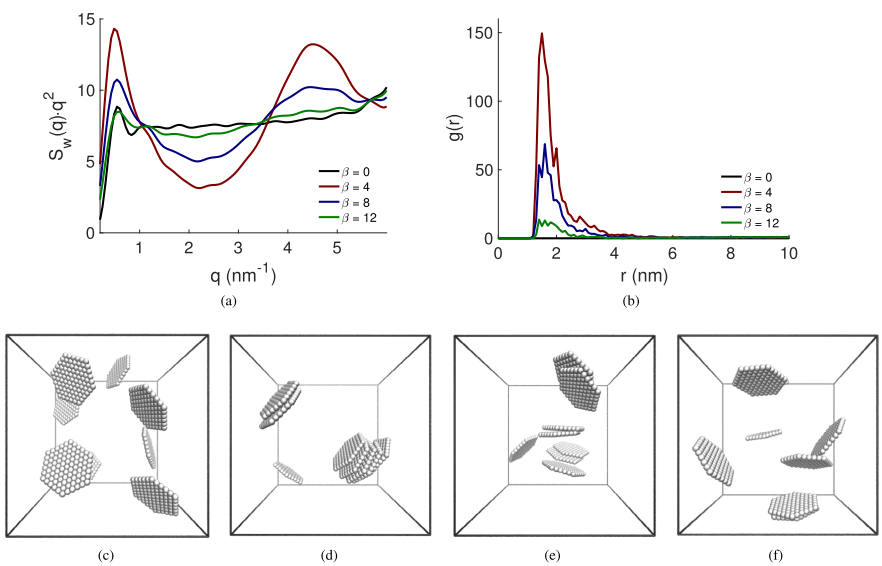


**Fig. 5.** (a) The platelet-platelet structure factors presented as Kratky plots ($S_w(q) \cdot q^2$) and (b) the radial distribution functions ($g(r)$) for the addition of trivalent salt. (c)–(f) Representative configurations at the stoichiometric charge-ratio ($\beta$) of (c) 0, (d) 4, (e) 8, and (f) 12. The counterions and the salt ions are omitted for clarity, and the platelets are shown in grey.

mean force between two like-charged spherical particles with addition of trivalent salt by D. G. Angelescu & P. Linse (2003) [37]. They showed that the stability of the colloidal dispersions went through three stages with an increase in trivalent salt: (i) a stable dispersion; (ii) a two-phase region; and (iii) a redissolution. The trend was also observed when changing the counterion valency from monovalent to divalent and finally to trivalent [37,38]. In addition, these phenomena were studied for latex particles with addition of the branched spherical polyelectrolyte dendrimer, considered as a highly charged multivalent species, where the same effects were observed [39–41]. Hence, with our model and the experimental techniques used, we can extend the knowledge over the attractive forces found in colloidal dispersions for spherical particles in the presence of multivalent ions to anisotropic particles with respect to shape and charge such as nanoplatelets as well.

## CRediT authorship contribution statement

**Maria Jansson:** Conceptualization, Methodology, Validation, Formal analysis, Investigation, Visualization, Writing - original draft, Writing - review & editing. **Domagoj Belić:** Methodology, Validation, Formal analysis, Investigation, Writing - review & editing, Visualization. **Jan Forsman:** Conceptualization, Validation, Writing - original draft, Writing - review & editing, Supervision. **Marie Skepö:** Conceptualization, Validation, Resources, Data curation, Writing - original draft, Writing - review & editing, Supervision, Project administration, Funding acquisition.

## Declaration of Competing Interest

The authors declare that they have no known competing financial interests or personal relationships that could have appeared to influence the work reported in this paper.

## Acknowledgements

TEM and cryo-TEM imaging were performed at the National Center for High Resolution Electron Microscopy (nCHREM) at Lund University. Computational resources were provided by the Swedish National Infrastructure for Computing (SNIC) through Lunarc, the Center for Scientific and Technical Computing at Lund University. The work was performed within the framework of the Swedish national strategic e-science research program eSSENCE. M.J. acknowledges the Royal Physiographic Society of Lund, Sweden, for financial support. D.B. acknowledges the financial support from the Crafoord Foundation.

## Appendix A. Supplementary data

Supplementary data associated with this article can be found, in the online version, at https://doi.org/10.1016/j.jcis.2020.06.045.

## References

[1] M. Quesada-Pérez, A. Martín-Molina, R. Hidalgo-Álvarez, Simulation of electric double layers undergoing charge inversion: mixtures of mono- and multivalent ions, Langmuir 21 (2005) 9231–9237, https://doi.org/10.1021/la0505925.
[2] P. Sinha, I. Szilagyi, F.J. Montes Ruiz-Cabello, P. Maroni, M. Borkovec, Attractive forces between charged colloidal particles induced by multivalent ions revealed by confronting aggregation and direct force measurements, J. Phys. Chem. Lett. 4 (2013) 648–652, https://doi.org/10.1021/jz4000609.
[3] T. Oncsik, G. Trefalt, Z. Csendes, I. Szilagyi, M. Borkovec, Aggregation of negatively charged colloidal particles in the presence of multivalent cations, Langmuir 30 (2014) 733–741, https://doi.org/10.1021/la4046644.
[4] T. Terao, T. Nakayama, Charge inversion of colloidal particles in an aqueous solution: screening by multivalent ions, Phys. Rev. E 63 (2001), https://doi.org/10.1103/PhysRevE.63.041401 041401.
[5] A. Delville, Influence of multivalent electrolytes on interionic correlations: a grand canonical monte carlo study of the electrostatic stability of charged interfaces, J. Phys. Chem. B 106 (2002) 7860–7868, https://doi.org/10.1021/jp020600f.
[6] F. Jiménez-Ángeles, M. Lozada-Cassou, A model macroion solution next to a charged wall: Overcharging, charge reversal, and charge inversion by macroions, J. Phys. Chem. B 108 (2004) 7286–7296, https://doi.org/10.1021/jp036464b.
[7] K. Besteman, M.A.G. Zevenbergen, H.A. Heering, S.G. Lemay, Direct observation of charge inversion by multivalent ions as a universal electrostatic phenomenon, Phys. Rev. Lett. 93 (2004), https://doi.org/10.1103/PhysRevLett.93.170802 170802.
[8] J.N. Israelachvili, Intermolecular and Surface Forces, 3rd Edition,., Academic Press, London, 2011. 10.1016/C2009-0-21560-1.
[9] BYK, Technical Information B-RI 21, LAPONITE Performance Additives..
[10] A. Meunier, Clays, first ed., Springer-Verlag, 2005, https://doi.org/10.1007/b138672.
[11] B. Jönsson, H. Wennerström, When ion-ion correlations are important in charged colloidal systems, in: Electrostatic Effects in Soft Matter and Biophysics, Springer, Netherlands, Dordrecht, 2001, pp. 171–204, https://doi.org/10.1007/978-94-010-0577-7_7.
[12] D.W. Thompson, J.T. Butterworth, The nature of Laponite and its aqueous dispersions, J. Colloid Interface Sci. 151 (1) (1992) 236–243, https://doi.org/10.1016/0021-9797(92)90254-J.
[13] S. Zhang, Q. Lan, Q. Liu, J. Xu, D. Sun, Aqueous foams stabilized by Laponite and CTAB, Colloids Surf. A 317 (2008) 406–413, https://doi.org/10.1016/j.colsurfa.2007.11.010.
[14] M. Manilo, N. Lebovka, S. Barany, Characterization of the electric double layers of multi-walled carbon nanotubes, Laponite and nanotube + Laponite hybrids in aqueous suspensions, Colloids Surf. A 462 (2014) 211–216, https://doi.org/10.1016/j.colsurfa.2014.09.006.
[15] S.L. Tawari, D.L. Koch, C. Cohen, Electrical double-layer effects on the brownian diffusivity and aggregation rate of Laponite clay particles, J. Colloid Interface Sci. 240 (2001) 54–66, https://doi.org/10.1006/jcis.2001.7646.
[16] B. Ruzicka, E. Zaccarelli, A fresh look at the Laponite phase diagram, Soft Matter 7 (2011) 1268–1286, https://doi.org/10.1039/c0sm00590h.
[17] K. Suman, Y.M. Joshi, Microstructure and soft glassy dynamics of an aqueous Laponite dispersion, Langmuir 34 (2018) 13079–13103, https://doi.org/10.1021/acs.langmuir.8b01830.
[18] A. Mourchid, A. Delville, J. Lambard, E. Lécolier, P. Levitz, Phase diagram of colloidal dispersions of anisotropic charged particles: Equilibrium properties, structure, and rheology of Laponite suspensions, Langmuir 11 (1995) 1942–1950.
[19] H. Tanaka, J. Meunier, D. Bonn, Nonergodic states of charged colloidal suspensions: Repulsive and attractive glasses and gels, Phys. Rev. E 69 (2004) 031404.
[20] P. Mongondry, J.F. Tassin, T. Nicolai, Revised state diagram of Laponite dispersions, J. Colloid Interface Sci. 283 (2005) 397–405.
[21] A. Mourchid, E. Lécolier, H. van Damme, P. Levitz, On viscoelastic, birefringent, and swelling properties of Laponite clay suspension: Revisited phase diagram, Langmuir 14 (1998) 4718–4723.
[22] Zetasizer Nano Series, User manual, Malvern Instruments Ltd. MAN 0317, 2012, 1.1..
[23] D.N. Mastronarde, Automated electron microscope tomography using robust prediction of specimen movements, J. Struct. Biol. 152 (2005) 36–51, https://doi.org/10.1016/j.jsb.2005.07.007.
[24] C.A. Schneider, W.S. Rasband, K.W. Eliceiri, NIH Image to ImageJ: 25 years of image analysis, Nat. Methods 9 (2012) 671–675, https://doi.org/10.1038/nmeth.2089.
[25] M.J. Abraham, D. van der Spoel, E. Lindahl, B. Hess, The GROMACS development team, GROMACS User Manual version 2018.2, www.gromacs.org, 2018..
[26] G. Torrie, J. Valleau, Nonphysical sampling distributions in Monte Carlo free-energy estimation: umbrella sampling, J. Comput. Phys. 23 (1977) 187–199, https://doi.org/10.1016/0021-9991(77)90121-8.
[27] Y.I. Yang, Q. Shao, J. Zhang, L. Yang, Y.Q. Gao, Enhanced sampling in molecular dynamics, J. Chem. Phys. 151 (2019), https://doi.org/10.1063/1.5109531 070902.
[28] S. Kumar, J.M. Rosenberg, D. Bouzida, R.H. Swendsen, P.A. Kollman, THE weighted histogram analysis method for free-energy calculations on biomolecules. I. The method, J. Comput. Chem. 13 (1992) 1011–1021, https://doi.org/10.1002/jcc.540130812.
[29] J.S. Hub, B.L. de Groot, D. van der Spoel, g_wham–A free weighted histogram analysis implementation including robust error and autocorrelation estimates, J. Chem. Theory Comput. 6 (2010) 3713–3720, https://doi.org/10.1021/ct100494z.
[30] G. Gutiérrez, B. Johansson, Molecular dynamics study of structural properties of amorphous $Al_2O_3$, Phys. Rev. B 65 (2002), https://doi.org/10.1103/PhysRevB.65.104202 104202.
[31] A.Y. Huang, J.C. Berg, High-salt stabilization of Laponite clay particles, J. Colloid Interface Sci. 296 (2006) 159–164, https://doi.org/10.1016/j.jcis.2005.08.068.
[32] J. Labanda, J. Llorens, Influence of sodium polyacrylate on the rheology of aqueous Laponite dispersions, J. Colloid Interface Sci. 289 (2005) 86–93, https://doi.org/10.1016/j.jcis.2005.03.055.

[33] J. Labanda, J. Sabaté, J. Llorens, Rheology changes of Laponite aqueous dispersions due to the addition of sodium polyacrylates of different molecular weights, Colloids Surf. A 301 (2007) 8–15, https://doi.org/10.1016/j.colsurfa.2007.01.011.
[34] N.N. Herrera, J.-M. Letoffe, J.-L. Putaux, L. David, E. Bourgeat-Lami, Aqueous dispersions of silane-functionalized Laponite clay platelets. A first step toward the elaboration of water-based polymer/clay nanocomposites, Langmuir 20 (2004) 1564–1571, https://doi.org/10.1021/la0349267.
[35] A. Thuresson, M. Segad, T.S. Plivelic, M. Skepö, Flocculated Laponite-PEG/PEO dispersions with multivalent salt: a SAXS, cryo-TEM, and computer simulation study, J. Phys. Chem. C 121 (2017) 7387–7396, https://doi.org/10.1021/acs.jpcc.7b01715.
[36] M.M. Doeff, J.S. Reed, Li ion conductors based on laponite/poly(ethylene oxide) composites, Solid State Ionics 113–115 (1998) 109–115, https://doi.org/10.1016/S0167-2738(98)00367-1.
[37] D.G. Angelescu, P. Linse, Monte carlo simulation of the mean force between two like-charged macroions with simple 1:3 salt added, J. Phys. Chem. C 19 (2003) 9661–9668, https://doi.org/10.1021/la030153a.
[38] P. Linse, V. Lobaskin, Electrostatic attraction and phase separation in solutions of like-charged colloidal particles, J. Phys. Chem. C 112 (2000) 3917–3927, https://doi.org/10.1063/1.480943.
[39] W. Lin, P. Galletto, M. Borkovec, Charging and aggregation of latex particles by oppositely charged dendrimers, Langmuir 20 (2004) 7465–7473, https://doi.org/10.1021/la049006i.
[40] M. Trulsson, J. Forsman, T. Åkesson, B. Jönsson, Simulations of latex particles immersed in dendrimer solutions, Langmuir 25 (2009) 6106–6112, https://doi.org/10.1021/la900102r.
[41] I. Popa, M. Trulsson, G. Papastavrou, M. Borkovec, B. Jönsson, Simulations of latex particles immersed in dendrimer solutions, Langmuir 25 (2009) 12435–12438, https://doi.org/10.1021/la902617x.

# Supplementary Materials. Nanoplatelet Interactions in the Presence of Multivalent Ions: The Effect of Overcharging and Stability

Maria Jansson[a,*], Domagoj Belić[b], Jan Forsman[a] and Marie Skepö[a,c,*]

[a]Theoretical Chemistry, Lund University, P.O. Box 124, SE-221 00, Lund, Sweden
[b]Physical Chemistry, Lund University, P.O. Box 124, SE-221 00 Lund, Sweden
[c]LINXS - Lund Institute of Advanced Neutron and X-ray Science, Scheelevägen 19, SE-223 70, Lund, Sweden

## 1. Transmission electron microscopy (TEM)

Representative TEM images for the Laponite® dispersions with addition of trivalent salt are shown in Figure S1.

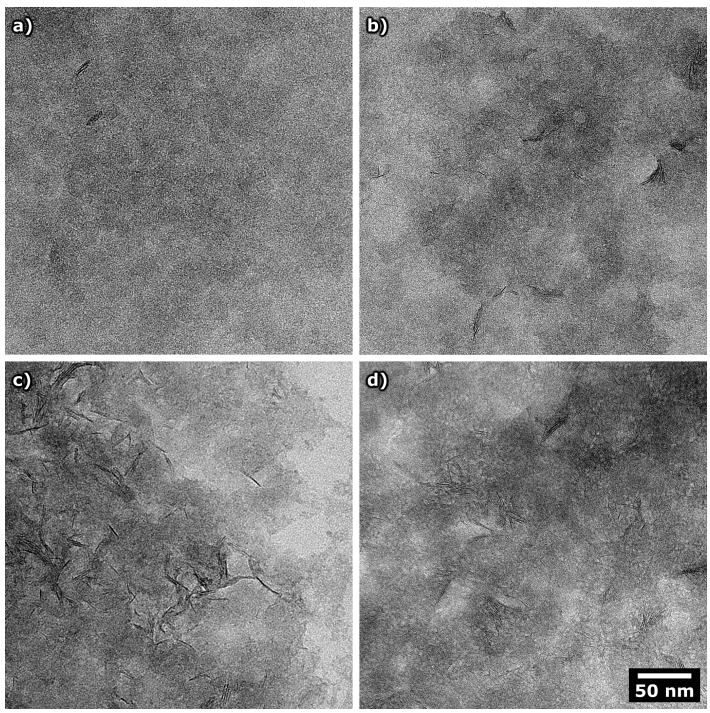


Figure S1: Representative TEM images for the Laponite® dispersions (0.01 wt%) with addition of trivalent salt at the stoichiometric charge-ratio of (a) 0, (b) 2, (c) 4, and (d) 8. The scale bar applies to all images.

*Corresponding author
maria.jansson@teokem.lu.se (M. Jansson); marie.skepo@teokem.lu.se (M. Skepö)
ORCID(s): 0000-0001-5316-4672 (M. Jansson); 0000-0002-8639-9993 (M. Skepö)

## 2. Quantitative analyses from cryo-TEM

Based on the acquired cryo-TEM images, the mean cross-sectional length was estimated from the size distribution analysis for the Laponite® dispersion at the stoichiometric charge-ratio of two shown in Figure S2. Furthermore, the inter-layer distance, or $d$-spacing, between parallel platelets was obtained from the spacing distributions (Figure S3) with a histogram bin size of 0.5 nm, where a bimodal distribution was found for the histogram bin size of 0.2 nm.

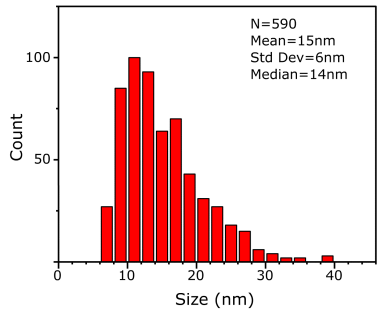


Figure S2: The size distribution, obtained from analysis of cryo-TEM images, of the platelets cross-sectional length for the Laponite® dispersion at the stoichiometric charge-ratio of two.

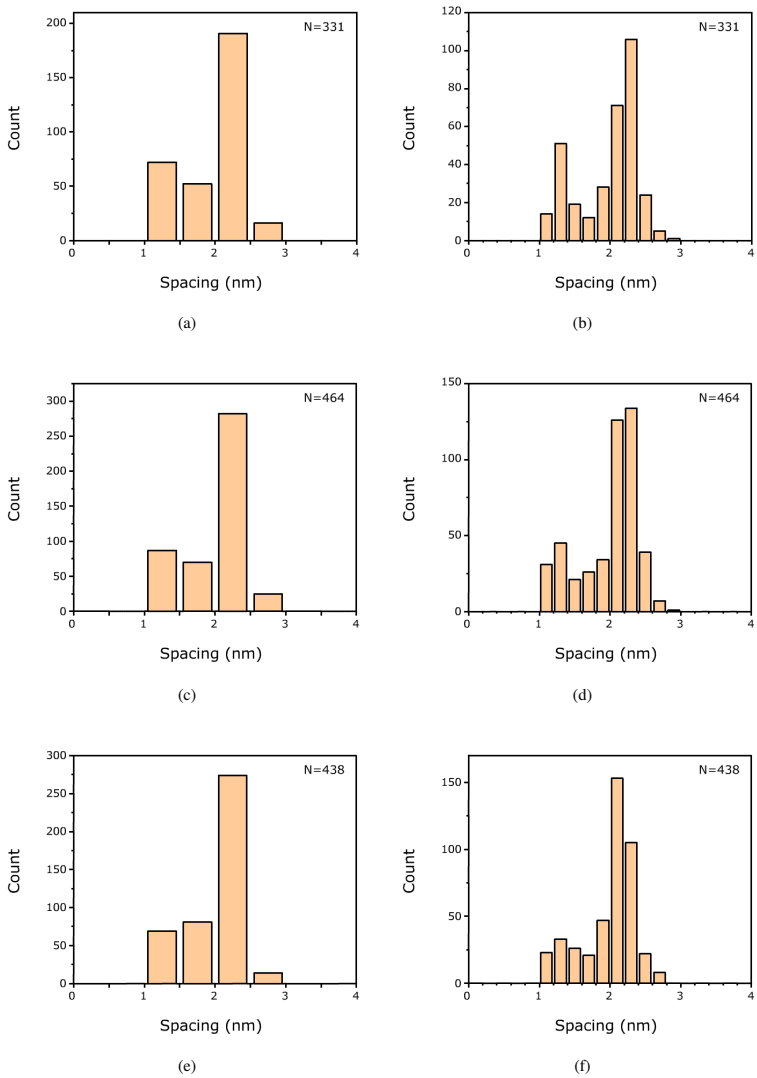


Figure S3: The spacing distributions, obtained from analysis of cryo-TEM images, with a histogram bin size of (a, c, e) 0.5 nm and (b, d, f) 0.2 nm for the Laponite® dispersion at the stoichiometric charge-ratio of (a, b) 2, (c, d) 4, and (e, f) 8.

## 3. Characterisation by Computer Simulations

### 3.1. Free energy between parallel platelets

The free energy of interaction between two parallel platelets with a surface charge density of $\sigma \approx$ -1.0 and -0.5 e/nm$^2$ for the addition of mono-, di-, and trivalent salt is shown as the potential of mean force (PMF) in Figures S4 and S5, respectively. The stoichiometric charge-ratio $\beta$, its corresponding Debye screening length $\kappa$, and the PMF at the separation of 1.5 $\pm$ 0.2 nm are shown in Table S1 for the platelets with $\sigma \approx$ -1.0 e/nm$^2$. Moreover, the PMF between the parallel platelets with $\sigma \approx$ -1.0 and -0.5 e/nm$^2$ at the separation of 1.5 $\pm$ 0.2 nm for the addition of trivalent salt is displayed in Table S2.

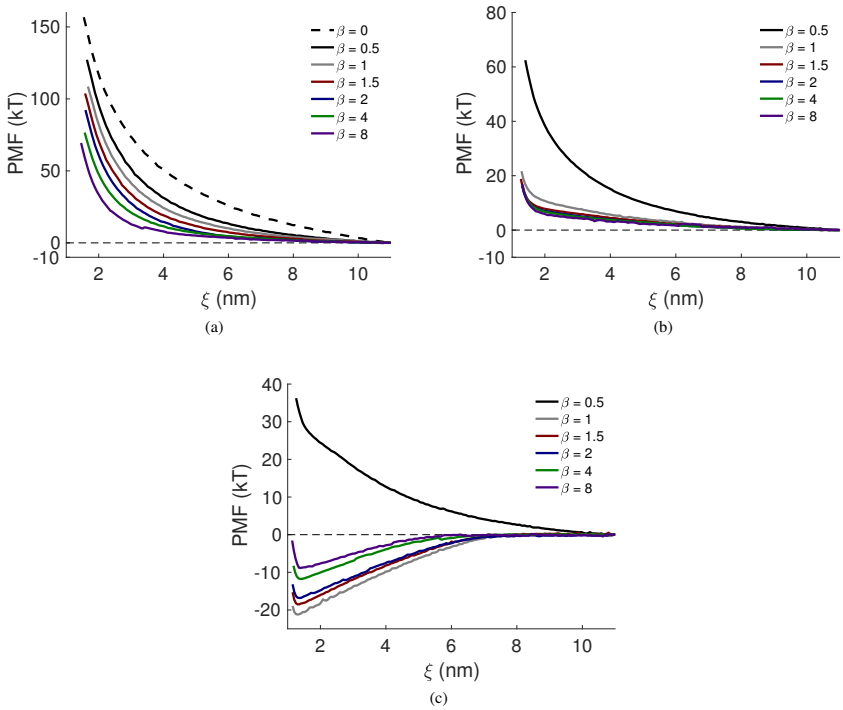


Figure S4: The potential of mean force (PMF) between two parallel platelets with $\sigma \approx$ -1.0 e/nm$^2$ as a function of the separation for the addition of (a) mono-, (b) di-, and (c) trivalent salt. The salt-free case, i.e. with only monovalent counterions ($\beta = 0$), has been included in (a) for comparison.

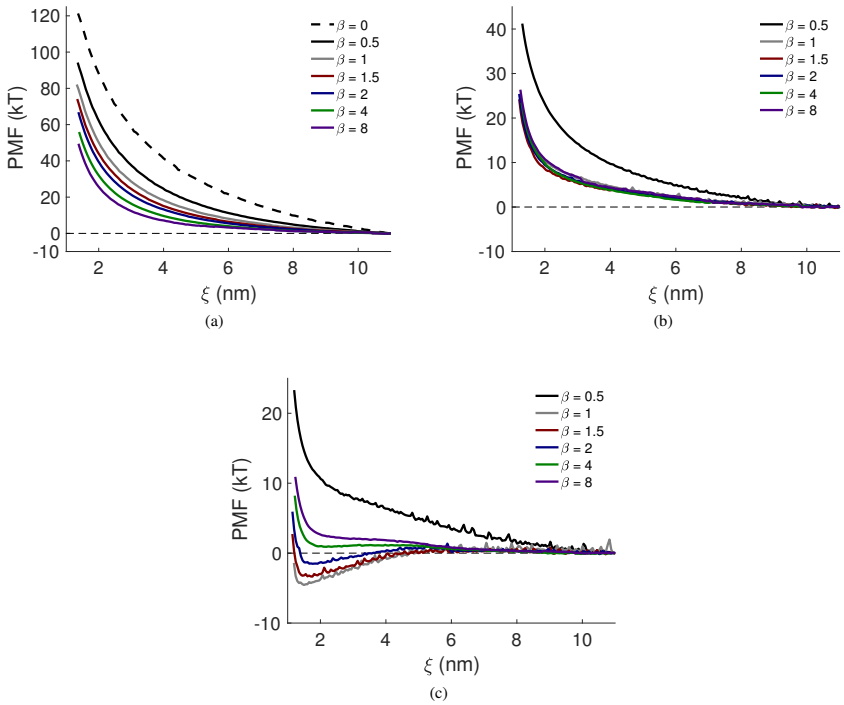


Figure S5: The potential of mean force (PMF) between two parallel platelets with $\sigma \approx$ -0.5 e/nm$^2$ as a function of the separation for the addition of (a) mono-, (b) di-, and (c) trivalent salt. The salt-free case, i.e. with only monovalent counterions ($\beta = 0$), has been included in (a) for comparison.

**Table S1**
The stoichiometric charge-ratio $\beta$, the Debye screening length $\kappa$, and the potential of mean force (PMF) between two parallel platelets with $\sigma \approx$ -1.0 e/nm$^2$ at the separation of $1.5 \pm 0.2$ nm.

| | $Z^+_{ion} = 1$ | | $Z^+_{ion} = 2$ | | $Z^+_{ion} = 3$ | |
|---|---|---|---|---|---|---|
| $\beta$ | $\kappa$ (nm) | PMF (kT) | $\kappa$ (nm) | PMF (kT) | $\kappa$ (nm) | PMF (kT) |
| 0 | $\infty$ | 142.4 | $\infty$ | 142.4 | $\infty$ | 142.4 |
| 0.5 | 3.12 | 122.7 | 2.54 | 62.48 | 2.20 | 31.00 |
| 1 | 2.20 | 104.6 | 1.80 | 17.18 | 1.56 | -20.90 |
| 1.5 | 1.80 | 95.78 | 1.47 | 12.47 | 1.27 | -18.28 |
| 2 | 1.56 | 83.67 | 1.27 | 12.16 | 1.10 | -16.78 |
| 4 | 1.10 | 64.98 | 0.90 | 12.37 | 0.78 | -11.76 |
| 8 | 0.78 | 48.42 | 0.64 | 12.14 | 0.55 | -8.83 |

**Table S2**
The stoichiometric charge-ratio $\beta$, the Debye screening length $\kappa$, and the potential of mean force (PMF) between two parallel platelets for the addition of trivalent salt at the separation of $1.5 \pm 0.2$ nm.

| | $\sigma \approx$ -1.0 e/nm$^2$ | | $\sigma \approx$ -0.5 e/nm$^2$ | |
|---|---|---|---|---|
| $\beta$ | $\kappa$ (nm) | PMF (kT) | $\kappa$ (nm) | PMF (kT) |
| 0 | $\infty$ | 142.4 | $\infty$ | 118.7 |
| 0.5 | 2.20 | 31.00 | 3.12 | 14.59 |
| 1 | 1.56 | -20.90 | 2.20 | -4.55 |
| 1.5 | 1.27 | -18.28 | 1.80 | -3.18 |
| 2 | 1.10 | -16.78 | 1.56 | -1.31 |
| 4 | 0.78 | -11.76 | 1.10 | 2.19 |
| 8 | 0.55 | -8.83 | 0.78 | 5.20 |

# Paper IV

Reprinted from *J. Colloid Interface Sci.*, 2019, **557**, 767–776
M. Jansson, S. Lenton, T. S. Plivelic and M. Skepö
©2019 with permission from Elsevier.

Journal of Colloid and Interface Science 557 (2019) 767–776

Contents lists available at ScienceDirect

Journal of Colloid and Interface Science

journal homepage: www.elsevier.com/locate/jcis

# Intercalation of cationic peptides within Laponite layered clay minerals in aqueous suspensions: The effect of stoichiometry and charge distance matching

Maria Jansson [a,*], Samuel Lenton [a,b], Tomás S. Plivelic [c], Marie Skepö [a,b,*]

[a] Theoretical Chemistry, Lund University, P.O. Box 124, SE-221 00 Lund, Sweden
[b] LINXS - Lund Institute of Advanced Neutron and X-ray Science, Scheelevägen 19, SE-223 70 Lund, Sweden
[c] MAX IV Laboratory, Lund University, P.O. Box 118, SE-221 00 Lund, Sweden

## GRAPHICAL ABSTRACT

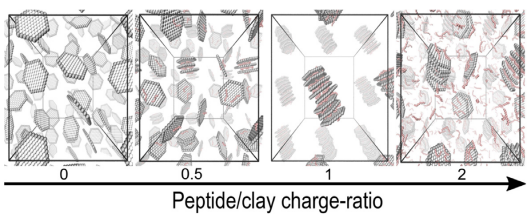


## ARTICLE INFO

*Article history:*
Received 26 July 2019
Revised 13 September 2019
Accepted 16 September 2019
Available online 19 September 2019

*Keywords:*
Intercalation
Clay
Laponite
Nano-platelets
Tactoids
Cationic peptides
Deca-Arginine
Small angle X-ray scattering
Zeta-potential
Molecular dynamics simulations

## ABSTRACT

Clays can be synthesised to have specific functional properties, which have been exploited in a range of industrial processes. A key characteristic of clay is the presence of a negatively charged surface, surrounded by an oppositely charged rim. Because of that, clays are able to sequester cationic compounds resulting in the formation of ordered layered structures, known as tactoids. Recent research has highlighted the possibility of utilising clay as a drug delivery compound for cationic peptides. Here, we investigate the process of intercalation by using the highly cationic peptide deca-arginine, and the synthetic clay Laponite, in aqueous suspensions with 2.5 wt% Laponite, and varying peptide concentrations. Small-angle X-ray scattering experiments show that tactoids are formed as a function of deca-arginine concentration in the dispersion, and for an excess of peptide, i.e. above a matched charge-ratio between the peptide and clay, the growth of the tactoids is limited, resulting in tactoidal dissolution. Zeta-potential measurements confirm that the observed dissolution is caused by overcharging of the platelets. By employing coarse-grained molecular dynamics simulations based on the continuum model, we are able to predict the tactoid formation, the growth, and the dissolution, in agreement with experimental results. We propose that the present simulation method can be a useful tool to tune peptide and clay characteristics to optimise and determine the extent of intercalation by cationic peptides of therapeutic interest.

© 2019 The Author(s). Published by Elsevier Inc. This is an open access article under the CC BY-NC-ND license (http://creativecommons.org/licenses/by-nc-nd/4.0/).

* Corresponding authors at: Theoretical Chemistry, Lund University, P.O. Box 124, SE-221 00 Lund, Sweden (M. Jansson and M. Skepö).
*E-mail addresses:* maria.jansson@teokem.lu.se (M. Jansson), marie.skepo@teokem.lu.se (M. Skepö).

https://doi.org/10.1016/j.jcis.2019.09.055
0021-9797/© 2019 The Author(s). Published by Elsevier Inc.
This is an open access article under the CC BY-NC-ND license (http://creativecommons.org/licenses/by-nc-nd/4.0/).

## 1. Introduction

There has been an enhanced interest in exploiting the physical properties of clays for various industrial and technological processes [1,2]. Clays are a broad class of inorganic materials, consisting of layered mineral silicates, which can be sourced either naturally or synthetically [3]. Both synthetic and natural clays are based on the same layered silicate structure, where the former can be selectively altered in order to tune the physical properties of the clay. Clays are used in a wide range of applications due to their large variety of functions, most commonly as rheological modifiers in an assortment of products including make-up and paint [4]. More recently, the interest in using synthetic clays as drug delivery vehicles has increased, due to their chemical stability and their relatively biologically inert properties [1,5–7]. One such example is the synthetically produced Laponite, which exhibits properties that are of specific interest in this area [8–10].

Laponite is a trioctahedral layered clay mineral, and consists of a negatively charged silica-sheet based surface, surrounded by a rim of exposed magnesium hydroxyl (MgOH) groups. The ideal chemical formula is written as $Na_{0.7}(Si_8Mg_{5.5}Li_{0.3})O_{20}(OH)_4$ [11], and the platelet has both an anisotropic charge and size, where the diameter is ~25 nm, and the thickness is ~1 nm, respectively. The surface charge of the platelet is negative, and defined from its cation exchange capacity (CEC), which is pH-dependent, and can be readily altered. Regarding CEC and Laponite, several values have been reported in the literature, e.g. ~0.75 mEq/g [12,13], ~0.65 mEq/g [14], and ~0.5 mEq/g [11]. The charge of the platelet edges is also pH-dependent, where the point of zero charge is at pH≈11, and thus, the edges are positively charged at lower pH, and negatively charged at higher pH [15]. The phase diagram of Laponite has been extensively studied in the literature, e.g. see the comprehensive review article by Ruzicka and Zaccarelli (2011) [16], and the references therein. The state diagram of Laponite is diverse, containing flocculants, isotropic liquids, isotropic gels, and nematic gels [17]. The size distribution of the ordered layered structure of Laponite, also known as tactoids, and the exfoliation process, can depend on the Laponite concentration [18]. At a concentration of approximately 2–3 wt%, Laponite exists in the repulsive glass, or Wigner glass state, where the process of structural ageing, i.e. gel or glass formation, has been observed [19].

Moreover, Laponite has been shown to possess antibacterial properties, as well as the ability to sequester cationic peptides [20]. The intercalation of the peptide between the silica sheets of the clay results in the formation of tactoids [14,20]. The tactoidal structure is stabilized by charge–charge interactions between the surface of the clay and the peptide. The process is entropically driven, due to the release of counterions associated with the clay when the peptide adsorbs on the clay surface [21,22]. Intercalation of cationic therapeutic peptides within the Laponite tactoidal structure can lead to higher efficiency, controlled release, and increased targeting efficacy [20].

In recent years, there has been a great interest in developing novel therapeutical compounds, including antibiotics and anticancer drugs, that are cationic in nature. The most well-known class are known as cationic antimicrobial peptides (CAMPs) [23,24]. It has been suggested that intercalation of cationic therapeutic peptides, within clays, may protect them from proteolysis, and provide a mechanism through which their release can be both controlled and target oriented [25]. Incorporation within a tactoidal clay structure may therefore increase both the bioavailability and the efficacy of CAMPs, as well as other cationic therapeutic peptides, or drug compounds [26,27]. Hence, Laponite may prove a useful candidate for sequestering and delivering cationic antibiotics.

One important limiting factor in employing synthetic clays as drug delivery vehicles is the lack of understanding of their colloidal behaviour in the presence of cationic peptides. Here, we study the tactoidal behaviour of Laponite in the presence of the cationic deca-arginine ($Arg_{10}$) peptide, which was chosen as a model peptide due to its highly cationic nature as well as relatively short sequence of ten amino acids. The former originates from the guanidinium cation ($Gdm^+$) group in the arginine side chain, which has a $pK_a$ value in water of 13.6 [28]. By using molecular dynamics simulations, we show the importance of the stoichiometric charge-ratio between the peptide and Laponite in regulating tactoid formation, and hence, peptide sequestration. The results obtained are confirmed by using the experimental techniques small angle X-ray scattering (SAXS), as well as zeta-potential ($\zeta$-potential) measurements.

## 2. Experimental section

### 2.1. Materials

The type of clay used throughout this study was the synthetic sodium Laponite-XLG XR from BYK Additives, with a CEC of ~0.5 mEq/g according to the technical information [11]. Analytical grade sodium chloride (purity, 99.5%) was purchased from MERCK, and Milli-Q water was used for the preparation of the solutions. $Arg_{10}$ with a molecular weight of 1.58 kDa was purchased from American Peptide (California, U.S.) as a lyophilised powder. Stock solutions of Laponite were prepared by dispersing 1 g of clay in 20 g aqueous suspension at two different ionic strengths, i.e. 10 and 150 mM NaCl. Thereafter, the sample were left to equilibrate for approximately 24 h.

Lyophilised $Arg_{10}$ peptide was dissolved in Milli-Q water, to a concentration of 20 mg/mL, and placed in 500–1000 Da MWCO Biotech CE dialysis tubing (Repligen, Massachusetts, U.S.). In order to remove impurities and buffer components remnant from the synthesis, the peptide was dialysed against Milli-Q water (500 times its volume), whilst stirring at room temperature. The dialysis step was then repeated three times against fresh Milli-Q water. Thereafter the samples were freeze-dried and collected as a lyophilised powder. The stock solution of $Arg_{10}$ was prepared by dissolving the lyophilised powder in Milli-Q water, where the concentration was determined from the absorbance at 214 nm, using a NanoDrop 2000 Spectrophotometer, with the extinction coefficient of $10800 \pm 100\ M^{-1}\ cm^{-1}$ [29].

Finally, the stock solutions of Laponite and $Arg_{10}$ were mixed, in order to obtain a Laponite mass fraction of 2.5wt%, which corresponds to a volume fraction of ~1%, assuming the particle density of Laponite as 2530 kg/m$^3$ [11]. The pH of the samples were set in the range of $8.8 \pm 0.9$ by addition of HCl, and measured prior to each experiment.

### 2.2. Small angle X-ray scattering

Small angle X-ray scattering (SAXS) measurements were performed at the SWING beamline of Soleil synchrotron (Saint-Aubin, France). The sample to detector distance was set to 1.5 m at 12 keV, corresponding to the $q$-range of $5{\cdot}10^{-2} < q < 7\ nm^{-1}$. Here $q$ is the scattering vector defined as $q = 4\pi \sin(\theta)/\lambda$, where $2\theta$ is the scattering angle, and $\lambda$ = 0.1 nm is the monochromatic beam wavelength. Furthermore, a hybrid pixel X-ray detector Eiger 4 M (Dectris) with $75 \times 75\ \mu m^2$ pixel size resolution was used. The samples were measured in 1.5 mm sealed glass capillaries, mounted on a multiple capillary holder, and thermalised at 25 °C. In order to minimise radiation damage, and increase data quality, ten exposures of 100 ms each were collected, at three different

positions of the sample. For data reduction, normalisation, and buffer subtraction, the beamline software Foxtrot, and the ATSAS package [30], were used.

In order to determine the average number of platelets per tactoid, a model scattering peak was fitted to the experimental data. In a narrow $q$-range, the scattering intensity can be approximated with a Lorentzian line shape:

$$q^2 I(q) \propto \frac{w}{(q - q_{\max})^2 + w^2} + b, \tag{1}$$

where $I(q)$ is the scattering intensity, $w$ is a measure of the width of the Bragg peak, $q_{\max}$ is the position of the maximum intensity of the Bragg peak, and $b$ is a fitting parameter of the background contribution around the peak. The full width at half maximum (FWHM) of the Bragg peak is equal to $2w$, and the average tactoid size can be expressed as $\langle N \rangle \approx q_{\max}/w$ [31–33]. The average distance, i.e. $d$-spacing, between the mid-plane of two adjacent clay platelets, was obtained from $q_{\max}$ via the relation: $d_{\text{Bragg}} = 2\pi/q_{\max}$, and the data was fitted between $q_{\max} \pm 0.5\text{nm}^{-1}$.

### 2.3. ζ-potential measurements

ζ-potential measurements were performed with a Malvern Zetasizer Nano ZS (Malvern Instruments), using disposable folded capillary cells at 25 ° C. The ζ-potential is obtained from a combination of electrophoresis, and laser doppler velocimetry techniques, which determines the velocity of a particle in a medium when an electric field is applied. The ζ-potential can then be calculated from the electrophoretic mobility of the particle by applying the Henry equation [34]:

$$U_{\text{E}} = \frac{2\epsilon\zeta f(\kappa a)}{3\eta}, \tag{2}$$

where $U_{\text{E}}$ is the electrophoretic mobility, $\epsilon$ is the dielectric constant, $\zeta$ is the ζ-potential, $\eta$ is the viscosity of the medium, and $f(\kappa a)$ is Henrys function, where $1/\kappa$ is the thickness of the electrostatic double layer, and $a$ is the particle radius. For the measurements, the classical Smoluchowski limit for compact double layers, corresponding to $\kappa a \gg 1$, was used.

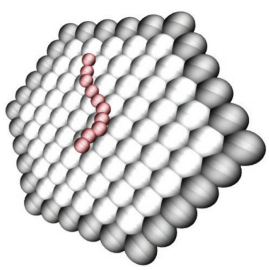

**Fig. 1.** Schematic representation of the simulation model for one platelet and one peptide. The face of the platelet (light grey) has a total charge of $Z_{\text{face}} = -61$, the rim of the platelet (dark grey) has a total charge of $Z_{\text{rim}} = +6$, and the peptide (red) consists of ten beads, each with a charge of $Z_{\text{bead}} = +1$. (For interpretation of the references to colour in this figure legend, the reader is referred to the web version of this article.)

## 3. Theoretical section

Molecular dynamics (MD) simulations were utilised to study the tactoid formation of the clay platelets upon addition of positively charged peptides.

### 3.1. The coarse-grained model

A schematic representation of the clay platelet, and the peptide, is shown in Fig. 1. One platelet is modelled as a finite hexagonal monolayer of connected coarse-grained spheres, denoted as sites, and the platelet has a thickness and a diameter of 1 and 11 nm, respectively. The model size is smaller than the experimental in order to reduce the computational cost. The platelet has a homogeneous charge distribution, where the unit charges are located in the centre of each site, and both face and rim charges have been added to represent the charge anisotropy of Laponite. The peptide is modelled as a positively charged chain consisting of connected coarse-grained beads (monomers). In the simulations, all the counterions were added explicitly, and modelled as freely moving charges with an excluded volume, where the total platelet and chain charges were neutralised by monovalent counterions. The stoichiometric charge-ratio ($\beta$) in the system is defined as the absolute value of the number of positive chain charges, divided by the total net negative charge of the platelets, i.e. $\beta = |(N_{\text{chains}} \cdot Z_{\text{chain}})/(N_{\text{platelets}} \cdot Z_{\text{platelet}})|$.

The reference system consisted of eight platelets, with a face charge of $Z_{\text{face}} = -61$, and a rim charge of $Z_{\text{rim}} = +6$. Hence, the total net charge of each platelet is $Z_{\text{platelet}} = -55$. Moreover, the peptide was modelled as a chain with ten charged beads to mimic $Arg_{10}$, each with a charge of $Z_{\text{bead}} = +1$. The number of chains were varied between $N_{\text{chains}} = 0$—180, in order to obtain a stoichiometric charge-ratio ranging from $\beta = 0$ to $\beta = 4$. Moreover, the general applicability of the model was investigated by modifying the peptide chain with respect to the chain length, the total charge of the chain, the charge of each bead, as well as the chains flexibility and bond length. The specifications of the systems are compiled in Table 1.

In the simulations, the solvent is treated implicitly as a dielectric continuum, with the dielectric constant $\epsilon_{\text{r}} = 78.3$. All the interactions in the system are assumed to be pairwise additive, and the electrostatic pair potential is defined as:

$$u_{ij}^{\text{EL}}(r_{ij}) = \frac{e^2 z_i z_j}{4\pi\epsilon_0\epsilon_{\text{r}} r_{ij}}, \tag{3}$$

where $e$ is the elementary charge, $z_i$ is the valency of particle $i$, $\epsilon_0$ is the permittivity of vacuum, and $r_{ij}$ is the centre-to-centre distance between particles $i$ and $j$. In addition, the particles also interact via a strictly repulsive, truncated, and shifted Lennard-Jones (TLJ) potential, defined as:

$$u_{ij}^{\text{TLJ}}(r_{ij}) = \begin{cases} \epsilon_{\text{TLJ}}\left[\left(\frac{\sigma_{ij}}{r_{ij}}\right)^{12} - 2\left(\frac{\sigma_{ij}}{r_{ij}}\right)^{6} + 1\right], & \text{if} r_{ij} < \sigma_{ij} \\ 0, & \text{otherwise.} \end{cases} \tag{4}$$

The strength of the short-ranged potential ($\beta\epsilon_{\text{TLJ}}$) was set to one, where $\beta = 1/k_{\text{B}}T$, $k_{\text{B}}$ is the Boltzmann constant, and $T$ = 298 K. $\sigma_{ij} = (\sigma_i + \sigma_j)/2$, and $\sigma_i$ is the diameter of species $i$, where $\sigma_{\text{site}} = 1$ nm, and $\sigma_{\text{ion}} = \sigma_{\text{bead}} = 0.4$ nm. Thus, the total potential between all pairs is defined as:

$$u_{ij}(r_{ij}) = u_{ij}^{\text{TLJ}}(r_{ij}) + u_{ij}^{\text{EL}}(r_{ij}). \tag{5}$$

Furthermore, all the adjacent sites within the platelet, and the adjacent beads within the chain, are connected by a harmonic bond-stretching potential:

**Table 1**
General applicability of the model - specifications of the systems (including eight platelets).

| System | Modification of the peptide | $N_{beads}$ | $Z_{bead}$ | $Z_{chain}$ | $N_{chains}$ | $k^{\theta}$ ($k_BT$/rad$^2$) | $b$ (nm) |
|---|---|---|---|---|---|---|---|
| | Reference system | 10 | 1 | 10 | 0–180 | 0 | 0.5 |
| G.I | Chain length | 5–20 | 1 | 5–20 | 88–22 | 0 | 0.5 |
| G.II | Total charge | 10 | 0.5–2 | 5–20 | 88–22 | 0 | 0.5 |
| G.III | Chain length and bead charge | 4–20 | 2.5–0.5 | 10 | 44 | 0 | 0.5 |
| G.IV | Flexibility | 10 | 1 | 10 | 44 | 0–400 | 0.5 |
| G.V | Bond length | 10 | 1 | 10 | 44 | 0 | 0.4–0.6 |
| G.VI | Charge position | 20 | 1 | 10 | 44 | 0 | 0.5 |

$$u_b(r_{ij}) = \frac{1}{2}k_b(r_{ij} - b)^2, \tag{6}$$

where $k_b$ is the force constant, and $b$ is the equilibrium bond length. The flexibility of the platelet, and the chain, were constrained by an harmonic bending potential between triplets of sites:

$$u(\theta_{ijk}) = \frac{1}{2}k^{\theta}(\theta_{ijk} - \theta^0)^2, \tag{7}$$

where $k^{\theta}$ is the force constant, $\theta_{ijk}$ is the bond angle between the sites $i$, $j$, and $k$, and $\theta^0 = \pi$.

### 3.2. Molecular dynamics simulations

The MD simulations were performed with the software package GROMACS (version 5.0.4) [35]. A cubic simulation box with three-dimensional periodic boundary conditions were used, with a box length of 33 nm, corresponding to a volume fraction with respect to the platelets of 1% ($\phi_c \approx 0.01$) for eight platelets. The time step was set to 10 fs, with a total of $3 \cdot 10^7$ steps. Newtons' equations of motion of freely moving species, i.e. the platelets, the counterions, and the chains, were integrated using the leap-frog algorithm. To account for the long-ranged electrostatic contribution, fast particle-mesh Ewald summation (PME) was utilised with a 6 nm real-space Coulomb cutoff, and a Fourier spacing equal to 0.6 nm. For an in depth description of the input parameters, the reader is referred to the user manual [35].

### 3.3. Structural analysis from simulations

The structural information obtained from the simulations was analysed by the total structure factor between the platelets, defined as:

$$S(q) = \left\langle \frac{1}{N}\sum_{i=1}^{N}\sum_{j=1}^{N}\frac{\sin(qr_{ij})}{qr_{ij}} \right\rangle, \tag{8}$$

where $N$ is the total number of platelet sites in the system, and $V$ is the total volume of the simulation box. Assuming an isotropic scattering, the equation of the total structure factor can be rewritten as:

$$S(q) = 1 + 4\pi\frac{N}{V}\int_0^{\infty}(g(r) - 1)r^2\frac{\sin(qr)}{qr}\mathrm{d}r, \tag{9}$$

where $g(r)$ is the radial distribution function (also denoted rdf) between all the platelet sites in the system. If $g(r)$ does not approach one at large separations due to the finite box length, a window function can be used to reduce artefacts, according to:

$$S_w(q) = 1 + 4\pi\frac{N}{V}\int_0^{\infty}(g(r) - 1)r^2\frac{\sin(qr)}{qr}\frac{\sin(\pi r/R_c)}{\pi r/R_c}\mathrm{d}r, \tag{10}$$

where $R_c$ is the maximum distance in $g(r)$ [36].

## 4. Results and discussion

### 4.1. Experimental characterisation of Laponite-Arg$_{10}$ mixtures

SAXS experiments were performed at a fixed Laponite concentration of 2.5wt%, while varying the concentration of $Arg_{10}$ so that the samples had a stoichiometric charge-ratio of $\beta$ = 0, 0.5, 2.5, and 10. The measurements were performed at two different ionic strengths at a fixed temperature of T = 25 ° C. The samples were measured directly after preparation, and thus, no ageing effect was observed. Fig. 2 shows the scattering intensities, as Kratky plots ($q^2I(q)$ vs. $q$), for the Laponite sample without addition of $Arg_{10}$, i.e. $\beta$ = 0. Here, no Bragg peaks are observed in the SAXS spectra, independent of the ionic strength. This indicates that neither tactoids nor fractions of platelet aggregates are found in the dispersion, and therefore the system is dominated by repulsive interactions. Upon addition of $Arg_{10}$, Bragg peaks are observed for all concentrations of $Arg_{10}$, implying tactoid formation within the systems (Fig. 2). A comparison between the intensities of the Bragg peaks shows a monotonic increase up to $\beta$ = 2.5, after which a lower intensity is observed for $\beta = 10$. The behaviour of the latter can be explained by a tactoidal dissolution due to overcharging of the platelets caused by the presence of the peptide, which thereby induces repulsive interactions. The maxima of the Bragg peaks are consistent between the measured samples, corresponding to a $d$-spacing of ~1.8 nm. This value is larger than what is usually reported for Laponite, which supports the fact that the peptides adsorb on the clay surface. The FWHM of the Bragg peaks decrease with increasing $\beta$, indicating that the tactoids grow in size with increasing $Arg_{10}$ concentration. This is confirmed from the analysis of the average number of platelets per tactoid, $\langle N \rangle$, which increases from ~2 to ~3, as $\beta$ increases from 0.5 to 2.5. The increased attraction in the systems can be explained from the CEC of Laponite, as the small monovalent counterions are exchanged with the larger more highly charged peptides. Hence, the SAXS-data indicate that small tactoids are formed until $\beta$ = 2.5, whereas when $\beta$ > 2.5, there is an excess of peptides in the system, and the overall tactoid size decreases, which implies that the platelet is overcharged.

To further validate this, the $\zeta$-potentials of the samples were determined and presented, see Fig. 3. Since the dispersions for the SAXS experiments are very dense, it was essential to reduce the concentration with a factor of 100, nevertheless, qualitative information can still be obtained due to the fact that the charge-ratio of the samples remains the same. For the Laponite dispersions without addition of $Arg_{10}$ ($\beta = 0$), the measured $\zeta$-potentials were −29, and −21 mV for the ionic strengths of 10 and 150 mM NaCl, respectively. This confirms that the Laponite platelets have a negative surface charge density. However, these values are less negative than other measured $\zeta$-potentials reported in the literature, i.e. −52 mV [37,38], −40–45 mV [39], −58 mV [12], and −45 mV [13]. This is reasonable since the $\zeta$-potential correlates to the CEC of the Laponite, which in this study was ~0.5 mEq/g, in comparison with previous studies where a CEC of ~0.75 mEq/g has been reported. As shown in Fig. 3, it was found that the $\zeta$-potential increased with an

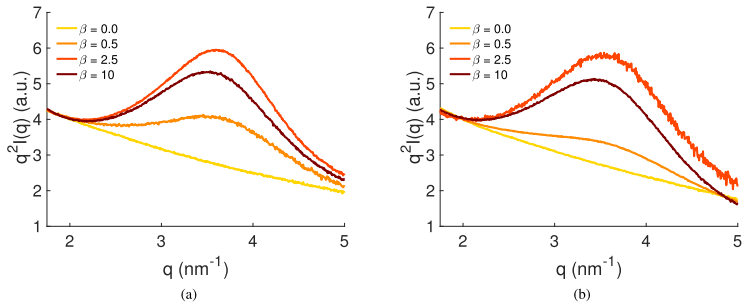


**Fig. 2.** SAXS intensities as Kratky plots over a narrow $q$-range for Laponite (2.5wt%), and Laponite-$Arg_{10}$ dispersions with varying stoichiometric charge-ratio, $\beta$, for (a) 10, and (b) 150 mM NaCl. The intensity curves are normalised at $q \approx 2$ nm$^{-1}$.

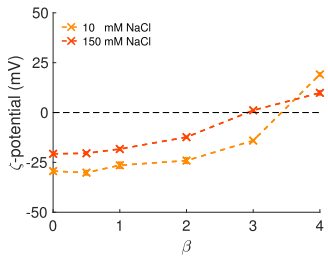


**Fig. 3.** $\zeta$-potential for Laponite, and Laponite-$Arg_{10}$ dispersions, as a function of the stoichiometric charge-ratio, $\beta$, for two ionic strengths. Error bars are smaller than the symbol size.

increase in charge-ratio, and that the $\zeta$-potential changes sign, from negative to positive for the highest charge-ratio, indicating that the system becomes overcharged. Moreover, the $\zeta$-potential also shows that the overcharging effect is more pronounced at low ionic strength, which emphasises the importance of the electrostatic interactions in the system.

### 4.2. MD simulations of Laponite-$Arg_{10}$ mixtures

The radial distribution functions determined from the MD simulations are shown with respect to the center-of-mass between the platelets in Fig. 4a, for the systems with $\beta$ = 0–2. The number of peaks in the rdfs indicates the size of the tactoids, where the first peak is equivalent to a structure where two platelets have aggregated in a face-to-face configuration at ∼2.4 nm, and the second peak corresponds to the situation when three platelets have aggregated in a face-to-face configuration at ∼2.4·2 nm, and so on. The first peak position shows that the distance between the surface of two adjacent platelets is ∼1.4 nm. Considering that the diameter of one $Arg_{10}$ bead is 0.4 nm (in the model), it can be concluded that the peptide is not tightly bound to the platelet. The height of the peak describes the probability of finding the specific configuration. For the system without addition of $Arg_{10}$, ($\beta = 0$), no peak is visible, indicating that the system does not contain any tactoids, and hence, that the system is dominated by repulsive interactions. The screening length that the counterions of the platelets induce is approximately 1.9 nm, which is larger than the distance between two platelets, and thus confirms that no electrical double layer interactions are present in the simulations. Upon addition of $Arg_{10}$, the number as well as the height of the peaks increase as $\beta$ approaches one, whereas for the higher charge-ratio, i.e. $\beta$ = 2, the number and the height of the peaks decrease. This indicates that at a low number of $Arg_{10}$, there are several smaller tactoids in the system, and as the number of peptides increases, the size of the tactoids increases until all platelets are stacked into one tactoid shown in the representative snapshot of the configuration in Fig. 4f. For $\beta > 1$, dissolution occurs, which means that the tactoid dissolves into smaller objects again, in line with results obtained regarding oppositely charged polyelectrolytes and macroions [40,41]. This behaviour is further proven by the calculated structure factors in Fig. 4b. Here, no Bragg peaks are found for $\beta < 1$, whereas for $\beta \geqslant 1$, Bragg peaks are observed, where the intensity of the peak decreases with an increase in $\beta$. To further analyse the simulation data, the average number of platelets per tactoid, $\langle N \rangle$, was calculated as a function of the stoichiometric charge-ratio, see Fig. 4c. Here it is shown that $\langle N \rangle$ is equal to one for $\beta = 0$, indicating that there are only single platelets in the system. Then $\langle N \rangle$ increases up to $\beta = 1$, at which a maximum point is reached, whereas at higher charge-ratios, a decrease in $\langle N \rangle$ is observed. This behaviour is further illustrated in the representative snapshots of the configurations in Fig. 4d–g. The obtained results indicate that $Arg_{10}$ promotes tactoid formation, which is then followed by a dissolution of the tactoids in the system due to overcharging of the platelets with $Arg_{10}$. By comparing the MD simulations with the SAXS data (Fig. 2), and the $\zeta$-potential measurements (Fig. 3), a qualitative agreement in the overall behaviour is observed.

### 4.3. Single-platelet simulations

To study the extent of overcharging, i.e. to which degree a platelet can be overcharged by a peptide, simulations consisting of one platelet fixed in the xyz-positions at the center of the simulation box were performed, with addition of $Arg_{10}$ corresponding to a total stoichiometric charge-ratio of the system ranging from 0 to 2.5. From the simulations, the distribution of $Arg_{10}$ as a function of the distance from the platelet surface is obtained. Fig. 5a shows that upon addition of $Arg_{10}$, the number of beads close to the surface increases, notice though that this is a smooth transition, until a plateau value is reached. The plateau corresponds to the concentration of $Arg_{10}$ in the bulk, where the gradient before the plateau is a measure of the tendency for the $Arg_{10}$ to interact with the platelet. Here a steeper gradient means that it is more likely to find the peptides at the surface of the platelet at that corresponding

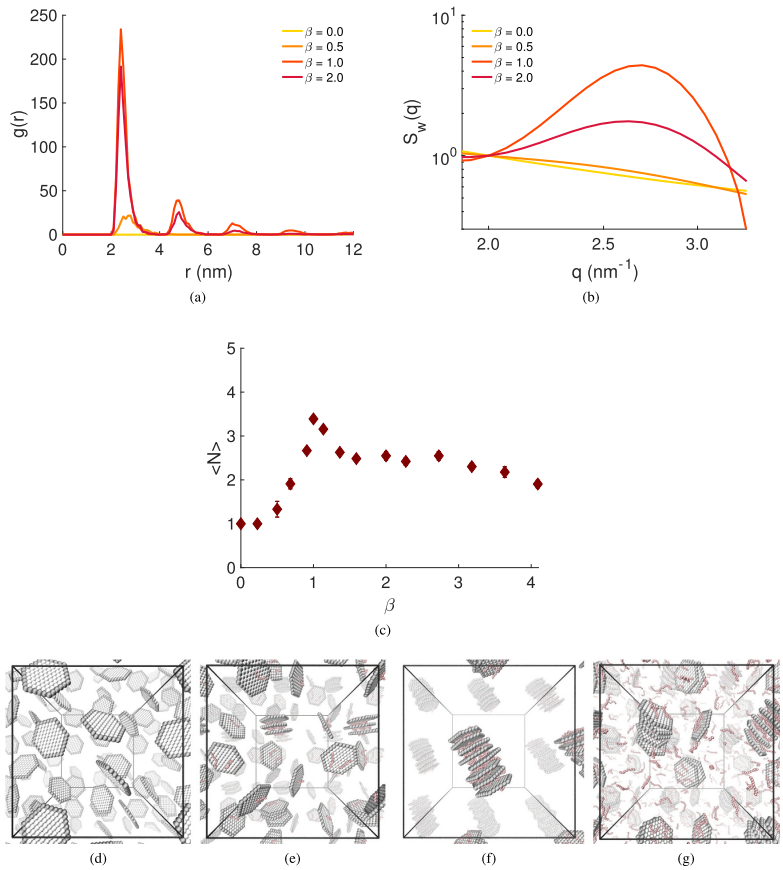


**Fig. 4.** (a) Radial distribution functions, and (b) structure factors, $S_w(q)$, from the MD simulations for the systems with a stoichiometric charge-ratio in the range of $\beta = 0$–2. The intensities are normalised at $q \approx 2$ nm$^{-1}$. (c) The average number of platelets per tactoid, $\langle N \rangle$, as a function of $\beta$. Notice that error bars are included in (c), although for most data points, the error is smaller than the symbol size. (d–g) Representative snapshots of the configurations with (d) $\beta = 0$, (e) $\beta = 0.5$, (f) $\beta = 1$, and (g) $\beta = 2$. The counterions are omitted for clarity, the platelets are shown in grey, the peptides are shown in red, and the cubic simulation box is shown in black (periodic images are shown outside the simulation box).

distance. Eventually the gradient reaches the plateau value, see Fig. 5b, which can be interpreted as the platelet being saturated by $Arg_{10}$, and thus, overcharged (if $\beta > 1$). As shown, the gradient increases with the charge-ratio in the system, indicating that more chains are in close contact with the platelet. The gradient was extracted through a linear regression at the distance $h = 1.1 \pm 0.2$ nm, and the fitted data can be found in the Supplementary data (Fig. 1). Also, it is found that the platelet becomes overcharged at $\beta > 1$, which is in qualitative agreement with the results obtained from the $\zeta$-potential measurements.

### 4.4. General applicability of the model

The generality of the study and the impact of the electrostatic interactions have been further evaluated by studying the reference system with $\beta = 1$. Fig. 6a shows how the structure factor is affected upon addition of explicit monovalent salt ions, and as visible, there are no discrepancies for the salt concentrations of 0–100 mM, whilst for 150 mM, the intensity of the Bragg peak is lower. This is probably caused by the weaker electrostatic attractions combined with the decrease in entropy gain, c.f., increased ionic strength in comparison to a salt-free system [42]. From the analysis of the average number of platelets per tactoid, $\langle N \rangle$, shown in Fig. 6b, it is observed that $\langle N \rangle$ decreases slightly upon addition of salt, which also indicates that there are stronger repulsive electrostatic interactions in the system due to electrostatic screening. However, in the continuum model used in this study, the electrostatic interactions within the system are usually overestimated, and thus, the salt effect can be neglected.

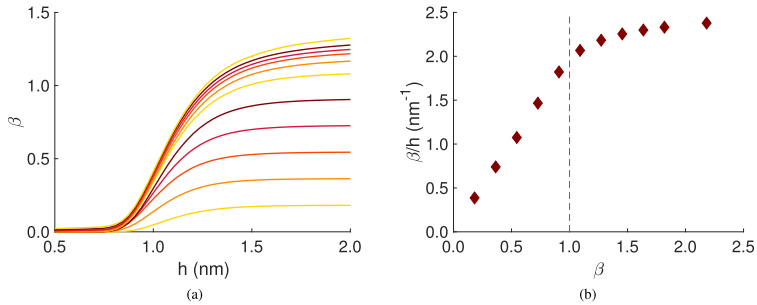


**Fig. 5.** (a) The distribution of peptide beads represented as the stoichiometric charge-ratio, $\beta$, from the single-platelet simulations as a function of the distance from the platelet surface, $h$, and (b) the gradient, $\beta/h$, extracted from (a) at the distance $h = 1.1 \pm 0.2$ nm as a function of $\beta$.

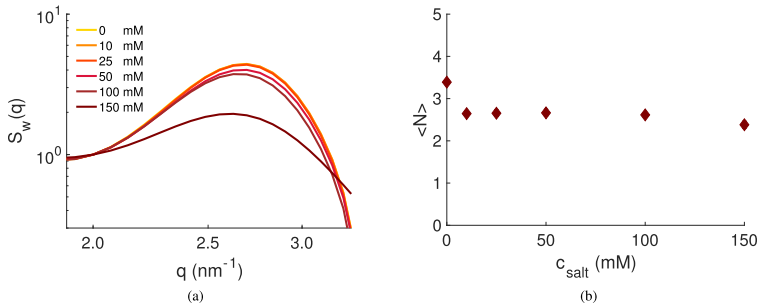


**Fig. 6.** (a) Structure factors, $S_w(q)$, from the MD simulations, where the intensities are normalised at $q \approx 2$ nm$^{-1}$, and (b) the average number of platelets per tactoid, as a function of salt concentration for the system with $\beta = 1$. In (b), the error bars are included, and smaller than the symbol size.

Having established that the salt concentration has a minimal effect on the intercalation of peptides and the consequent formation of tactoids, we next used simulations to investigate how the altering of the peptide properties influences the system, see Table 1 for specifications. Fig. 7a shows the effect of the peptide length (defined as $N_{beads}$), referred as system G.I, on the tactoid formation. It is found that the tactoids increase in size up to the peptide sequence used in this study (10), after which the size of the tactoids formed decreases slightly. This suggests that a sequence containing a minimum number of charged residues is an important regulator of tactoid formation. Peptides that exert a biological function do not typically contain a homogeneous sequence of charged residues. Therefore, we next investigated the effects of altering the total charge of the peptide chain, defined as $Z_{chain} = N_{beads} \cdot Z_{bead}$, whilst keeping the number of beads constant (system G.II). The results are shown in Fig. 7b, where we can observe that, not surprisingly, there is a large influence on the formation of tactoids in the system, where tactoids are formed for $Z_{chain} > 8$, followed by an increase in tactoid size. Moreover, two plateau regions are found for $10 < Z_{chain} < 14$ and $16 < Z_{chain} < 20$, respectively, indicating that peptides with slightly dissimilar charge can give rise to the same behaviour with respect to the intercalation into layered clay minerals. Peptides of different types may have the same total charge, but differ with respect to the size of the chain as well as the charge of each residue. This effect was studied by keeping the total charge of the peptide constant, whilst varying the number of beads and the charge of each bead, i.e. system G.III. Fig. 7c shows that a maximum is found at the peptide sequence used in this study, after which the size of the tactoids decreases rapidly towards one, indicating that there are only single platelets in the system. This suggests that there is an optimum with respect to the peptide properties for the intercalation, and that the number of beads as well as the charge of each bead have a greater effect than the total charge of the chain. To account for the varying flexibility observed in different peptide chains, the strength of the bead–bead potential in Eq. (7) was altered in system G.IV, with $k^{\theta} = 0$, 4, 40, and 400 $k_BT$/rad$^2$. By decreasing the flexibility of the peptide, i.e. increasing $k^{\theta}$, it was found that the tactoid formation remained unchanged. However, the distance between the platelets within the tactoids decreases slightly from ~1.4 to ~1.1 nm, which originates from a tighter binding of the peptide to the platelet when its flexibility decreases.

Alternation of the peptide sequence was performed to study the effect of charge distance matching between the peptide and the platelet. First, the bond length within the peptide was altered, where for the reference system, the peptides bond length is $b = 0.5$ nm, and the distance between the sites within the platelet is $b = 1.0$ nm, thus, three beads of the peptide match two charges of the platelet. For the simulations of system G.V, the peptides bond length was set to $b = 0.4$, 0.5, and 0.6 nm, where the distance between the platelet and the peptide was found to increase with

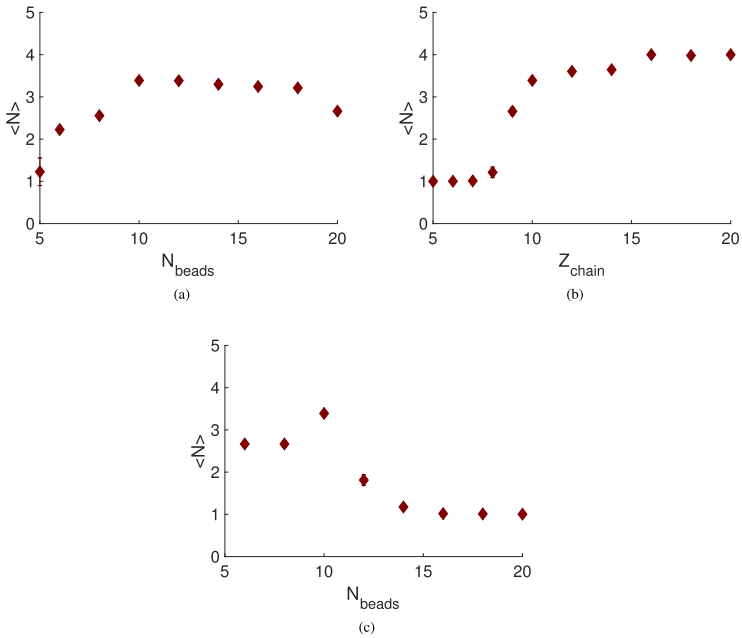


**Fig. 7.** The average number of platelets per tactoid obtained from the MD simulations for the alternation of the peptide chain with respect to (a) the chain length, (b) the total charge, and (c) the chain length as well as the charge of each bead within the chain. Error bars are included, for most data points the error is smaller than the symbol size.

bond length, i.e. from ∼1.2 to ∼1.6 nm for $b = 0.4$ to 0.6. Further, the average number of platelets per tactoid was ∼2.7, ∼3.4, and ∼2.1 for $b = 0.4$, 0.5, and 0.6 nm, respectively, indicating that $b = 0.5$ nm is an optimal bond length of the peptide with respect to the tactoid formation due to the charge distance matching between the peptide and the platelet. Secondly, the charge separation was investigated by altering the positions of the charges within the peptide by setting a positive charge ($Z_{bead} = +1$) for every second bead, and a neutral charge for every other bead, corresponding to system G.VI. It should be noted that it was necessary to increase the peptide length ($N_{beads}$), meanwhile conserving a constant net charge of the chain. From the simulations, no tactoid formation was observed when the peptide became longer and bulkier, thus, it is more favourable for the system to maximise the chain entropy. This is shown in the radial distribution function in Fig. 8a, where no peaks are observed for the modified chain. It was also found that the peptide adsorbs onto the platelet, however, with a larger distance between the platelet and the peptide than

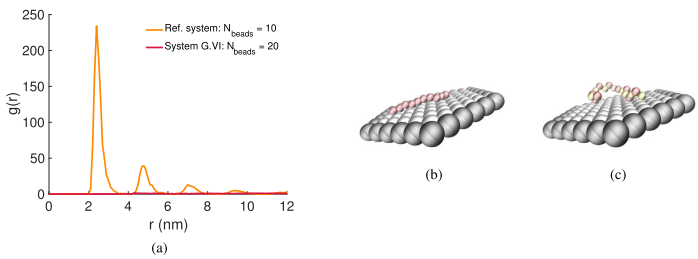


**Fig. 8.** (a) Radial distribution functions showing the effect of charge distance matching by modifying the position of the charges within the peptide chain. (b–c) Representative snapshots of the configurations from the single-platelet simulations for (b) the reference system with all beads positively charged, and (c) the system with every second bead positively charged, note that $N_{beads} = 20$. The counterions are omitted for clarity, the platelet is shown in grey, and the peptide is shown in red and orange, where the red beads are positively charged and the orange beads are neutral. (For interpretation of the references to colour in this figure legend, the reader is referred to the web version of this article.)

for the reference system, which is illustrated in the representative snapshots of the configurations from the single-platelet simulations in Fig. 8b–c. Additional radial distribution functions, and representative snapshots of the configurations for the modification of the peptide properties, are found in the Supplementary data (Figs. 2–6).

When considering sequestration of charged peptides by synthetic clays, physical properties of both the peptide of interest, and the clay, need to be considered. In this study the clay model remained constant in order to reduce the number of variable parameters, however, alternation of the platelet charge distribution, and size, is the basis for future work. For instance, charge vacancies in the platelet can be added to represent the location of charges in Laponite (or other types of clay). Moreover, the effect of platelet size can also be taken into consideration. However, the interactions in the system is to a first approximation proportional to the area of the platelets, and thus, the attraction between the platelets would increase with size.

## 5. Conclusion

Experimentally, we have observed that Laponite can intercalate the cationic peptide $Arg_{10}$, and promote tactoid formation. The mechanism is dependent on the stoichiometric charge-ratio $\beta$, where an initial increase in $\beta$ results in the formation of tactoids, whilst for an excess, i.e. $\beta > 1$, the overcharging effect results in a limited growth of the tactoids, and tactoidal dissolution. By using MD simulations, we were able to capture the intercalation of the peptide, and identify the stoichiometric charge-ratio at which tactoid formation is initiated, maximised, as well as when tactoidal dissolution due to overcharging is observed. The results from the simulations are in qualitative agreement with the experimental evidences, and the observed behaviour is illustrated in Fig. 9. Furthermore, we make predictions on the behaviour of the peptide intercalation based on the sequence length, the net charge of the chain, and the effect of charge distance matching. The information gained, combined with the ability to simulate such systems, could provide useful physical insight into the intercalation of other cationic peptides within clays, suggesting specific conditions where clays may act as a targeted drug release system. We therefore propose that the method presented here could be useful for testing and refining the properties of both the synthetic clay, and the peptide targets, to optimise sequestration, and consequently aid in the design and testing of efficient drug delivery systems. The incorporation of peptides within clays may act as a promising method for drug delivery, increasing the bioavailability of the sequestered peptide, and protecting it from proteolysis.

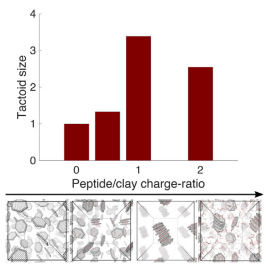


**Fig. 9.** The tactoid size as a function of the peptide/clay charge-ratio, and representative snapshots of the configurations illustrating the non-montonical behaviour of the tactoid size with increasing charge-ratio.

## Acknowledgements

Computational resources were provided by the Swedish National Infrastructure for Computing (SNIC) through LUNARC, the Center for Scientific and Technical Computing at Lund University. We acknowledge Soleil, the French Synchotron Facility in Paris, for providing beamtime, and Dr. J. Perez for providing assistance during measurements at the SWING beamline. This work was performed within the framework of the Swedish national strategic e-science research program eSSENCE. The Lars Hierta Memorial Foundation and the Royal Society of Physiography are greatly acknowledged for financial support.

## Appendix A. Supplementary material

Supplementary data associated with this article can be found, in the online version, at https://doi.org/10.1016/j.jcis.2019.09.055.

## References

[1] A.K. Gaharwar, L.M. Cross, C.W. Peak, K. Gold, J.K. Carrow, A. Brokesh, K.A. Singh, 2D nanoclay for biomedical applications: regenerative medicine, therapeutic delivery, and additive manufacturing, Adv. Mater. 31 (23) (2019) 1900332, https://doi.org/10.1002/adma.201900332.
[2] Y. Jin, A. Compaan, W. Chai, Y. Huang, Functional nanoclay suspension for printing-then-solidification of liquid materials, ACS Appl. Mater. Interfaces 9 (23) (2017) 20057–20066, https://doi.org/10.1021/acsami.7b02398.
[3] P. Liu, Polymer modified clay minerals: a review, Appl. Clay Sci. 38 (1) (2007) 64–76, https://doi.org/10.1016/j.clay.2007.01.004.
[4] H.A. Patel, R.S. Somani, H.C. Bajaj, R.V. Jasra, Nanoclays for polymer nanocomposites, paints, inks, greases and cosmetics formulations, drug delivery vehicle and waste water treatment, Bull. Mater. Sci. 29 (2) (2006) 133–145, https://doi.org/10.1007/BF02704606.
[5] S.M.M. Meira, A.I. Jardim, A. Brandelli, Adsorption of nisin and pediocin on nanoclays, Food Chem. 188 (2015) 161–169, https://doi.org/10.1016/j.foodchem.2015.04.136.
[6] S. Jayrajsinh, G. Shankar, Y.K. Agrawal, L. Bakre, Montmorillonite nanoclay as a multifaceted drug-delivery carrier: a review, J. Drug Deliv. Sci. Technol. 39 (2017) 200–209, https://doi.org/10.1016/j.jddst.2017.03.023.
[7] E.C. dos Santos, Z. Rozynek, E.L. Hansen, R. Hartmann-Petersen, R.N. Klitgaard, A. Løbner-Olesen, L. Michels, A. Mikkelsen, T.S. Plivelic, H.N. Bordallo, J.O. Fossum, Ciprofloxacin intercalated in fluorohectorite clay: identical pure drug activity and toxicity with higher adsorption and controlled release rate, RSC Adv. 7 (2017) 26537–26545, https://doi.org/10.1039/C7RA01384A.
[8] H. Tomás, C.S. Alves, J. Rodrigues, Laponite: a key nanoplatform for biomedical applications?, Nanomed Nanotechnol. Biol. Med. 14 (7) (2018) 2407–2420, https://doi.org/10.1016/j.nano.2017.04.016.
[9] L. Zheng, B. Zhou, X. Qiu, X. Xu, G. Li, W.Y. Lee, J. Jiang, Y. Li, Direct assembly of anticancer drugs to form Laponite-based nanocomplexes for therapeutic co-delivery, Mater. Sci. Eng.: C 99 (2019) 1407–1414, https://doi.org/10.1016/j.msec.2019.02.083.
[10] T. Jiang, G. Chen, X. Shi, R. Guo, Hyaluronic acid-decorated Laponite nanocomposites for targeted anticancer drug delivery, Polymers 11 (1). https://doi.org/10.3390/polym11010137.
[11] BYK, Technical Information B-RI 21, LAPONITE Performance Additives, 2016.
[12] S. Zhang, Q. Lan, Q. Liu, J. Xu, D. Sun, Aqueous foams stabilized by Laponite and CTAB, Colloids Surf. A: Physicochem. Eng. Aspects 317 (2008) 406–413, https://doi.org/10.1016/j.colsurfa.2007.11.010.
[13] M. Manilo, N. Lebovka, S. Barany, Characterization of the electric double layers of multi-walled carbon nanotubes, laponite and nanotube + laponite hybrids in aqueous suspensions, Colloids Surf. A: Physicochem. Eng. Aspects 462 (2014) 211–216, https://doi.org/10.1016/j.colsurfa.2014.09.006.
[14] D.W. Thompson, J.T. Butterworth, The nature of Laponite and its aqueous dispersions, J. Colloid Interface Sci. 151 (1) (1992) 236–243, https://doi.org/10.1016/0021-9797(92)90254-J.
[15] S.L. Tawari, D.L. Koch, C. Cohen, Electrical double-layer effects on the brownian diffusivity and aggregation rate of Laponite clay particles, J. Colloid Interface Sci. 240 (2001) 54–66, https://doi.org/10.1006/jcis.2001.7646.
[16] B. Ruzicka, E. Zaccarelli, A fresh look at the Laponite phase diagram, Soft Matter 7 (2011) 1268–1286, https://doi.org/10.1039/c0sm00590h.
[17] A. Mourchid, E. Lécolier, H. van Damme, P. Levitz, On viscoelastic, birefringent, and swelling properties of Laponite clay suspensions: revisited phase diagram, Langmuir 14 (1998) 4723–4781, https://doi.org/10.1021/la980117p.
[18] L. Rosta, H.R. von Gunten, Light scattering characterization of Laponite sols, J. Colloid Interface Sci. 134 (1990) 397–406, https://doi.org/10.1016/0021-9797(90)90149-I.
[19] J. Yu, O. Andersson, G.P. Johari, Effects of nanometer-size Laponite disks on thermal conductivity and specific heat of water and ice, and the gelation time, Colloid Polym. Sci. 293 (2015) 901–911, https://doi.org/10.1007/s00396-014-3481-8.

[20] S.M. Häffner, L. Nyström, K.L. Browning, H.M. Nielsen, A.A. Strömstedt, M.J.A. van der Plas, A. Schmidtchen, M. Malmsten, Interaction of Laponite with membrane components-consequences for bacterial aggregation and infection confinement, ACS Appl. Mater. Interfaces 11 (17) (2019) 15389–15400, https://doi.org/10.1021/acsami.9b03527.
[21] F.M. van der Kooij, H.N.W. Lekkerkerker, Formation of nematic liquid crystals in suspensions of hard colloidal platelets, J. Phys. Chem. B 102 (1998) 7829–7832, https://doi.org/10.1021/jp981534d.
[22] A. Shalkevich, A. Stradner, S.K. Bhat, F. Muller, P. Schurtenberger, Cluster, glass, and gel formation and viscoelastic phase separation in aqueous clay suspensions, Langmuir 23 (7) (2007) 3570–3580, https://doi.org/10.1021/la062996i.
[23] T. Latendorf, U. Gerstel, Z. Wu, J. Bartels, A. Becker, A. Tholey, J.-M. Schröder, Cationic intrinsically disordered antimicrobial peptides (cidamps) represent a new paradigm of innate defense with a potential for novel anti-infectives, Scient. Rep. 9 (1) (2019) 3331, https://doi.org/10.1038/s41598-019-39219-w.
[24] D. Ciumac, H. Gong, X. Hu, J.R. Lu, Membrane targeting cationic antimicrobial peptides, J. Colloid Interface Sci. 537 (2019) 0021–9797, https://doi.org/10.1016/j.jcis.2018.10.103.
[25] H. Zazo, C.I. Colino, J.M. Lanao, Current applications of nanoparticles in infectious diseases, J. Control. Release 224 (2016) 86–102, https://doi.org/10.1016/j.jconrel.2016.01.008.
[26] E.P. Rebitski, P. Aranda, M. Darder, R. Carraro, E. Ruiz-Hitzky, Intercalation of metformin into montmorillonite, Dalton Trans. 47 (2018) 3185–3192, https://doi.org/10.1039/C7DT04197G.
[27] E.P. Rebitski, G.P. Souza, S.A. Santana, S.B. Pergher, A.C. Alcântara, Bionanocomposites based on cationic and anionic layered clays as controlled release devices of amoxicillin, Appl. Clay Sci. 173 (2019) 35–45, https://doi.org/10.1016/j.clay.2019.02.024.
[28] M. Vazdar, J. Heyda, P.E. Mason, G. Tesei, C. Allolio, M. Lund, P. Jungwirth, Arginine magic: guanidinium like-charge ion pairing from aqueous salts to cell penetrating peptides, Acc. Chem. Res. 51 (2018) 1455–1464, https://doi.org/10.1021/acs.accounts.8b00098.
[29] G. Tesei, M. Vazdar, M.R. Jensen, C. Cragnell, P.E. Mason, J. Heyda, M. Skepö, P. Jungwirth, M. Lund, Self-association of a highly charged arginine-rich cell-penetrating peptide, PNAS 114 (43) (2017) 11428–11433, https://doi.org/10.1073/pnas.1712078114.
[30] D. Franke, M.V. Petoukhov, P.V. Konarev, A. Panjkovich, A. Tuukkanen, H.D.T. Mertens, A.G. Kikhney, N.R. Hajizadeh, J.M. Franklin, C.M. Jeffries, D.I. Svergun, ATSAS 2.8: a comprehensive data analysis suite for small-angle scattering from macromolecular solutions, J. Appl. Crystallogr. 50 (4) (2017) 1212–1225, https://doi.org/10.1107/S1600576717007786.
[31] M. Segad, S. Hanski, U. Olsson, J. Ruokolainen, T. Åkesson, B. Jönsson, Microstructural and swelling properties of Ca and Na montmorillonite: (in situ) observations with cryo-TEM and SAXS, J. Phys. Chem. C 116 (13) (2012) 7596–7601, https://doi.org/10.1021/jp300531y.
[32] M. Segad, B. Jönsson, B. Cabane, Tactoid formation in montmorillonite, J. Phys. Chem. C 116 (46) (2012) 25425–25433, https://doi.org/10.1021/jp3094929.
[33] M. Segad, Microstructure determination of IQ-WB clays: a direct procedure by small-angle X-ray scattering, J. Appl. Crystallogr. 46 (2013) 1316–1322, https://doi.org/10.1107/S0021889813020931.
[34] Zetasizer Nano Series, User manual, Malvern Instruments Ltd. MAN 0317 (2012) 1.1.
[35] M.J. Abraham, D. van der Spoel, E. Lindahl, B. Hess, the GROMACS development team, GROMACS User Manual version 5.0.4, <www.gromacs.org>, 2014.
[36] G. Gutiérrez, B. Johansson, Molecular dynamics study of structural properties of amorphous $Al_2O_3$, Phys. Rev. B 65 (2002) 104202, https://doi.org/10.1103/PhysRevB.65.104202.
[37] J. Labanda, J. Llorens, Influence of sodium polyacrylate on the rheology of aqueous Laponite dispersions, J. Colloid Interface Sci. 289 (2005) 86–93, https://doi.org/10.1016/j.jcis.2005.03.055.
[38] J. Labanda, J. Sabaté, J. Llorens, Rheology changes of Laponite aqueous dispersions due to the addition of sodium polyacrylates of different molecular weights, Colloids Surf. A: Physicochem. Eng. Aspects 301 (2007) 8–15, https://doi.org/10.1016/j.colsurfa.2007.01.011.
[39] A.Y. Huang, J.C. Berg, High-salt stabilization of Laponite clay particles, J. Colloid Interface Sci. 296 (2006) 159–164, https://doi.org/10.1016/j.jcis.2005.08.068.
[40] M. Jonsson (Skepö), P. Linse, Polyelectrolyte-macroion complexation. I. Effect of linear charge density, chain length, and macroion charge, J. Chem. Phys. 115 (2001) 3406–3418, https://doi.org/10.1063/1.1385792.
[41] M. Skepö, P. Linse, Complexation, phase separation, and redissolution of polyelectrolyte-macroion solutions, Macromolecules 36 (2003) 508–519, https://doi.org/10.1021/ma020634l.
[42] M. Skepö, P. Linse, Dissolution of a polyelectrolyte-macroion complex by addition of salt, Phys. Rev. E 66 (2002) 051807, https://doi.org/10.1103/PhysRevE.66.051807.

# Intercalation of cationic peptides within Laponite layered clay minerals in aqueous suspensions: The effect of stoichiometry and charge distance matching

Maria Jansson [a,*], Samuel Lenton [a,b], Tomás S. Plivelic [c] and Marie Skepö [a,b,*]

[a] *Theoretical Chemistry, Lund University, P.O. Box 124, SE-221 00 Lund, Sweden*
[b] *LINXS - Lund Institute of Advanced Neutron and X-ray Science, Scheelevägen 19, SE-223 70 Lund, Sweden*
[c] *MAX IV Laboratory, Lund University, P.O. Box 118, SE-221 00 Lund, Sweden*

## 1. Supplementary material

### 1.1. Single-platelet simulations

The linear regression at the distance $h = 1.1 \pm 0.2$ nm extracted from the distribution of peptide beads as a function of the distance from the platelet surface are shown in Figure 1.

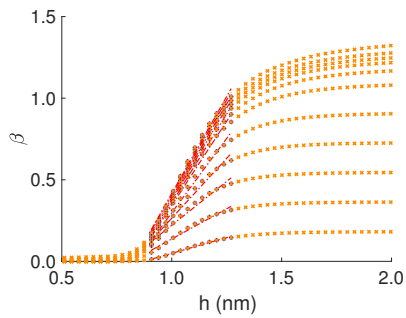


Figure 1: The distribution of peptide beads represented as the stoichiometric charge-ratio, $\beta$, from the single-platelet simulations as a function of the distance from the platelet surface, $h$, where the linear regressions at $h = 1.1 \pm 0.2$nm are shown as the dashed red lines.

### 1.2. General applicability of the model

Radial distribution functions and representative snapshots of the configurations from the simulations for the study of the peptide properties are shown for the alternation of the chain with respect to the chain length, the total charge, the chain length as well as the charge of each bead, the flexibility, and the bond length in Figure 2–6, respectively.

*Corresponding authors at: Theoretical Chemistry, Lund University, P.O. Box 124, SE-221 00 Lund, Sweden (M. Jansson and M. Skepö).
*Email addresses:* maria.jansson@teokem.lu.se (M. Jansson ); marie.skepo@teokem.lu.se (M. Skepö )

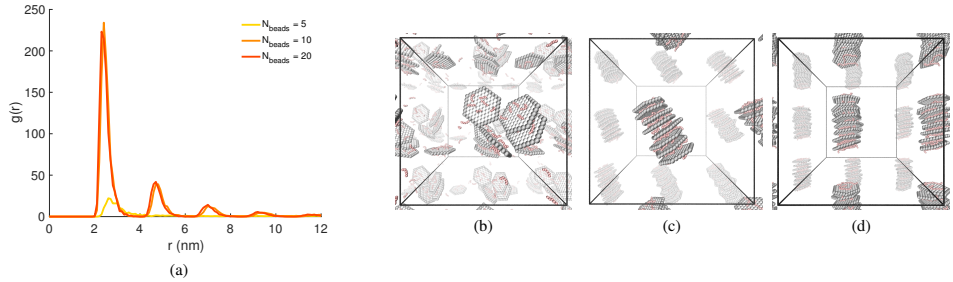


Figure 2: (a) Radial distribution functions showing the effect of modifying the peptides chain length. (b–d) Representative snapshots of the configurations with (b) $N_{\text{beads}} = 5$, (c) $N_{\text{beads}} = 10$, and (d) $N_{\text{beads}} = 20$. The counterions are omitted for clarity, the platelets are shown in grey, the peptides are shown in red, and the cubic simulation box is shown in black (periodic images are shown outside the simulation box).

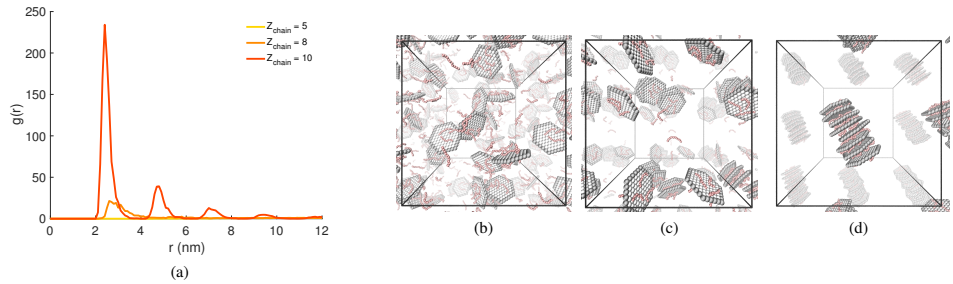


Figure 3: (a) Radial distribution functions showing the effect of modifying the peptides total charge. (b–d) Representative snapshots of the configurations with (b) $Z_{\text{chain}} = 5$, (c) $Z_{\text{chain}} = 8$, and (d) $Z_{\text{chain}} = 10$. The counterions are omitted for clarity, the platelets are shown in grey, the peptides are shown in red, and the cubic simulation box is shown in black (periodic images are shown outside the simulation box).

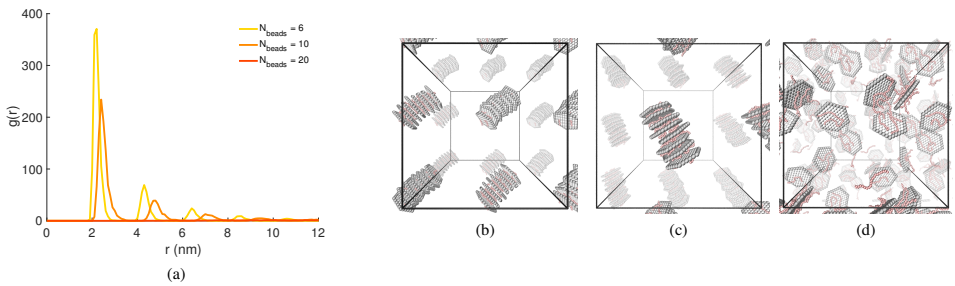


Figure 4: (a) Radial distribution functions showing the effect of modifying the peptides chain length as well as the charge of each bead. (b–d) Representative snapshots of the configurations with (b) $N_{\text{beads}} = 6$, (c) $N_{\text{beads}} = 10$, and (d) $N_{\text{beads}} = 20$. The counterions are omitted for clarity, the platelets are shown in grey, the peptides are shown in red, and the cubic simulation box is shown in black (periodic images are shown outside the simulation box).

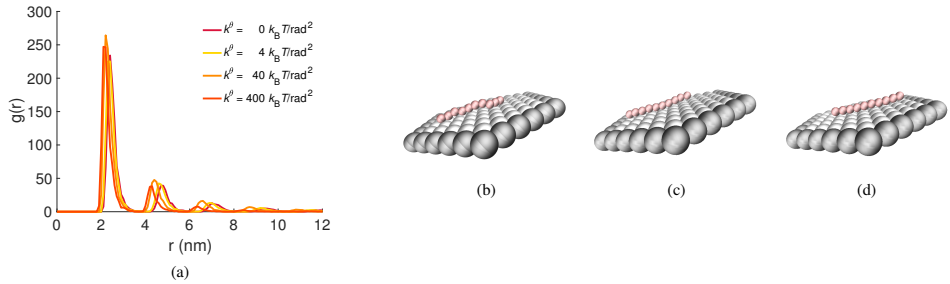


Figure 5: (a) Radial distribution functions showing the effect of modifying the peptides flexibility. (b–d) Representative snapshots of the configurations from the single-platelet simulations with (b) $k^\theta = 0\ k_B T/\text{rad}^2$, (c) $k^\theta = 40\ k_B T/\text{rad}^2$, and (d) $k^\theta = 400\ k_B T/\text{rad}^2$. The counterions are omitted for clarity, the platelet is shown in grey, and the peptide is shown in red.

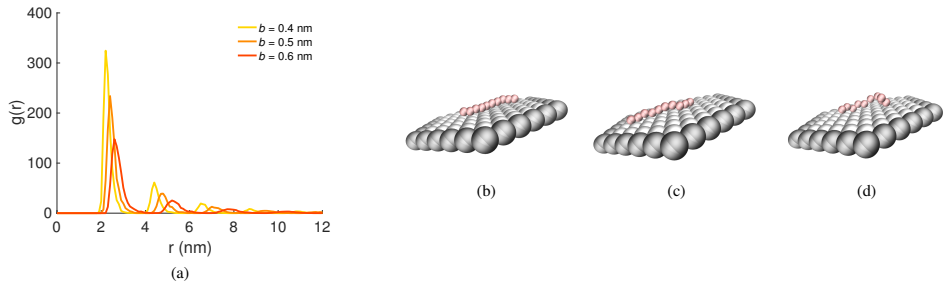


Figure 6: (a) Radial distribution functions showing the effect of charge distance matching with respect to the peptides bond length. (b-d) Representative snapshots of the configurations from the single-platelet simulations with (b) $b = 0.4$nm, (c) $b = 0.5$nm, and (d) $b = 0.6$nm. The counterions are omitted for clarity, the platelet is shown in grey, and the peptide is shown in red.

# Paper v

Reprinted from *Int. J. Mol. Sci.*, 2019, **20**, 6217
M. Jansson and M. Skepö
©2019 with permission from MDPI.

International Journal of
*Molecular Sciences*

MDPI

*Article*

# Polyelectrolyte-Nanoplatelet Complexation: Is It Possible to Predict the State Diagram?

**Maria Jansson [1,*] and Marie Skepö [1,2,*]**

[1] Theoretical Chemistry, Lund University, P.O. Box 124, SE-221 00 Lund, Sweden
[2] LINXS—Lund Institute of Advanced Neutron and X-ray Science, Scheelevägen 19, SE-223 70 Lund, Sweden
* Correspondence: maria.jansson@teokem.lu.se (M.J.); marie.skepo@teokem.lu.se (M.S.)

Received: 20 October 2019; Accepted: 4 December 2019; Published: 10 December 2019


**Abstract:** The addition of polyelectrolytes (PEs) to suspensions of charged colloids, such as nanoplatelets (NPs), is of great interest due to their specific feature of being either a stabilizing or a destabilizing agent. Here, the complexation between a PE and oppositely charged NPs is studied utilizing coarse-grained molecular dynamics simulations based on the continuum model. The complex formation is evaluated with respect to the stoichiometric charge-ratio within the system, as well as by the alternation of the chain properties. It is found that the formed complexes can possess either an extended or a compact shape. Moreover, it is observed that the chain can become overcharged by the oppositely charged NPs. With an increase in chain length, or a decrease in chain flexibility, the complex obtains a more extended shape, where the NPs are less tightly bound to the PE. The latter is also true when reducing the total charge of the chain by varying the linear charge density, whereas in this case, the chain contracts. With our coarse-grained model and molecular dynamics simulations, we are able to predict the composition and the shape of the formed complex and how it is affected by the characteristics of the chain. The take-home message is that the complexation between PEs and NPs results in a versatile and rich state diagram, which indeed is difficult to predict, and dependent on the properties of the chain and the model used. Thus, we propose that the present model can be a useful tool to achieve an understanding of the PE-NPs complexation, a system commonly used in industrial and in technological processes.

**Keywords:** polyelectrolyte; nanoplatelet; complexation; molecular dynamics simulations; charge stoichiometry; chain length; linear charge density; chain flexibility

## 1. Introduction

The complexation between polyelectrolytes (PEs) and oppositely charged colloidal particles is of great interest for various industrial and technological processes [1,2]. PEs are highly soluble in water due to their charged nature and adsorb strongly to oppositely charged particles [3–8]. There exists a large variety of natural and synthetic PEs with different properties, which are used for a wide range of applications [9,10]. One specific feature is that a suspension of charged colloids can be either stabilized or destabilized with the addition of an oppositely charged PE [11–13]. Nanoplatelets (NPs), such as clays, have both an anisotropic shape and charge, where the lateral dimensions can be several orders of magnitude larger than the thickness [14]. The surface, i.e., the face of the NP, usually holds a high negative charge, while the rim can either be negative, neutral, or positive, depending on the pH of the solution [15,16]. The complex formation of PEs and NPs depends strongly on the properties of the macromolecules and a variation of those results in a state diagram that contains a rich and versatile variety of structures. The effect of

the PEs' properties has been studied previously for PE-macroion complexation by utilizing canonical Monte Carlo simulations [17,18]. The authors investigated the complex formation between one PE and an addition of oppositely charged spherical macroions with respect to the linear charge density, length, and flexibility. It was found that the capacity to complex macroions decreased with a reduction in the linear charge density or in the chain length, where the former gave rise to a looser complex and the latter to the opposite. Further, it was observed that with a decrease in the flexibility of the PE, the ability to overcharge the complex increased, where the macroions in the complex became more linearly arranged.

Recently, the intercalation of a highly charged unstructured peptide within the layered structure of the synthetic clay LAPONITE®[19] was studied [20]. It was found that complexes consisting of stacked NPs, also denoted tactoids, were formed as a function of the peptide concentration. Above a matched charge-ratio between the peptide and the clay, the growth of the tactoids was inhibited, and a tactoidal dissolution was observed, caused by the excess of chains and, thus, overcharging of the NPs by the former. In the present work, the complexation between a positively charged PE and anisotropically charged NPs, where the latter consists of a negatively charged surface and a positively charged rim, is studied with coarse-grained molecular dynamics (MD) simulations based on the continuum model. The importance of the stoichiometric charge-ratio on the formed complex, as well as on the inherent PE properties is investigated. Furthermore, alternation of the PEs properties is performed in order to determine the preferred shape and the composition of the formed complex, as well as the conformation of the PE. By using MD simulations, we show that the complex formation depends strongly on the PE properties and that the complex adopts a variety of different structures.

## 2. Theoretical Section

### *2.1. The Coarse-Grained Model*

In the simulation model, the NP is modeled as a finite hexagonal monolayer of connected coarse-grained spheres, defined as sites. The thickness and the diameter of the NP were 1 and 11 nm, respectively, where the diameter was smaller than the experimental one in order to reduce the computational cost. The model of the NP was mimicking the properties of clay [21]. The unit charges were located at the center of each site to obtain a homogeneous charge distribution over the NP. Charge anisotropy was implemented by adding both face and rim elementary charges with $Z_{\text{face}} = -61$, and $Z_{\text{rim}} = +6$; hence, the total net elementary charge of the NP was $Z_{\text{p}} = -55$. The PE was modeled as a positively charged chain of connected coarse-grained beads, each with a elementary charge of $Z_{\text{b}} = +1$. A schematic representation of the NP, i.e., the clay platelet, and the PE is shown in Figure 1.

The total NP and PE charges were neutralized by monovalent counterions, which were added explicitly, and modeled as freely moving charges. The dimensionless stoichiometric charge-ratio in the system, and the complexed charge-ratio, will be used throughout to describe the system and the complex with respect to under- and overcharging. The former is defined as the absolute value of the NPs' total net negative charge divided by the number of positive PE charges, i.e.,

$$\beta = \left| \frac{N_{\text{p}} \cdot Z_{\text{p}}}{N_{\text{b}} \cdot Z_{\text{b}}} \right|. \tag{1}$$

$N_{\text{p}}$ is the number of NPs, which was varied from one to 16, in order to obtain a stoichiometric charge-ratio of $\beta = 0.13$–$2.0$, and $N_{\text{b}}$ is the number of beads within the PE chain. The complexed charge-ratio is defined as the ratio between the complexed NPs' total net negative charge and the total positive charges of the PE, i.e.,

$$\beta^c = \left| \frac{N_p^c \cdot Z_p}{N_b \cdot Z_b} \right|, \quad (2)$$

where $N_p^c$ is the number of NPs complexed to the PE. Hence, the case $\beta < 1.0$ represents a system with more PE charges than NP charges, $\beta = 1.0$ an equal amount of PE and NP charges, and $\beta > 1.0$ and excess of NP charges. Moreover, $\beta^c < 1.0$ refers to an undercharged complex, $\beta^c = 1.0$ to a neutral complex, and $\beta^c < 1.0$ to an overcharged complex.

**Figure 1.** Schematic representation of the coarse-grained model for a system consisting of one nanoplatelet (NP) and one polyelectrolyte (PE) with $N_b = 440$. The face (light grey) and the rim (dark grey) of the NP have a total charge of $Z_{face} = -61$ and $Z_{rim} = +6$, respectively, and the PE beads (red) each have a charge of $Z_b = +1$. The NP is modeled to mimic a clay platelet.

To investigate how the complexation between the PE and the NPs depends on the properties of the former, the effect of the chain length, the total charge through the linear charge density, and the flexibility were studied. For the chain length, the number of beads was varied between 440 and 800, with an addition of eight NPs. Regarding the total charge and the flexibility, the PE with $N_b = 440$ was used with varied linear charge density or angular potential. Furthermore, the effect of the NPs' rim was studied by setting the rim charge in the model to zero for the PE with $N_b = 488$. The reader should notice that a PE with a length of 440 and 488 either matches the total net negative charge or the negative face charges of a system where eight NPs have been added. The specifications of the systems evaluated in this study are compiled in Table 1.

**Table 1.** Specifications of the systems.

| System | $N_p$ | $Z_{face}$ | $Z_{rim}$ | $N_{chains}$ | $N_b$ | $Z_b$ | $k^\theta$ ($k_BT$/rad$^2$) |
|---|---|---|---|---|---|---|---|
| S.I | 1–16 | −61 | 6 | 1 | 440 | 1 | 0 |
| S.II | 8 | −61 | 6 | 1 | 440–800 | 1 | 0 |
| S.III | 1–16 | −61 | 6 | 1 | 440 | 0.25–1 | 0 |
| S.IV | 1–16 | −61 | 6 | 1 | 440 | 1 | 0–400 |
| S.V | 1–16 | −61 | 6 | 1 | 488 | 1 | 0 |
| S.VI | 1–16 | −61 | 0 | 1 | 488 | 1 | 0 |

In the simulations, the solvent was treated implicitly as a dielectric continuum with the dielectric constant of $\epsilon_r = 78.3$. All the interactions in the system were assumed to be pairwise additive, and the electrostatic pair potential is defined as:

$$u_{ij}^{\mathrm{EL}}(r_{ij}) = \frac{e^2 z_i z_j}{4\pi\epsilon_0\epsilon_r r_{ij}}, \tag{3}$$

where $e$ is the elementary charge, $z_i$ is the valency of beads/sites within the PE/NP $i$, $\epsilon_0$ is the permittivity of the vacuum, and $r_{ij}$ is the center-to-center distance between beads/sites $i$ and $j$. In addition, the beads/sites also interact via a strictly repulsive, truncated, and shifted Lennard–Jones (TLJ) potential, defined as:

$$u_{ij}^{\mathrm{TLJ}}(r_{ij}) = \begin{cases} \epsilon_{\mathrm{TLJ}}\left[\left(\frac{\sigma_{ij}}{r_{ij}}\right)^{12} - 2\left(\frac{\sigma_{ij}}{r_{ij}}\right)^{6} + 1\right], & \text{if } r_{ij} < \sigma_{ij} \\ 0, & \text{otherwise} \end{cases}. \tag{4}$$

The strength of the short range potential was set to $\beta\epsilon_{\mathrm{TLJ}} = 1$, where $\beta = 1/\ k_{\mathrm{B}}T$, $k_{\mathrm{B}}$ is the Boltzmann constant, and $T$ = 298 K. $\sigma_{ij} = (\sigma_i + \sigma_j)/2$, and $\sigma_i$ is the diameter of species $i$, where $\sigma_{ion} = \sigma_b = 0.4$ nm and $\sigma_{site} = 1.0$ nm. Thus, the total potential between all pairs is defined as:

$$u_{ij}(r_{ij}) = u_{ij}^{\mathrm{TLJ}}(r_{ij}) + u_{ij}^{\mathrm{EL}}(r_{ij}). \tag{5}$$

Furthermore, all the adjacent beads/sites within the PE/NP are connected by a harmonic bond potential:

$$u_b(r_{ij}) = \frac{1}{2}k^b(r_{ij} - b)^2. \tag{6}$$

$k^b$ is the force constant, and $b$ is the equilibrium bond length, where $b = 0.5$ and 1.0 nm for the PE and the NP, respectively. The flexibilities of the PE/NP were constrained by a harmonic angular potential between triplets of beads/sites:

$$u(\theta_{ijk}) = \frac{1}{2}k^\theta(\theta_{ijk} - \theta^0)^2, \tag{7}$$

where $k^\theta$ is the force constant, $\theta_{ijk}$ is the bond angle between beads/sites $i$, $j$, and $k$, and $\theta^0 = \pi$.

### *2.2. Molecular Dynamics Simulations*

The MD simulations were performed with the software package GROMACS (Version 5.0.4) [22]. A cubic simulation box with three-dimensional periodic boundary conditions was used, with a box length of 100 nm, corresponding to a volume fraction of ∼0.005–0.08%, and ∼0.002–0.003% for 1–16 NPs and for the chain length of $N_{\mathrm{b}} = 440$–800, respectively. Due to the very low volume fraction of the added particles, the dielectric constant of the solution was not expected to be affected. The time step was set to 10 fs, with a total of $10^7$ steps. Newton's equation of motion of freely moving species, i.e., the NPs, the PE, and the counterions, was integrated using the leap-frog algorithm. To account for the long range electrostatic contribution, fast particle-mesh Ewald summation was utilized with a 6 nm real-space Coulomb cutoff and a Fourier spacing equal to 0.6 nm. The thermostat was v-rescale, a temperature coupling using velocity rescaling with a stochastic term, and the solvent was treated implicitly with the dielectric constant of $\epsilon_{\mathrm{r}} = 78.3$. For an in-depth description of the input parameters, the reader is referred to the user manual [22]. The convergence of the system was evaluated from the complexation probability ($P_{\mathrm{c}}(i_{\mathrm{b}})$) function. This provides information about the probability that the bead, $i_{\mathrm{b}}$, in the PE is complexed with either one or several NPs and, thus, is a measure of the convergence of the sampling, i.e., both ends of the PE should experience the same environment. The threshold at which the bead was set to be complexed was determined from the bead-NP separation obtained from the radial distribution functions (data not

shown) to <1.4 nm, i.e., when the separation between the center-of-mass of one PE bead and the NP did not exceed the distance $r = R_{site} + R_b + 0.7$ nm. The complexation probability function ranged from zero to one, where the lower boundary corresponded to the case where the bead was never complexed with the NP and the upper boundary corresponded to the case where the bead was always in a complex. The $P_c(i_b)$ for the reference system S.I is shown in Figure 2, and it is observed that all of the beads had a high complexation probability for $\beta \geq 1.0$. For $\beta = 0.5$, the beads within the PE displayed both high and low complexation probabilities, which implies that not all of the beads were involved in the complex. However, simulations for replicates of the systems with different initial configurations were performed from which the same results were obtained, and hence, it can be concluded that they converged.

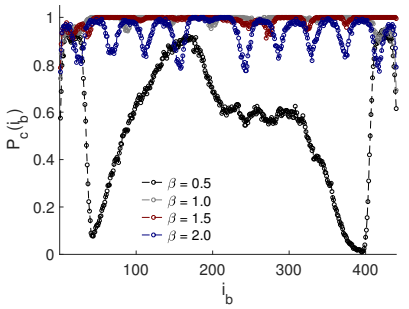


**Figure 2.** Complexation probability, $P_c(i_b)$, as a function of the bead number, $i_b$, for $N_b = 440$.

### *2.3. Structural Analysis*

The structural information obtained from the simulations was analyzed by the NP-NP structure factor, defined as:

$$S(q) = \left\langle \frac{1}{N} \sum_{i=1}^{N} \sum_{j=1}^{N} \frac{\sin(qr_{ij})}{qr_{ij}} \right\rangle, \tag{8}$$

where $N$ is the total number of NP sites in the system. Assuming an isotropic scattering, the equation of the total structure factor can be rewritten as:

$$S(q) = 1 + 4\pi \frac{N}{V} \int_0^\infty (g(r) - 1) r^2 \frac{\sin(qr)}{qr} dr, \tag{9}$$

where *g(r)* is the radial distribution function between all the NP sites in the system. If *g(r)* is not approaching one at large separations due to the finite box length, a window function can be used to reduce the artifacts, according to:

$$S_w(q) = 1 + 4\pi \frac{N}{V} \int_0^\infty (g(r) - 1) r^2 \frac{\sin(qr)}{qr} \frac{\sin(\pi r / R_c)}{\pi r / R_c} dr, \tag{10}$$

where $R_c$ is the maximum distance in *g(r)* [23].

## 3. Results and Discussion

### *3.1. Composition of the PE-NP Complex*

As a first step, the formation and composition of the formed complexes in the reference system, S.I, were considered. Figure 3 shows the average number of NPs complexed to the PE, $\langle N \rangle$, as a function of the number of NPs added into the system. It was observed that there was a linear increase in complexation to $N_p = 10$ and that a plateau was reached. Moreover, from the complexed charge-ratio, $\beta^c$, it was found that the PE became overcharged by approximately 25%; see Figure S1 in the Supplementary Materials. This number was of the same order as was reported by Jonsson and Linse, when studying the complexation between a PE and oppositely charged spherical macroions [17,18].

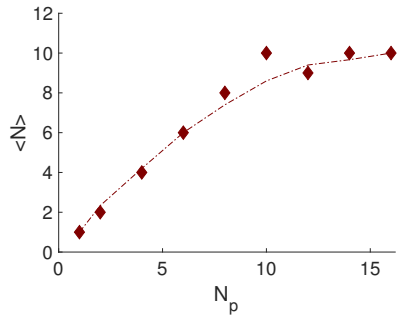


**Figure 3.** The average number of NPs complexed to the PE, $\langle N \rangle$, as a function of the number of NPs, $N_p$, added into the system. The dashed-dotted line is an implemented smooth function.

The shape of the formed complexes was determined from the NP-NP structure factors, $S_w(q)$, presented as Kratky plots in Figure 4. Focusing on the low $q$-region, it was shown that when the PE was either under- or overcharged by the opposite charges of the NP, as for $\beta = 0.5$ and 2.0, the complex possessed a more extended shape, whereas when it was net neutral, or only slightly overcharged ($\beta = 1.0$–$1.5$), the complex obtained a compact shape. Furthermore, the peak intensity decreased with an increase in $\beta$, indicating that the most well ordered structure of the NPs was found at $\beta = 1.0$. This was confirmed by the high $q$-region where both $\beta = 1.0$ and 1.5 exhibited Bragg peaks. At $\beta > 1.5$, the periodicity between the NPs decreased, suggesting a dissolution of the complex. The average distance, i.e., the $d$-spacing, between the mid-plane of two adjacent NPs was $d_{\text{Bragg}} = 2.2$ and 2.3 nm for $\beta = 1.0$ and 1.5, respectively, determined from the relation: $d_{\text{Bragg}} = 2\pi/q_{\text{max}}$, where $q_{\text{max}}$ is the position of the maximum intensity of the Bragg peak. These numbers were in correlation with the distances reported in the study regarding the intercalation of a highly charged peptide within LAPONITE®[19] layered clay minerals [20]. Moreover, the complexation of NPs induced by multivalent ions, such as calcium, was studied by a combination of MD simulations with experimental techniques [24]. The reported distance between the NPs was approximately ∼1.3 nm, which was almost half the size of the distance found in this study. Hence, this denotes that the distance between NPs was not affected by the PE length; instead, it depended on the type of added agent, i.e., a PE or an ion.

The conformation of the PE was analyzed by the normalized radius of gyration, $R_g/R_g^0$, i.e., $R_g$ of the PE in the system with NPs divided by $R_g$ of the undisturbed chain. From Figure 5, it is shown that the PE in the complex was more contracted than the undisturbed PE and that $R_g/R_g^0$ exhibited two pronounced minima for $\beta = 1.0$ and 1.5, where the Kratky plots indicated a compact shape of the obtained complexes.

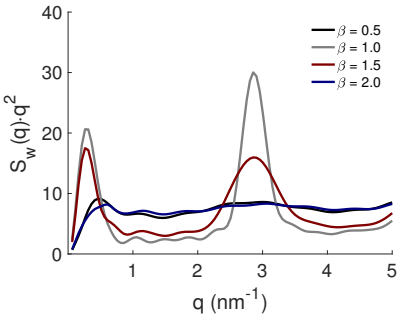


**Figure 4.** The NP-NP structure factors, $S_w(q)$, presented as Kratky plots for the PE with $N_b = 440$.

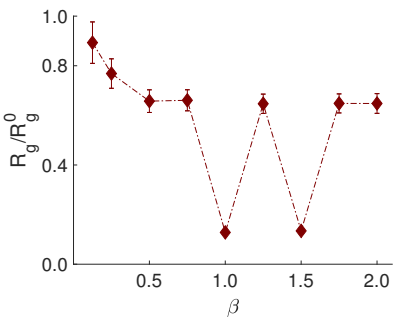


**Figure 5.** The normalized radius of gyration, $R_g/R_g^0$, of PE as a function of the stoichiometric charge-ratio, $\beta$. Error bars are included, and for some data points, the error is smaller than the symbol size. The dashed-dotted line is a guide for the eye.

From the simulations, representative snapshots of the systems were extracted (see Figure 6), where two different structures of the complex depending on $\beta$ were found, i.e., a band-like formation, as well as a stack of NPs, the latter for $\beta = 1.0$ and 1.5. These snapshots validated the above mentioned results regarding the shape and conformation of the PE within the complex and concluded that the state diagram of the obtained complexes was clearly depending on $\beta$.

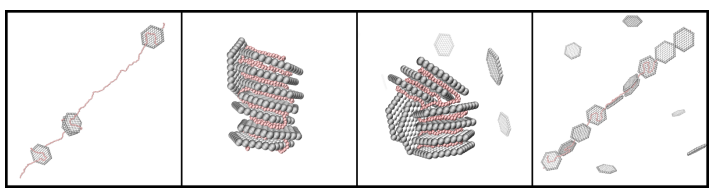

**Figure 6.** Representative snapshots of the different structures with $\beta = 0.5$, 1.0, 1.5, and 2.0 (from left to right). The counterions are omitted for clarity; the NPs are shown in grey; and the PE is shown in red.

### *3.2. Effect of PE Length*

The effect of the PE properties on the complexation between the PE and the NPs was studied; see the system S.II in Table 1 for specifications. Here, the number of the latter was constant, $N_p = 8$, whereas the

length of the former was varied between $N_b = 440$–$800$. As expected, all NPs were complexed to the PE, and the reader should notice that when the PE length was increasing, the degree of undercharging was also increasing, i.e., there was an excess of PE charges in the system. The Kratky plot between the NPs in Figure 7 shows that the formed complexes attained a compact shape independently of the number of beads within the PE, although there was a linear decrease in the intensity as is visible by the peak positions at low $q$, indicating that the periodicity between the NPs decreased. This was further confirmed by the Bragg peaks at high $q$, where its position shifted towards lower $q$-values with an increase in PE length, i.e., the distance between the NPs was increasing; see Table 2.

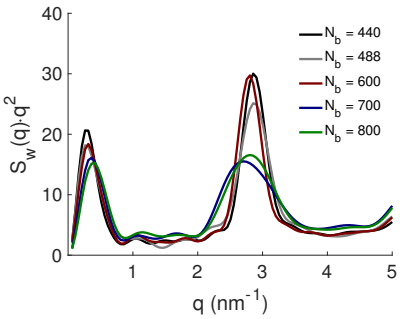


**Figure 7.** The NP-NP structure factor, $S_w(q)$, presented as Kratky plots for the effect of PE length.

Furthermore, the normalized radius of gyration $R_g/R_g^0$ increased with $N_b$, and the representative snapshots in Figure 8 show that the NPs were forming smaller distinct clusters along the PE in a face-to-face configuration when $N_b$ was increasing, i.e., $\beta^c < 1$. Hence, the free energy of the system was decreasing due to the balance between the increase in conformational entropy of the PE and the enhanced electrostatic attractive energy between the NPs and the PE.

**Table 2.** Number of PE beads, $N_b$, stoichiometric charge-ratio in the system, $\beta$, complexed charge-ratio, $\beta^c$, average number of NPs complexed to the PE, $\langle N \rangle$, normalized radii of gyration, $R_g/R_g^0$, and the NP-NP $d$-spacing, $d_{Bragg}$, for the effect of the PE length.

| $N_b$ | $\beta$ | $\beta^c$ | $\langle N \rangle$ | $R_g/R_g^0$ | $d_{Bragg}$ (nm) |
|---|---|---|---|---|---|
| 440 | 1.00 | 1.00 | 8 | 0.13 | 2.21 |
| 488 | 0.90 | 0.90 | 8 | 0.14 | 2.22 |
| 600 | 0.73 | 0.73 | 8 | 0.19 | 2.27 |
| 700 | 0.63 | 0.63 | 8 | 0.37 | 2.41 |
| 800 | 0.55 | 0.55 | 8 | 0.60 | 2.34 |

The effect of the number of NPs was also investigated. An excess of NPs displayed a linear increase in the average number of NPs complexed to the PE, although $\beta^c$ and $R_g/R_g^0$ converged to 1.1 and 0.1, respectively (data not shown).

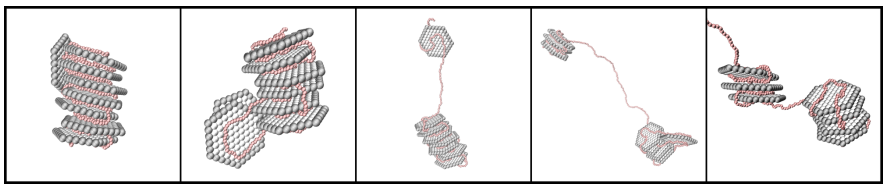

**Figure 8.** Representative snapshots of the complex formed for the PE with $N_b = 440$, 488, 600, 700, and 800 (from left to right). The counterions are omitted for clarity; the NPs are shown in grey; and the PE is shown in red.

### *3.3. Effect of the PE Total Charge*

The effect of the linear charge density, and thereby the total charge of the PE, defined as $Z_{chain} = N_b \cdot Z_b$, was altered in the system S.III, whilst keeping the length of the PE constant. Figure 9 show that $\langle N \rangle$ was decreasing with respect to the decrease of the total charge of the PE, although the possibility of overcharging was increasing, as displayed in Table 3 and in Figure S2 in the Supplementary Materials. For example, comparison of $\beta = 2.0$ resulted in $\beta^c$ of 1.25, 1.5, and 2.0 for $Z_b$ of 1.0, 0.5, and 0.25. Notice that this was independent of the linear charge density of the PE, where the maximum number of complexed NPs was reached; cf. plateau-values.

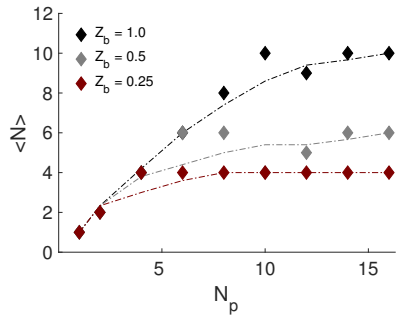


**Figure 9.** The average number of NPs complexed to the PE, $\langle N \rangle$, as a function of the number of NPs, $N_p$, added to the system. The dashed-dotted lines are an implemented smooth function.

**Table 3.** Number of NPs, $N_p$, charge of each PE bead, $Z_b$, stoichiometric charge-ratio in the system, $\beta$, complexed charge-ratio, $\beta^c$, and normalized radii of gyration, $R_g/R_g^0$, for the effect of the PE total charge.

| $N_p$ | $Z_b$ | $\beta$ | $\beta^c$ | $R_g/R_g^0$ | $Z_b$ | $\beta$ | $\beta^c$ | $R_g/R_g^0$ | $Z_b$ | $\beta$ | $\beta^c$ | $R_g/R_g^0$ |
|---|---|---|---|---|---|---|---|---|---|---|---|---|
| 1 | 1.0 | 0.13 | 0.13 | 0.89 | 0.5 | 0.25 | 0.25 | 0.76 | 0.25 | 0.50 | 0.50 | 0.47 |
| 2 | | 0.25 | 0.25 | 0.77 | | 0.50 | 0.50 | 0.47 | | 1.00 | 1.00 | 0.18 |
| 4 | | 0.50 | 0.50 | 0.66 | | 1.00 | 1.00 | 0.15 | | 2.00 | 2.00 | 0.39 |
| 6 | | 0.75 | 0.75 | 0.66 | | 1.50 | 1.50 | 0.73 | | 3.00 | 2.00 | 0.37 |
| 8 | | 1.00 | 1.00 | 0.13 | | 2.00 | 1.50 | 0.76 | | 4.00 | 2.00 | 0.37 |
| 10 | | 1.25 | 1.25 | 0.65 | | 2.50 | 1.00 | 0.76 | | 5.00 | 2.00 | 0.36 |
| 12 | | 1.50 | 1.13 | 0.13 | | 3.00 | 1.25 | 0.19 | | 6.00 | 2.00 | 0.34 |
| 14 | | 1.75 | 1.25 | 0.65 | | 3.50 | 1.50 | 0.27 | | 7.00 | 2.00 | 0.34 |
| 16 | | 2.00 | 1.25 | 0.65 | | 4.00 | 1.50 | 0.26 | | 8.00 | 2.00 | 0.36 |

From the NP-NP structure factors, $S_w(q)$, presented as Kratky plots in Figure 10a, it was observed that the shape of the complexes were dependent on the total charge of the PE and that there was a transition from a compact to more elongated shape when $Z_b$ was decreasing. Furthermore, the Bragg peak was only visible for $Z_b = 1.0$, implying that the face-to-face configuration of the NPs was replaced by a looser structure. These results correlated with the fact that the PE became more contracted with a decrease in the total charge of the PE for $\beta^c = 1.0$ (see the normalized radius of gyration $R_g/R_g^0$ in Table 3), which probably was an effect of an increase in its conformational entropy. The above given results correlated well with the snapshots presented in Figure 10b, and in Figure S3 in the Supplementary Materials.

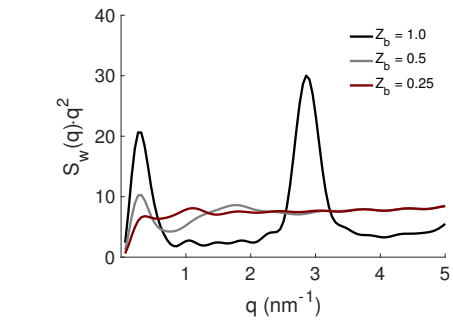


(**a**)

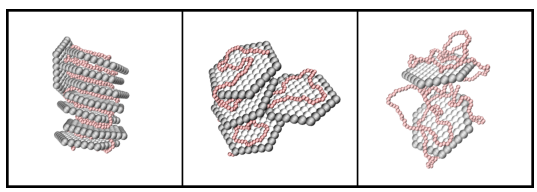

(**b**)

**Figure 10.** (**a**) The NP-NP structure factors, $S_w(q)$, presented as Kratky plots, and (**b**) representative snapshots of the structures with $Z_b = 1.0$, 0.5, and 0.25 (from left to right) for $\beta^c = 1.0$. The counterions are omitted for clarity; the NPs are shown in grey; and the PE is shown in red.

### *3.4. Effect of PE Flexibility*

The effect of the flexibility of the PE on the formed complexes was investigated by varying the strength of the bead-bead angular potential in Equation (7) of the PE, refereed to as the system S.IV, while keeping the PE length constant. The angular force constant $k^\theta$ was set to 0, 40, and 400 $k_BT/\text{rad}^2$, in order to mimic a flexible, a semiflexible, and a stiff chain. Here, both the average number of complexed NPs, as well as the degree of overcharging were within statistical uncertainties, equal independent of PE flexibility; see Figure S4 and Table S1 in the Supplementary Materials. The Kratky plots in Figure 11a for $N_p = 8$, i.e., $\beta^c = 1.0$, show that the complex became less compact when the PE flexibility was decreasing, which was also confirmed by the diminishing Bragg peak. The normalized radius of gyration showed that the conformation of the PE was remarkably different among the complexes, where it became 0.13, 0.60, and 1.03 with increasing stiffness. Notice though that within the complex where the stiff PE resided, it became even more elongated than for the undisturbed PE in the bulk. These trends are confirmed by the representative snapshots in Figure 11b, and in Figure S5 in the Supplementary Materials.

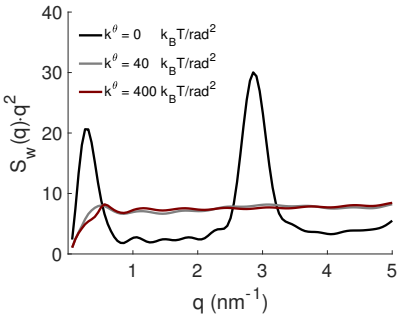


(**a**)

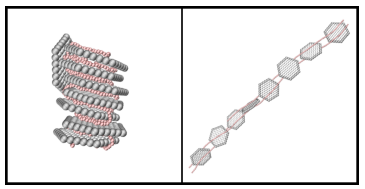

(**b**)

**Figure 11.** (**a**) The NP-NP structure factors, $S_w(q)$, presented as Kratky plots, and (**b**) representative snapshots of the complexes with $k^\theta = 0$, and 400 $k_BT/\text{rad}^2$ (from left to right) for $N_p = 8$. The counterions are omitted for clarity; the NPs and the PE are shown in grey and red, respectively.

The PE flexibility can give rise to a rich state diagram with respect to $\beta^c$, for example for $N_p = 12$, i.e., when the PE was slightly overcharged by NP charges, a Bragg peak for the semiflexible PE began to be discerned, and generally, the repulsive interactions among the NPs in the complex gave rise to a looser structure. These features are shown in the Kratky plots and the representative snapshots in Figure 12. The position of the Bragg peak for the semiflexible PE corresponded to a $d$-spacing of ∼2.1 nm, which was smaller than for the flexible one with $d_{\text{Bragg}} = 2.3$ nm, originated from a stronger adsorption of the PE to the NPs. Moreover, the periodicity between the latter was reduced when increasing the stiffness since the PE possessed a lower chain conformational entropy.

### *3.5. Effect of NP Charge and Rim*

Generally, the interaction between the PE and the NP was governed by electrostatic interactions, where the driving force of complexation was due to the gain in entropy upon counterion release, and the structure of the formed complex depended on the electrostatic attractive interaction between the PE and the NPs in combination with the PE conformational entropy. The NP had a negatively charged face and a positively charged rim, where the latter corresponded to approximately 10% of the former. Here, we studied the impact of the rim charge by comparing three different systems: (a) the PE with $N_b = 440$ where the NP had a net negative charge of $Z_p = -55$, i.e., both face and rim charges were taken into consideration; (b) the length of the PE was increased to $N_b = 488$, and thus, it neutralized only the face charges of a total of eight NPs, although the rim charge was still present; whereas in (c), the same system as in (b) was evaluated with the exception that the rim charge of the NP was set to zero.

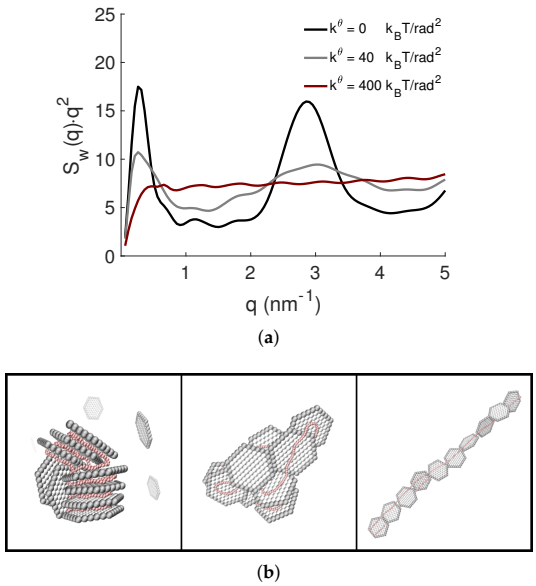


**Figure 12.** (**a**) The NP-NP structure factors, $S_w(q)$, presented as Kratky plots, and (**b**) representative snapshots of the complexes with $k^\theta = 0$, 40, and 400 $k_BT$/rad$^2$ (from left to right) for $N_P = 12$. The counterions are omitted for clarity; the NPs and the PE are shown in grey and red, respectively.

There were no larger discrepancies regarding the average number of complexed NPs between the different systems (see Figure S6 and Table S2 in the Supplementary Materials); nor in the shape of the complexes, which were compact; see the Kratky plots obtained from the NP-NP structure factor in Figure 13a. The main effect is shown at higher $q$-values where the most pronounced Bragg peak was observed when there was a charge-matching between the PE charge and the net charge of the NPs. The Bragg peak became less affected if there was charge-matching between the PE and the face of the NP where the rim charge was intact. By eliminating the rim, the intensity of the Bragg peak decreased noticeably, where also the width of the peak became broader. The positions of the Bragg peaks were consistent throughout ($d_{\text{Bragg}} = 2.2$ nm), indicating that the type of charge-matching within the system, or that the type of rim charge of the NPs, did not affect the adsorption of the PE to the NPs; instead, the main effect of the rim charge was visible in the shape, the structure, as well as in the configuration of the formed complex, which is clearly shown in the state diagram in Figure 13b, and in Figure S7 in the Supplementary Materials. Here, the periodicity of the NPs within the complex was reduced when eliminating the rim charges, resulting in a less ordered structure of stacked NPs with both face-to-face and face-to-edge configurations.

Furthermore, by considering the type of charge-matching between the PE and the NPs in the system, different state diagrams were obtained, illustrated in Figure 14, as an effect of the systems' charge-ratio. For the system with charge-matching between the PE charge and the net charge of the NPs, the state diagram contained two different shapes of the complexes, an extended band-like formation, as well as a compact stack of NPs; while for the system where the PE was charge-matched with the face charges of the NPs, only the compact structure was obtained, with a variety of different configurations.

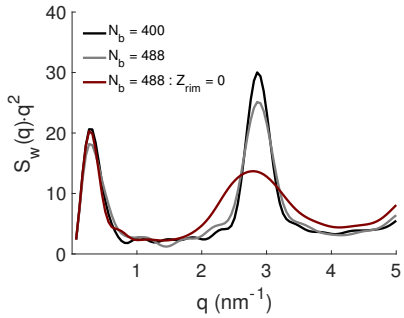


(**a**)

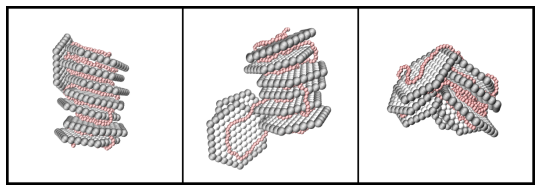

(**b**)

**Figure 13.** (**a**) The NP-NP structure factors, $S_w(q)$, presented as Kratky plots, and (**b**) representative snapshots of the different structures with the PE length of $N_b = 440$, 488, and 488 with $Z_{rim} = 0$ (from left to right) for $\beta^c = 1.0$. The counterions are omitted for clarity; the NPs and the PE are shown in grey and in red, respectively.

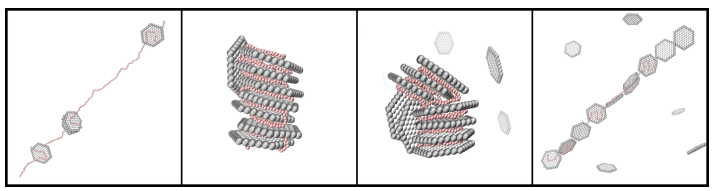

(**a**)

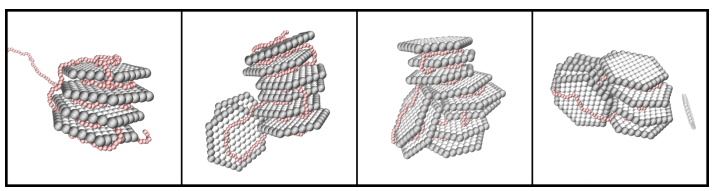

(**b**)

**Figure 14.** Representative snapshots of the different structures with $\beta = 0.5$, 1.0, 1.5, and 2.0 (from left to right) for (**a**) $N_b = 440$, and (**b**) $N_b = 488$. The counterions are omitted for clarity; the NPs and the PE are shown in grey and in red, respectively.

## 4. Conclusions

The complexation between one PE and anisotropically charged NPs was studied as a function of the number of NPs, as well as the PE properties. It was found that the structure, the shape, and the configuration of the formed complex depended on both the NP-PE charge-ratio in the system, as well as on the PE properties. For the PE that was charge-matched with the total charge of the NP, i.e., $N_b = 440$, the PE conformation depended strongly on the charge-ratio, $\beta$, in the system, where the most contracted PE was found at $\beta = 1.0$ and 1.5. Further, depending on $\beta$, the complex can display both extended and compact shapes. For the PE that was charge-matched with the face of the NPs, i.e., $N_b = 488$, the contraction of the PE decreased until the net charge of the complex was zero, i.e., $\beta = 1.0$. For $\beta > 1.0$, the PE conformation was unaffected by the number of complexed NPs, where it possessed a compact shape, consisting of stacked NPs. Considering the PE properties, an increase in the length resulted in an extension of the PE, and a less tightly bound complex was formed, whereas the shape of the complex was unaffected, resulting in stacked NPs. By reducing the total charge of the PE through the linear charge density, it became more contracted, while the complex obtained a less tightly bound structure. Upon decreasing the flexibility of the PE, a reduction in contraction was observed, where the complex was mainly in the extended band-like configuration.

Furthermore, the complex formation was also assumed to depend on the NPs' properties; however, in this study, the model remained constant in order to reduce the number of variable parameters. By increasing the NPs' size, the attractive interactions between the PE and the NPs are enhanced, since the interactions in the system are to a first approximation proportional to the area of the latter.

The information gained in this study concludes that the complexation between PEs and NPs could result in a versatile and rich state diagram, which indeed is difficult to predict, and dependent on the properties of the PE and the details of the model used. Due to the fact that the NPs have an anisotropic charge, and that both the PE and the NPs are highly charged, the systems might get stuck in semi-equilibrium, which makes possible structures and configurations even more difficult to foresee. This was also observed by simulating replicates of the systems to ensure convergence and avoid non-equilibrium structures. Nevertheless, with our simulation model, it was possible to tune both the characteristics of the PE and the NPs, and thus, we propose that the present model can be an useful tool to achieve a hint and an understanding of the PE-NP complexation.

**Supplementary Materials:** The following are available online at http://www.mdpi.com/1422-0067/20/24/6217/s1.

**Author Contributions:** M.J. and M.S. contributed equally to the conceptualization, methodology, formal analysis, visualization, and writing of the article. Supervision, project administration, and funding acquisition were performed by M.S.

**Funding:** This research was funded by the Swedish national strategic e-science research program eSSENCE.

**Acknowledgments:** Computational resources were provided by the Swedish National Infrastructure for Computing (SNIC) through LUNARC, the Center for Scientific and Technical Computing at Lund University.

**Conflicts of Interest:** The authors declare no conflict of interest.

### Abbreviations

The following abbreviations are used in this manuscript:

| | |
|---|---|
| PE | Polyelectrolyte |
| NP | Nanoplatelet |
| MD | Molecular dynamics |

## References


1. Böhm, N.; Kulicke, W.M. Optimization of the use of polyelectrolytes for dewatering industrial sludges of various origins. *Colloid Polym. Sci.* **1997**, *275*, 73–81. [CrossRef]
2. Patel, H.A.; Somani, R.S.; Bajaj, H.C.; Jasra, R.V. Nanoclays for polymer nanocomposites, paints, inks, greases and cosmetics formulations, drug delivery vehicle and waste water treatment. *Bull. Mater. Sci.* **2006**, *29*, 133–145. [CrossRef]
3. Netz, R.R.; Joanny, J.F. Complexation between a Semiflexible Polyelectrolyte and an Oppositely Charged Sphere. *Macromolecules* **1999**, *32*, 9026–9040. [CrossRef]
4. Manias, E.; Touny, A.; Wu, L.; Strawhecker, K.; Lu, B.; Chung, T.C. Polypropylene/Montmorillonite Nanocomposites. Review of the Synthetic Routes and Materials Properties. *Chem. Mater.* **2001**, *13*, 3516–3523. [CrossRef]
5. Stoll, S.; Chodanowski, P. Polyelectrolyte Adsorption on an Oppositely Charged Spherical Particle. Chain Rigidity Effects. *Macromolecules* **2002**, *35*, 9556–9562. [CrossRef]
6. Messina, R.; Holm, C.; Kremer, K. Like-charge colloid–polyelectrolyte complexation. *J. Chem. Phys.* **2002**, *117*, 2947. [CrossRef]
7. Messina, R.; Holm, C.; Kremer, K. Polyelectrolyte adsorption and multilayering on charged colloidal particles. *J. Polym. Sci. B Polym. Phys.* **2004**, *42*, 3557–3570. [CrossRef]
8. Szilagyi, I.; Trefalt, G.; Tiraferri, A.; Maroni, P.; Borkovec, M. Polyelectrolyte adsorption, interparticle forces, and colloidal aggregation. *J Polym. Sci. Pol. Phys.* **2014**, *42*, 3557–3570. [CrossRef]
9. Jiang, H.; Taranekar, P.; Reynolds, J.R.; Schanze, K.S. Conjugated Polyelectrolytes: Synthesis, Photophysics, and Applications. *Angew. Chem. Int.* **2009**, *48*, 4300–4316. [CrossRef]
10. Mecerreyes, D. Polymeric ionic liquids: Broadening the properties and applications of polyelectrolytes. *Prog. Polym. Sci.* **2011**, *36*, 1629–1648. [CrossRef]
11. Pefferkorn, E. The role of polyelectrolytes in the stabilisation and destabilisation of colloids. *Adv. Colloid Interface Sci.* **1995**, *56*, 33–104. [CrossRef]
12. Hierrezuelo, J.; Sadeghpour, A.; Szilagyi, I.; Vaccaro, A.; Borkovec, M. Electrostatic Stabilization of Charged Colloidal Particles with Adsorbed Polyelectrolytes of Opposite Charge. *Langmuir* **2010**, *26*, 15109–15111. [CrossRef] [PubMed]
13. Szilagyi, I.; Sadeghpour, A.; Borkovec, M. Destabilization of Colloidal Suspensions by Multivalent Ions and Polyelectrolytes: From Screening to Overcharging. *Langmuir* **2012**, *28*, 6211–6215. [CrossRef] [PubMed]
14. Michot, L.J.; Bihannic, I.; Porsch, K.; Maddi, S.; Baravian, C.; Mougel, J.; Levitz, P. Phase Diagrams of Wyoming Na-Montmorillonite Clay. Influence of Particle Anisotropy. *Langmuir* **2004**, *20*, 10829–10837. [CrossRef]
15. Tawari, S.L.; Koch, D.L.; Cohen, C. Electrical Double-Layer Effects on the Brownian Diffusivity and Aggregation Rate of Laponite Clay Particles. *J. Colloid Interface Sci.* **2001**, *240*, 54–66. [CrossRef]
16. Delhorme, M.; Jönsson, B.; Labbez, C. Monte Carlo simulations of a clay inspired model suspension: The role of rim charge. *Soft Matter* **2012**, *8*, 9691. [CrossRef]
17. Jonsson, M.; Linse, P. Polyelectrolyte-macroion complexation. I. Effect of linear charge density, chain length, and macroion charge. *J. Chem. Phys.* **2001**, *115*, 3406. [CrossRef]
18. Jonsson, M.; Linse, P. Polyelectrolyte-macroion complexation. I. Effect of chain flexibility. *J. Chem. Phys.* **2001**, *115*, 10975. [CrossRef]
19. BYK Additives & Instruments. *BYK Technical Information B-RI 21 LAPONITE® Performance Additives*; BYK Additives & Instruments: Wesel, Germany, 2016.
20. Jansson, M.; Lenton, S.; Plivelic, T.S.; Skepö, M. Intercalation of cationic peptides within Laponite layered clay minerals in aqueous suspensions: The effect of stoichiometry and charge distance matching. *J. Colloid Interface Sci.* **2019**, *557*, 767–776. [CrossRef]
21. Jönsson, B.; Labbez, C.; Cabane, B. Interaction of Nanometric Clay Platelets. *Langmuir* **2008**, *24*, 11406–11413. [CrossRef]

22. Abraham, M.J.; van der Spoel, D.; Lindahl, E.; Hess, B.; The GROMACS development team. GROMACS User Manual Version 5.0.4. 2014. Available online: www.gromacs.org (accessed on October 2019).
23. Gutiérrez, G.; Johansson, B. Molecular Dynamics Study of Structural Properties of Amorphous $Al_2O_3$. *Phys. Rev. B* **2002**, *65*, 104202. [CrossRef]
24. Thuresson, A.; Jansson, M.; Plivelic, T.; Skpö, M. Temperature Response of Charged Colloidal Particles by Mixing Counterions Utilizing $Ca^{2+}/Na^{+}$ Montmorillonite as Model System. *J. Phys. Chem. C* **2017**, *121*, 7951–7958. [CrossRef]

© 2019 by the authors. Licensee MDPI, Basel, Switzerland. This article is an open access article distributed under the terms and conditions of the Creative Commons Attribution (CC BY) license (http://creativecommons.org/licenses/by/4.0/).

# Supplementary Materials: Polyelectrolyte-Nanoplatelet Complexation: Is it possible to predict the state diagram?

**Maria Jansson [1,*] and Marie Skepö [1,2,*]**

## 1. Composition of the PE-NP Complex

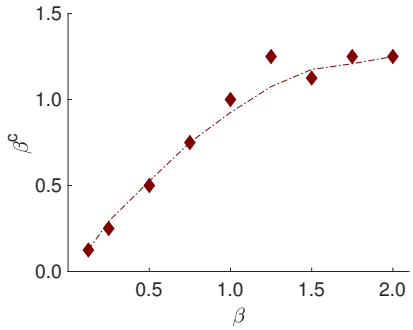


**Figure S1.** The complexed charge-ratio, $\beta^c$, as a function of the stoichiometric charge-ratio in the system, $\beta$. The dash-dotted line is an implemented smooth function.

## 2. Effect of PE Total Charge

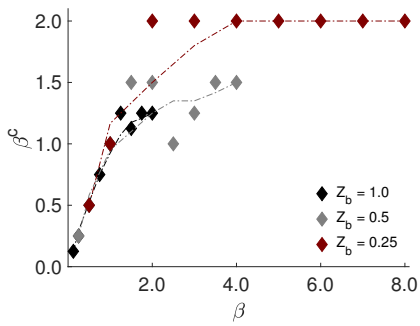


**Figure S2.** The complexed charge-ratio, $\beta^c$, as a function of the stoichiometric the charge-ratio, $\beta$, in the system. The dash-dotted lines are an implemented smooth function.

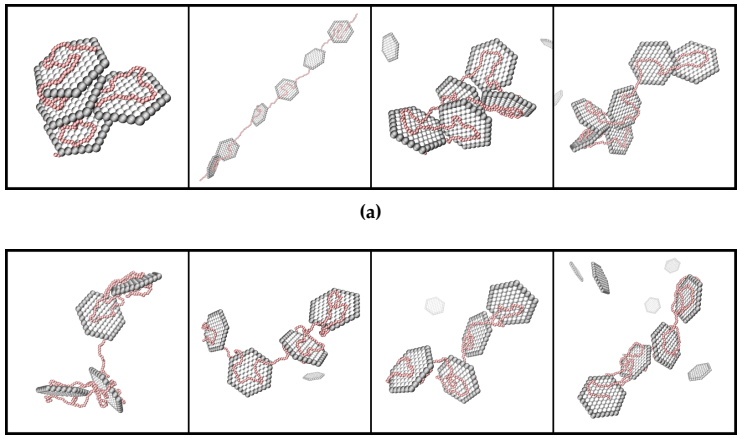

**(a)**

**(b)**

**Figure S3.** Representative snapshots of the structures with $\beta = 0.5$, 1.0, 1.5, and 2.0 (from left to right) for (a) $Z_b = 0.5$, and (b) $Z_b = 0.25$. The counterions are omitted for clarity, the NPs are shown in grey, and the PE is shown in red.

## 3. Effect of PE Flexibility

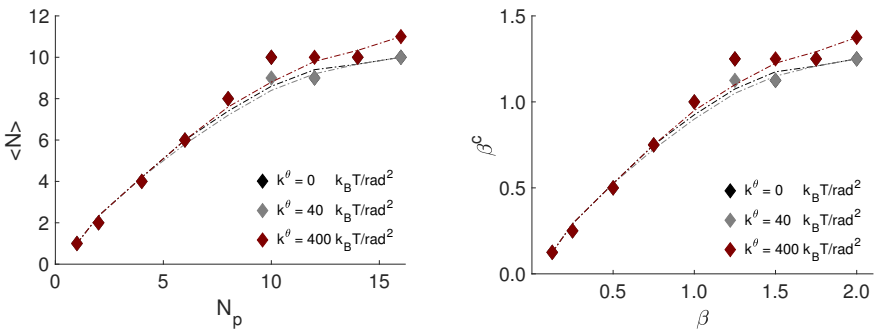


**(a)** **(b)**

**Figure S4.** (a) The average number of NPs complexed to the PE, $\langle N \rangle$, as a function of the number of NPs, $N_p$. (b) The complexed charge-ratio, $\beta^c$, as a function of the stoichiometric charge-ratio, $\beta$, in the system. The dash-dotted lines are an implemented smooth function.

**Table S1.** Number of NPs, $N_\mathrm{p}$, stoichiometric charge-ratio in the system, $\beta$, angular force constant, $k^\theta$, complexed charge-ratio, $\beta^c$, average number of NPs complexed to the PE, $\langle N \rangle$, and normalised radii of gyration, $R_g/R_g^0$, for the effect of the PE flexibility. (The unit of $k^\theta$ is $k_\mathrm{B}T/\mathrm{rad}^2$).

| $N_\mathrm{p}$ | $\beta$ | $k^\theta$ | $\beta^c$ | $\langle N \rangle$ | $R_g/R_g^0$ | $k^\theta$ | $\beta^c$ | $\langle N \rangle$ | $R_g/R_g^0$ | $k^\theta$ | $\beta^c$ | $\langle N \rangle$ | $R_g/R_g^0$ |
|---|---|---|---|---|---|---|---|---|---|---|---|---|---|
| 1 | 0.13 | 0 | 0.13 | 1 | 0.89 | 40 | 0.13 | 1 | 0.94 | 400 | 0.13 | 1 | 0.92 |
| 2 | 0.25 | | 0.25 | 2 | 0.77 | | 0.25 | 2 | 0.83 | | 0.25 | 2 | 0.81 |
| 4 | 0.50 | | 0.50 | 4 | 0.66 | | 0.50 | 4 | 0.62 | | 0.50 | 4 | 0.76 |
| 6 | 0.75 | | 0.75 | 6 | 0.66 | | 0.75 | 6 | 0.61 | | 0.75 | 6 | 0.60 |
| 8 | 1.00 | | 1.00 | 8 | 0.13 | | 1.00 | 8 | 0.60 | | 1.00 | 8 | 1.03 |
| 10 | 1.25 | | 1.25 | 10 | 0.65 | | 1.13 | 9 | 0.15 | | 1.25 | 10 | 1.02 |
| 12 | 1.50 | | 1.13 | 9 | 0.13 | | 1.13 | 9 | 0.17 | | 1.25 | 10 | 1.03 |
| 14 | 1.75 | | 1.25 | 10 | 0.65 | | 1.25 | 10 | 0.61 | | 1.25 | 10 | 1.03 |
| 16 | 2.00 | | 1.25 | 10 | 0.65 | | 1.25 | 10 | 0.66 | | 1.38 | 11 | 1.01 |

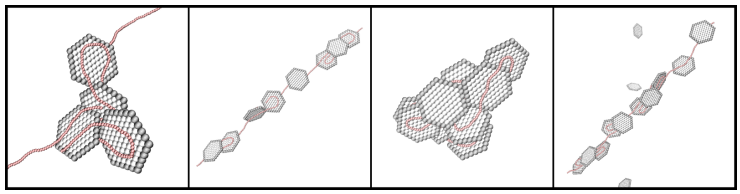

**(a)**

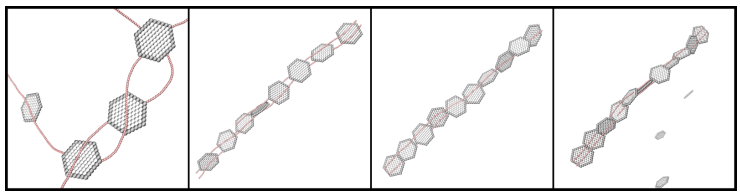

**(b)**

**Figure S5.** Representative snapshots of the structures with $\beta = 0.5$, 1.0, 1.5, and 2.0 (from left to right) for (a) $k^\theta = 40\ k_\mathrm{B}T/\mathrm{rad}^2$, and (b) $k^\theta = 400\ k_\mathrm{B}T/\mathrm{rad}^2$. The counterions are omitted for clarity, the NPs are shown in grey, and the PE is shown in red.

## 4. Effect of NP Charge and Rim

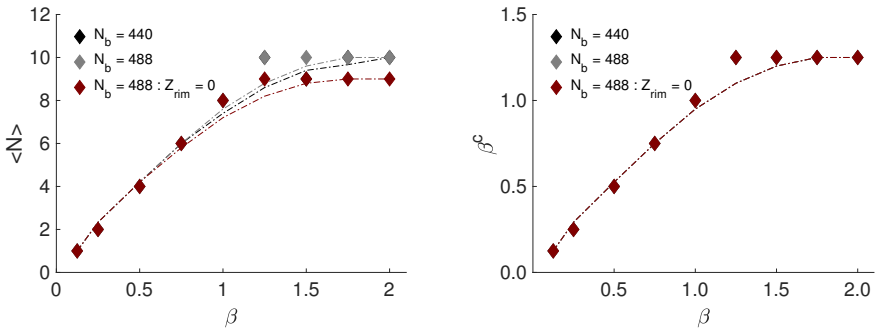


**Figure S6.** (a) The average number of NPs complexed to the PE, $\langle N \rangle$, as a function of the number of NPs, $N_\mathrm{p}$. (b) The complexed charge-ratio, $\beta^c$, as a function of the stoichiometric the charge-ratio, $\beta$, in the system. The dash-dotted lines are an implemented smooth function.

**Table S2.** Number of NPs, $N_\mathrm{p}$, stoichiometric charge-ratio in the system, $\beta$, complexed charge-ratio, $\beta^c$, number of PE beads, $N_\mathrm{b}$, average number of NPs complexed to the PE, $\langle N \rangle$, and normalised radii of gyration, $R_g/R_g^0$, for the effect of the NP charge and rim.

| $N_\mathrm{p}$ | $\beta$ | $\beta^c$ | $N_\mathrm{b}$ | $\langle N \rangle$ | $R_g/R_g^0$ | $N_\mathrm{b}$ | $\langle N \rangle$ | $R_g/R_g^0$ | $N_\mathrm{b}$ | $\langle N \rangle$ | $R_g/R_g^0$ |
|---|---|---|---|---|---|---|---|---|---|---|---|
| 1 | 0.13 | 0.13 | 440 | 1 | 1.01 | 488 | 1 | 1.01 | 488 | 1 | 0.94 |
| 2 | 0.25 | 0.25 | | 2 | 0.92 | | 2 | 0.92 | with $Z_\mathrm{rim} = 0$ | 2 | 0.78 |
| 4 | 0.50 | 0.5 | | 4 | 0.53 | | 4 | 0.53 | | 4 | 0.38 |
| 6 | 0.75 | 0.75 | | 6 | 0.34 | | 6 | 0.34 | | 6 | 0.16 |
| 8 | 1.00 | 1.00 | | 8 | 0.14 | | 8 | 0.14 | | 8 | 0.12 |
| 10 | 1.25 | 1.25 | | 10 | 0.13 | | 10 | 0.13 | | 9 | 0.12 |
| 12 | 1.50 | 1.25 | | 9 | 0.13 | | 10 | 0.13 | | 9 | 0.12 |
| 14 | 1.75 | 1.25 | | 10 | 0.13 | | 10 | 0.13 | | 9 | 0.12 |
| 16 | 2.00 | 1.25 | | 10 | 0.13 | | 10 | 0.13 | | 9 | 0.13 |

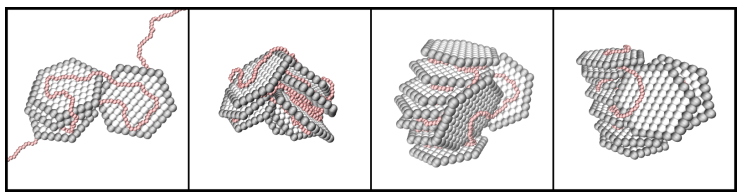

**Figure S7.** Representative snapshots of the structures with $\beta = 0.5$, 1.0, 1.5, and 2.0 (from left to right) for $N_\mathrm{b} = 488$ with $Z_\mathrm{rim} = 0$. The counterions are omitted for clarity, the NPs are shown in grey, and the PE is shown in red.

Printed by Media-Tryck, Lund 2020 NORDIC SWAN ECOLABEL 3041 0903

ISBN: 978-91-7422-754-3

Theoretical Chemistry
Department of Chemistry
Faculty of Science
Lund University